OCCASION

This publication has been made available to the public on the occasion of the 50th anniversary of the United Nations Industrial Development Organisation.

DISCLAIMER

This document has been produced without formal United Nations editing. The designations employed and the presentation of the material in this document do not imply the expression of any opinion whatsoever on the part of the Secretariat of the United Nations Industrial Development Organization (UNIDO) concerning the legal status of any country, territory, city or area or of its authorities, or concerning the delimitation of its frontiers or boundaries, or its economic system or degree of development. Designations such as "developed", "industrialized" and "developing" are intended for statistical convenience and do not necessarily express a judgment about the stage reached by a particular country or area in the development process. Mention of firm names or commercial products does not constitute an endorsement by UNIDO.

FAIR USE POLICY

Any part of this publication may be quoted and referenced for educational and research purposes without additional permission from UNIDO. However, those who make use of quoting and referencing this publication are requested to follow the Fair Use Policy of giving due credit to UNIDO.

CONTACT

Please contact publications@unido.org for further information concerning UNIDO publications.

For more information about UNIDO, please visit us at www.unido.org

UNITED NATIONS INDUSTRIAL DEVELOPMENT ORGANIZATION
Vienna International Centre, P.O. Box 300, 1400 Vienna, Austria
Tel: (+43-1) 26026-0 · www.unido.org · unido@unido.org

HYDRODYNAMIC

Design Guide

for SMALL FRANCIS
and PROPELLER TURBINES

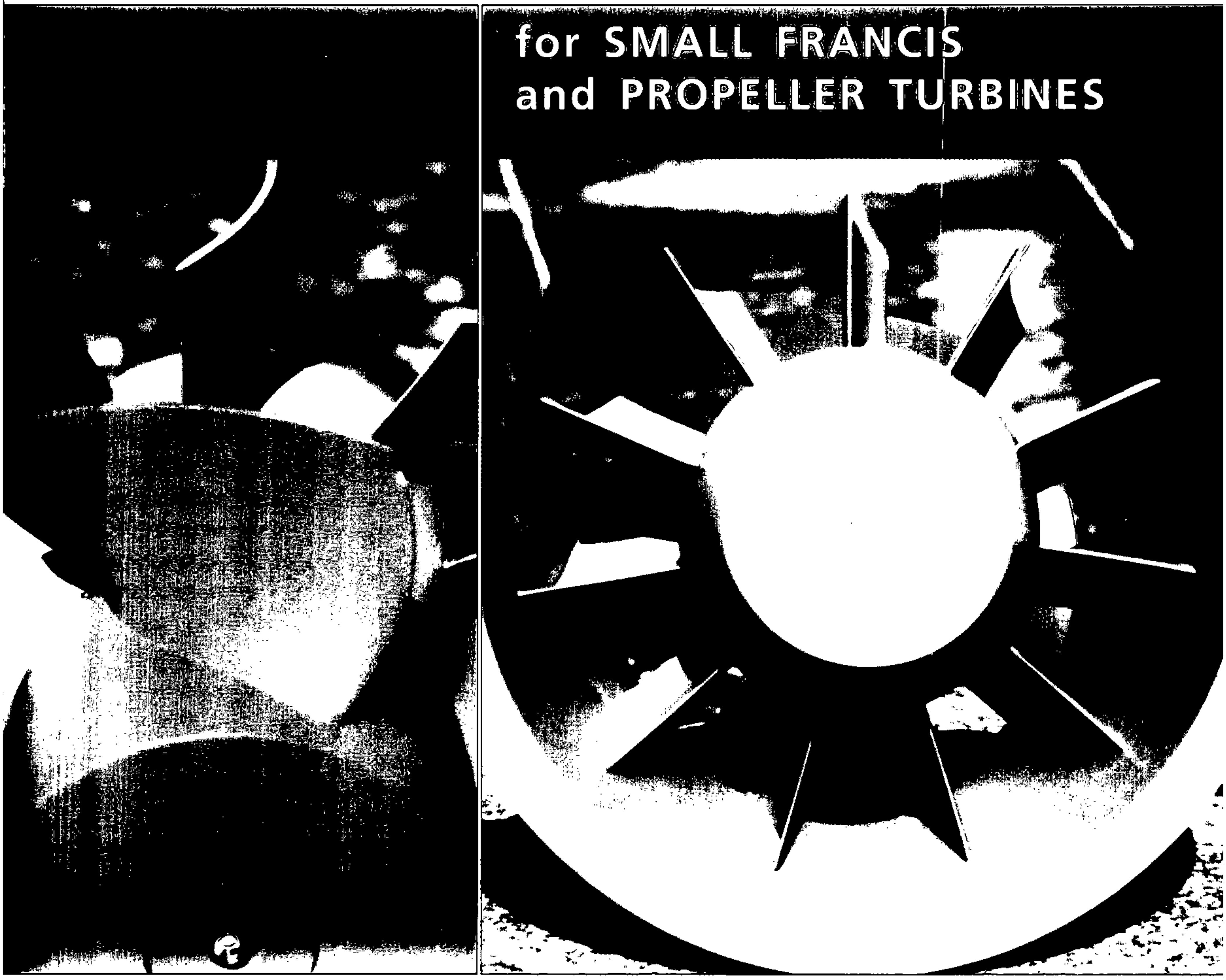

UNITED NATIONS INDUSTRIAL DEVELOPMENT ORGANIZATION

economy environment employment

R. Hothersall

Hydrodynamic design guide for small Francis and propeller turbines

G. Anestis and C. Gürkök *(editors)*

UNITED NATIONS INDUSTRIAL DEVELOPMENT ORGANIZATION
VIENNA, AUSTRIA
2004

Copyright © 2004 United Nations Industrial Development Organization

The description and classification of countries and territories in this publication and the arrangement of the material do not imply the expression of any opinion whatsoever on the part of the Secretariat of the United Nations Industrial Development Organization concerning the legal status of any country, territory, city or area, or of its authorities, or concerning the delimitation of its frontiers or boundaries, or regarding its economic system or degree of development. Designations such as "developed", "industrialized" and "developing" countries and "newly industrialized countries" are intended for statistical convenience and do not necessarily express a judgment about the stage reached by a particular country or area in the development process.

The mention of firm names or commercial products does not imply endorsement by UNIDO.

Material in this publication may be freely quoted or reprinted, but acknowledgement is requested, together with a copy of the publication containing the quotation or reprint.

The United Nations Industrial Development Organization, UNIDO, was established in 1966 and became a specialized agency of the United Nations in 1985. As part of the United Nations common system, UNIDO is working to alleviate poverty by enhancing the productivity of small- and medium-sized enterprises in developing countries and countries in transition. Productivity enhancement is central to poor countries achieving the Millennium Development Goals. UNIDO's core competencies to increase productivity, create jobs and ensure social progress, lie in promotion of the private sector, agro-industrial development, investment promotion, building export capacity, management of technology, environmental problems and the use of energy.

Enhancing the productivity of small- and medium-sized enterprises in developing countries is a vital part of the development agenda. But in broader terms of international development assistance, UNIDO Director-General Carlos Magariños says, "We have one single agenda, and the actions taken by each of the agencies in the multilateral system must address this agenda".

Contents

Nomenclature V

Foreword IX

Preface XI

1 Introduction to water turbines 1
- 1.1 Turbine types 1
- 1.2 Turbine selection 9

2 Overview of the turbine design process 11
- 2.1 Design procedure for Francis turbines 11
- 2.2 Design procedure for propeller turbines 13

3 Basic theory 15
- 3.1 Net head 16
- 3.2 Specific speed and other non-dimensional parameters 16
- 3.3 Conservation of momentum 19
- 3.4 Conservation of mass 22
- 3.5 Conservation of energy 22
- 3.6 Guide vane function 22
- 3.7 Simple radial equilibrium 23
- 3.8 Blade circulation, blade loading, incidence and deviation 25
- 3.9 Mean streamline analysis 32

4 Cavitation 37
- 4.1 Turbine setting 38
- 4.2 Cavitation damage 40

5 Draft tube design 45

6 Performance characteristics 55

7 Designing efficient turbines 61
- 7.1 Hydrodynamic design guidelines 62
- 7.2 Losses 63
- 7.3 Leakage, tip clearance and disk friction loss 70

8 Turbine envelope geometry 73

9 Throughflow calculations 79
9.1 Stream function theory 81
9.2 Meridional streamline library for Francis turbines 85
9.3 Throughflow analysis of tubular type propeller turbines .. 86

10 Blade design 91
10.1 Francis blade design by Prasil transform 91
10.2 Francis blade design by the mean streamline method 95
10.3 Propeller blade design 99
10.4 Guide vanes 100

11 Spiral casing and stay vanes 105
11.1 Spiral casing design method 106
11.2 Stay vane design guidelines 109

12 Thrust loads, seals and bearings 111
12.1 Thrust load analysis 111
12.2 Shaft seals 116
12.3 Main bearings 116

13 Manufacturing methods and materials 119
13.1 Manufacturing methods 119
13.2 Materials 123

14 Propeller design example 127

15 Francis turbine design example 141
15.1 Specific speed and design flowrate 141
15.2 Runner envelope 143
15.3 Draft tube design, setting and cavitation conditions 144
15.4 Runner design 146
15.5 Guide vane design 151
15.6 Stay vane inlet and outlet diameters 153
15.7 Spiral casing design 153
15.8 Guide vane & stay vane matching 155

References 157

Nomenclature

General

η efficiency
ν kinematic viscosity
Ω angular velocity (fluid)
ω angular velocity (blading)
ω vorticity
ψ stream function
ψ_T Zweifel loading coefficient
ρ density
σ cavitation parameters
σ slip factor
C_F skin friction coefficient
H_n net head
N angular velocity (rpm, rev/min)
n_s $N\sqrt{P}/H_n^{5/4}$
n_q $N\sqrt{Q}/H^{3/4}$
P power output
p pressure
Q volume flow rate
U blade speed

Blade angles

χ_1 blade inlet angle *
χ_2 blade outlet angle *
θ angle in the circumferential direction
θ camber
ζ stagger
ϕ streamline inclination to axial direction

Constants

g acceleration due to gravity

Flow variables – rotating frame

δ deviation (angle between outlet flow angle and blade outlet angle, $\delta = \alpha_2 - \chi_2$ or $\delta = \beta_2 - \chi_2$ for guide vanes or runner respectively

i incidence (angle between inlet flow direction and blade inlet direction, $i = \alpha_1 - \chi_1$ or $i = \beta_1 - \chi_1$ for guide vanes or runner respectively)

β_1 flow inlet angle *

β_2 flow outlet angle *

W_1 inlet flow velocity relative to blade

W_2 outlet flow velocity relative to blade

Flow variables – stationary frame

α_1 flow inlet angle

α_2 flow outlet angle

V absolute velocity

V_m meridional velocity, $V_m = \sqrt{V_x^2 + V_R^2}$

$V_{\theta 1}$ tangential component of velocity into blade row, likewise for V_2, W_1, W_2, etc.

V_{r1} radial component of velocity into blade row, likewise for V_2, W_1, W_2, etc.

V_{x1} axial component of velocity into blade row, likewise for V_2, W_1, W_2, etc.

Geometric variables

A cross sectional area

D diameter

σ solidity c/s

B spanwise passage width

c blade chord

m distance in meridional direction $\mathrm{d}m = \sqrt{\mathrm{d}x^2 + \mathrm{d}r^2}$

s blade pitch

s distance along streamline $\mathrm{d}s = \sqrt{\mathrm{d}x^2 + \mathrm{d}r^2 + r^2\mathrm{d}\theta^2}$

t blade thickness

x distance in the axial direction

y distance in the pitchwise direction

z distance normal to x and y

Z number of blades

Subscripts

$1/1$ full load
1 blade inlet
2 blade exit
2 draft tube inlet
3 draft tube outlet
sat saturation condition
θ circumferential direction
$\wedge$ peak efficiency
$\perp$ perpendicular discharge
gv guide vane
m meridional direction
r radial direction
sv stay vane
atm atmospheric pressure or head
dt draft tube

Superscripts

i inner
o outer

* Unless otherwise stated, all blade and flow angles are taken from the circumferential direction within a meridional stream surface.

SI units are generally used unless otherwise stated. The units of power are kW. Other variables are defined in the text.

Foreword

As the UN agency charged with promoting industrial development, UNIDO focuses on an increase in productivity growth, with the aim facilitating client countries' efforts to attain sustainable economic growth. Energy is central to achieving the interlinked economic, social and environmental goals of sustainable economic growth. But in realizing this important target, the kinds of energy generated and the ways in which it is used requires new perspectives.

Since publication in 1987 of the Bruntland Report, *Our Common Future,* there have been calls to rethink radically the relationship between societies and the environment in general, and in particular the relationship between industry and the environment. The dangers of environmental degradation caused by human activity are, by now, widely acknowledged. Therefore, the international community has embarked on concerted efforts to understand the nature of these issues and to implement policies, programmes and projects to mitigate the most urgent of these issues.

Against this background of growing environmental awareness, UNIDO has become a partner to the Global Environment Facility (GEF). Established in 1991, GEF helps developing countries and countries with economies in transition, fund projects and programmes that protect the global environment. GEF grants support projects related to biodiversity, climate change, international waters, land degradation, ozone layer depletion, and persistent organic pollutants (POPs). As a partner of GEF with the status of an Executing Agency with Expanded Opportunities, UNIDO has been involved in execution of projects in the areas of climate change, POPs and international waters.

Pollution factors appearing in those areas affect not only human beings. They damage the environment so severely that the existence of many other forms of life is threatened in addition to the inorganic environment being adversely affected through such mechanisms as soil erosion or climate change (i.e. greenhouse gases emissions leading to enhanced global warming).

Anthropogenic carbon dioxide emitters, resulting from the increasing combustion of fossil fuels that growing industrialization has brought with it in the last 150 years, have contributed to a measurable increase in the carbon dioxide content of the atmosphere, with a consequent increase in global average temperature levels. Moreover, extensive deforestation in tropical rain forests and in the sub-arctic taiga, which previously contained huge carbon deposits, has further increased the release of carbon to the atmosphere as well as reducing the potential for carbon sequestration.

Technical means of extracting carbon dioxide from air and water exist and could be used for reducing carbon dioxide accumulation in the troposphere, but those means are very costly and, therefore, not practical. It is possible to conserve energy by its more efficient efficient use or through renewable sources of energy. . Renewable energy can also provide commercially attractive solutions to meet specific needs for energy services, create employment opportunities and offer possibilities for local manufacturing.

Hydroelectricity is one of the most promising sources of renewable energy. It is non-exhaustible, non-polluting and often more economically attractive than other options. Although the number of hydropower plants that can be built is finite, only a third of the potential sites deemed economically feasible have been utilized.

Energy is a prerequisite for sustainable development and to combat poverty. Supplying modern energy services to the two billion persons who still cook with traditional solid fuels and lack access to commercial energy is one of the most pressing problems facing humanity today. The vast majority of them live in rural areas of the poorest regions of the world. Living standards there can be significantly improved by shifting from direct combustion of biomass fuels to clean, efficient liquid or gaseous fuels and electricity. Because of the problems of supplying grid electricity for small, scattered, peak loads, decentralized electricity generation is becoming more attractive. As small-scale hydropower, is a locally available resource which can be exploited to deliver electricity or mechanical power to rural areas, it figures prominently among the decentralized energy generation systems.

Through its rural energy projects and programmes, UNIDO promotes the productive (income generating) uses of energy for rural ecologically sustainable development and poverty alleviation. In addition, UNIDO's energy programmes and projects cover capacity building activities related to renewable energy technology as well as assembly and manufacture of energy equipment/structures in developing countries.

This book is based mainly on the content and findings of a GEF funded project on renewable energy and energy capacity building based in Sri Lanka. The project was implemented by UNIDO on behalf of the United Nations Development Programme (UNDP) and the Government of Sri Lanka. The project had two main areas of focus, firstly to build the country's professional capacity in the renewable energy and energy efficiency industry for design and implementation of energy projects and secondly, to encourage private sector investment in selected projects on renewable energy sources including small and mini hydro. Among the activities geared towards this goal, a number of courses on water turbine design were held and the content of these courses and their related activities (combined with findings from other relevant UNIDO funded projects in Ecuador and Mali) serve as basis for the preparation of this book.

Editors

Preface

This book has been developed mainly from courses on water turbine design that I conducted ass UNIDO Consultant in Sri Lanka during the years 2000, 2001 and 2002.

The aim of this book is to assist engineers to design the flow passages and blade shapes of small Francis and propeller turbines with power outputs typically on the order of a few hundred kilowatts. Why only propeller and Francis turbines? Basically, there is a gap in the literature in this area with the last comprehensive book on water turbine design, *Hydraulic Turbines, Their Design and Equipment*" by Miroslav Nechleba, published in 1957. Nechleba's book is an excellent design guide and highly recommended as a companion to this volume is based on 1940's technology.

This book differs from earlier one in several respects. It is not as comprehensive and no new proprietary information has been added. The hydrodynamic methods presented in this publication are a mixture of recent technology and some 1950s' and 1960s' methods and generally compliment or supersede Nechleba's procedures. However, some of the specific design guideline information, such as flow envelope variation with specific speed, has been obtained from open literature and may not represent the latest design practice.

Modern technology makes use of proprietary methods, which include the use of quasi-3D and full-3D computational fluid dynamics software (see www.aotearoasoftware.com for a typical approach), together with comprehensive laboratory test data. Modern methods, with regard to water turbine design, have improved efficiencies and cavitation margins slightly. They have also improved the understanding of the complexities of flow. The main advantages of using modern methods primarily lie, however, with significantly reducing design and manufacturing lead times.

An emphasis is placed in this book on gaining a physical understanding of what is happening within these machines. The mathematics is kept as simple as possible.

There are some obvious dangers to treating aspects of this subject superficially, namely the possibility that a poor design will result through lack of theoretical understanding. To improve theoretical understanding, references are supplied in the text to point the way for further study. It also makes sense to start by designing small turbines and build up experience gradually.

This book contains references to specific manufacturers' products, to provide designers with a starting point in the design process. It has not been done to endorse any particular product. There may be better products available and the designer should carry out his own investigations to select suitable products.

This book does not attempt to structurally size the turbine components, though some consideration is given to manufacturing methods, to suitable turbine materials and sealing geometry. The structural design methods of Nechleba [1957] and Engineering Monograph No. 30, Bureau of Reclamation [1962] can be used for structural design. Modern finite element methods should also be considered.

Two design examples are presented in this book: a Francis turbine with a spiral casing and a propeller turbine. At the time of publication, neither of these turbines had been put into service. This is obviously a disadvantage as the proof of the pudding is in the eating, a saying of relevance, for a design guide that purports to be something of a cookbook.

My thanks go to UNIDO for sponsoring my involvement in this publication. Further, special thanks go to Dr. Cahit Gürkök and Dr. Georgios Anestis for their guidance, support and inputs. Dr. Jonathan Harrington and Mark Carey proof-read my text, corrected my grammar and typeset most of the book. Richard Cave and Ra Cleave worked on the two turbine designs, both of which are in the process of being manufactured. Artwork was produced by Craig McNeill and Tristan Gilmour. Boio John assisted with the typing. Without the enthusiastic and committed involvement of these people, this book could not have been completed.

A number of manufacturers and organizations kindly gave their permission to use their photographs or artwork. These organisations are: BHR Group United Kingdom, Dover Publications, GE Hydro Norway, International Electrotechnical Commission (IEC) Geneva Switzerland, International Water Power and Dam Construction Wilmington Publishing, Ossberger Weissenburg Germany, Trustpower New Zealand, VA TECH HYDRO Z¨urich, Voith Esac Hydro, and Voith Siemens Hydro Power Generation Heidenheim Germany. Figures 1.1 c, 1.2 a, b, c, 1.6, 3.9, 3.10, 4.2, 5.2, 5.5 a, b, 7.5, 12.6, 13.1 b, 13.2 a, 13.3 and 15.1 are copyright Aotearoa Software Ltd. Individual acknowledgements appear in the text as required.

Much of my understanding of turbomachinery design was gained while working under the late Harland Topham. I regret that he is not still here to assist in reviewing this work. I also acknowledge useful inputs arising from discussions with Dr Ian Huntsman which clarified my ideas on radial inflow turbomachinery. Ian Lees, of Trustpower NZ Ltd; kindly took time out to discuss operation and maintenance issues of hydroelectric plant, an area of which I know little. Prof. Dr. Thomas Staubli reviewed the material in the book. His contributions have been most valuable.

This book was written in a very short time frame -weeks rather than months.

Mistakes will, inevitably, come to light. I am sure there are certainly better procedures and design approaches in the public domain that could have been included. If there is a second edition - as I hope there will be - I should be grateful for contributions or corrections that will improve the next edition.

Rik Hothersall
Christchurch, New Zealand

1 Introduction to water turbines

Common turbine types in use for power outputs below 5 MW are Pelton, turgo, Francis, Kaplan and propeller turbines. Below 500kW, the cross–flow turbine could also be considered. This Chapter provides a brief description of each turbine type and the issues involved in turbine selection.

1.1 Turbine types

In Figures 1.1–1.3 the varieties of turbines in common use are illustrated.

1.1.1 Impulse turbines

Pelton, turgo and cross–flow turbines have free surface flow on their runners or wheels and are classified as impulse turbines. Impulse turbines convert all the net head into kinetic energy in a nozzle. The impulse runners or wheels rotate in air and not water. Generally the impulse turbines do not have draft tubes (see Chapter 5) whereas Kaplan, Francis and propeller turbines (reaction turbines) do. It is possible, with impulse turbines, to operate in a sealed chamber and make use of a pseudo draft tube that uses some of the head between the runner and the tailrace. This is, however, not common.

Figure 1.4 plots turbine application areas on a logarithmic scale of head against flowrate. Figure 1.4 is not an exact statement of turbine application regimes; many factors contribute to the selection of a particular turbine for a given site.

If the water contains abrasive materials, Pelton and turgo wheels may be preferred due to easier maintenance of worn components. The use of a spear valve to control the flow is very efficient and turbine part load efficiencies for Pelton and turgo wheels are generally better than reaction turbines (with the exception of the Kaplan turbine). See Figure 1.5. Pelton and turgo wheels can also utilize deflectors for load rejection and governing. This feature is not available for cross–flow or any of the reaction turbine types.

The cross–flow turbine is unusual in many regards. It has an efficiency, with net head defined as per IEC 60193 [1999], between 70 and 80%. It competes well with Francis and Pelton turbines for outputs less than 500 kW.

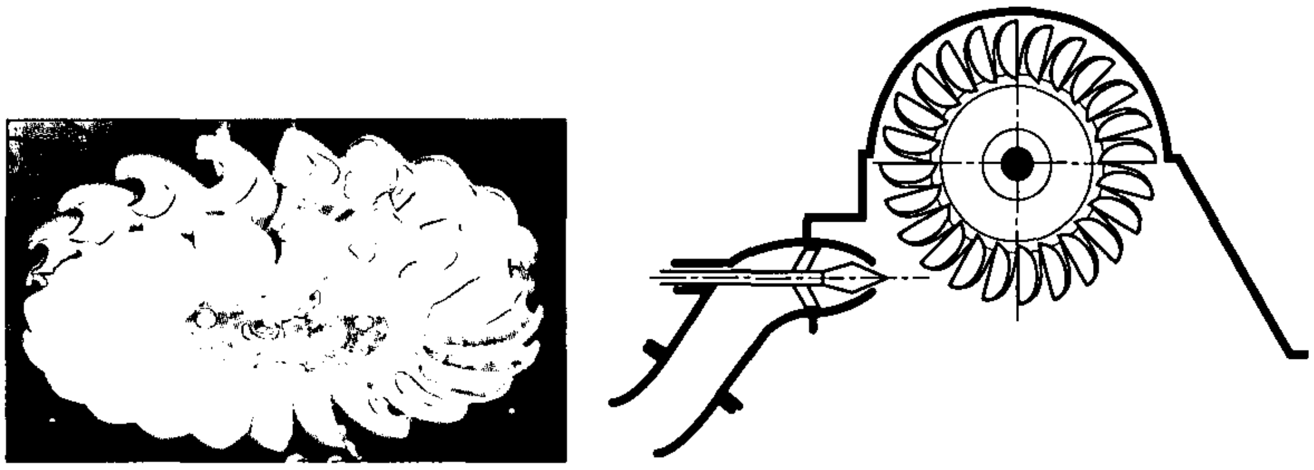

(a) Vertical Pelton wheel, 5 nozzles. (Reproduced courtesy VA TECH HYDRO)

(b) Horizontal Pelton wheel schematic.

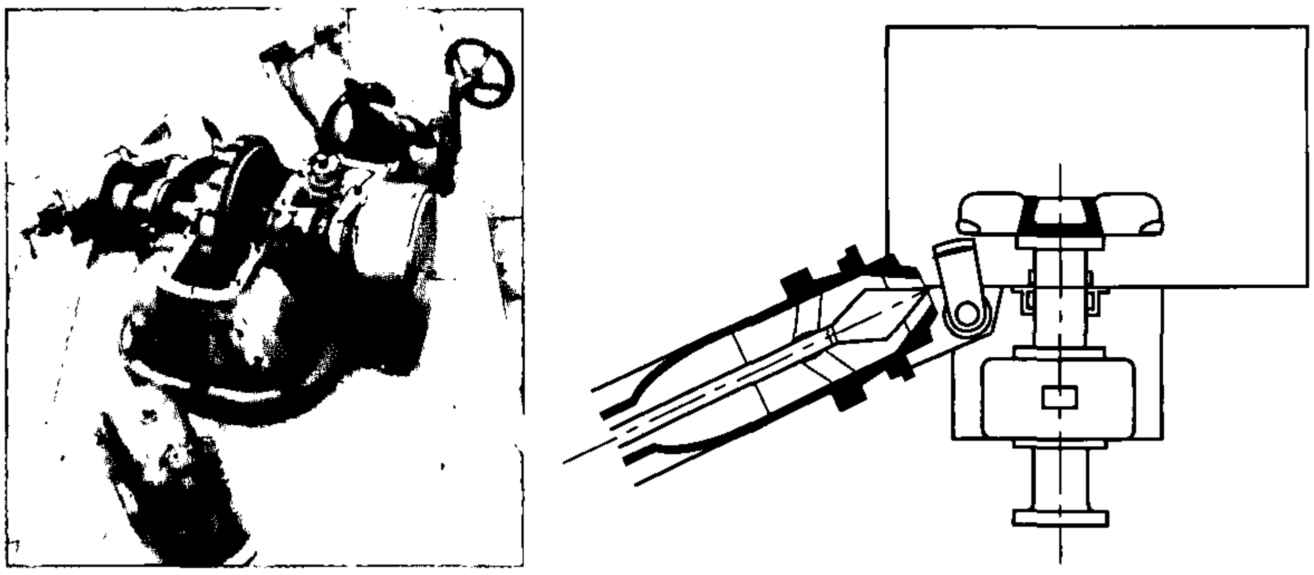

(c) Pre-war Turgo wheel, Bulolo gold fields, Papua New Guinea.

(d) Turgo wheel schematic.

Fig. 1.1. Turbine types.

Above 500kw, the lower efficiency of the cross-flow may result in alternative turbine types being more economic. By increasing the runner width only, a wide range of flows for a given head can be accommodated. Some actual cross-flow applications are superimposed on Figure 1.4. The runner is easy to manufacture but the runner shape is potentially structurally weak and needs to be designed carefully to avoid fatigue failure. The flow control device is in the form of a single or double vane (2/3, 1/3 width). This vane operates surprisingly efficiently using the Coanda principle; specifically, at part load the flow remains attached to the lower surface of the flow control vane, refer to Figure 1.6 (b). This effect becomes even more marked at lower flows.

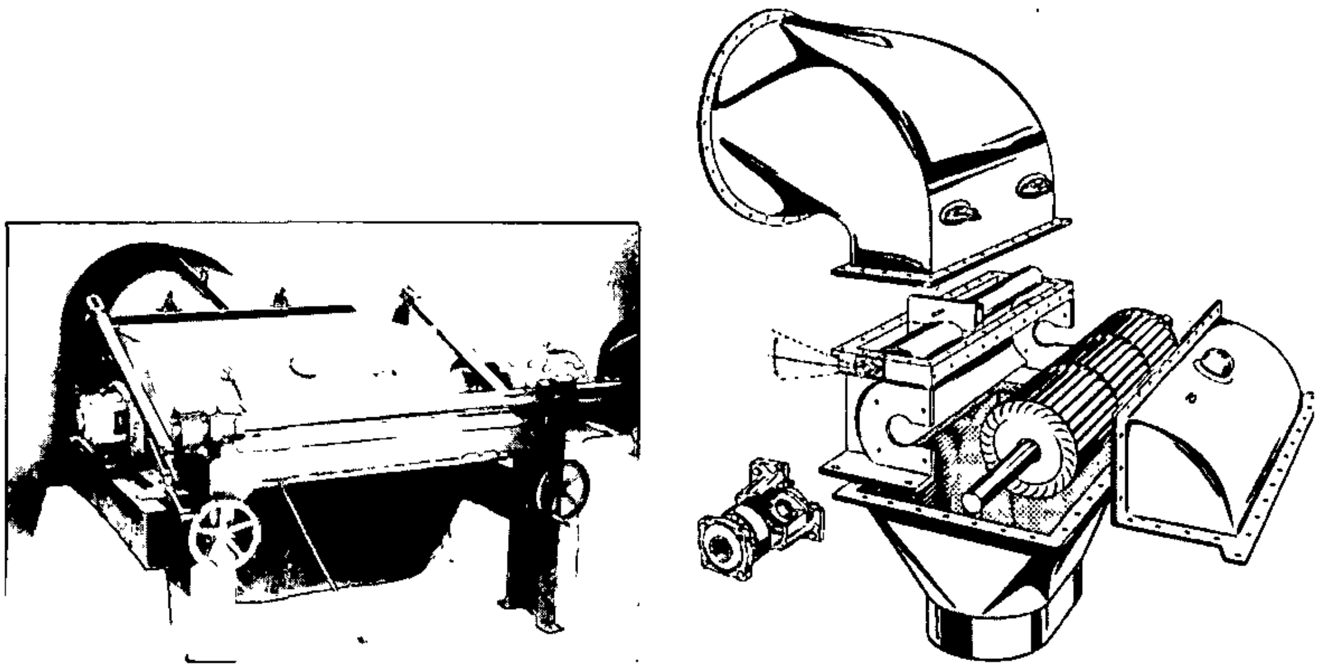

(a) Cross-flow turbine with double regulation.

(b) Exploded view of cross-flow turbine. (Reproduced courtesy Ossberger)

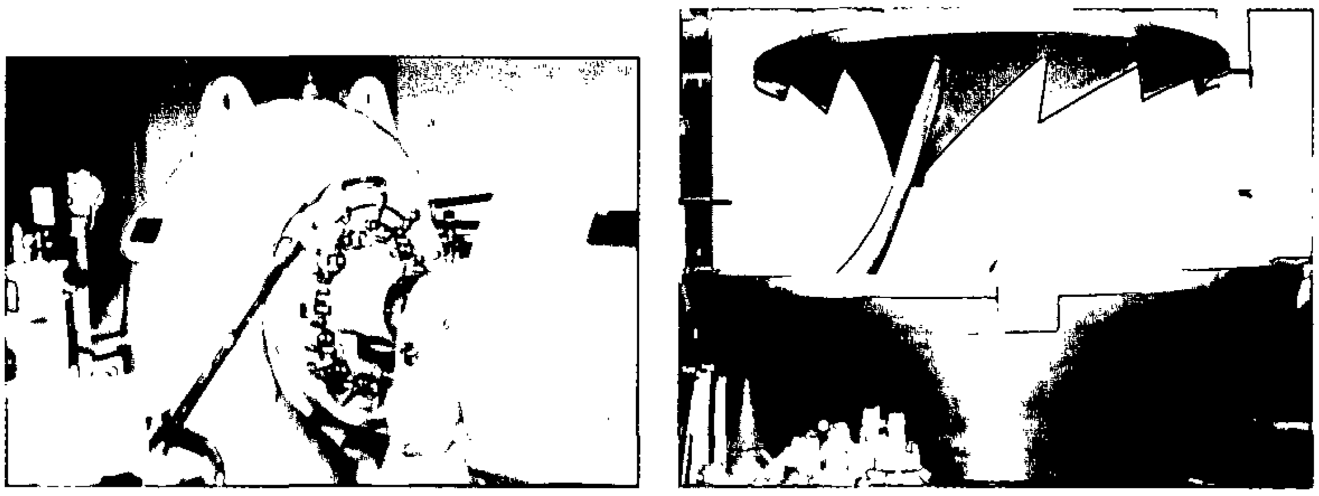

(c) Francis turbine, horizontal arrangement.

(d) Francis runner, Benmore, New Zealand.

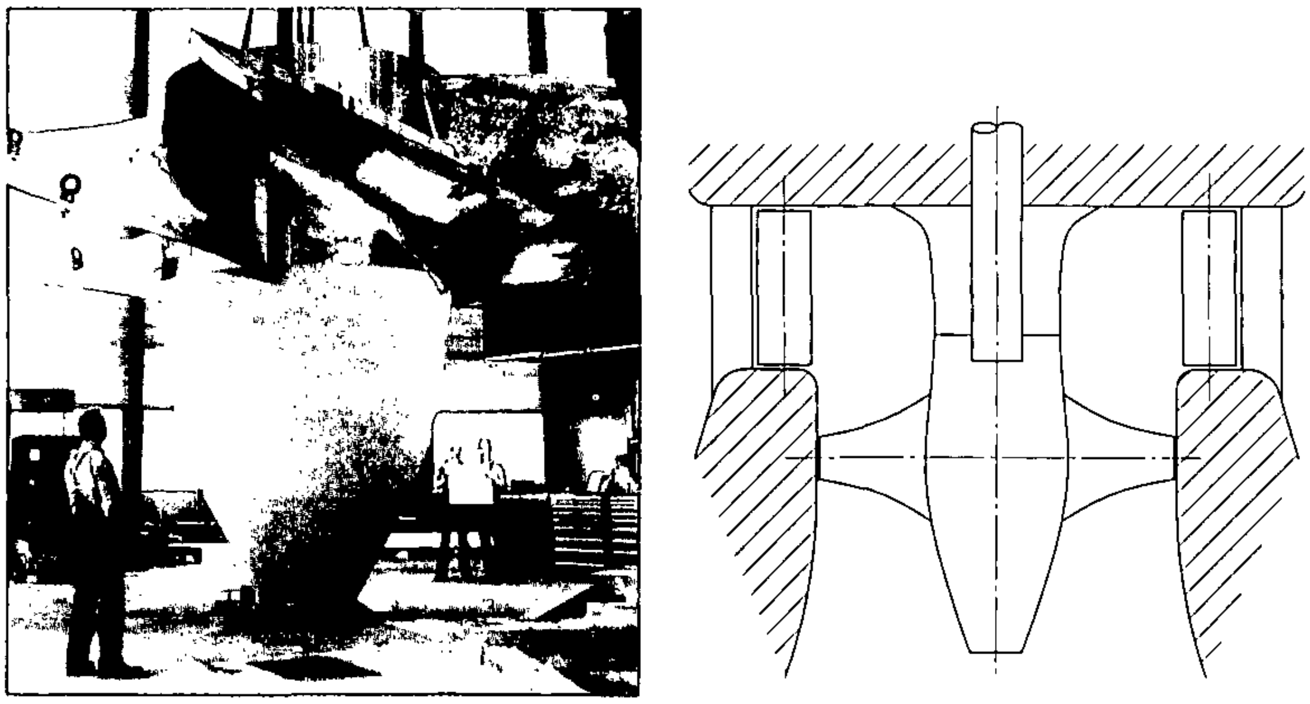

(e) Kaplan runner. (Reproduced courtesy VA TECH HYDRO)

(f) Kaplan cross-sectional schematic.

Fig. 1.2. Turbine types (cont.).

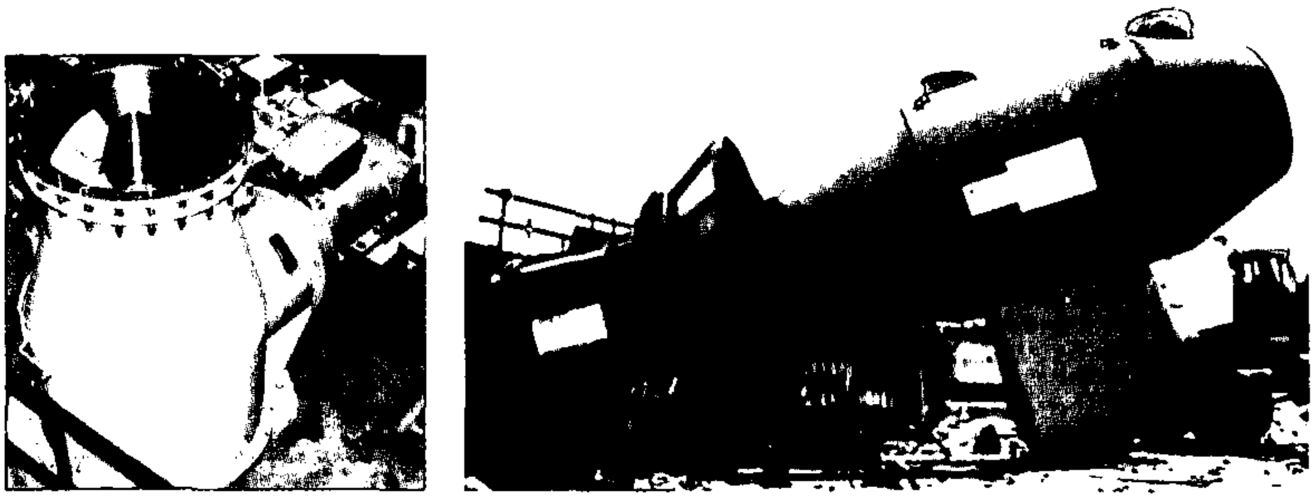

(a) Propeller turbine, right-angles drive.

(b) Propeller turbine, tubular arrangement. (Reproduced courtesy Voith Esac Hydro)

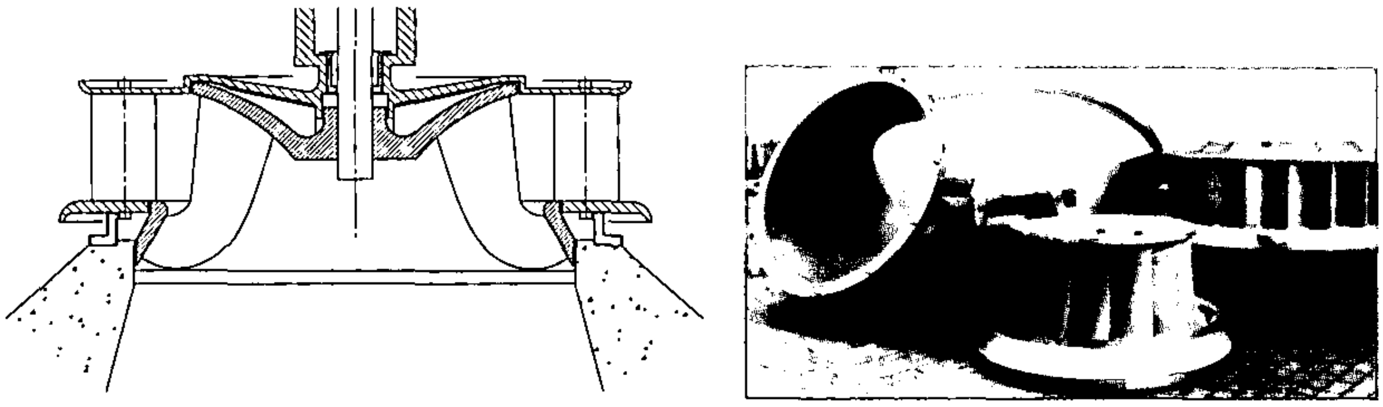

(c) Open flume Francis cross-sectional schematic. (Reproduced courtesy Voith Siemens)

(d) Open flume Francis turbine components. (Reproduced courtesy Voith Siemens)

Fig. 1.3. Turbine types (cont.).

1.1.2 Reaction turbines

Reaction turbines, comprising Francis, Kaplan and Propeller type turbines, operate with their flow passages full, ie no free surface. There is a conversion of pressure into velocity within the runner. This contrasts with impulse turbines where all the pressure is converted into velocity within a nozzle outside of the runner.

The Francis turbine has two basic variants, the more common spiral casing design and the open flume design. Turbines with relatively low power outputs are likely to be horizontally mounted. It is also possible that very small Francis turbines, say under 200 kW, may also be considered for vertical mounting. Refer to Figure 1.7.

Kaplan turbines have either rectangular concrete (occasionally steel-lined) scroll casings or the pressure vessel type spiral (scroll) casings discussed in

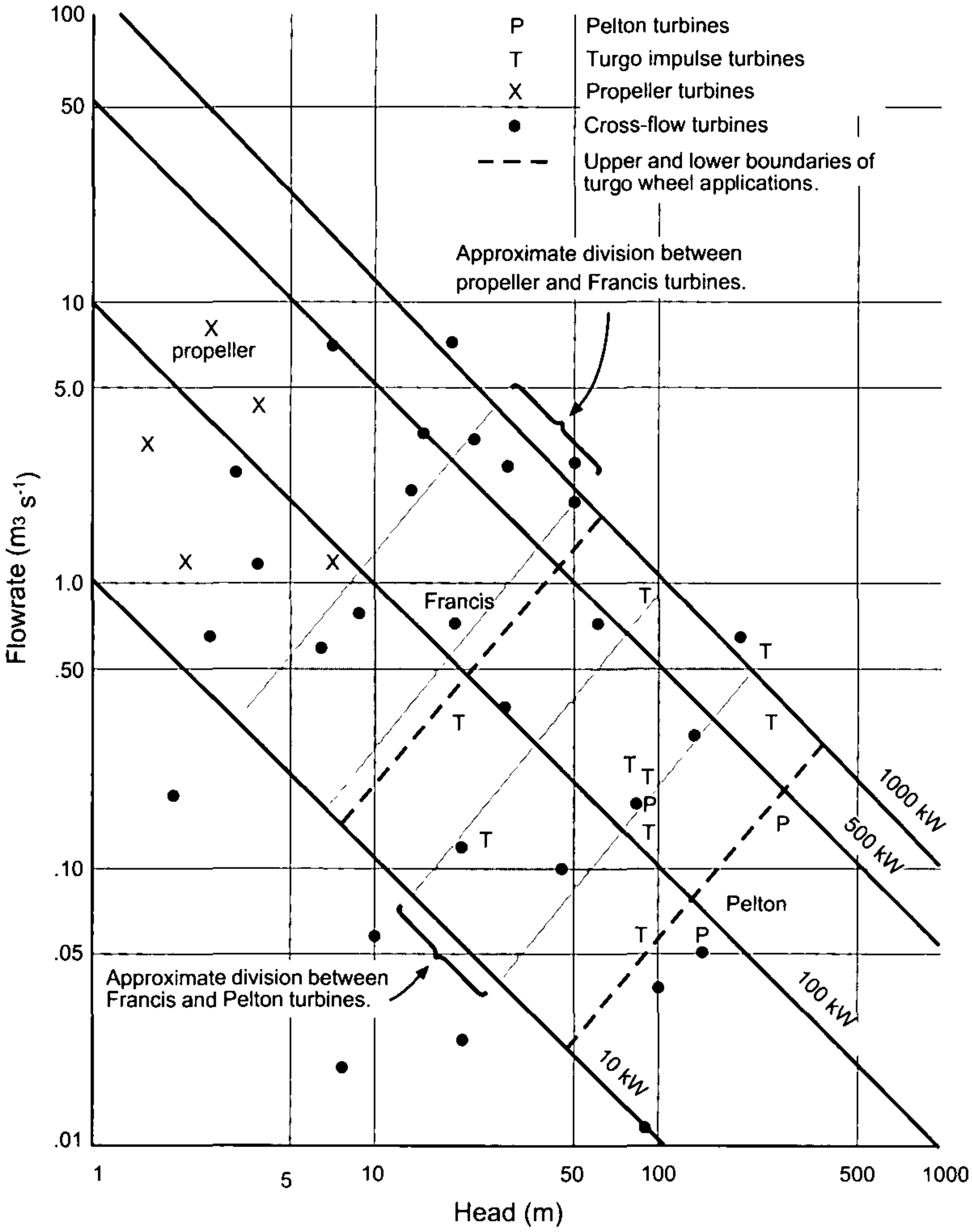

Fig. 1.4. Turbine application ranges for outputs of one megawatt or less.

Chapter 11. The Kaplan turbine will usually have adjustable blades and adjustable guide vanes. This dual combination results in good part load efficiencies and greater manufacturing expense. If a Kaplan turbine has fixed blades, then it will sometimes be referred to as a propeller turbine.

Tubular propeller turbines have guide vanes in place of a spiral casing. These turbines are sometimes referred to as bulb turbines if the generator is placed within a bulb in the flow path. Three tubular propeller turbine

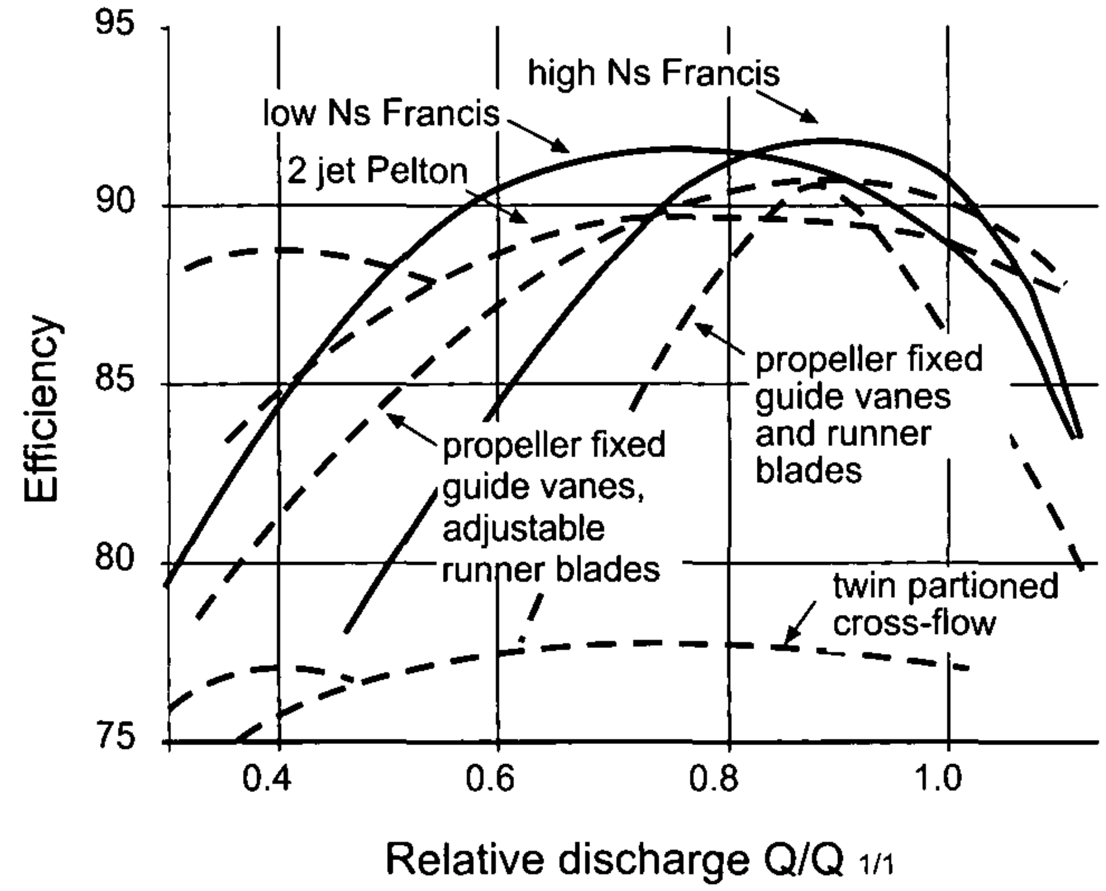

Fig. 1.5. Part load efficiencies of small water turbines.

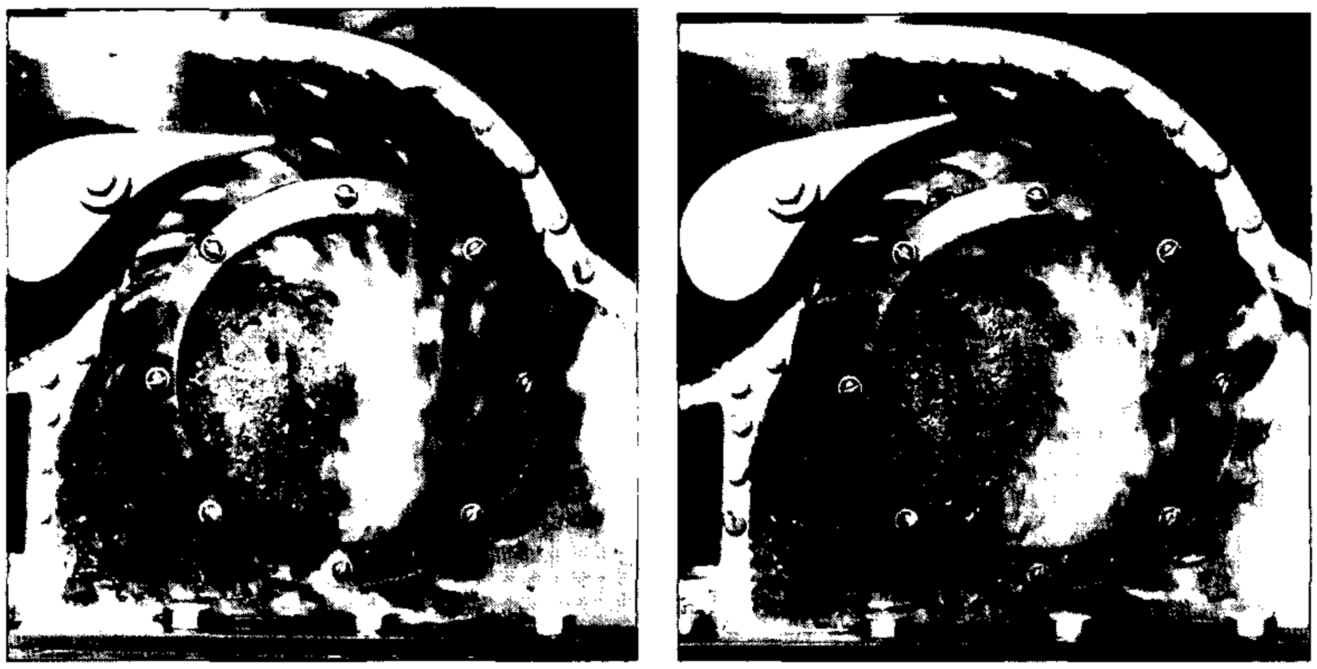

(a) Full flow.

(b) $^3/_4$ flow.

Fig. 1.6. Flow patterns in a cross-flow turbine.

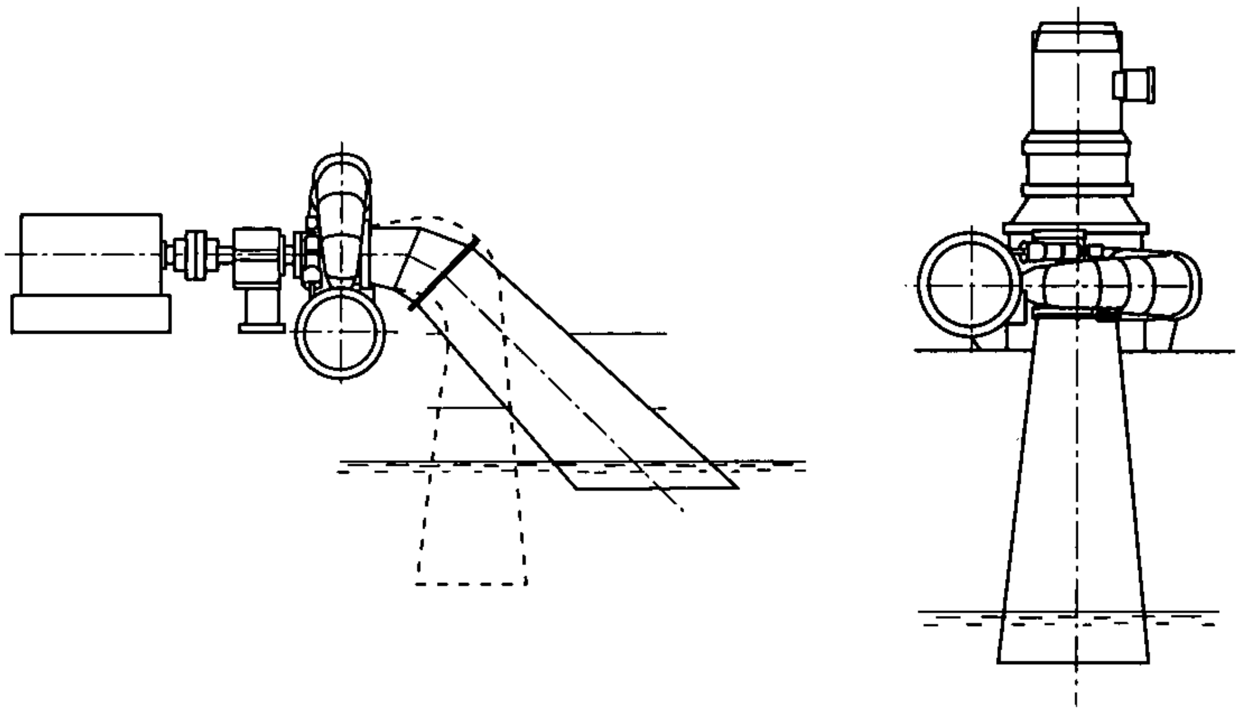

(a) Horizontal (b) Vertical

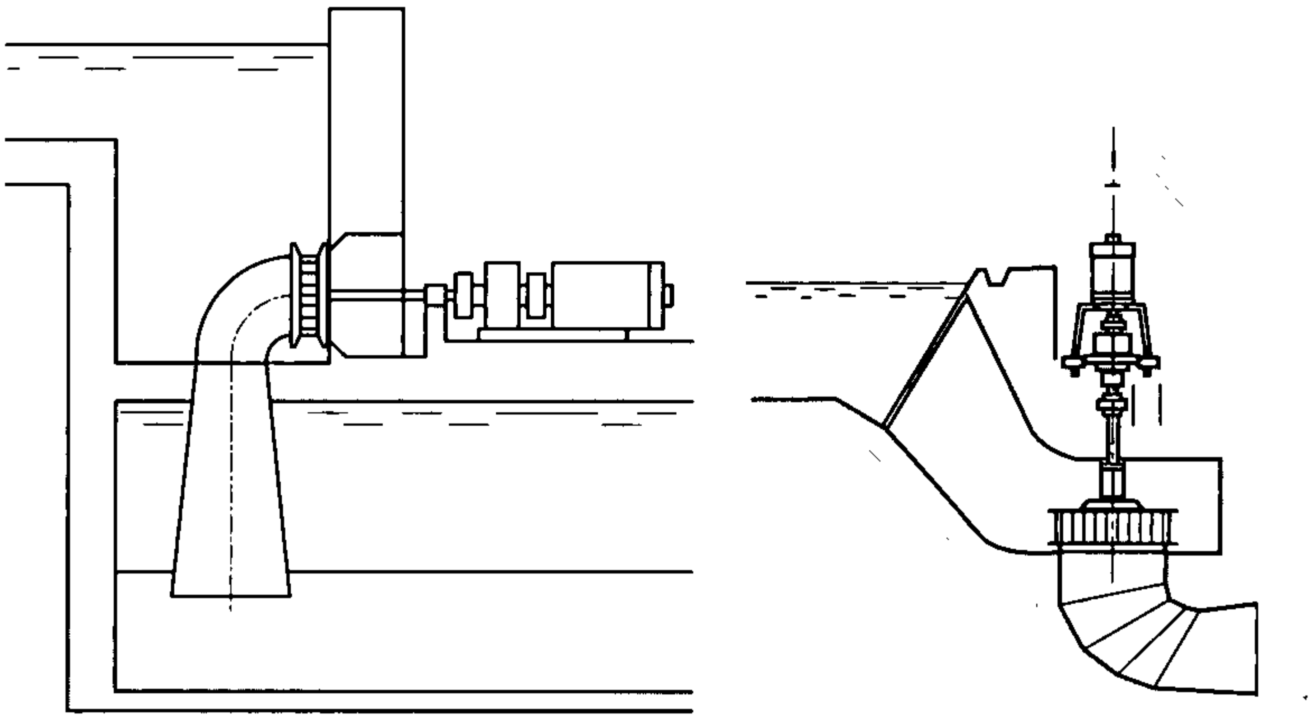

(c) Horizontal, open flume (d) Vertical, open flume

Fig. 1.7. Francis turbine arrangements. (Adapted from Voith Siemens material)

arrangements are shown in Figure 1.8, together with a syphon type arrangement suitable for heads of 5 m or less.

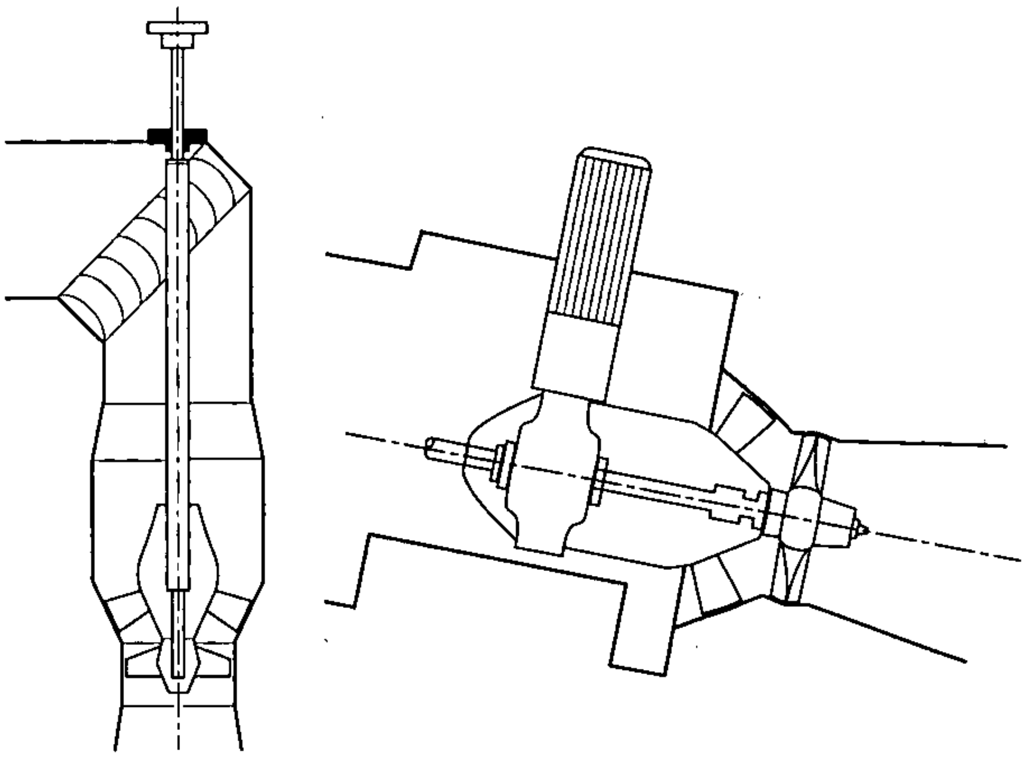

(a) Vertical shaft

(b) Pit (Adapted from Voith Siemens material)

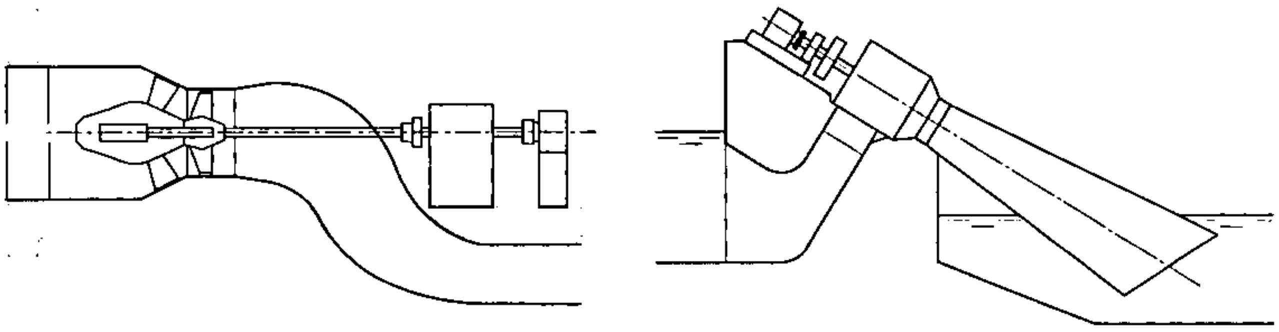

(c) S-type (Adapted from Voith Siemens material)

(d) Syphon (Adapted from Voith Siemens material)

Fig. 1.8. Propeller turbine arrangements.

Propeller turbines can be operated, when coupled to frequency converters, at variable speed.

1.2 Turbine selection

A simplified turbine selection process might consider the following:

1. Decide on the number of turbines.
2. Select two or three suitable turbine types using Figure 1.4 or based on experience using specific speed (see Chapter 3).
3. Calculate the turbine setting based on synchronous speeds (see Chapter 4).
4. Determine an approximate cost for the turbines, generator and power house based on these decisions. Consider practical aspects. For example, if the turbine is below the tailrace, dewatering may require a sealing system at the draft tube exit (for very small turbines, you may simply lift the turbine out). *
5. Calculate the energy generated by the different turbines based on part load efficiencies, Figure 1.5, and other pertinent factors, for example the percentage time spent at different part load conditions. This latter issue is dependent on the flow duration curve, the amount of water storage, the number of turbines chosen and the tariff rate for electricity sales. *

* Topic is outside the scope of this publication.

Steps 1–5 would be repeated with different arrangements until an optimal solution has been determined.

As an example, you may have a 500 kW site permitting selection of cross–flow, open flume Francis or propeller type turbines. With the cross–flow not all the head is utilized, see Figure 1.9. The head available to the cross–flow turbine is less than H_n for the Francis turbine by the distance A. The lack of a diffusing draft tube means $V_{\text{out, cross–flow}} > V_{\text{out, Francis}}$. The kinetic energy lost at the draft tube exit is thus greater for the cross–flow than for the Francis turbine. To the cross–flow turbine's advantage is a much flatter part load effciency curve. Hothersall [1987] presents a more detailed comparison.

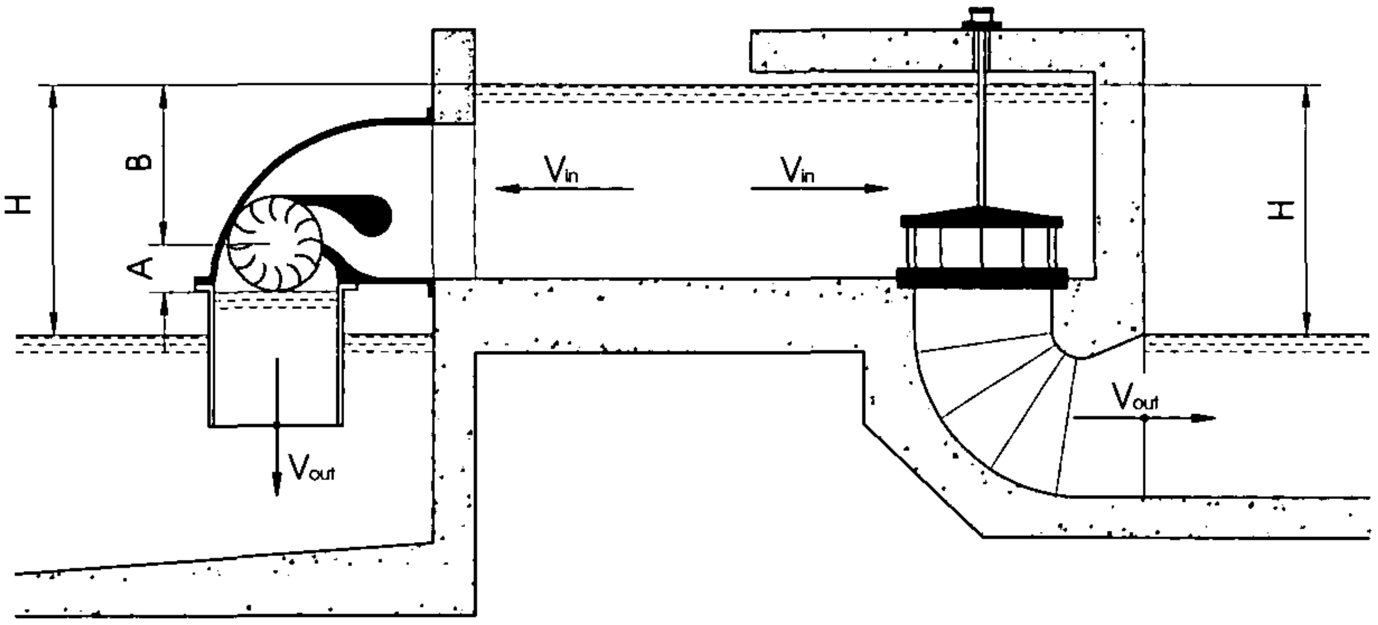
H
B
A
Vin
Vin
H
Vout
Vout

Fig. 1.9. Head comparison: open-flume versus crossflow. (Reproduced courtesy International Water Power & Dam Construction)

2 Overview of the turbine design process

This Chapter presents a summary of the hydrodynamic design processes that might be adopted when designing Francis and propeller turbines from scratch. Chapters 14 and 15 follow these procedures.

For the reader who is not familiar with the names and function of turbine components, a brief description using Figure 2.1 follows. This Figure shows a high specific speed Francis turbine cross-sectional view called the meridional view. The meridional view (plane) is defined as an axial plane on which blade leading and trailing edges, as well as streamlines and velocity vectors, are drawn by circular projection. The turbine runner comprises a set of blades, a hub, sometimes called the crown, and a skirt. Other names, such as rim, shroud or band, are also common for the skirt. The runner converts the angular momentum (rV_θ component) of the flow into torque. This torque is carried by the shaft to the generator. The guide vanes are adjustable and allow the flow to be regulated. If the Francis turbine is to be designed as a fixed flow device, the guide vanes can be dispensed with. The stay vanes, usually of flat plate or circular arc construction, provide structural strength to the spiral casing. Simpler turbines (and many older designs) use bolts instead of stay vanes. The spiral casing is effectively a welded pressure vessel of reducing area as it sweeps around the turbine. Its function is to distribute water uniformly around the turbine runner and introduce angular momentum to the flow. The head cover and bottom cover fulfil a structural role. The draft tube, not shown in Figure 2.1, is located at the turbine exit, and usually connects onto the lower seal ring.

Propeller turbines have similar features.

2.1 Design procedure for Francis turbines

1. Determine the specific speed for the turbine based on peak efficiency and select a turbine exit diameter. See Chapter 3 and Chapter 15.
2. Determine the flowrate for perpendicular discharge and for maximum discharge. Use the approximate turbine performance characteristics provided for this. Select the design flowrate.
3. Determine the arrangement, eg horizontal or vertical.

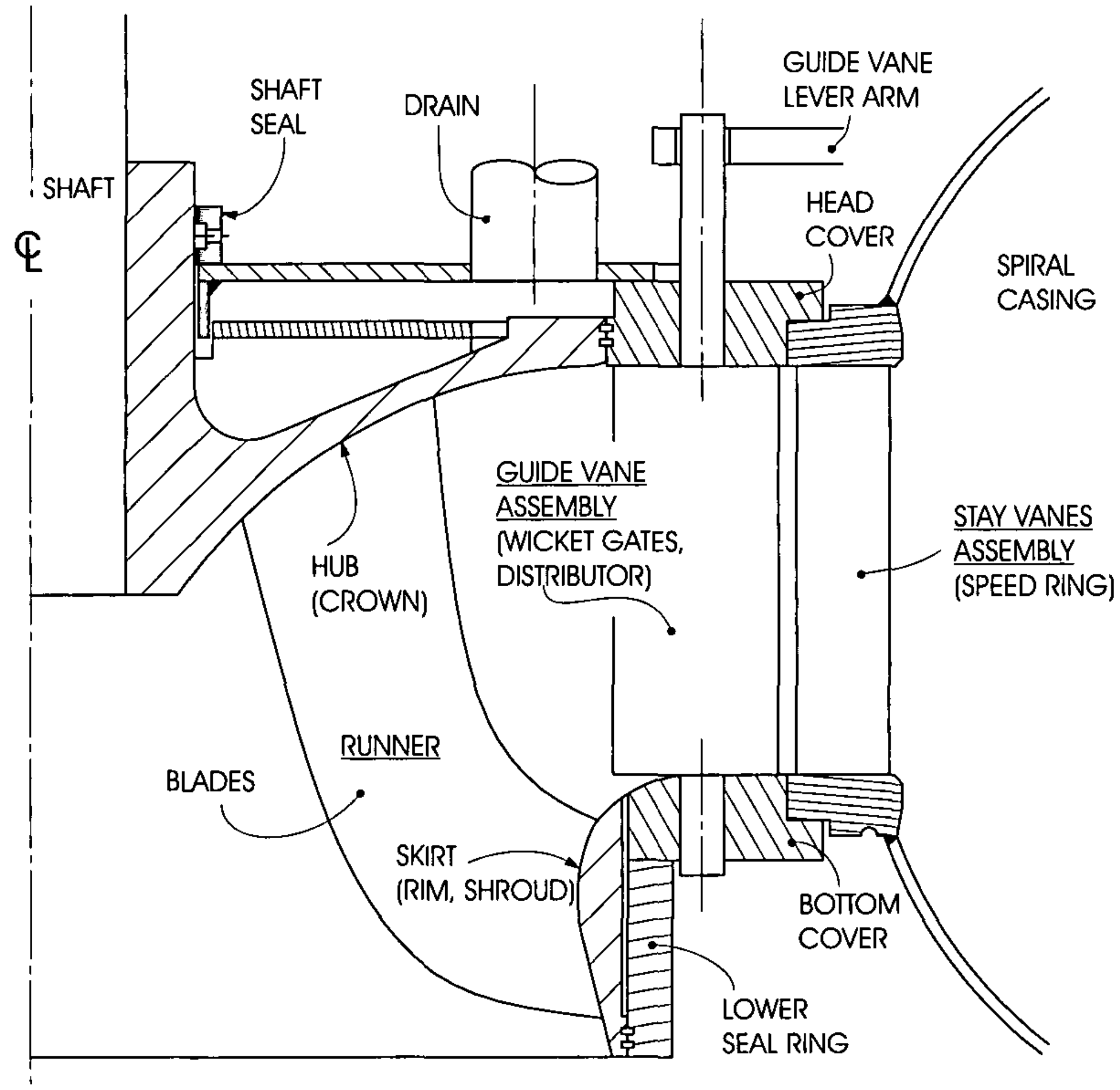
SHAFT
℄
SHAFT SEAL
DRAIN
GUIDE VANE LEVER ARM
HEAD COVER
SPIRAL CASING
HUB (CROWN)
GUIDE VANE ASSEMBLY (WICKET GATES, DISTRIBUTOR)
STAY VANES ASSEMBLY (SPEED RING)
RUNNER
BLADES
SKIRT (RIM, SHROUD)
BOTTOM COVER
LOWER SEAL RING

Fig. 2.1. Francis turbine cross-sectional view with key components labelled.

4. Establish the % Kinetic Energy (KE) entering the draft tube and select a rV_θ distribution which optimises draft tube performance whilst not losing too much kinetic energy associated with the V_θ swirl component at the runner exit. Design draft tube.
5. Use the simple radial equilibrium equation, to determine velocity and pressure distribution under the runner.
6. Sketch a runner envelope geometry based on specific speed and the envelope library provided. Use the non-dimensional specific velocities to determine the approximate positions of the leading and trailing edges.
7. Estimate the rV_θ distribution at the turbine runner blade inlet using the Euler Equation.
8. Estimate the rV_θ distribution at the guide vane exit using the free vortex law (conservation of angular momentum). Determine the guide vane an-

gle at the design flowrate operating point and compare with established practice.

9. Establish meridional streamlines in the runner envelope space using the through flow procedures provided. Refer to Figure 3.3 and Chapter 9.
10. Recalculate the rV_θ leaving the guide vane and the rV_θ change across the runner. Adjust design until the required fluid deflections are achieved on the corresponding stream surfaces.
11. Design blade sections that deflect the flow by the require amount on each stream surfaces. Prasil transform or mean streamline methods provide a simplified design procedure to establish the runner geometry. Blade thickness has to be determined from hydrodynamic and structural considerations. These methods are described in Chapter 10.
12. Lay out the guide vane arrangement.
13. Lay out the spiral casing and stay ring assembly (speed ring).
14. Locate the seal positions and calculate hydraulic thrust.
15. Review the hydraulic design and adjust. Proceed with the detail structural design.

2.2 Design procedure for propeller turbines

Follow the procedures as outlined for the Francis turbine. The principle differences in procedure are listed below:

- Use the Zweifel [1945] loading coefficient to determine the runner hub axial chord. Repeat for guide vane hub axial chord. This may require the shifting of the guide vanes radially outwards to reduce their loading. See Figure 1.8 (a) for example.
- Simple radial equilibrium calculations can be applied downstream and upstream of the runner. The throughflow calculations only need to be carried out if the turbine is a Kaplan or there is a strong radial velocity component to the flow.
- Create runner camber line geometry using the mean streamline method and correct for incidence and deviation.
- Check for cavitation performance.
- Create guide vane geometry. Use straight generators if they have to close or if they are to be rolled from plate.

3 Basic theory

This Chapter develops basic theory directly applicable to the design and manufacture of small Francis and propeller turbines. Section 3.1 defines net head. Section 3.2 deals with the non-dimensional parameters widely used in conjunction with turbomachinery design. The basic governing equations – momentum, continuity and energy – are developed in Sections 3.3–3.5. The function of the adjustable turbine guide vanes is discussed in Section 3.6. Section 3.7 introduces the concept of radial equilibrium. Section 3.8 covers blade circulation, loading, incidence and deviation. A method, based on mean streamline analysis, for calculating the local pressures and velocities on the blade surface is outlined in Section 3.9. Additional theory is introduced as required in subsequent chapters.

Other sources include:

Nechleba [1957] An excellent companion to this design guide. Provides a single comprehensive, but somewhat dated, guide to turbine design.
Cumpsty [1989] A highly recommended text on compressor design. Contains no specific material on hydraulic turbine design, but contains good physical explanations of the fluid dynamic processes occurring in turbomachinery.
Lewis [1996] Includes discussion of radial equilibrium equations and throughflow calculations. Used as the primary source for the discussion of these topics in this Chapter and Chapter 9.
Wislicenus [1965, 1986] Excellent pump design texts.
Mosonyi [1987] A general hydropower development book including much of interest to the turbine designer.
Massey [1989] General fluid mechanics text.
Duncan et al. [1970] Another general fluid mechanics text.

There are many more texts, covering aspects of turbomachinery design. However, the designer of Francis and propeller turbines should find the above mentioned references sufficient.

3.1 Net head

With reference to Figure 3.1, net head is defined, according to IEC 60193 [1999], by

$$H_n = H' - \frac{V_2^2}{2g}, \tag{3.1}$$

and, according to ASME [1949], by

$$H_n = H' - \frac{V_e^2}{2g}, \tag{3.2}$$

These definitions are clearly different; the latter being marginally superior from the viewpoint of maximising energy production (see Hothersall [1988]).

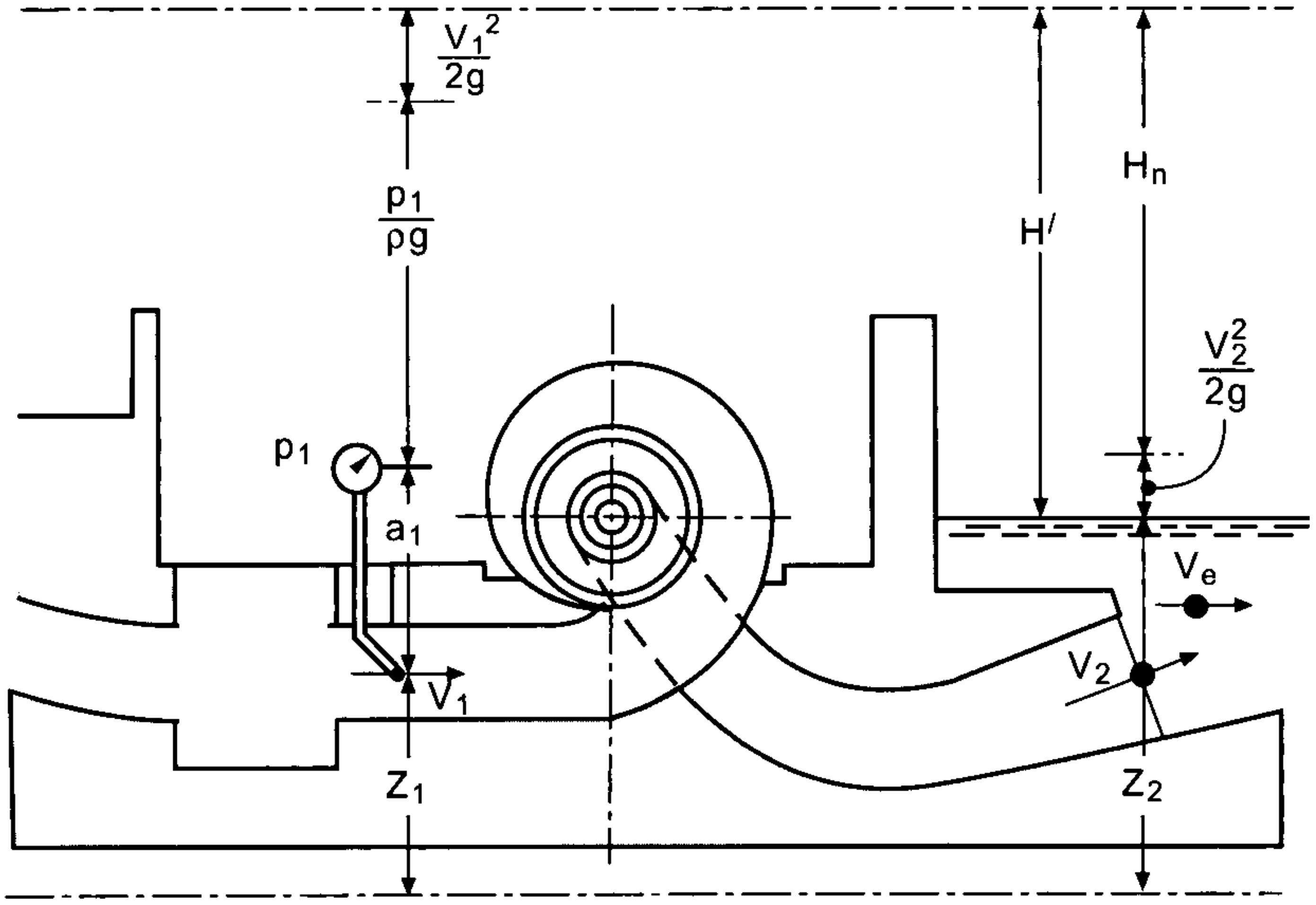
$\frac{V_1^2}{2g}$
$\frac{p_1}{\rho g}$
p_1
a_1
V_1
Z_1
H'
H_n
$\frac{V_2^2}{2g}$
V_e
V_2
Z_2

Fig. 3.1. Net head definitions. (Adapted from IEC 60193)

3.2 Specific speed and other non-dimensional parameters

Specific speed (SI units) is defined as

$$n_s = \frac{NP^{1/2}}{H_n^{5/4}} \tag{3.3}$$

with the rotational speed N, the power P and the head H_n having units of rpm, kW and m respectively. Clearly specific speed is not dimensionless; it is however the degenerate form of the non-dimensional ratio

$$\frac{NP^{1/2}}{\rho^{1/2}(gH)^{5/4}}$$

with the ρ and g terms omitted as they are sensibly the same for all turbines encountered in practice. As Massey [1989] points out, the term 'specific speed is most unfortunate as it is neither dimensionless ('specific') nor a speed. Instead it is better regarded as a 'shape factor', and it is its ability to describe the shape of a turbine design independently of turbine size that makes specific speed useful to the turbine designer. Figure 3.2 illustrates the variation in turbine shape with specific speed.

Occasionally, particularly in older works such as Nechleba [1957] and Quayle [1984], metric specific is used, with metric horsepower being used in place of kW, i.e.

$$N_s = \frac{N(\text{metric hp})^{1/2}}{H_n^{5/4}} \tag{3.4}$$

As metric hp $= kW/0.7355$

$$n_s = 0.8576 N_s. \tag{3.5}$$

Common in Europe is to use a specific speed definition based on flowrate. Eg

$$n_q = \frac{N(Q)^{\frac{1}{2}}}{H^{\frac{3}{4}}} \tag{3.6}$$

n_s is used in this book. It is usual to state the specific speed of a Pelton or turgo wheel as the specific speed per jet (i.e. total kW/number of jets). Alternatively, for multi-jet machines the total power may be used, permitting direct comparison with Francis turbines. Table 3.1 illustrates the range of specific speeds that can be achieved by different turbine types. This table can be used as an initial selection guide. The highest specific speeds are achieved by tubular/bulb type propeller turbines, usually in tidal applications.

Other dimensionless parameters and relationships of use to the turbine designer are:

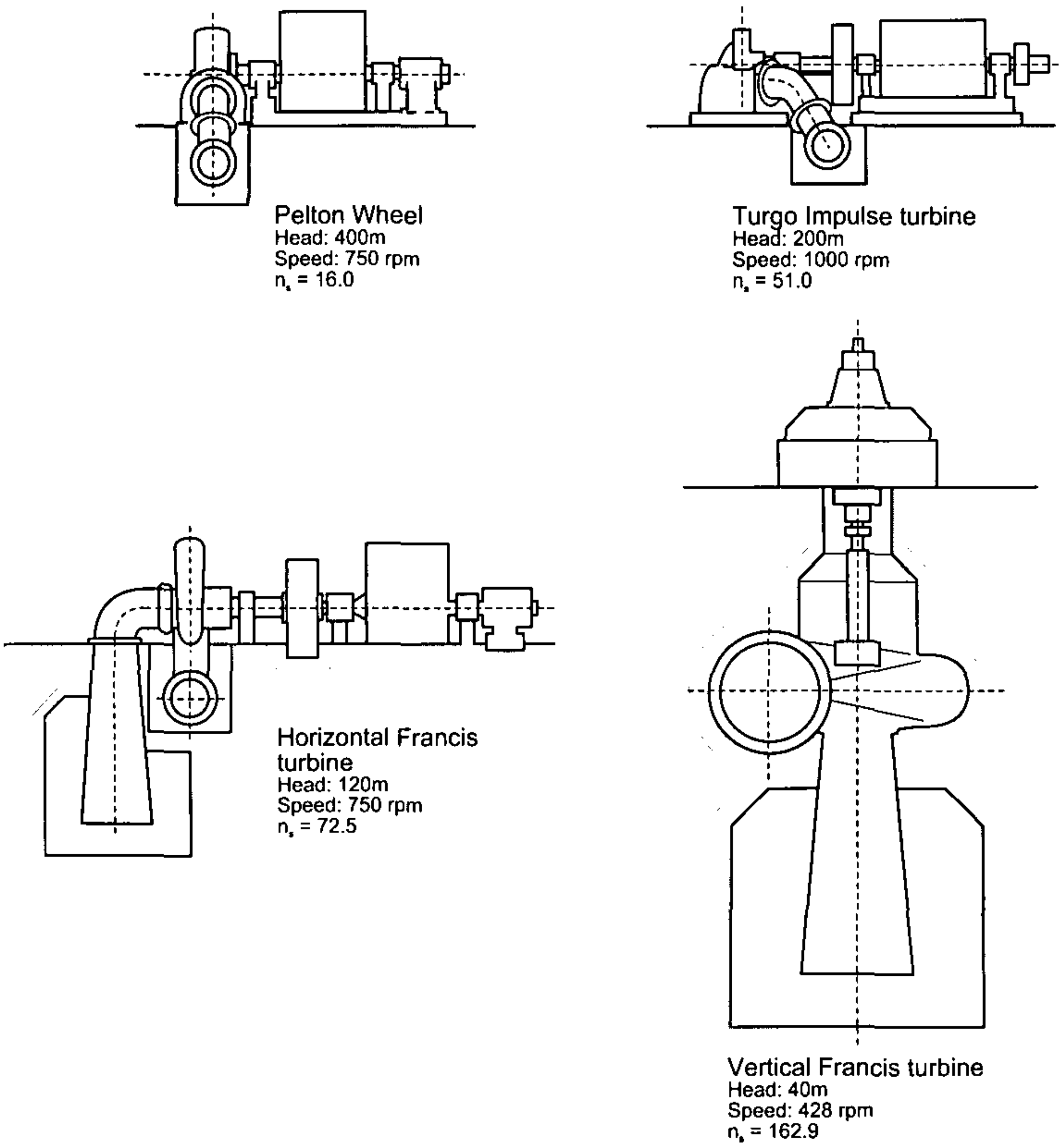
Pelton Wheel
Head: 400m
Speed: 750 rpm
$n_s = 16.0$
Turgo Impulse turbine
Head: 200m
Speed: 1000 rpm
$n_s = 51.0$
Horizontal Francis turbine
Head: 120m
Speed: 750 rpm
$n_s = 72.5$
Vertical Francis turbine
Head: 40m
Speed: 428 rpm
$n_s = 162.9$

Fig. 3.2. Turbine shape variation with specific speed. Adapted from Williams [1996].

Turbine type	Specific speed range
Pelton	4 – 26
Turgo	20 – 56
Cross–flow	20 – 170
Francis (spiral casing)	45 – 300
Francis (open flume)	255 – 345
Kaplan and Propeller	255 – 860

Table 3.1. Specific speed range for different turbine types.

$$n_{11} = \frac{ND_{ref}}{\sqrt{H_n}}, \tag{3.7}$$

$$q_{11} = \frac{Q}{(D_{ref})^2\sqrt{H_n}}, \tag{3.8}$$

$$n_s = 3.13 n_{11}\sqrt{\eta q_{11}}, \tag{3.9}$$

$$KU = \frac{\pi D_{ref} N}{60\sqrt{2gH_n}} = \frac{\pi}{60\sqrt{2g}} n_{11}, \tag{3.10}$$

$$\text{e.g. } KU_2^o = \frac{\pi D_2^o N}{60\sqrt{2gH_n}}, \tag{3.11}$$

$$KV = \frac{4Q}{\pi (D_{ref})^2 \sqrt{2gH_n}}, \tag{3.12}$$

$$\text{e.g. } KV_{m2}^o = \frac{4Q}{\pi (D_2^o)^2 \sqrt{2gH_n}}. \tag{3.13}$$

n_{11} and q_{11} are referred to as the *unit speed* and *unit flowrate* respectively and D_{ref} is a reference diameter, Refer to Figure 6.1 . KU and KV are refered to as peripheral velocity coefficient and velocity coefficient respectively.

3.3 Conservation of momentum

This section provides an introductory explanation of the momentum transfer process within a turbomachine. The term rV_θ is introduced and the Euler equation is developed.

Figure 3.3 shows the meridional view of a Francis turbine. The guide vanes and the runner blades are illustrated with their leading and trailing edges projected circumferentially onto the meridional plane. It is quite common for the trailing edges of a Francis runner to lie in a meridional plane, but this may not be the case for the runner leading edges.

The quasi three-dimensional approach to turbine design is to split the meridional flow passage into 4 sections, sometimes called partial turbines, labelled I, II, III and IV in Figure 3.3. These sections are bounded by stream surfaces, shown as streamlines in Figure 3.3 and labelled 1 through 5. The axisymmetric stream surface labelled 4 in Figure 3.3 is replotted in Figures 3.4 (a)–(c). The velocity diagrams of Figures 3.4 (a)–(c) correspond to the positions labelled gv, 1 and 2 in Figure 3.3. Line gv in Figure 3.3 represents the guide vane trailing edge.

At positions gv, 1 and 2 the radius is r_{gv}, r_1 and r_2 respectively. Similarly the tangential velocities are $V_{\theta_{gv}}$, $V_{\theta 1}$ and $V_{\theta 2}$ with V_θ positive in the direction of runner rotation.

The power output of the turbine is given by

$$P = \eta \rho g Q H_n. \tag{3.14}$$

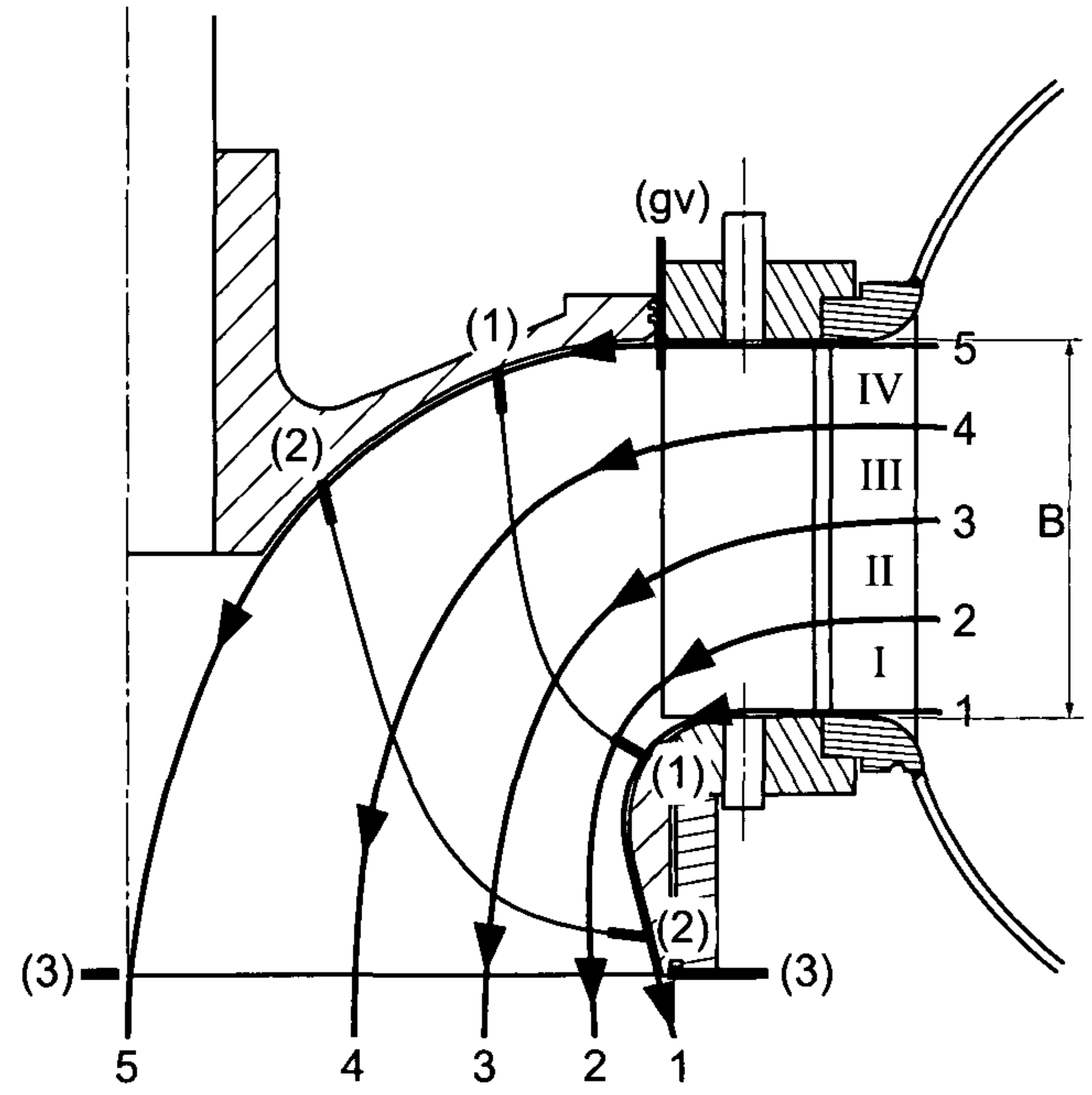

Fig. 3.3. Meridional view of Francis turbine.

At exit from the guide vanes the flow has a swirling motion with a velocity $V_{m_{gv}}$ in the meridional direction, and $V_{\theta_{gv}}$ in the tangential direction (see Figure 3.4 (a)). The angular momentum of the flow is $\rho Q(r_{gv}V_{\theta_{gv}})$ at exit from the guide vanes. Likewise the angular momentum is $\rho Q(r_1 V_{\theta 1})$ at runner inlet (Figure 3.4 (b)) and $\rho Q(r_2 V_{\theta 2})$ at runner outlet (Figure 3.4 (c)).

Conservation of angular momentum requires that

$$r_{gv}V_{\theta_{gv}} = r_1 V_{\theta 1}. \tag{3.15}$$

The Euler equation

$$T = \rho Q\left(r_1 V_{\theta 1} - r_2 V_{\theta 2}\right). \tag{3.16}$$

relates the torque on the runner to the rate of change of angular momentum.

The rV_θ at the inlet and exit to the blade row has a very significant effect on the shape of the blades. The Euler equation can be re-written as

$$gH_n = (U_1^2 - U_2^2) + (U_2 W_{\theta 2} - U_1 W_{\theta 1}). \tag{3.17}$$

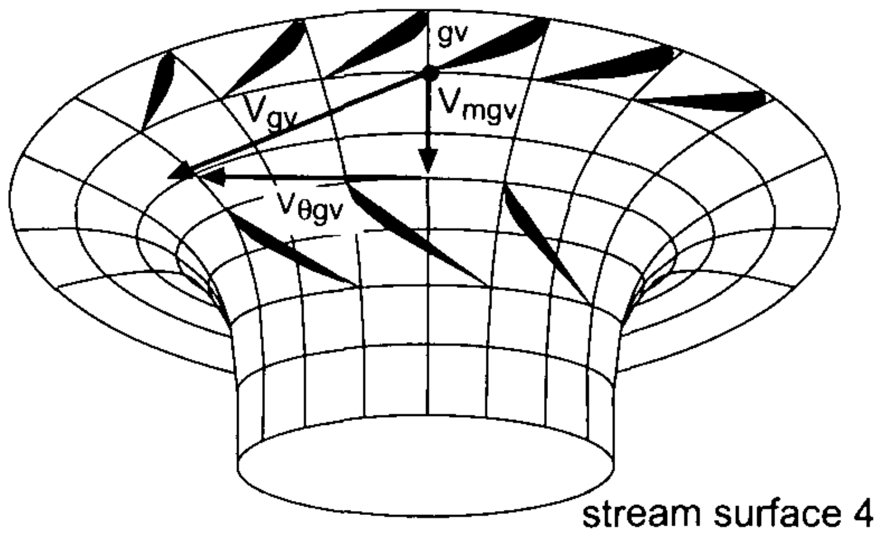
gv
V_gv
V_mgv
V_θgv
stream surface 4

(a) Guide vane exit

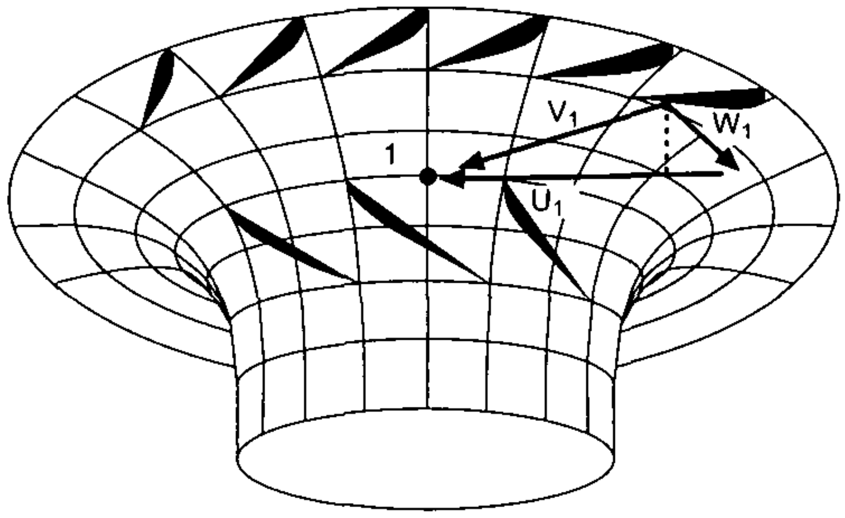

(b) Runner inlet

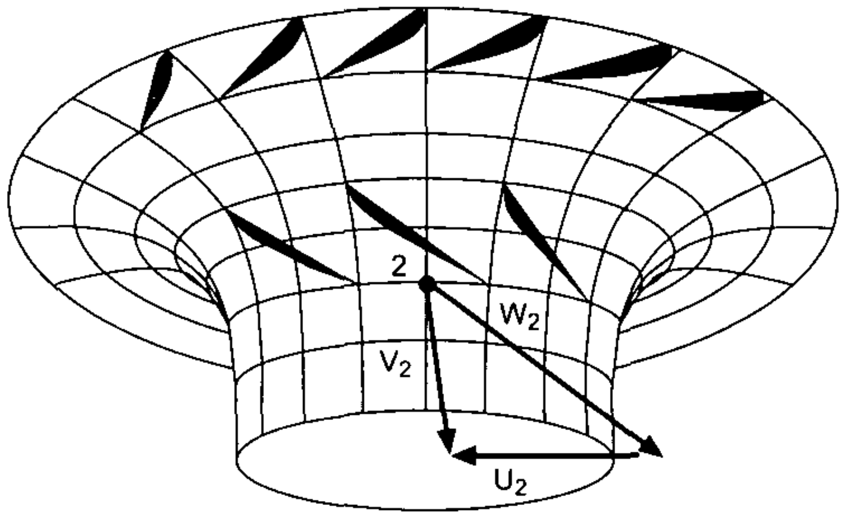

(c) Runner outlet

Fig. 3.4. Velocity diagrams on stream surface 4 of Figure 3.3.

The first term on the RHS of this equation represents the work done due to change of radius (the Coriolis term) and the second represents the work done by the blades, in a relative frame of reference, due to deflection of the flow.

An alternative representation of Equation 3.17 is

$$H_n = \frac{\omega}{g}(r_1 V_{\theta 1} - r_2 V_{\theta 2}). \tag{3.18}$$

This equation is exact for a shrouded runner such as a Francis turbine if every water particle can be accounted for. In practice, a factor η_h, the runner hydraulic efficiency, is introduced to account for real flow effects, rendering Equation 3.18

$$\eta_h H_n = \frac{\omega}{g}(r_1 V_{\theta 1} - r_2 V_{\theta 2}). \tag{3.19}$$

Typical values for η_h lie between 0.93 and 0.96, and can be different for each partial turbine. $\eta_h H_n$ represents the useful work/unit weight extracted by the runner from the flow. Note that η_h used here allows the blade angles at exit to be calculated. η_h does not represent the overall hydraulic efficiency of the turbine which includes draft tube, guide vane, stay vane, spiral casing and leakage losses.

3.4 Conservation of mass

For incompressible flow through each of the partial turbines defined in Figure 3.3

$$A_1 V_{m1} = A_2 V_{m2}. \tag{3.20}$$

3.5 Conservation of energy

The principle of conservation of energy, embodied in the first law of thermodynamics, dictates that, between positions 1 and 2

$$\frac{p_1}{\rho g} + \frac{V_1^2}{2g} + z_1 = \frac{p_2}{\rho g} + \frac{V_2^2}{2g} + z_2 + \eta_h H_n + \text{losses}. \tag{3.21}$$

Obviously, this equation can be applied between positions 1 and 2 on streamline 4 of Figure 3.3.

3.6 Guide vane function

The guide vane angle α_{gv} is measured from the closed position for which $\alpha_{gv} = 0$.

Referring to Figure 3.3,

$$Q = 2\pi r_{gv} B V_{m_{gv}}, \tag{3.22}$$

$$V_{\theta_{gv}} = V_{m_{gv}} \cot \alpha_{gv}. \tag{3.23}$$

Applying the law of conservation of angular momentum

$$r_{gv} V_{\theta_{gv}} = r_1 V_{\theta 1} \tag{3.24}$$

The Euler equation is

$$g \eta_h H_n = \omega (r_1 V_{\theta 1} - r_2 V_{\theta 2}). \tag{3.25}$$

At the runner exit

$$V_{\theta 2} \approx U_2 - V_{m2} \cot \beta_2. \tag{3.26}$$

Combining equations 3.22 through 3.26 gives

$$Q = \frac{g \eta_h H_n + \omega^2 r_2^2}{\dfrac{\omega \cot \alpha_{gv}}{2\pi B} + \dfrac{\omega r_2 \cot \beta_2}{\pi (D_2^o)^2/4}}. \tag{3.27}$$

3.7 Simple radial equilibrium

The analysis presented in this Section is based on Lewis [1996]. With reference to Figure 3.5 (a), at position 1, V_m = constant and $V_\theta = V_r = 0$. At position 3, $V_r = 0$. Considering the element defined in Figure 3.5 (b) $\mathrm{d}m = \rho \mathrm{d}x \mathrm{d}r r \mathrm{d}\theta$. Applying $F = ma$ in the radial direction

$$\begin{aligned}
&(p + \mathrm{d}p)(r + \mathrm{d}r)\,\mathrm{d}\theta\,\mathrm{d}x - pr\mathrm{d}\theta\,\mathrm{d}x - 2(p + \mathrm{d}p/2)\,\mathrm{d}x\,\mathrm{d}r \sin(\mathrm{d}\theta/2) \\
&= \mathrm{d}m\, V_\theta^2/r \\
&= \rho\,\mathrm{d}x\,\mathrm{d}r\,r\mathrm{d}\theta\, V_\theta^2/r
\end{aligned}$$

so, for simple radial equilibrium ($V_r = 0$),

$$\frac{1}{\rho}\frac{\mathrm{d}p}{\mathrm{d}r} = \frac{V_\theta^2}{r}. \tag{3.28}$$

For incompressible flow, Bernoulli's equation can be manipulated to give

$$\begin{aligned}
\frac{p_o}{\rho} &= \frac{p}{\rho} + \tfrac{1}{2}V^2 = \frac{p}{\rho} + \tfrac{1}{2}\left(V_m^2 + V_r^2 + V_\theta^2\right) \\
\therefore \quad \frac{1}{\rho}\frac{\mathrm{d}p_o}{\mathrm{d}r} &= \frac{1}{\rho}\frac{\mathrm{d}p}{\mathrm{d}r} + V_m \frac{\mathrm{d}V_m}{\mathrm{d}r} + V_\theta \frac{\mathrm{d}V_\theta}{\mathrm{d}r} \quad \text{for } V_r = 0.
\end{aligned}$$

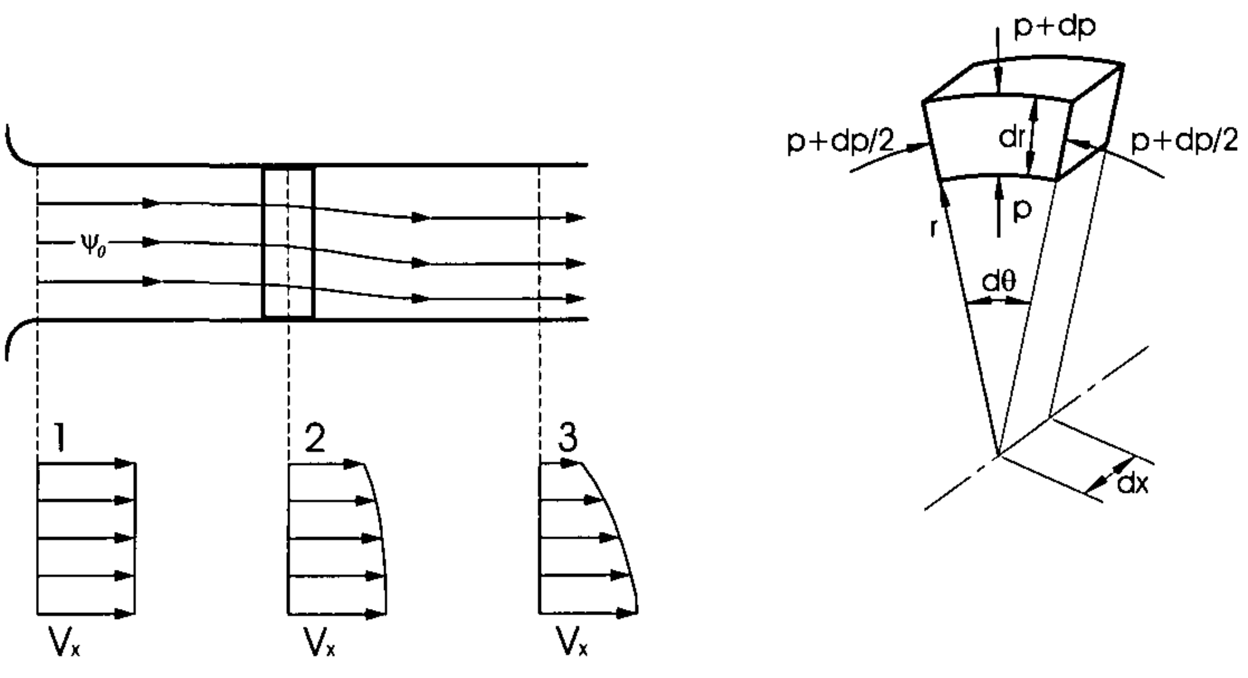

(a) Meridional view (b) Infinitesimal element

Fig. 3.5. Radial equilibrium.

Incorporating Equation 3.28 yields

$$\frac{1}{\rho}\frac{\mathrm{d}p_o}{\mathrm{d}r} = V_m\frac{\mathrm{d}V_m}{\mathrm{d}r} + \frac{V_\theta}{r}\frac{\mathrm{d}(rV_\theta)}{\mathrm{d}r}\,. \tag{3.29}$$

Rearranging this last equation and integrating gives

$$V_m(r) = \sqrt{K_i + \frac{2}{\rho}\sum_{r=r_n}^{r}\Delta p_o - 2\sum_{r=r_n}^{r}\frac{V_\theta}{r}\Delta(rV_\theta)}.$$

where $p_o = \rho g h_o$ and K_i is the constant of integration determined such that continuity is satisfied. Thus

$$V_m(r) = \sqrt{K_i + 2g\sum_{r=r_n}^{r}\Delta h_o - 2\sum_{r=r_n}^{r}\frac{V_\theta}{r}\Delta(rV_\theta)}. \tag{3.30}$$

Equation 3.30 can be used to determine the meridional velocity distribution $V_m(r)$ for a given tangential velocity distribution $V_\theta(r)$ so long as the radial velocity V_r is everywhere zero or at least negligible.

When V_r is significant, potential flownet, stream function or streamline curvature methods have to be used (see Chapter 9 or Nechleba [1957]). Note that the potential flownet can only be used if rV_θ is constant along the guide vane trailing edge. See Chapter 9 for an explanation.

3.8 Blade circulation, blade loading, incidence and deviation

Figure 3.6 shows blades developed from section ZZ.

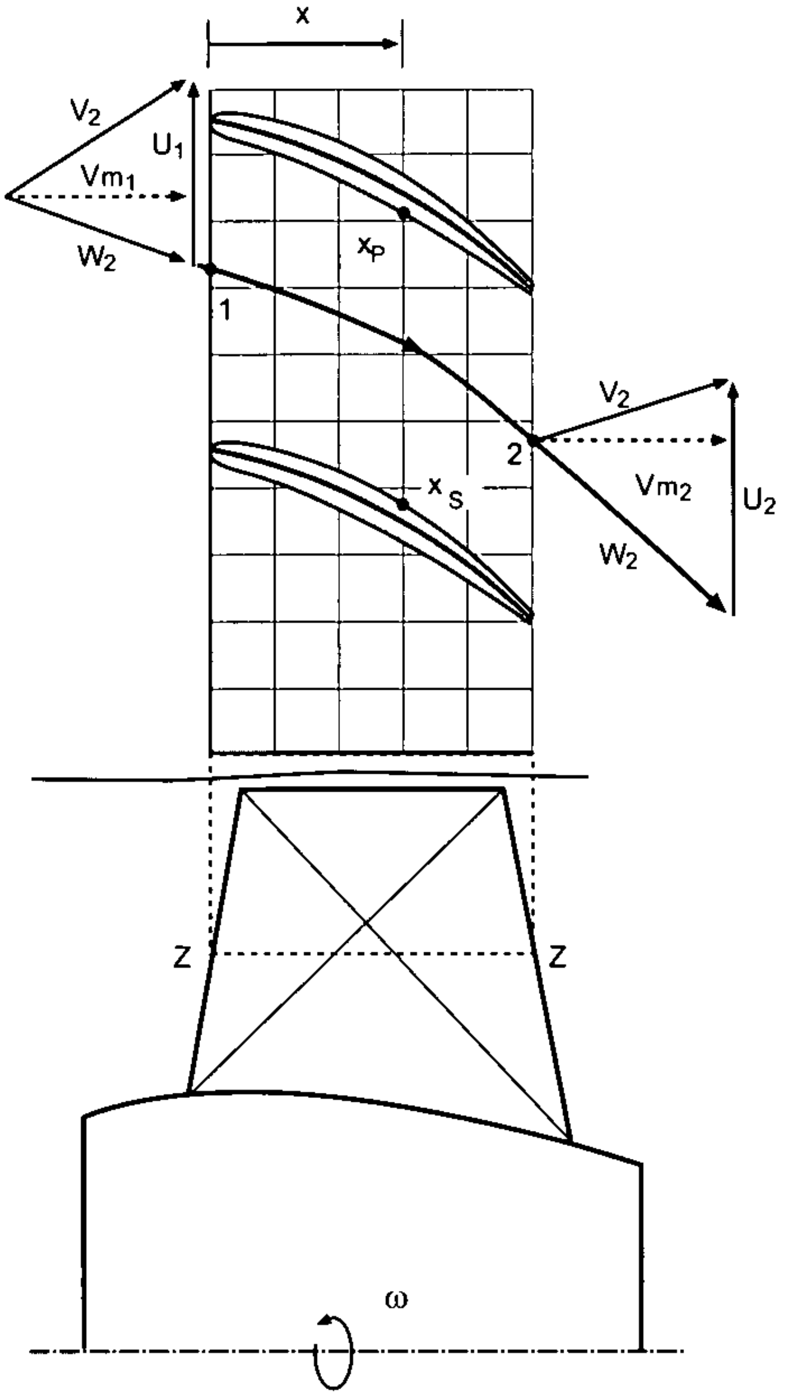

Fig. 3.6. Developed blade section ZZ.

Consider a distance x along the blade passage. The centripetal acceleration of the fluid, due to its deflection by the curvature of the blades, requires a pressure difference across the passage. For example, at point x_p, the pressure $p_p > p_s$ where p_s is the pressure at x_s on the suction face. This pressure difference, or blade loading, must go to zero at the trailing edge, a requirement known as the Kutta-Joukowsky condition. The pressure in the flow at any point can only take one value. Thus, from some point along the blade, the pressure difference must reduce progressively to the trailing edge. It is not possible for the flow to follow the curvature of the blade camberline right up to the trailing edge as the pressure difference across the blade passage will not support the centripetal acceleration. The flow has to adjust its direction; this adjustment is called deviation and is illustrated in Figure 3.7.

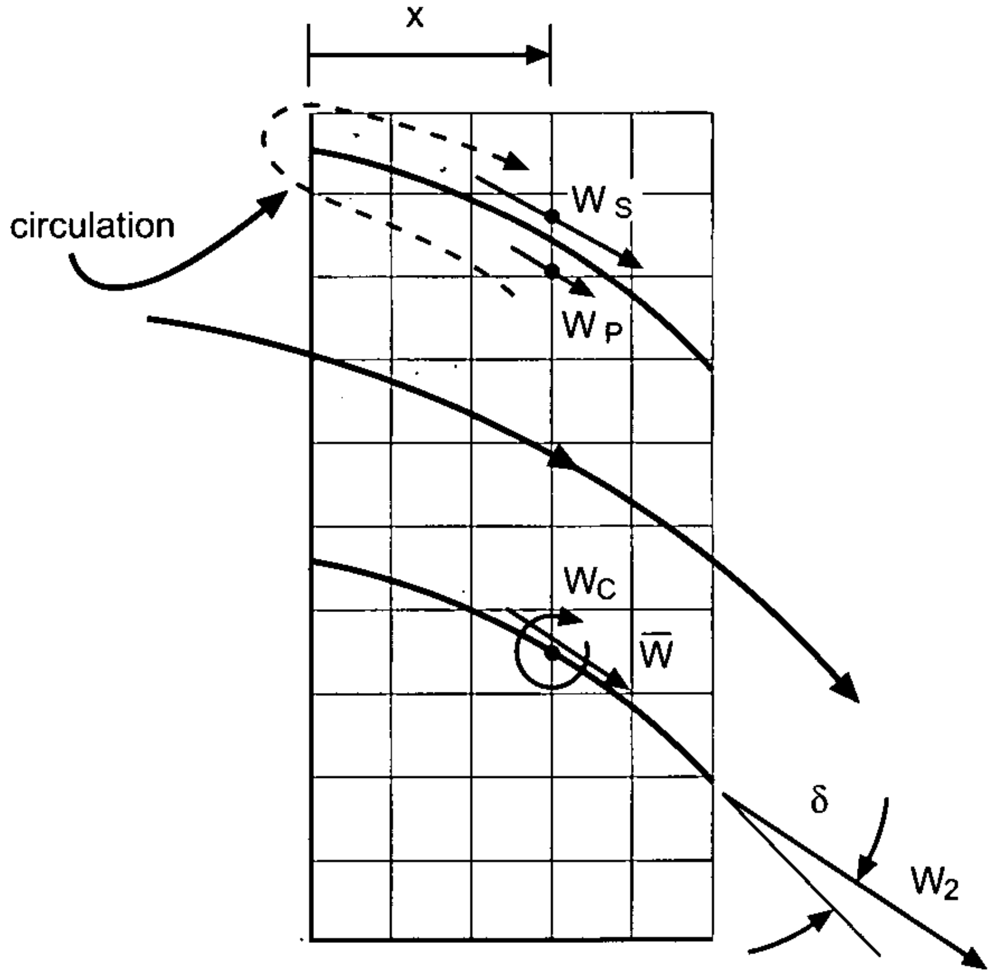

Fig. 3.7. Circulation and deviation.

Circulation around the blade is a useful concept, as it provides a measure of blade loading. Mathematically, it is defined as

$$\oint W ds$$

with the circle indicating the integration is performed once along the entire blade surface in the anticlockwise direction.

Associated with the concept of circulation is the circulation velocity, W_c. The magnitude of this velocity is a measure of blade loading. The direction of the circulation around a blade is useful in predicting how the stagnation point at the leading edge moves due to blade loading. The concept of circulation can also be used to predict local pressures and velocities over the blade surface. Regarding Figure 3.7, if $\bar{W}$ is taken as the mean velocity at distance x, then, as an approximation,

$$W_p = \bar{W} - W_c, \qquad (3.31)$$
$$W_s = \bar{W} + W_c.$$

In Figure 3.7, the camberline only is shown with the mean velocity $\bar{W}$ and the circulation velocity W_c superimposed at distance x into the cascade.

If it is assumed that, between the inlet and distance x, an equal amount of work has been done by the water on each side of the blade, then

$$\frac{p_p}{\rho g} + \frac{W_p^2}{2g} = \frac{p_s}{\rho g} + \frac{W_s^2}{2g}. \qquad (3.32)$$

Figure 3.8 shows the geometry of a parabolic camberline with an inlet angle of 58°and an exit angle of 21°to the tangential.

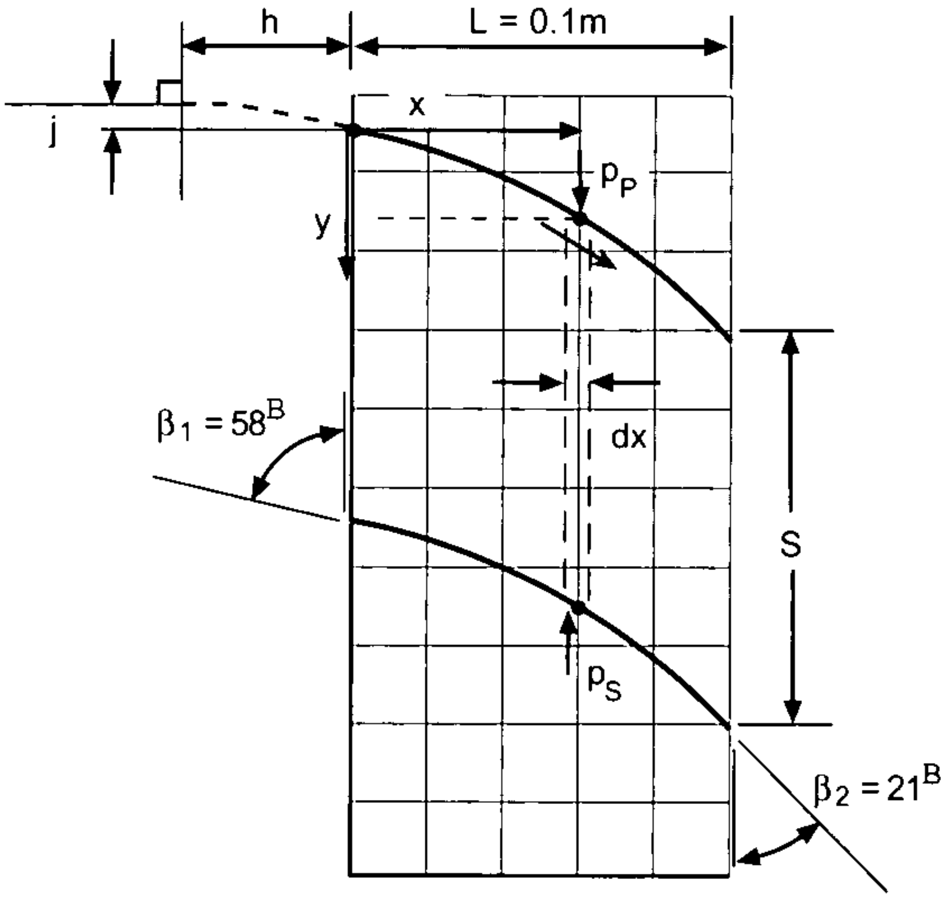

Fig. 3.8. Parabolic camberline geometry.

Consider a fluid element of unit width, depth $\mathrm{d}x$ and length s. The equation for a parabola is $y + j = k(h + x)^2$ or

$$y = kx^2 + 2khx.$$

When $x = y = 0$, $\dfrac{\mathrm{d}j}{\mathrm{d}h} = \cot\beta_1 = 2kh$ thus $h = \cot\beta_1/(2k)$ and

$$y = kx^2 + \cot\beta_1 x \quad \text{and} \quad \frac{\mathrm{d}y}{\mathrm{d}x} = \cot\beta = 2kx + \cot\beta.$$

When $x = L$, $\beta = \beta_2$ and $\cot\beta_2 = 2kL + \cot\beta_1$ thus

$$k = \frac{\cot\beta_2 - \cot\beta_1}{2L} \tag{3.33}$$

and $\cot\beta = W_\theta / V_m = 2kx + \cot\beta_1$.

The geometry of a 2D parabolic blade profile of entry angle β_1 and exit angle β_2 is given by

$$y = \frac{\cot\beta_2 - \cot\beta_1}{2L}.x^2 + \cot\beta_1.x \tag{3.34}$$

To simplify, let V_m = constant as would be the case for a 2D cascade with thin blades. Then

$$\begin{aligned} W_\theta &= V_m(2kx + \cot\beta_1), \\ \frac{\mathrm{d}W_\theta}{\mathrm{d}t} &= \frac{\partial W_\theta}{\partial x}\frac{\mathrm{d}x}{\mathrm{d}t} = \frac{\partial W_\theta}{\partial x}V_m, \\ \frac{\mathrm{d}W_\theta}{\mathrm{d}t} &= 2kV_m^2. \end{aligned}$$

Now $\dfrac{\mathrm{d}W_\theta}{\mathrm{d}t} = 2kV_m^2$ is the tangential acceleration of the fluid element and from Newton's second law, $F = ma$,

$$\text{tangential force on element} = (\rho \mathrm{d}xs)(2kV_m^2),$$

and

$$p_p - p_s = \mathrm{d}p = \frac{\mathrm{d}F}{\mathrm{d}x} = (\rho s)(2kV_m^2).$$

From Equations 3.31, 3.32 and 3.34

$$\begin{aligned} \mathrm{d}p &= -\tfrac{1}{2}\rho\left\{(\bar{W} + W_c)^2 - (\bar{W} - W_c)^2\right\}, \\ &= -\tfrac{1}{2}\rho 4\bar{W}W_c, \\ W_c &= -skV_m\sin\beta. \end{aligned} \tag{3.35}$$

Increasing the circulation velocity increases the blade loading. Using fewer blades increases the pitch s and thus increases the blade loading. The rate of blade turning with respect to x (i.e. k) also affects the blade loading.

Equation 3.35 applies to parabolic blades, The same analysis can be applied to blades of circular arc. In this case

$$W_c = \frac{sV_m(\cos\beta_2 - \cos\beta_1)}{2L\sin^2\beta}. \tag{3.36}$$

It can be seen that, for the same fluid deflection between inlet and outlet, blades with parabolic camberlines are less loaded than those with circular arc camberlines in the trailing edge region.

A general form for Equations 3.35 and 3.36 can be developed in three-dimensional space. With reference to Figure 3.9(a), a particle lying at X, halfway between positions A and B, has a tangential acceleration,

$$a_t = \frac{MV}{dt} = \Omega V_r + r\frac{\delta\Omega}{\delta t} + V_r\Omega$$

where Ω and ω are the angular velocities about the axis zz of the fluid particle and runner respectively. Using Figure 3.9 (c) to find that,

$$\Omega = w + \frac{V_m \cot\beta}{r}$$

the tangential acceleration may be written as,

$$a_t = \frac{d(V_m \cot\beta)}{dt} - \frac{V_m^2 \cot\beta \sin\phi}{r} + 2V_m \sin\phi \left[w + \frac{V_m \cot\beta}{r} \right]$$

Redefining s to be the streampath and using a similar approach to the previous analyses, it may be found:

$$W_c = \frac{\pi r \sin\beta}{Z} \left[\frac{\partial(V_m \cot\beta)}{\partial s} + \frac{V_m \cot\beta \sin\phi}{r} + 2\omega \sin\phi \right] \tag{3.37}$$

The sign convention defined in Figure 3.9 (c) must be adhered to when applying Equation 3.37. Equation 3.37 can be used to determine an approximate value for W_c given a blade shape at point X. The influence of stream tube contraction ($\partial V_m/\partial s$), the inclination of the stream lines from the radial (ϕ) and the blade number Z can also be investigated. For axial flow, $\phi = 0$ and Equation 3.37 will reduce to Equation 3.35 or Equation 3.36, depending on the relationship between β and blade pitch. It is worth noting that these analyses assume that V_m remains constant with θ.

Equation 3.37 provides a practical limit to what can be calculated manually (or with a spreadsheet). The next step is to use Euler solvers (no viscosity term) or Navier Stokes flow solvers (full equations of motion with viscosity modelled). These later methods require complex software and significant computing power.

Zweifel [1945] provides a blade loading coefficient, ψ_T, that has found use in axial flow turbine hub sections.

For constant axial velocity V_m,

$$\psi_T = 2\frac{s}{L}\sin^2\beta_2 \left(\cot\beta_2 - \cot\beta_1\right). \tag{3.38}$$

Zweifel [1945] showed that cascades have minimum loss when $\psi_T \approx 0.8$. Equation 3.38 can be used to determine L for a given fluid deflection and blade pitch s.

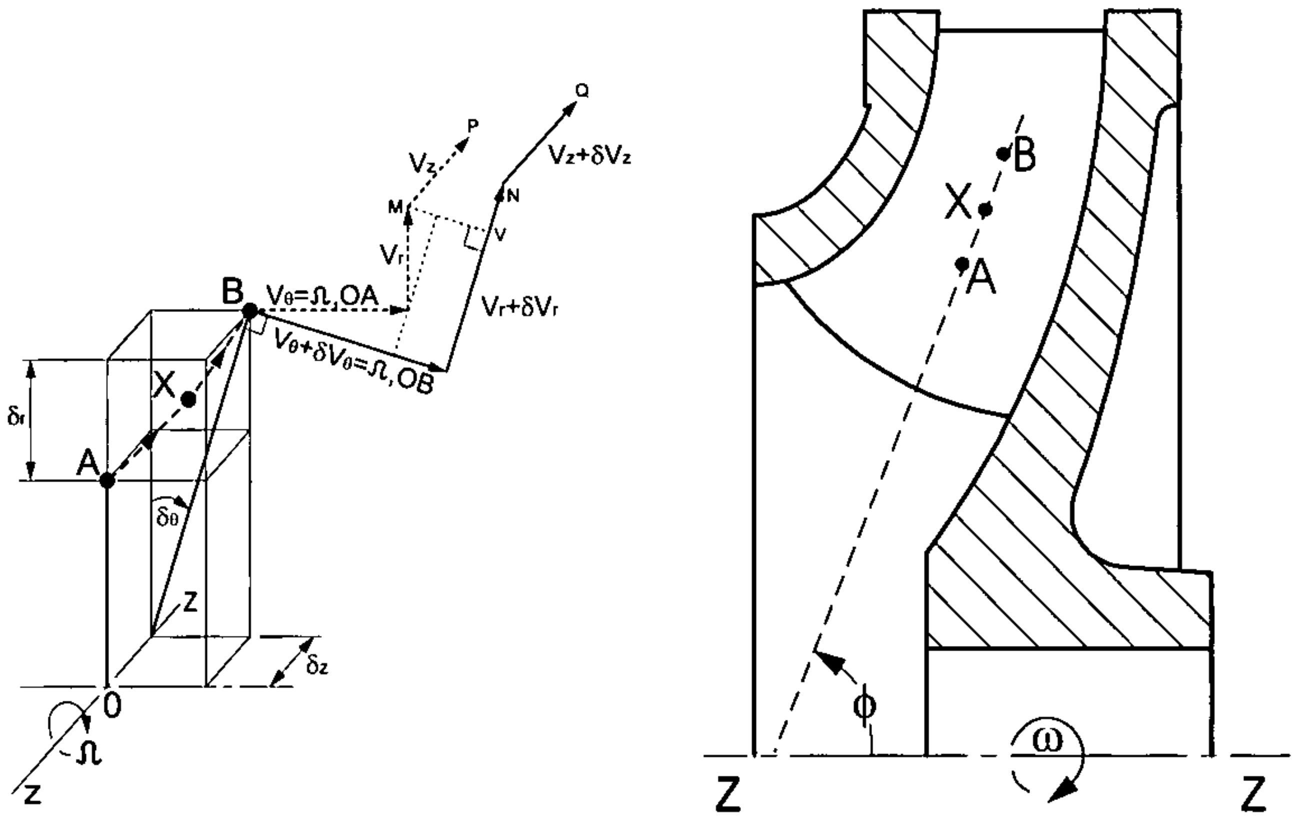
Q
P
V_z
$V_z+\delta V_z$
M
N
V_r
V
B
$V_\theta=\Omega.OA$
$V_r+\delta V_r$
$V_\theta+\delta V_\theta=\Omega.OB$
X
δr
A
$\delta\theta$
Z
δz
0
Ω
Z
B
X
A
ϕ
Z
ω
Z

(a) Particle in space

(b) Meridional view

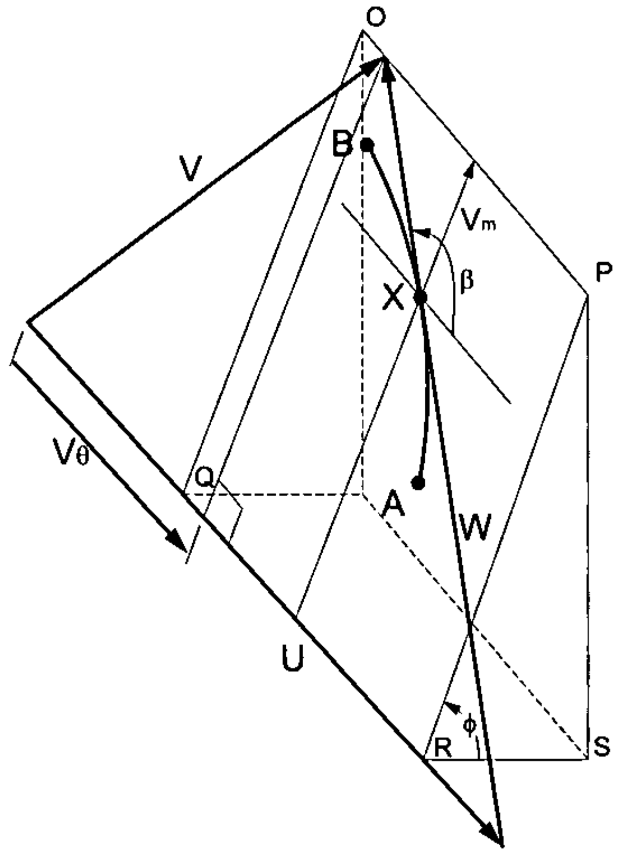
O
V
B
V_m
β
P
X
$V\theta$
Q
A
W
U
ϕ
R
S

(c) Sign convention

Fig. 3.9. Acceleration of a particle in space.

Coriolis forces have a significant effect on the flow in radial machines. It increases the loading on the blades over the loading associated with fluid deflection. The magnitude of this increase is predicted by Equation 3.17.

The Coriolis effect also influences the flow incidence on a Francis turbine runner blade. In Figure 3.10, the stagnation point is shown on the graph and on the blade. High loadings due to Coriolis forces are the reason for the stagnation point progressing onto the pressure surface. Without any blade loading, due say to Coriolis or fluid deflection or blockage effects, the fluid would strike the blade close to the nose of the blade with an incidence i. The effect of the loading is to generate a circulation velocity which changes the flow direction from $i = 5°$ to $i = 25°$ say. The velocity plot is against percentage surface length. So the flow direction is negative to the left of the stagnation point. This is seen on the velocity plot as a negative velocity, but still on the pressure face. Where the velocity is plotted exactly at the leading edge, there are two positions on the velocity versus surface length graph at +4.0 and −4.0 which are in effect the same point on the blade. The velocity just after the leading edge on the stagnation point on the suction face is seen to be very high and decelerating. This will cause flow separation due to the very high adverse pressure gradient. However the accelerating flow after this velocity spike on the suction face should cause the flow to reattach quickly and little loss is experienced. More critical is the possibility that the circulation velocity is so high that the flow on the pressure face is reversed. Whilst the flow reversal on the pressure face is an inviscid effect, in practice, such a flow reversal might result in pressure face separation and a significant loss.

The incidence induced by Coriolis loading can be estimated using an equation due to Wiesner [1967],

$$\sigma_w = 1 - \frac{\sqrt{\sin \chi_1}}{Z^{0.7}} = 1 - \frac{V_s}{U_1}. \tag{3.39}$$

This equation was originally developed to estimate pump ‘slip’, an effect due principally to the Coriolis loading at the blade trailing edge. Figure 3.11 illustrates how Equation 3.39 is applied.

All slip factors must be multiplied by $\sin \phi$ (ϕ is the angle of meridional flow direction relative to the rotational axis) when the flow departs from the radial direction. See Figure 3.14.

For axial flow turbines, Coriolis loading is generally not a significant term. Incidence is affected by blade loading due to the blade stagger and camber, Figure 3.12 (a), and by blade blockage effects, Figure 3.12 (b).

Deviation can be predicted using Carter's rule [Carter, 1950]

$$\delta^o = m\theta \frac{s}{c} \tag{3.40}$$

See Figure 3.13. Again, where a change of radius occurs, the deviation associated with Coriolis loading needs to be accounted for using Equation 3.39

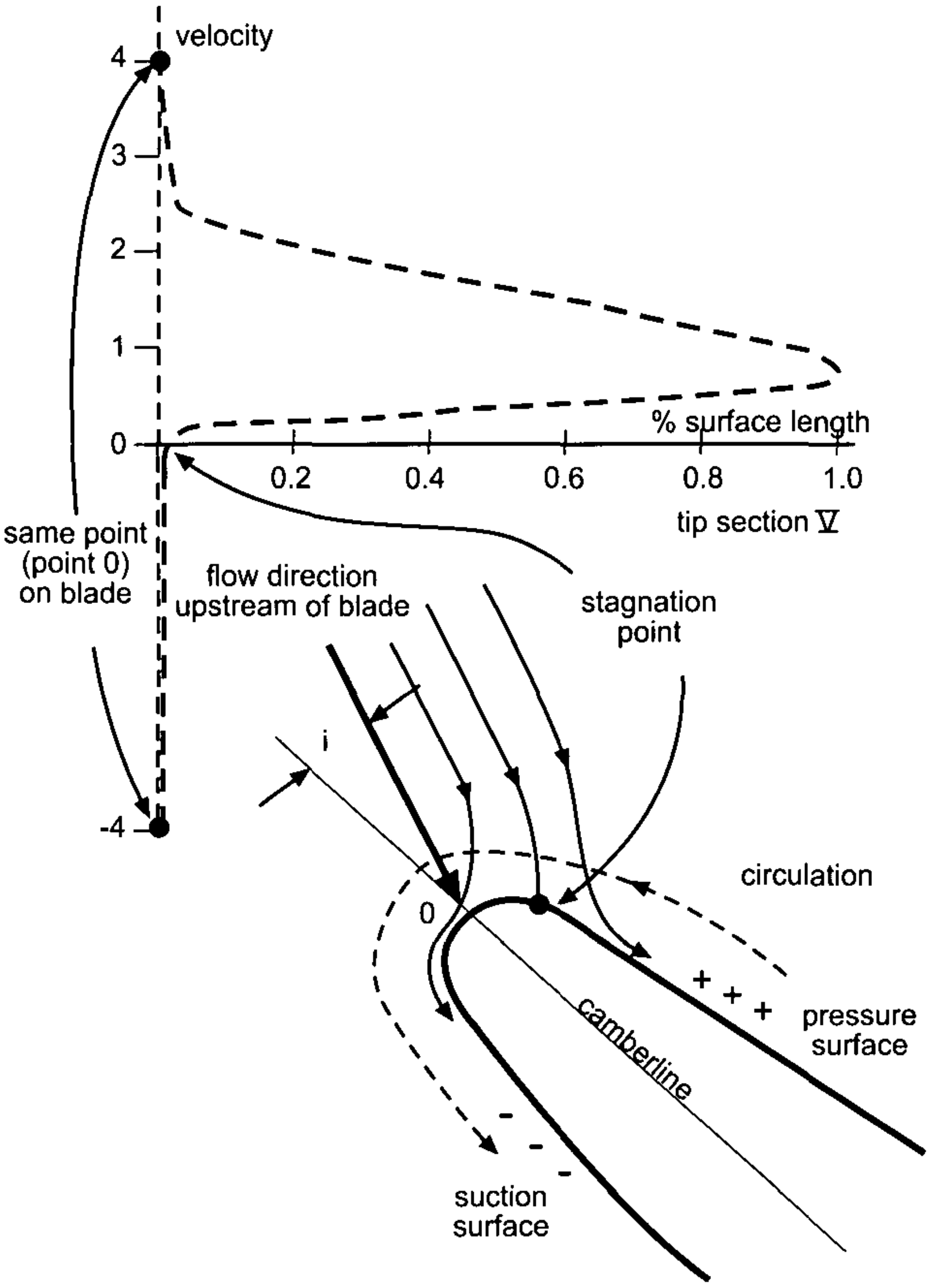
velocity
4
3
2
1
0
-4
% surface length
0.2
0.4
0.6
0.8
1.0
tip section V
same point
(point 0)
on blade
flow direction
upstream of blade
stagnation
point
i
0
circulation
+ + +
pressure
surface
camberline
- - -
suction
surface

Fig. 3.10. Incidence loading due to Coriolis loading.

and the sin ϕ term. Chapters 14 and 15 provide examples of how these effects are accounted for in the design process.

3.9 Mean streamline analysis

In Section 3.3, Euler's equation linking the total change in angular momentum along any given stream surface to the total blade force or torque. Mean streamline analysis derives essentially the same equation for an elemental step within a blade-stream surface intersection, Figure 3.14.

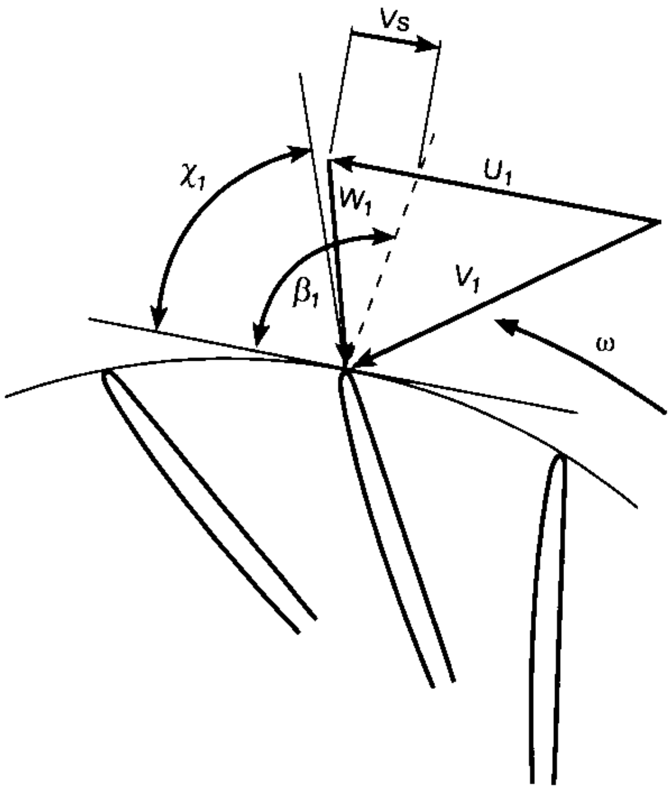

Fig. 3.11. Francis turbine leading edge.

The mean relative velocity $\bar{W}$ follows the camberline geometry of the blade section.

Consider an element of flow of length δm, thickness δn, width $2\pi r - Zt$, and tangential area A, where t is the circumferential blade thickness and Z is the number of blades.

$$\begin{aligned} \delta T &= \delta \dot{m}\, \delta(rV_\theta), \\ \delta P &= \delta \dot{m}\, \delta(UV_\theta) = (p_p - p_s)Zr\omega\, \delta A, \\ \rho V_m \omega(2\pi r - Zt)\, \delta n\, \delta(rV_\theta) &= (p_p - p_s)Zr\omega\, \delta m\, \delta n. \end{aligned}$$

Writing $\delta(rV_\theta) = \dfrac{\partial(rV_\theta)}{\partial m}\, \delta m$ then

$$\Delta p = p_p - p_s = \rho V_m \left\{ \frac{2\pi}{Z} - \frac{t}{r} \right\} \frac{\partial(rV_\theta)}{\partial m}\,. \tag{3.41}$$

The pressure difference Δp is related to the relative velocities on the pressure and suction faces, W_p and W_s respectively. Combining Equations 3.31 and 3.32

$$p_p + \tfrac{1}{2}\rho W_p^2 = p_s + \tfrac{1}{2}\rho W_s^2$$

$$\text{therefore} \qquad \Delta p = -\tfrac{1}{2}\rho\left[(\bar{W} + W_c)^2 - (\bar{W} - W_c)^2\right]$$

$$\text{therefore} \qquad \Delta p = -2\rho \bar{W} W_c. \tag{3.42}$$

Equations 3.41 and 3.42 imply that for a known distribution rV_θ with streamline distance s, and a known V_m, then the blade pressure difference

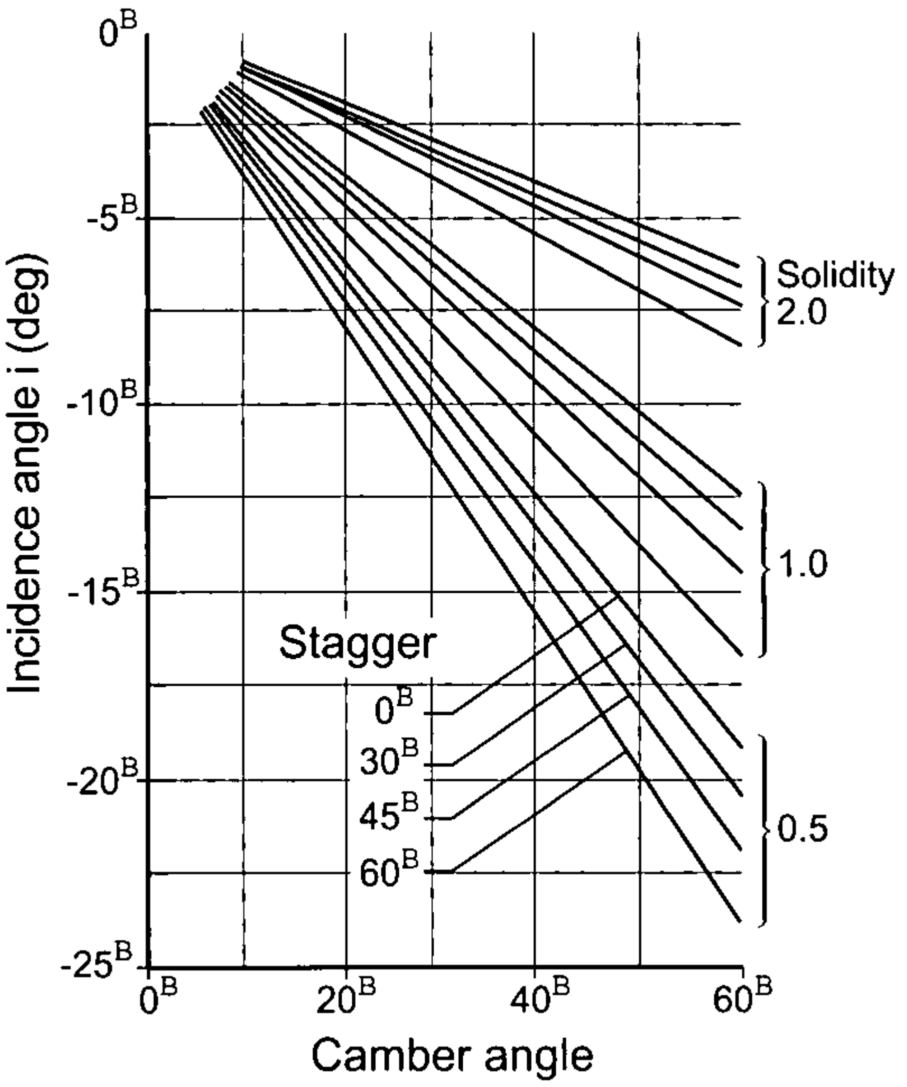

(a) Blade loading. Adapted from Weinig [1935]

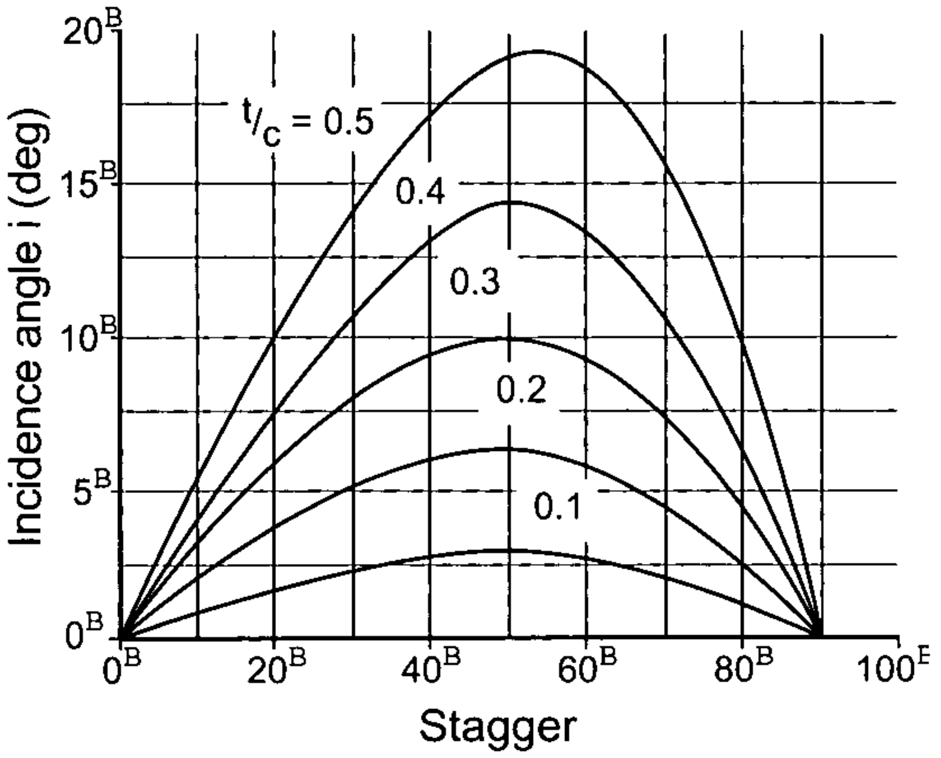

(b) Blade blockage. Adapted from Stanitz [1953]

Fig. 3.12. Factors influencing incidence angle (other than Coriolis).

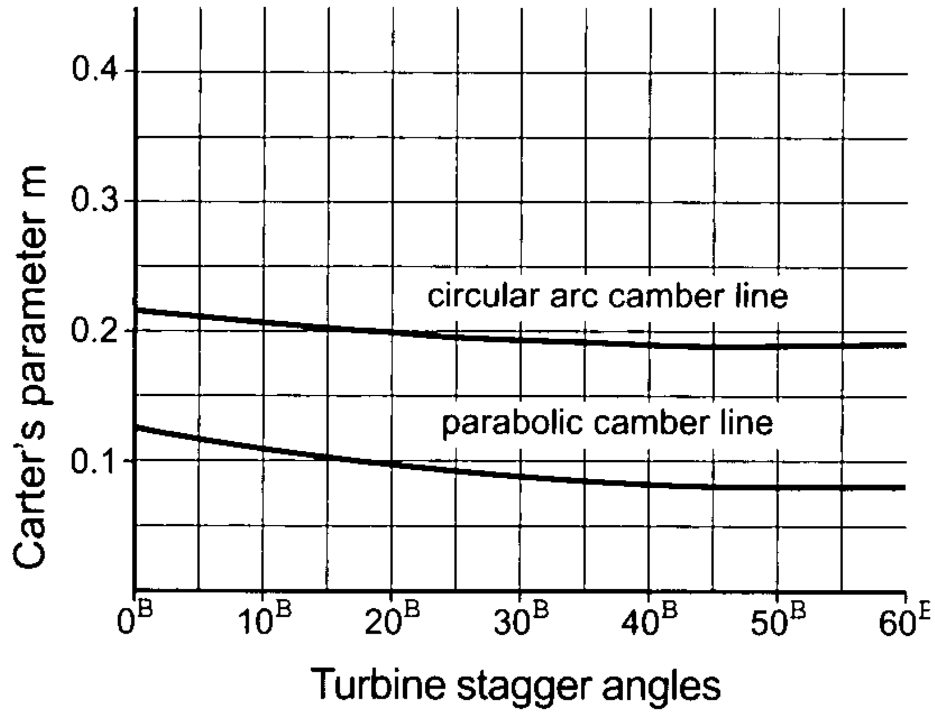

Fig. 3.13. Carter's rule for deviation. Adapted from Carter [1950].

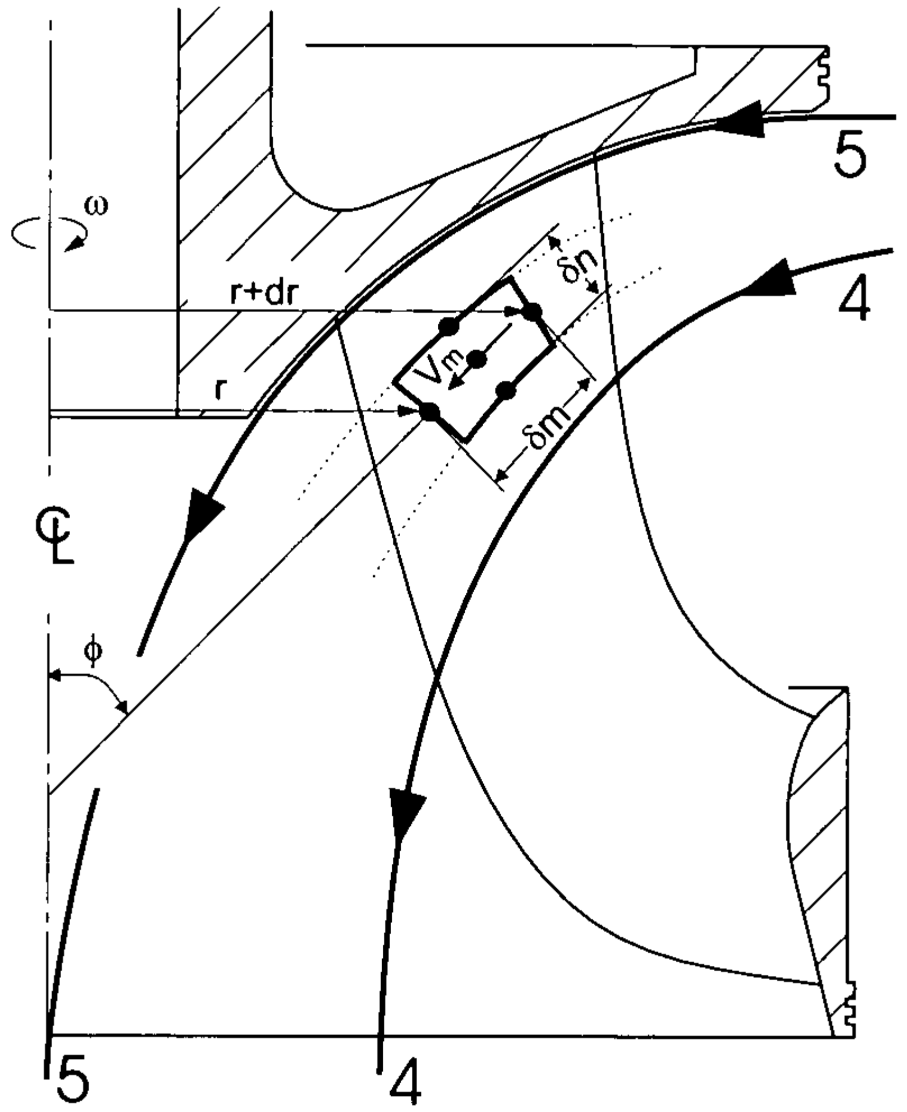
ω
r+dr
r
δn
Vm
δm
5
4
℄
ϕ
5
4

Fig. 3.14. Elemental section lying along a stream surface within the blade row.

Δp and circulation velocity W_c can be found. The local mean pressure $\bar{p}$ is then

$$\frac{p_1}{\rho g} + \frac{V_1^2}{2g} + z_1 = \frac{\bar{p}}{\rho g} + \frac{V^2}{2g} + z + \frac{U_1 V_{\theta 1} - U V_\theta}{g} + \text{losses.} \qquad (3.43)$$

4 Cavitation

Cavitation in water turbines involves the formation of vapour cavities in regions of low pressure and their subsequent collapse in regions of higher pressure. The implosion of cavities close to a solid surface can cause damage. The most common problem associated with cavitation is erosion and the ensuing loss of performance and ultimately component failure. In the most extreme case, cavitation can result in blockage of the flow passages causing significant efficiency loss and a breakdown in performance. Good cavitation primers are Wislicenus [1986] and Knapp [1952], Knapp et al. [1970].

In Francis turbines, the most common location of cavitation and associated damage is on the suction face of the runner blades near the trailing edge and skirt, on the skirt itself and the draft tube inlet cone. Occasionally, with high specific speed runners it can also occur near the leading edge. Flow between the guide vanes and the head and bottom cover clearance gaps can also result in cavitation and damage. See Figures 4.1 (a) and (b).

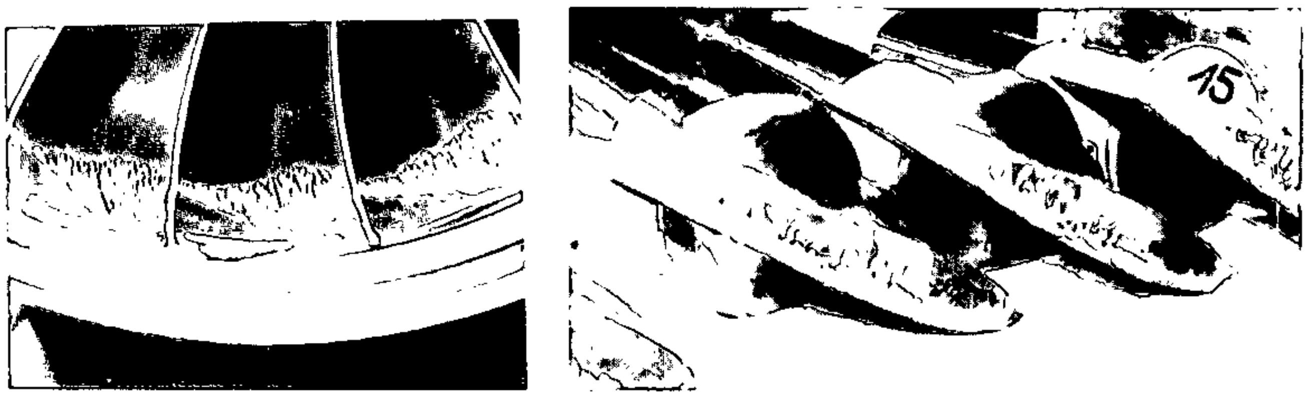

(a) Cavitation erosion on Francis runner

(b) Cavitation erosion on the ends of guide vanes

Fig. 4.1. Cavitation damage. (Reproduced courtesy VA TECH HYDRO)

Cavitation problems are more likely to arise at high load and very low load away from the best efficiency point. They can arise if the turbine is placed too high above the tailrace. Cavitation problems may also be caused by poor blade and skirt design, or incorrect materials selection for the runner.

4.1 Turbine setting

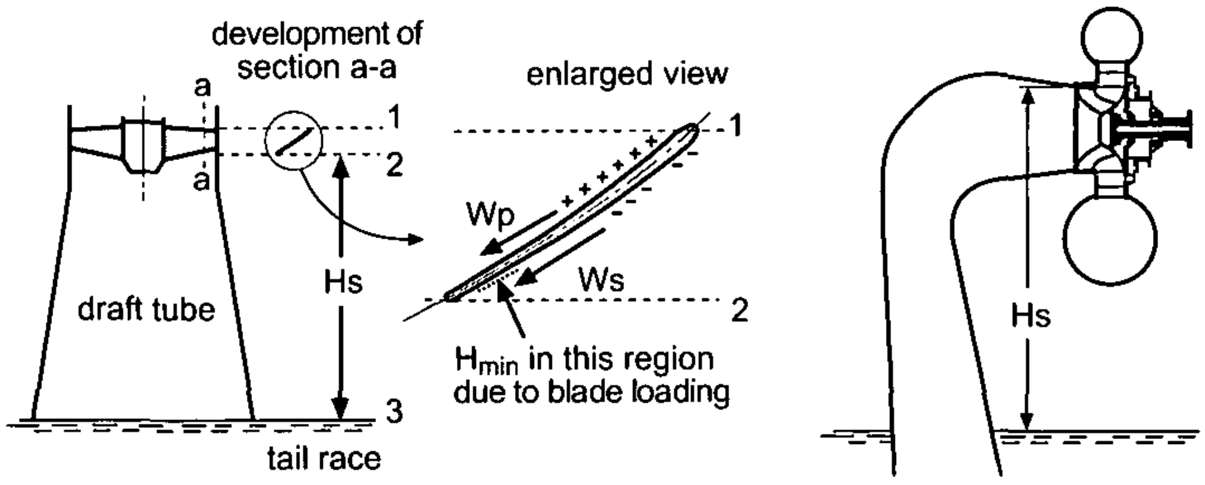
development of section a-a
a
a
1
2
Hs
3
draft tube
tail race
enlarged view
1
Wp
Ws
2
H_{min} in this region due to blade loading
Hs

(a) Vertical propeller turbine

(b) Horizontal Francis turbine

Fig. 4.2. Definition of turbine setting H_s.

Considering Figure 4.2 and applying Bernoulli's equation between sections (2) and (3) with (3) as the datum

$$\frac{p_2}{\rho g} + \frac{V_2^2}{2g} + z_2 = \frac{p_3}{\rho g} + \frac{V_3^2}{2g} + z_3 + \text{losses}. \tag{4.1}$$

Let p_2 and p_3 be absolute pressures. $V_3^2/2g$ can be classified as a loss and section (3) can be far enough away from the draft tube exit that p_3 can be taken to be atmospheric. Thus

$$\frac{p_2}{\rho g} = H_{\text{min}}, \qquad \frac{p_3}{\rho g} = H_{\text{atm}}, \qquad z_2 - z_3 = H_s.$$

H_{min} is the minimum pressure head on the blade surface. H_{atm} is the atmospheric pressure head. H_s is referred to as the turbine setting, taken as positive when the turbine is 'set' above the tailrace.

Rearranging Equation 4.1

$$\frac{V_2^2}{2g} - \left\{\frac{V_3^2}{2g} + \text{losses}\right\} = H_{\text{atm}} - H_{\text{min}} - H_s. \tag{4.2}$$

The terms on the left hand side of Equation 4.2 are proportional to the net head across the turbine, i.e.

$$\sigma H_n = H_{\text{atm}} - H_{\text{min}} - H_s. \tag{4.3}$$

The constant of proportionality σ is known as the turbine sigma.

Cavitation occurs when $H_{\text{min}} \approx H_v$ where H_v is the vapour pressure head, at the given water temperature. Then Equation 4.3 becomes

$$\sigma_T H_n = H_{\text{atm}} - H_v - H_s. \tag{4.4}$$

σ_T is known as the Thoma cavitation parameter and is sometimes referred to as the plant sigma. For no cavitation to occur $H_{\text{min}} > H_v$ or

$$\sigma_T > \sigma. \tag{4.5}$$

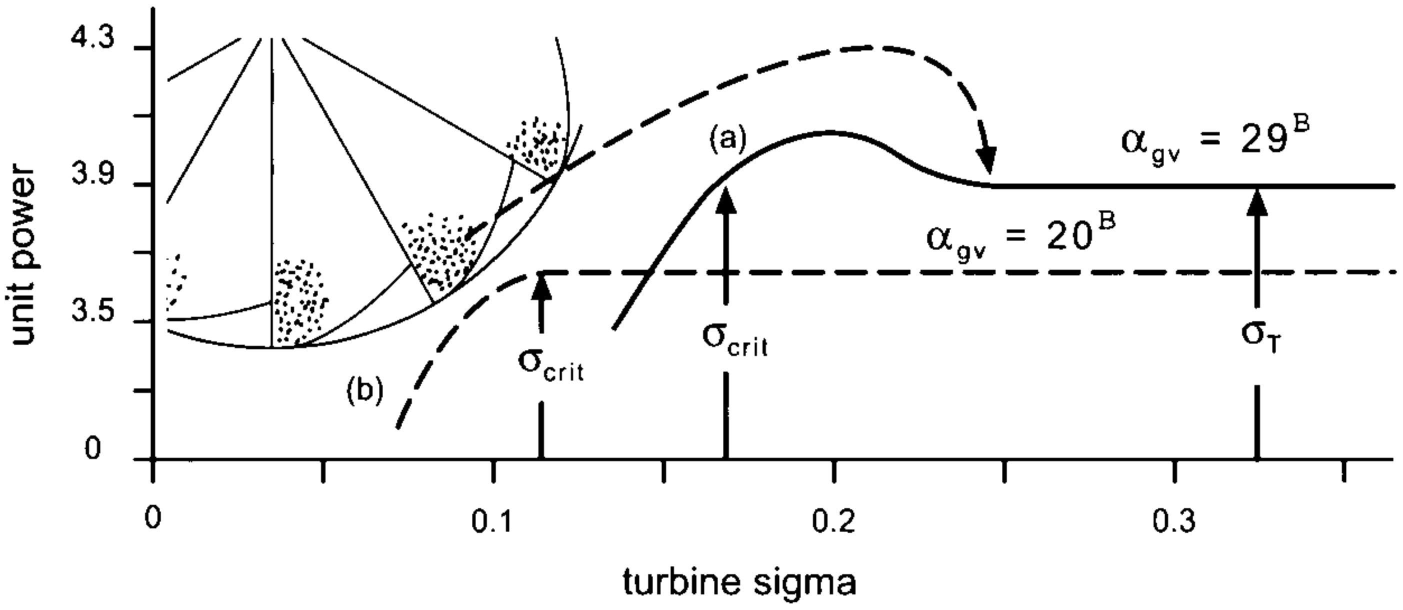

Fig. 4.3. Turbine sigma variation with reducing test rig pressure.

A model turbine can be tested at constant power for a given guide vane setting, e.g. $\alpha_{gv} = 29°$, and one of the terms in Equation 4.3, and the ambient pressure in the rig, H_{amb}, rather than the atmospheric pressure H_{atm}, is varied. (This requires a specially constructed cavitation rig). As H_{amb} ($= H_{\text{atm}}$) is reduced, σ reduces and turbine output remains constant until $\sigma = 0.24$ in the example shown in Figure 4.3. A small increase in output may occur as σ is further reduced, solid curve (a), after which the output falls dramatically. The point at which the performance begins to breakdown is called σ_{crit} or critical sigma. This is approximately 0.16 in the Figure for $\alpha_{gv} = 29°$. When the guide vane setting is changed, say to $\alpha_{gv} = 20°$, a new cavitation plot and a new σ_{crit} (0.12) is obtained. Values of critical sigma, marking turbine performance breakdown, can be plotted on the turbine performance characteristic as illustrated in Figure 4.4 for both changes in guide vane and unit speed settings.

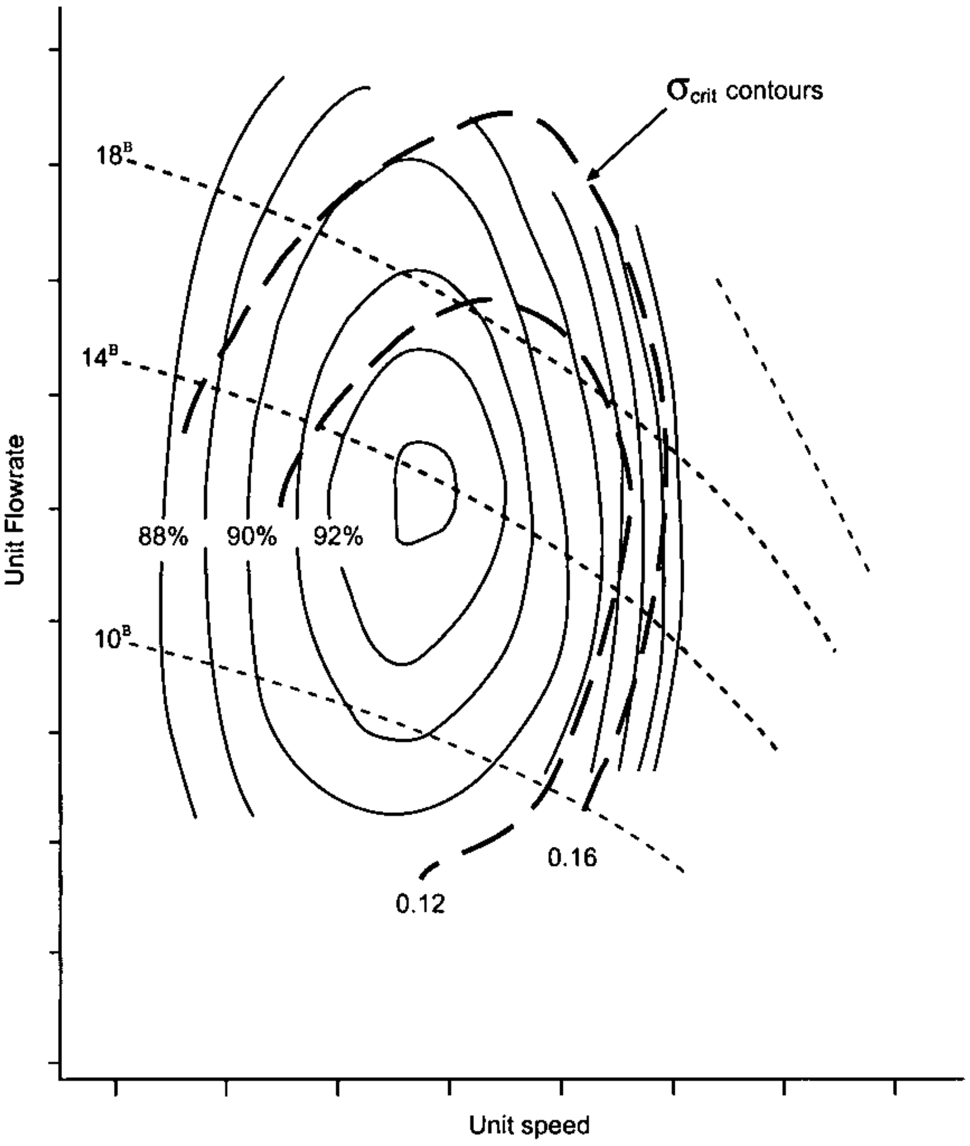

Fig. 4.4. Turbine performance characteristic with lines of constant critical sigma, σ_{crit}, plotted.

Figures 4.5(a) and 4.5(b) provide a guide to predicting the turbine setting from the specific speed. These figures present lines of best fit to actual turbine setting data. However, they are likely to apply strictly to large water turbines and may be insufficiently conservative for the smaller turbines that are the focus of this book.

Figure 4.6 can be used to calculate the variation in vapour pressure head, H_v, with temperature. Figure 4.7 illustrates the variation in atmospheric pressure head with altitude. Taking account of the elevation (altitude) of the powerhouse is necessary.

4.2 Cavitation damage

Prediction of damage is empirical and strongly dependent on the pressure gradient driving bubble collapse.

For large water turbines, it is seldom economic to have the setting sufficiently low that no cavitation damage occurs. Cavitation erosion is excessive

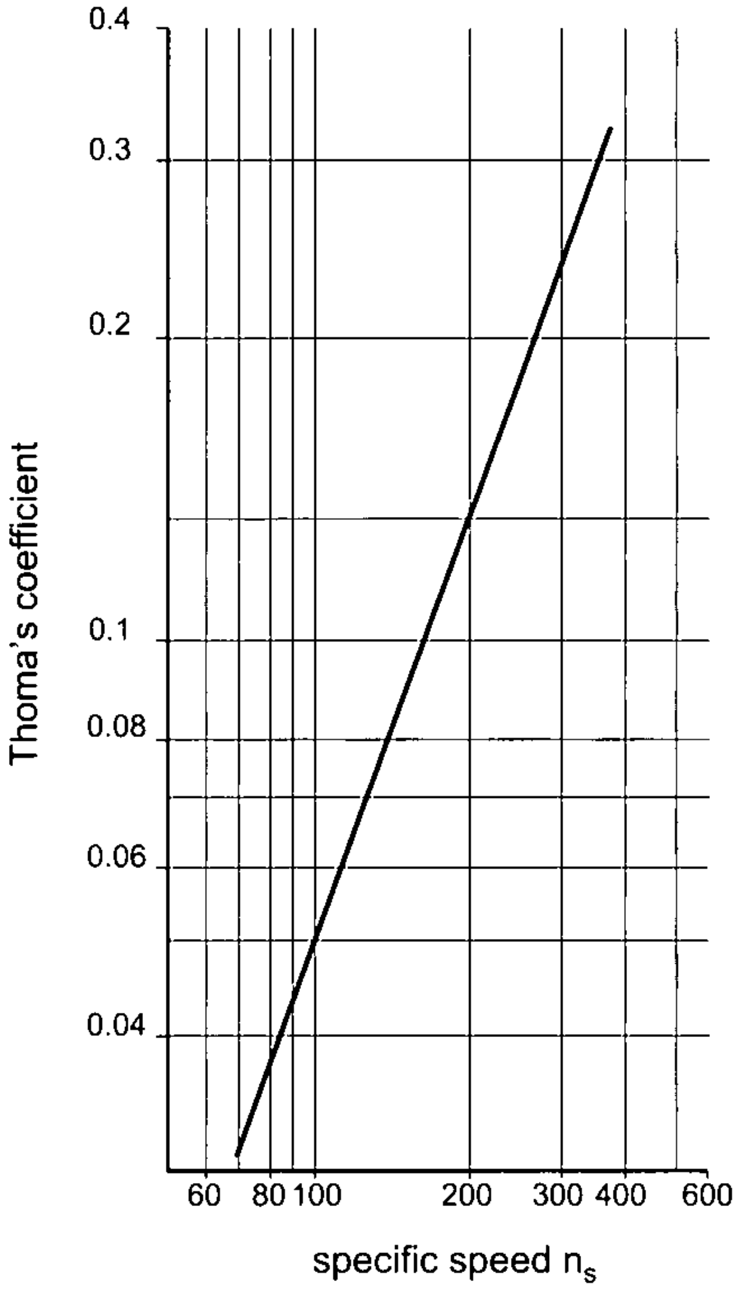

(a) Francis turbines. Adapted from de Siervo and de Leva [1976].

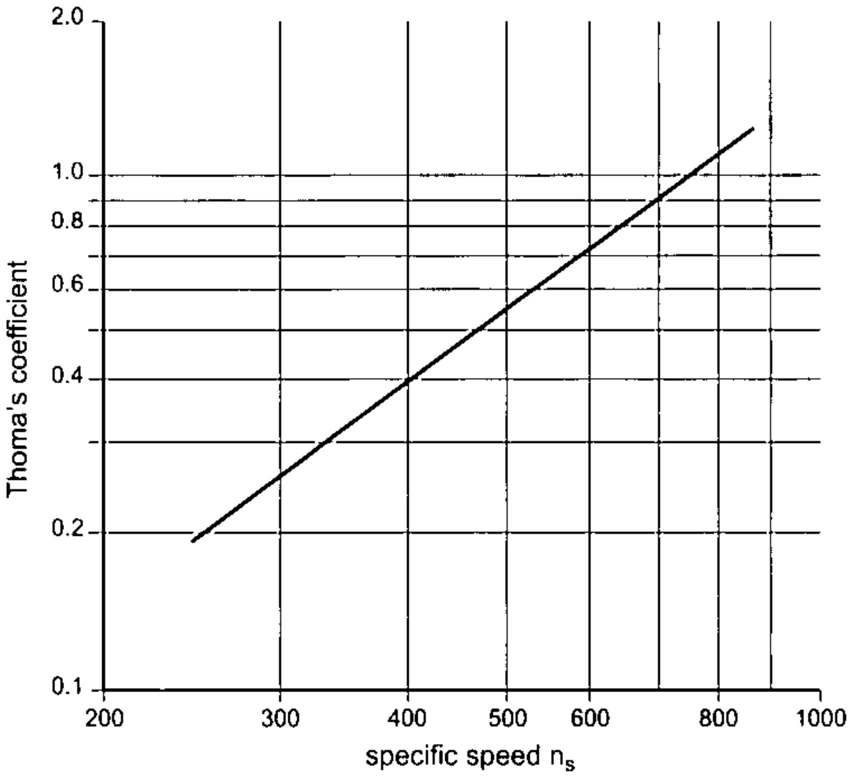

(b) Kaplan and propeller turbines. Adapted from de Siervo and de Leva [1977].

Fig. 4.5. Thoma's sigma versus specific speed. (Reproduced courtesy International Water Power & Dam Construction)

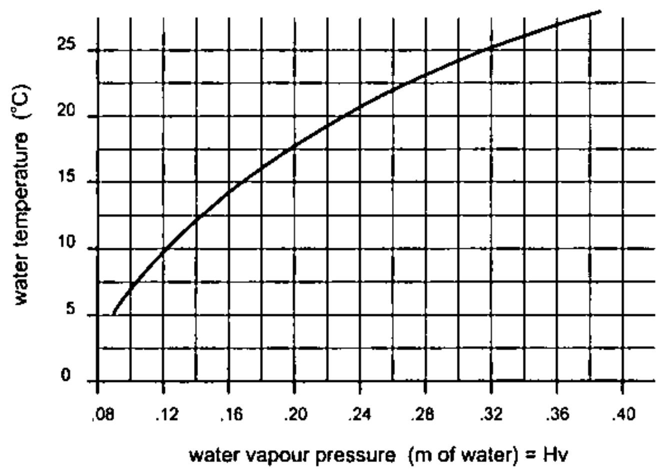

Fig. 4.6. Variation in water vapour pressure head with temperature.

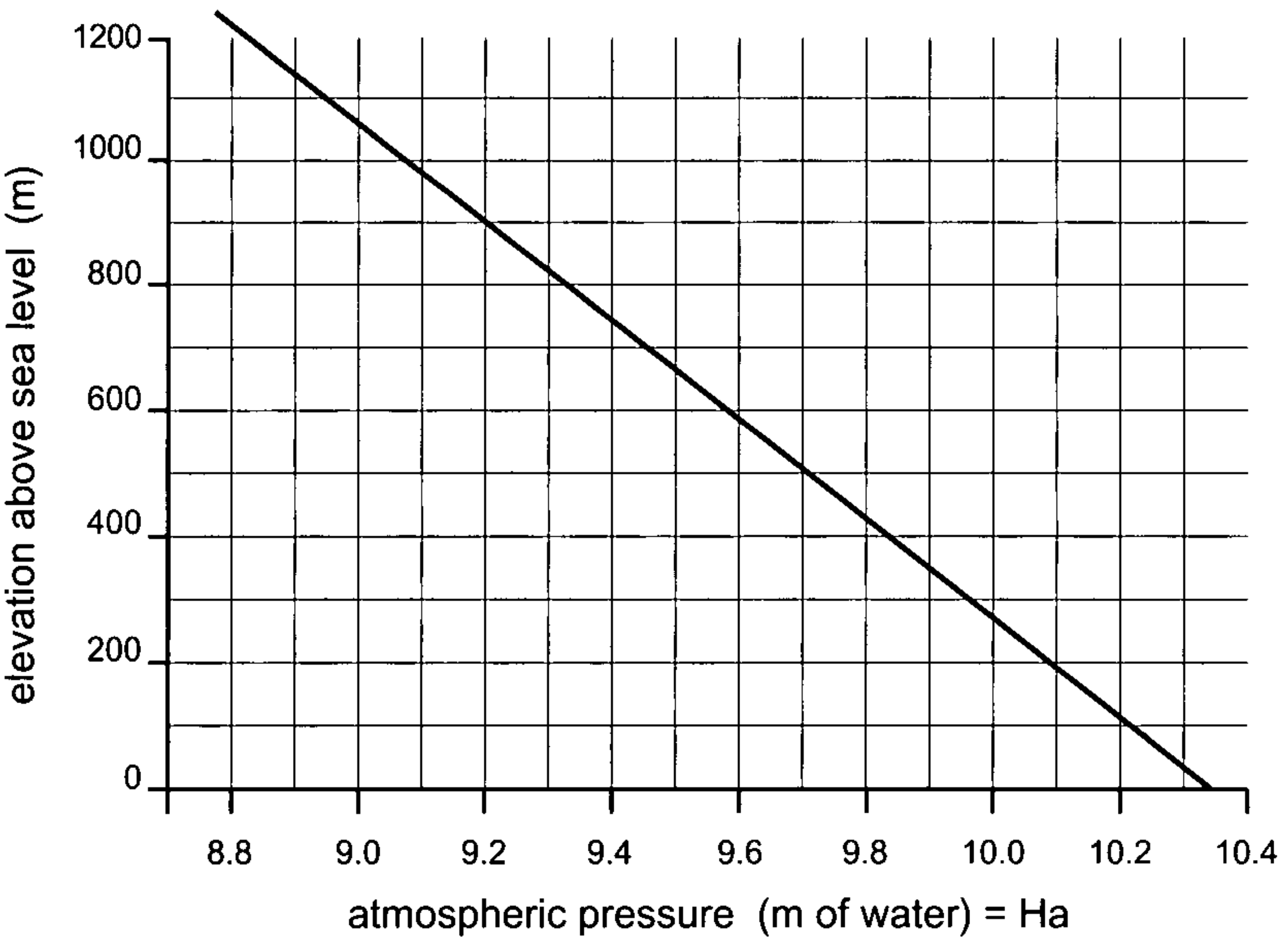

Fig. 4.7. Variation in atmospheric pressure head with altitude.

if it becomes the critical path for weld repair during routine maintenance. For example, 180 man hours are available over a six day maintenance period every 2 years to repair the 3.9m Francis runner at Benmore, New Zealand. During this time, with three people under runner, 23kg of weld can be deposited and ground. The amount of weld material is sometimes specified as a proportion of the runner diameter, e.g.

$$1.5 \times (3.9\text{m})^2 = 23\text{kg}$$

A typical cavitation guarantee in a tender document might require no more than $1.0D^2$ kg of weld material to be deposited for each 8000 hours of operation. Note this formula is an empirical factor and does not have consistent units.

What is sometimes not understood is that for these cavitation guarantees to be economic, it must be possible to assemble a welding team inside the draft tube and weld without removing the runner. For small water turbines this is not the case. Cavitation repairs are often much more costly as the turbine usually has to be dismantled, with more down time accruing. Thus, for small turbines, it is likely to be more economic to reduce the turbine setting, adopt more expensive runner materials or both, in order to avoid cavitation erosion.

4.2.1 Materials performance under cavitating conditions

Figure 4.8 shows the cavitation erosion performance of a common 0.2% carbon manganese steel, a 13-4 chrome nickel martensitic stainless steel and associated welding consumables.

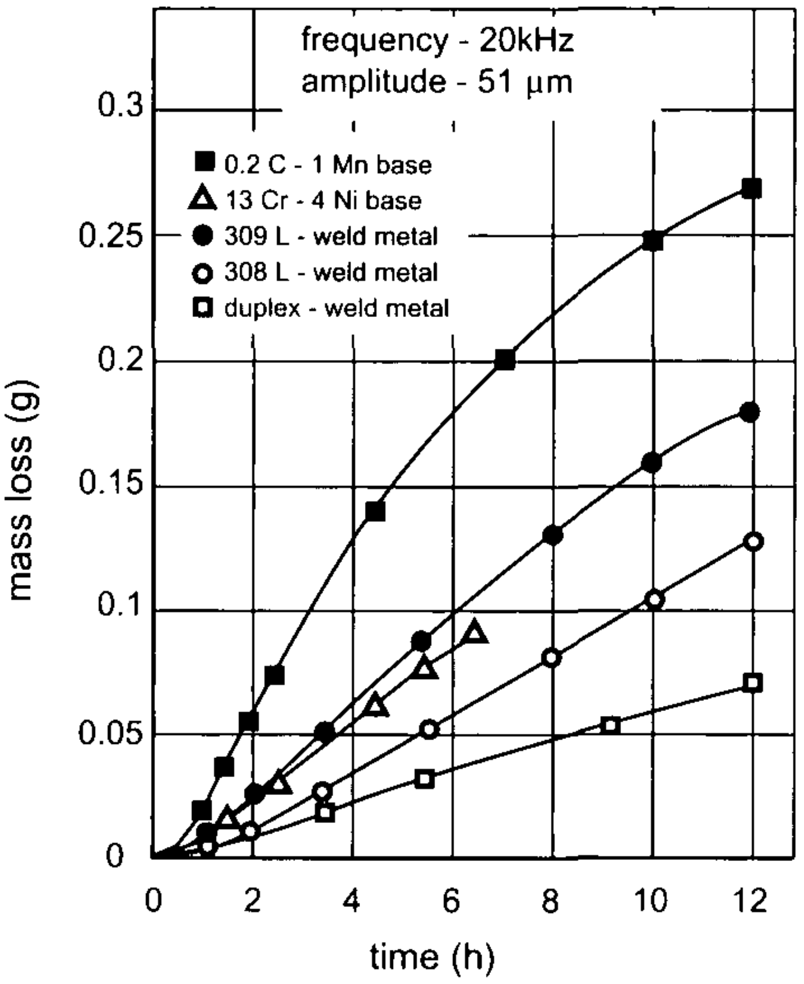

Fig. 4.8. Metal loss due to cavitation erosion. Adapted from Akhtar [1986]. (Reproduced courtesy International Water Power & Dam Construction)

Table 4.1 provides a list of typical turbine materials and the relative loss of material experienced under cavitating conditions. Aluminium bronze (AB2) and 13-4 stainless steel are good materials if the runner is to be cast. 18/8 and 17/4 stainless steels have been used when the runner is to be fabricated. There are other materials that perform well. See Chapter 13 for further details.

material	cavitation rate (mg/h)
A-27 – cast	35.0
CA6NM – cast	15.0
308 Stainless Steel – welded	15.0
301 Stainless Steel – welded	6.0
Stellite® 21 – welded	1.4
Stellite® 6 – welded	0.7

Table 4.1. Cavitation rate of materials using the vibratory cavitation test. Adapted from Simoneau [1991].

Cast iron will have erosion rates more than twice those of cast steel. Aluminium bronze (AB2) will be somewhat better than cast stainless steel. Note that different compositions, methods of application and test methods will introduce some variability into these results.

The US Army Corps of Engineers Construction Engineering Research Laboratories (CERL) have a web page www.cecer.army.mil/techreports/boycav as of 2002, with further information.

5 Draft tube design

To keep costs down, turbine size is kept as small as possible. This results in high velocities exiting from the turbine. The primary function of the draft tube is to recover the kinetic energy at the turbine runner exit. A secondary function of the draft tube is to utilize the head provided by the difference between the turbine centreline elevation and the tailrace elevation. Where the turbine setting is below the tailrace water level, this secondary function does not apply.

A measure of the effectiveness of the draft tube in recovering the kinetic energy at the turbine runner exit is provided by the draft tube efficiency. Draft tube efficiency η_{DT} is defined as

$$\eta_{\mathrm{dt}} = \frac{H_{\mathrm{atm}} - H_2}{V_2^2/2g}, \tag{5.1}$$

where H_{atm} and H_2 are the piezometric heads at draft tube exit and inlet respectively and V_2 is the flow velocity at draft tube inlet. This efficiency definition only applies where uniform axial flow pertains at the draft tube inlet and includes the exit velocity head as a loss.

If a test was conducted on a draft tube model, with uniform axial flow at inlet, the pressure distribution along the inside and outside walls of the draft tube would look similar to Figure 5.1. The draft tube efficiency in this example would be 0.8 or 80%.

For non-uniform flow into the draft tube, a mass averaged formula such as

$$\eta_{\mathrm{dt}} = \frac{-\int_0^{R_2} p_2 r \mathrm{d}r V_{m_2}}{\frac{1}{2}\rho \int_0^{R_2} r \mathrm{d}r V_{m_2} V_2^2} \tag{5.2}$$

might be applied, where p_2 is the pressure at the runner exit plane, relative to the draft tube exit pressure.

A common fallacy is to consider extending the draft tube leg with the intention of increasing the exit area and reducing the kinetic energy thrown away; thus "saving energy". Extending the diffusing leg too far results in flow separation and increased losses. Minimum losses are achieved when the draft tube efficiency is a maximum. Draft tube efficiencies around 85%, perhaps a little more, should be possible. The most efficient draft tube (potentially)

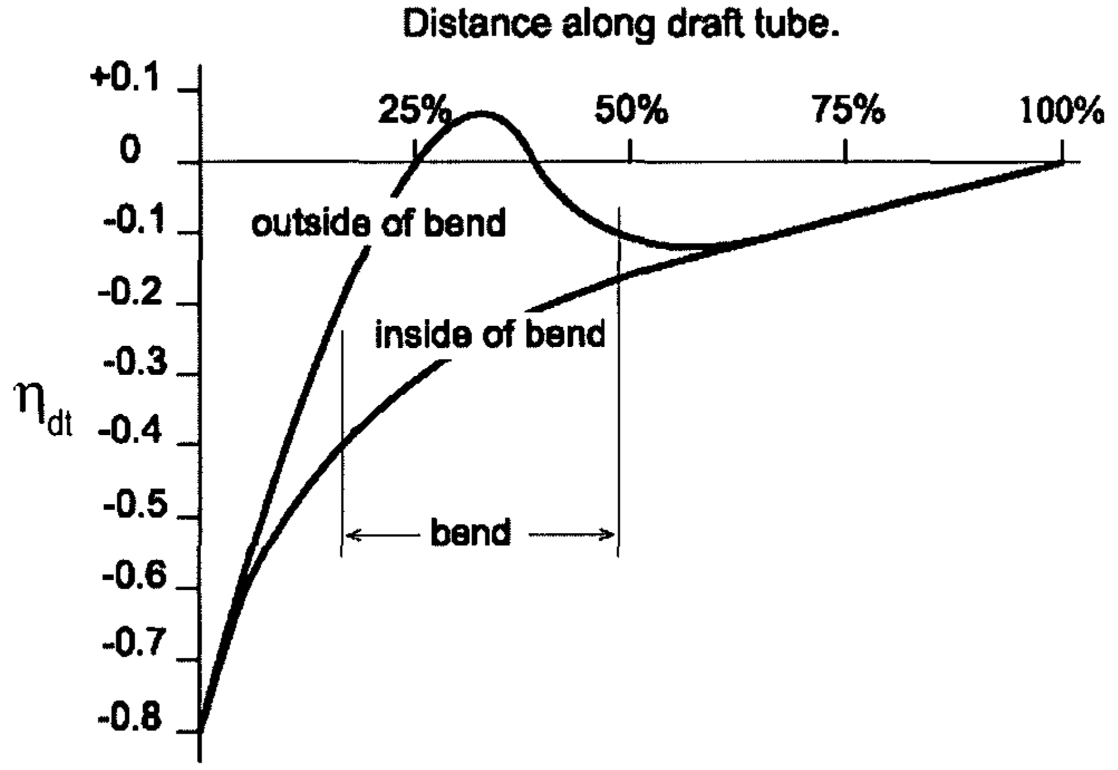

Fig. 5.1. Non-dimensional draft tube pressure variation with distance along draft tube.

is a plain conical draft tube with no elbow, for example see Figure 1.7 (b). Except for very small turbines of a few hundred kW or less, conical draft tubes, arranged vertically, require too much excavation and are thus not common.

Figure 5.2 shows the plan and side views of two Francis turbine elbow type draft tubes which have been non-dimensionalised on the basis of their inlet diameters. Noticeable differences in design are apparent, particularly with regard to their depth and length. Shallower draft tubes were in vogue in the 1950s and 1960s as they kept excavation costs to a minimum. However, as turbine power densities increased, operating Francis turbines with shallow draft tubes at part load often incurred unacceptable power swings and penstock pressure surges. The cause of these surges and power swings was attributed to the cavity rope which formed during part load operation and which extended sinuously as far down as the draft tube bend. See Figure 5.3. As the rope rotated, transitory stall occurred which resulted in the diffuser performance crashing and the creation of a synchronous pressure surge in the draft tube and penstock. Modern draft tubes, as indicated by Thicke [1981] and suggested by Figure 5.2, have a deeper construction to reduce the problems of part load stabilities. As a major part of the draft tube recovery is provided by the draft tube inlet cone – see Figure 5.1 for example – one might expect an improvement in draft tube efficiency over the more compressed designs.

The draft tube is essentially a diffusing passage with a nominal outlet to inlet area of ratio of between 3 and 4. Draft tube features typically comprise an inlet cone, bend and outlet leg. Experience suggests that with this com-

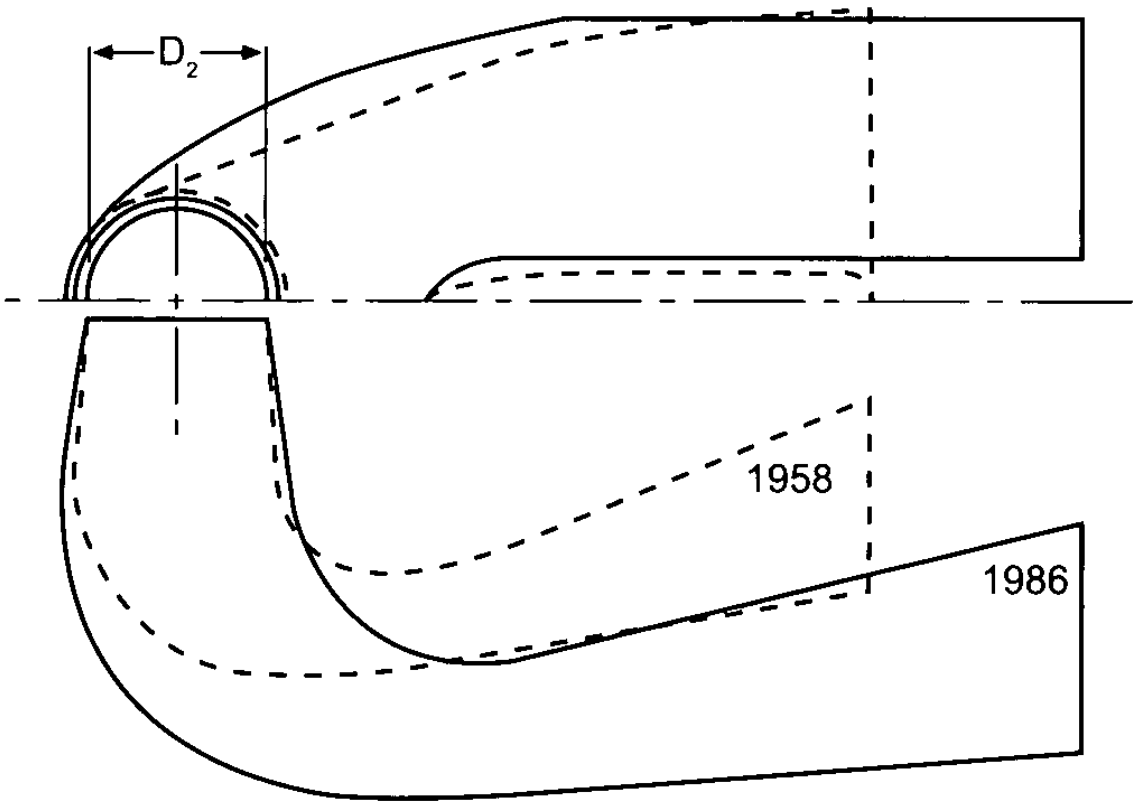

Fig. 5.2. Elbow type draft tube designs.

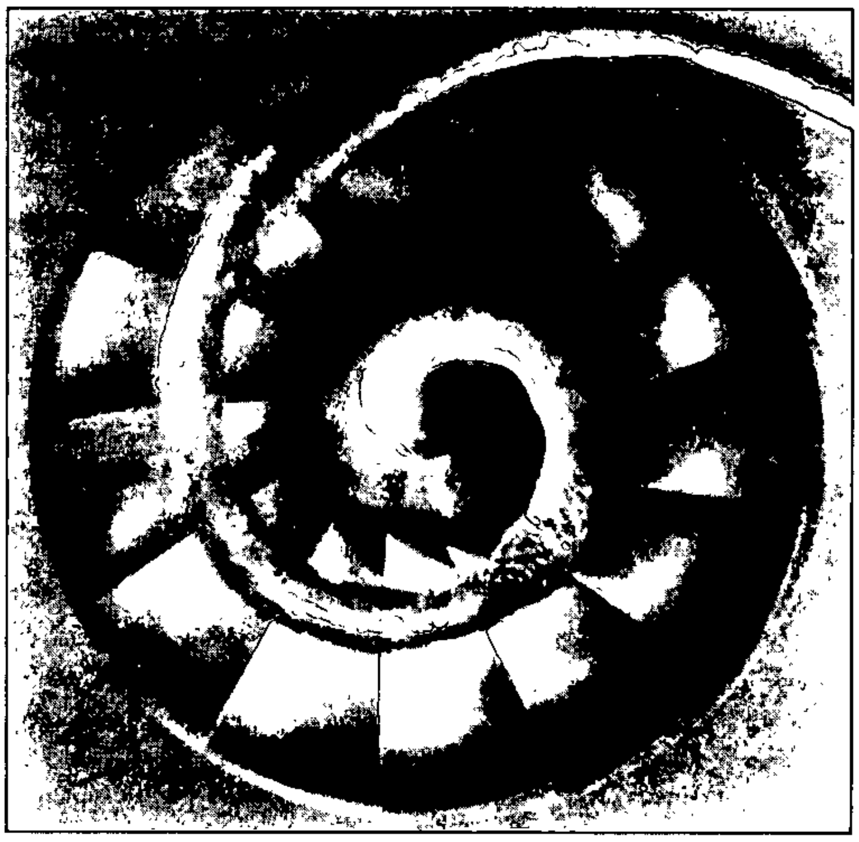

Fig. 5.3. Cavity rope in draft tube at part load (viewed from below, looking up at the Francis runner outlet). (Reproduced courtesy VA TECH HYDRO)

bination of features and area ratio, continuous diffusion is not possible if the best draft tube efficiencies are to be obtained. Figure 5.4 presents the non-dimensionalised area versus draft tube centreline distances of the draft tubes illustrated in Figure 5.2. The 1958 and 1986 designs both have accelerating flow in their bends. This acceleration of the flow re-energises the boundary layer and thus avoids separation and its associated high losses.

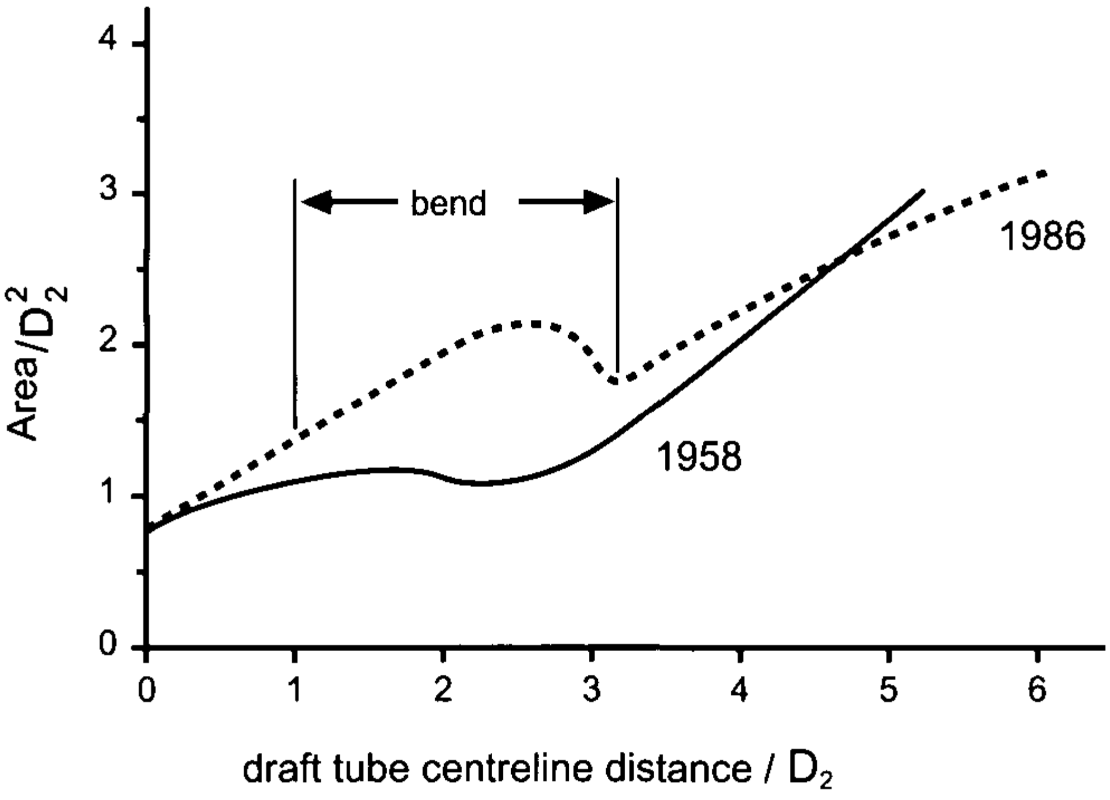

Fig. 5.4. Area ratio variation with draft tube non-dimensionalised length.

Table 5.1 presents estimated efficiencies of the three draft tubes together with an energy balance.

Draft tube	Metric specific speed	Draft tube efficiency (%)	Energy at runner exit as % of net head	Energy at draft exit as % of net head	Energy recovered as % of net head
1958	330	80	20	1.5	16
1986	230	85	5.4	0.35	4.6
—	900	85	70	—	59

Table 5.1. Draft tube energy balance for turbines of different specific speeds.

The energy levels at the runner and draft tube exit stations as presented in Table 5.1 are calculated from the respective mean velocities. Due to high turbulence intensities, the energy at the draft tube exit will be substantially understated. For example, the 1958 draft tube has a calculated energy level of 1.5% at the draft tube exit whereas the true energy level will be approximately 4%. It is in fact possible to recover some of the kinetic energy linked with these intense turbulent eddies by the deployment of a non-diffusing extension. Miller [1990] provides experimental verification.

Table 5.1 also illustrates the increased importance of good draft tube design as specific speed increases. For 'straight flow' propeller turbines with specific speeds as high as 860, the draft tube's role is crucial with up to 75% of the energy at the runner exit, as percentage of the net head, needing to be recovered.

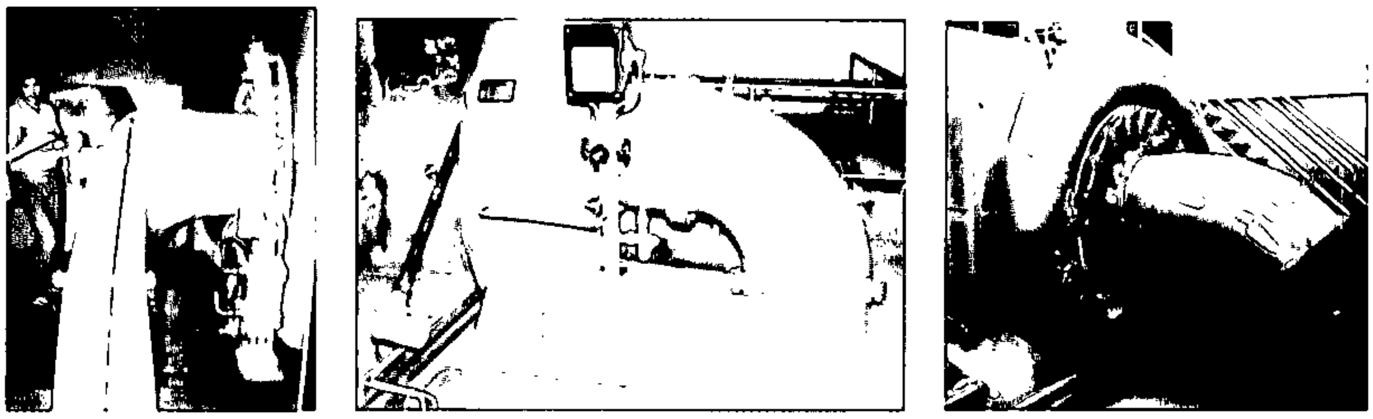

(a) Elbow

(b) Constant area bend and leg

(c) Expanding bend (Reproduced courtesy GE HYDRO)

Fig. 5.5. Draft tube types.

Figure 5.5(a) shows a horizontal Francis turbine with an elbow type draft tube. This is an unusual arrangement, presumably adopted due to space restrictions. More normal is a cone, then the 90° bend, then either a straight section or an expanding section for low and medium specific speed Francis turbines. For high specific speed Francis or propeller turbines, a cone, a 30° (or less) bend, a transition piece (circular to rectangular), and a rectangular diffusing leg is one option. Alternatively, a cone-bend-cone configuration is a possibility. There is some evidence that the rectangular section can partially recover the V_θ KE component of the flow leaving the runner.

Two draft tube designs are shown in Figures 5.6 and 5.7. Using Figure 5.8, the first cone in Figure 5.6 could have an area ratio of say 1.8, followed by a small bend, of say 20°, then an expanding leg with an area ratio of 2.5 might be acceptable. For Figure 5.7, the cone has $N/R_1 = 0.8$ and a 1.2 area ratio, also $R/D = 1.5$.

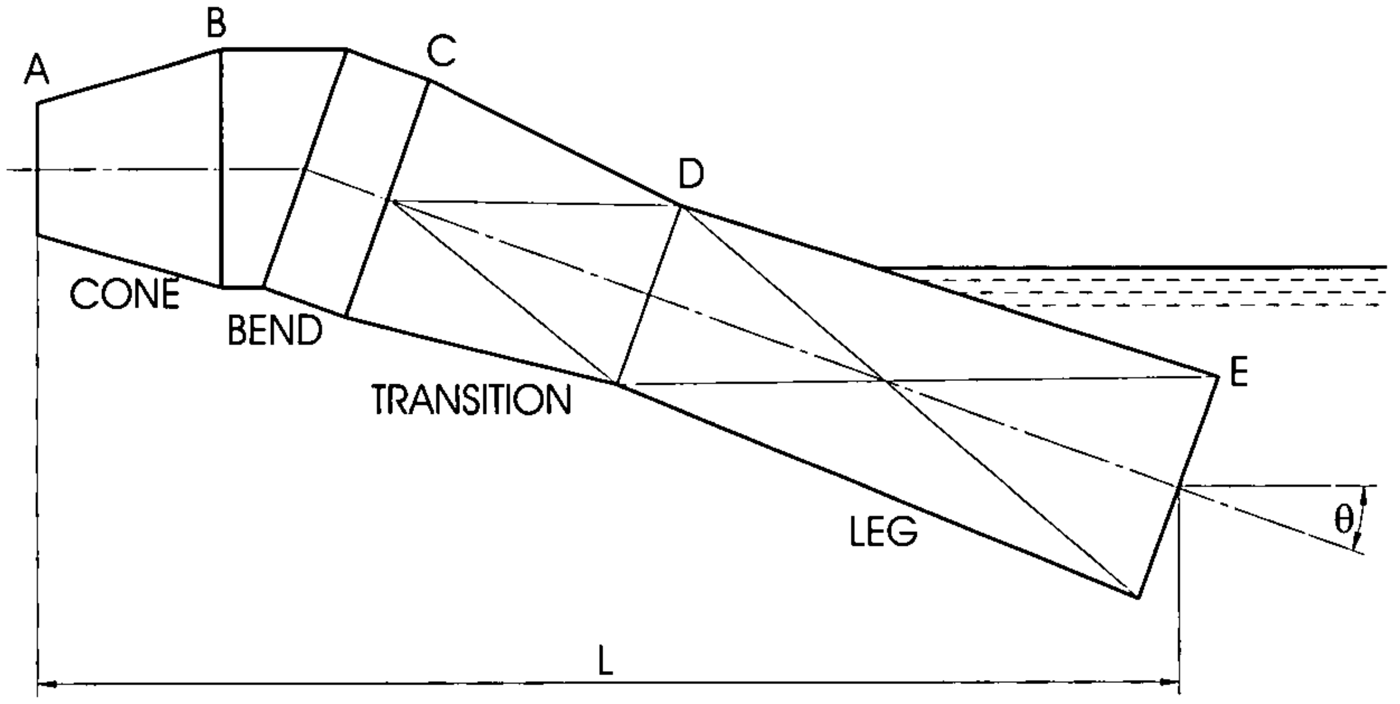
A
B
C
D
E
CONE
BEND
TRANSITION
LEG
θ
L

Fig. 5.6. Possible draft tube design for a high specific speed horizontal Francis turbine.

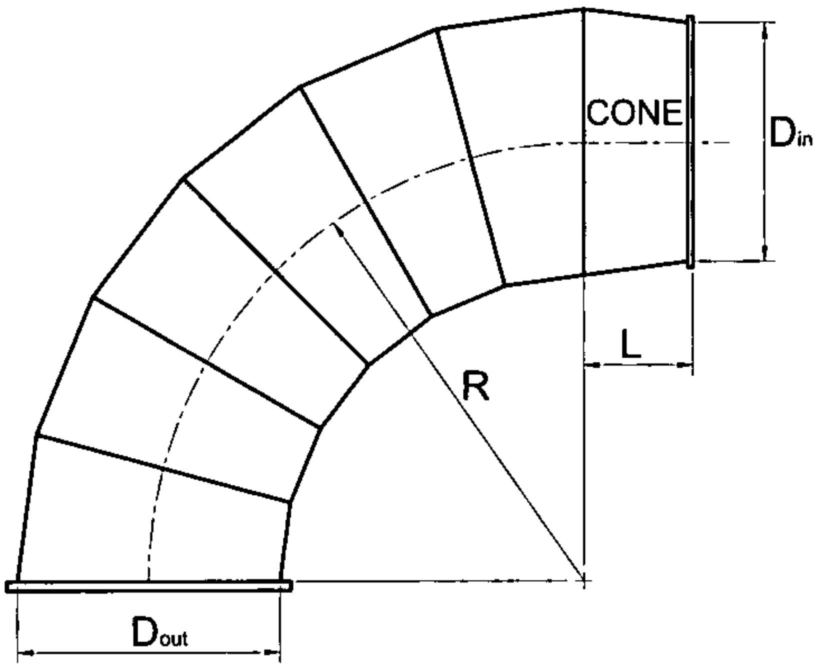
CONE
D_{in}
L
R
D_{out}

Fig. 5.7. Possible draft tube inlet cone/bend arrangement for a low to medium specific speed horizontal Francis turbine.

Figures 5.9 and 5.10 can be used to design draft tubes. Draft tube performance is highly sensitive to the thickness of the boundary layer. A thick boundary layer will separate earlier than a thin boundary layer. Francis turbines provide a thin turbulent boundary layer which is favourable to good diffuser performance. Propeller turbines provide an even more favourable inlet boundary layer conditions due to the rotating tip vortices which are generated by the blade tips and sweep the draft tube inlet cone.

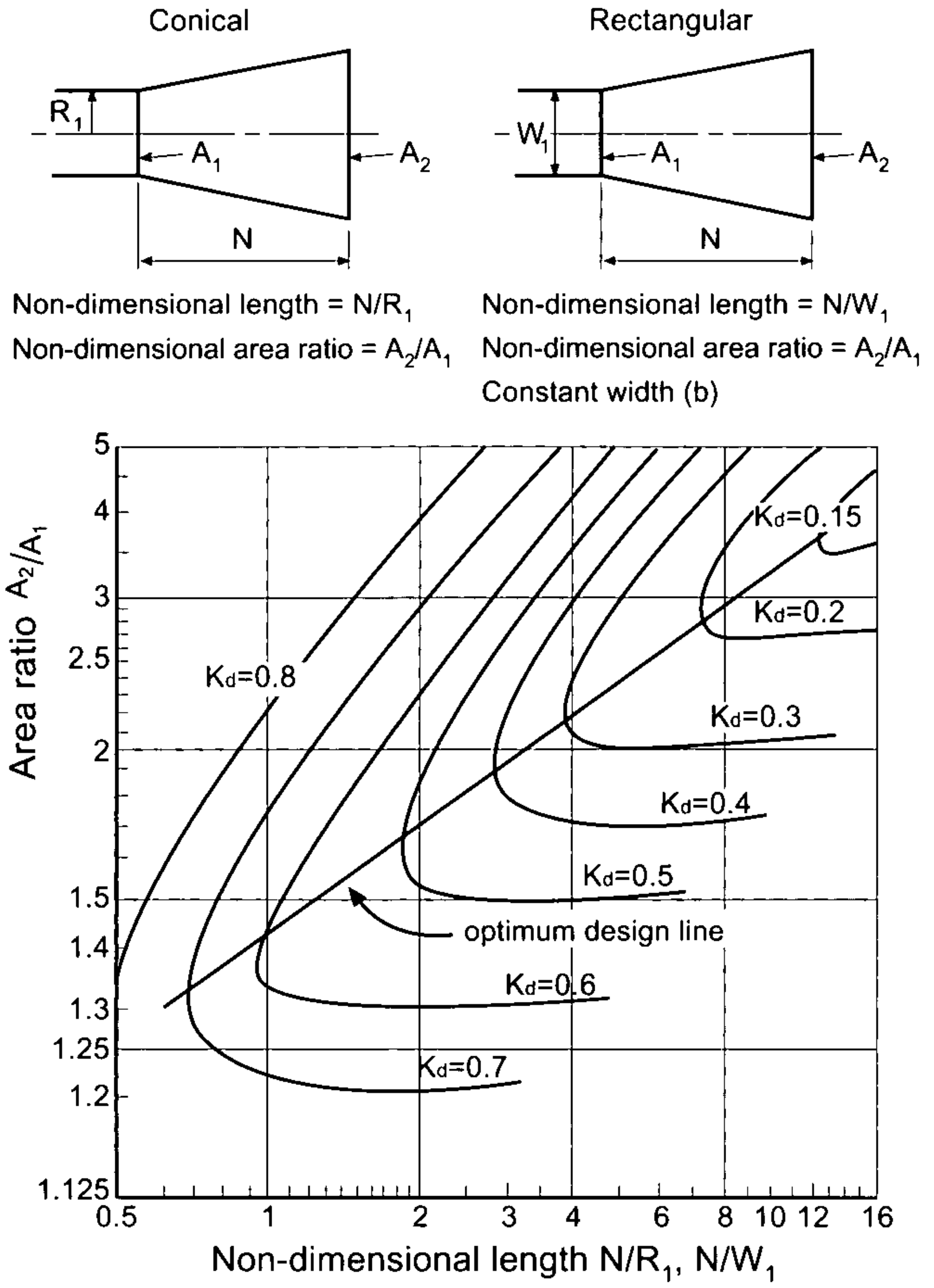

Fig. 5.8. Loss coefficients K_d for conical diffusers with a free discharge and a thin inlet boundary layer. Adapted from Miller [1990] (Reproduced courtesy BHR Group)

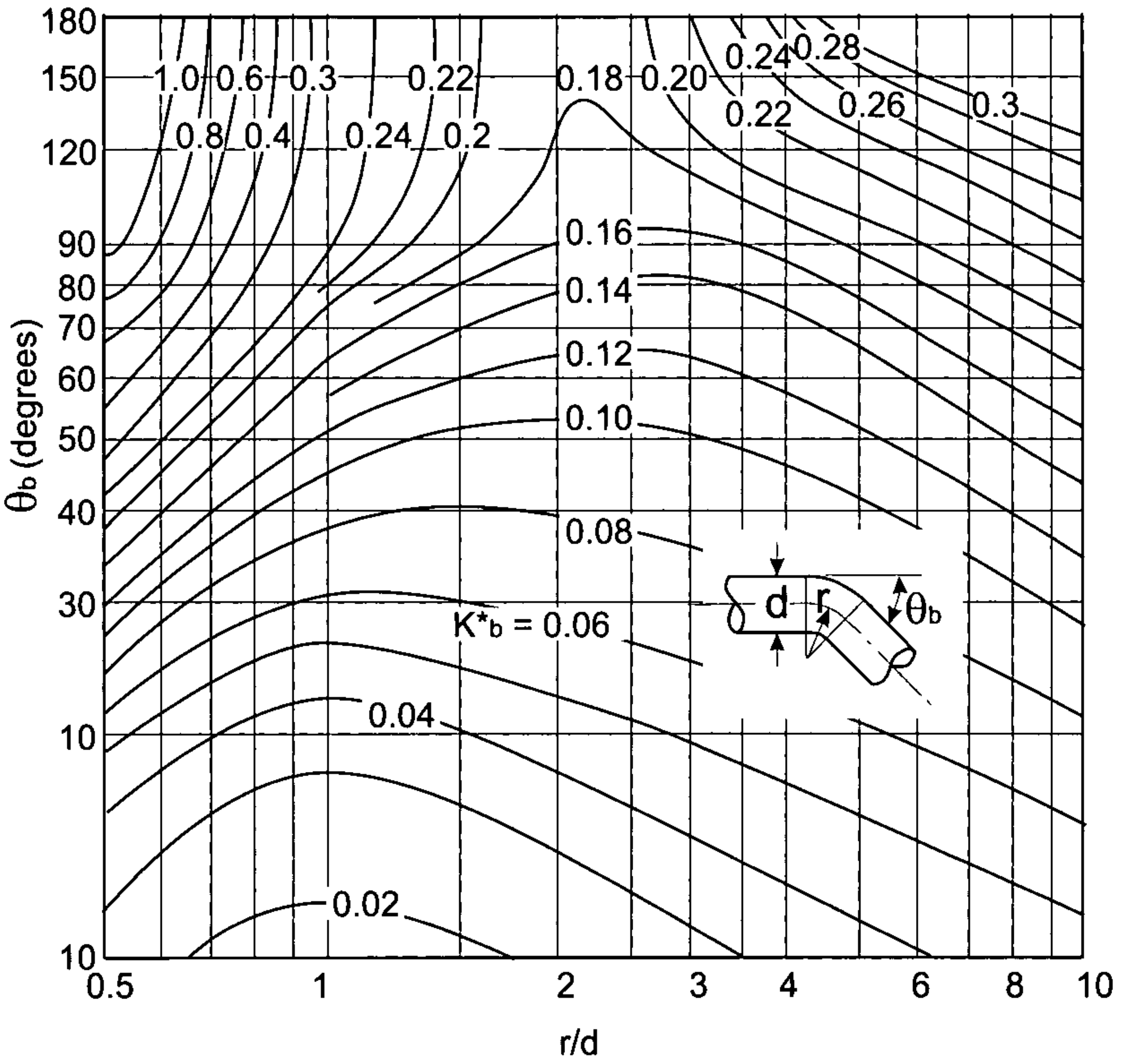

Fig. 5.9. Loss coefficients K_b^* for circular section bends (Re=1×10^6). Adapted from Miller [1990] (Reproduced courtesy BHR Group)

What this means is that for Francis and propeller turbines, the first cone is likely to perform slightly better than Figure 5.8 would indicate. The cautionary note here is that combined diffusing-turning-diffusing sections interact with one another, usually with a poorer combined performance.

To use Figures 5.8–5.10, the following equations apply.

- For a diffuser with free discharge

$$K_d = 1 - \eta_{dt}. \tag{5.3}$$

- For a diffuser with a straight constant area section at outlet and a thin boundary layer, Figure 5.8 can be adjusted to exclude the velocity head in the outlet pipe as a loss.
  Eg.

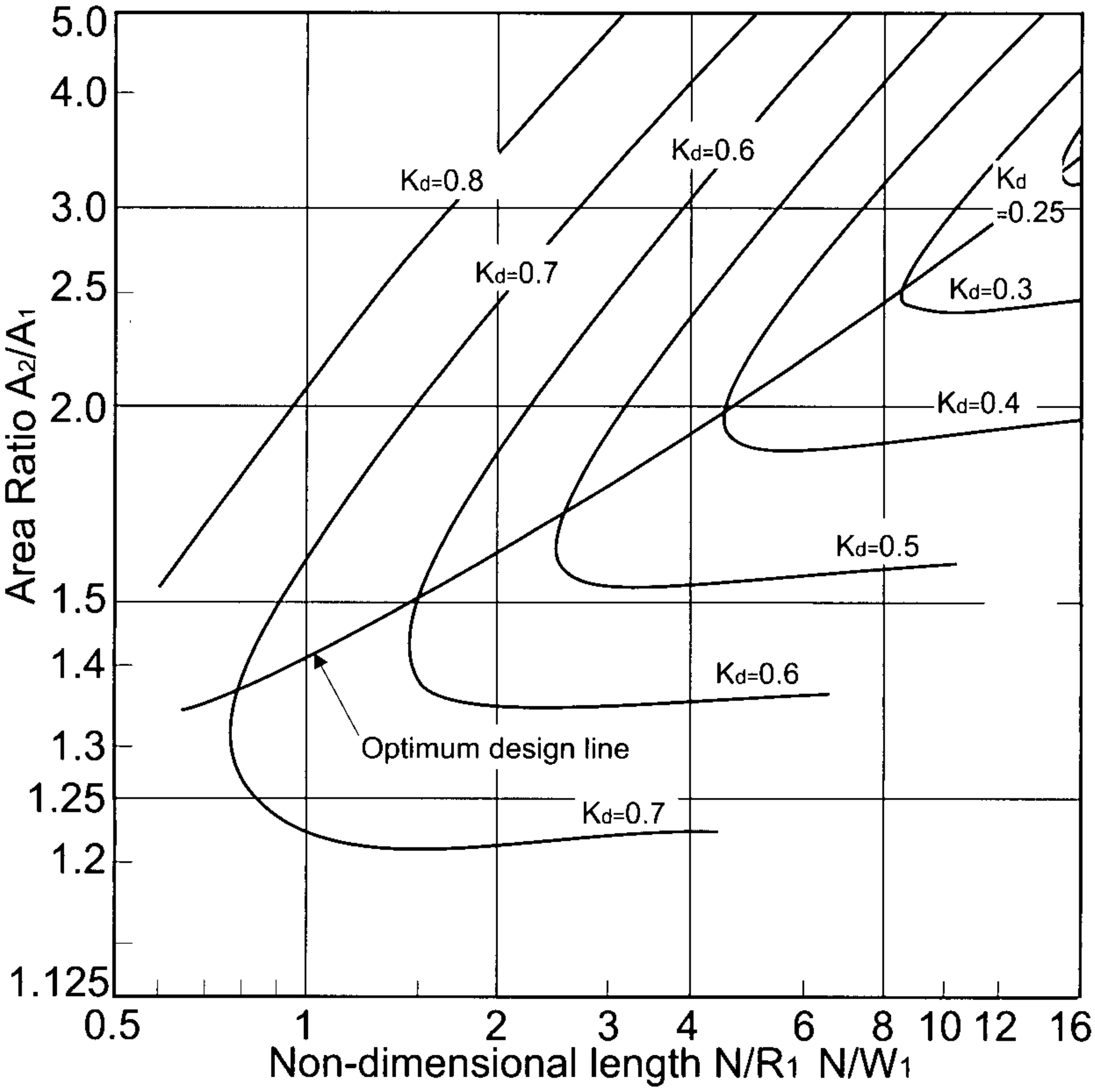

Fig. 5.10. Loss coefficients K_d for conical diffusers with a free discharge and a *thick* inlet boundary layer. Adapted from Miller [1990] (Reproduced courtesy BHR Group)

$$K_{d_{\text{Outlet Pipe}}} = K_d - \left(\frac{A_1}{A_2}\right)^2$$

Figure 5.9 shows the variation in loss coefficient for circular bends

$$K_b^* = \frac{\text{head loss}}{V^2/2g}. \tag{5.4}$$

Figure 5.10 presents loss coefficients for conical diffusers with a free discharge and a thick inlet boundary layer. Figure 5.10 could be used for a conical diffusing leg of a draft tube.

Miller [1990] provides further details of miscellaneous correction factors and component interactions. However, the use of Figures 5.8–5.10 will provide a good starting point for draft tube design.

6 Performance characteristics

A turbine performance characteristic is shown in Figure 6.1. These diagrams contain a map of how the turbine performs under different speeds and flow rates, and are determined from careful model turbine testing. The performance characteristics sometimes go by other names such as hill diagrams or mussel curves.

Unit flow rate q_{11} and unit speed n_{11} define the axes. Unit speed is defined in Section 3.2 and involves a reference diameter (see Figure 6.1 inset). Different manufacturers use different reference diameters. The reference diameter must be known before the turbine performance characteristic can be created or used.

Contours of constant efficiency η are plotted. Guide vane lines, α_{gv}, show the relationship between q_{11} and n_{11} for a given guide vane setting. The guide vane lines end on the runaway speed curve. This curve represents the maximum speed the turbine will reach for a particular guide vane setting under no load conditions. The cavitation performance is also shown with contours of σ_{crit} plotted. In the example shown as Figure 6.1, the same value of σ_{crit} can be reached at both low and high load conditions.

Using the non-dimensional relationships provided in Chapter 3, the performance of the prototype (full size) turbine can be calculated. Subscripts m and p refer to model and prototype quantities. For the prototype, selecting a synchronous speed N_p and prototype head range H_{np_1} and H_{np_2} will yield the prototype reference diameter D_p. Slight variations in D_p will position the H_{np_1} and H_{np_2} lines to optimize the turbine setting and cavitation performance. The H_{np_1} and H_{np_2} lines reflect maximum and minimum heads respectively that the prototype turbine will experience.

Prototype efficiencies tend to be slightly higher than model efficiencies due to the higher Reynolds numbers experienced. This increase in efficiency from model to prototype is called majoration and can be estimated using

$$\frac{1-\eta_p}{1-\eta_m} = 0.4 + 0.6\left(\frac{D_m}{D_p}\frac{\nu_p}{\nu_m}\sqrt{\frac{H_m}{H_p}}\right)^{\frac{1}{5}} \tag{6.1}$$

or alternate formulae given in IEC 60193 [1999] or BS EN 60995: 1995.

The prototype flow rate is

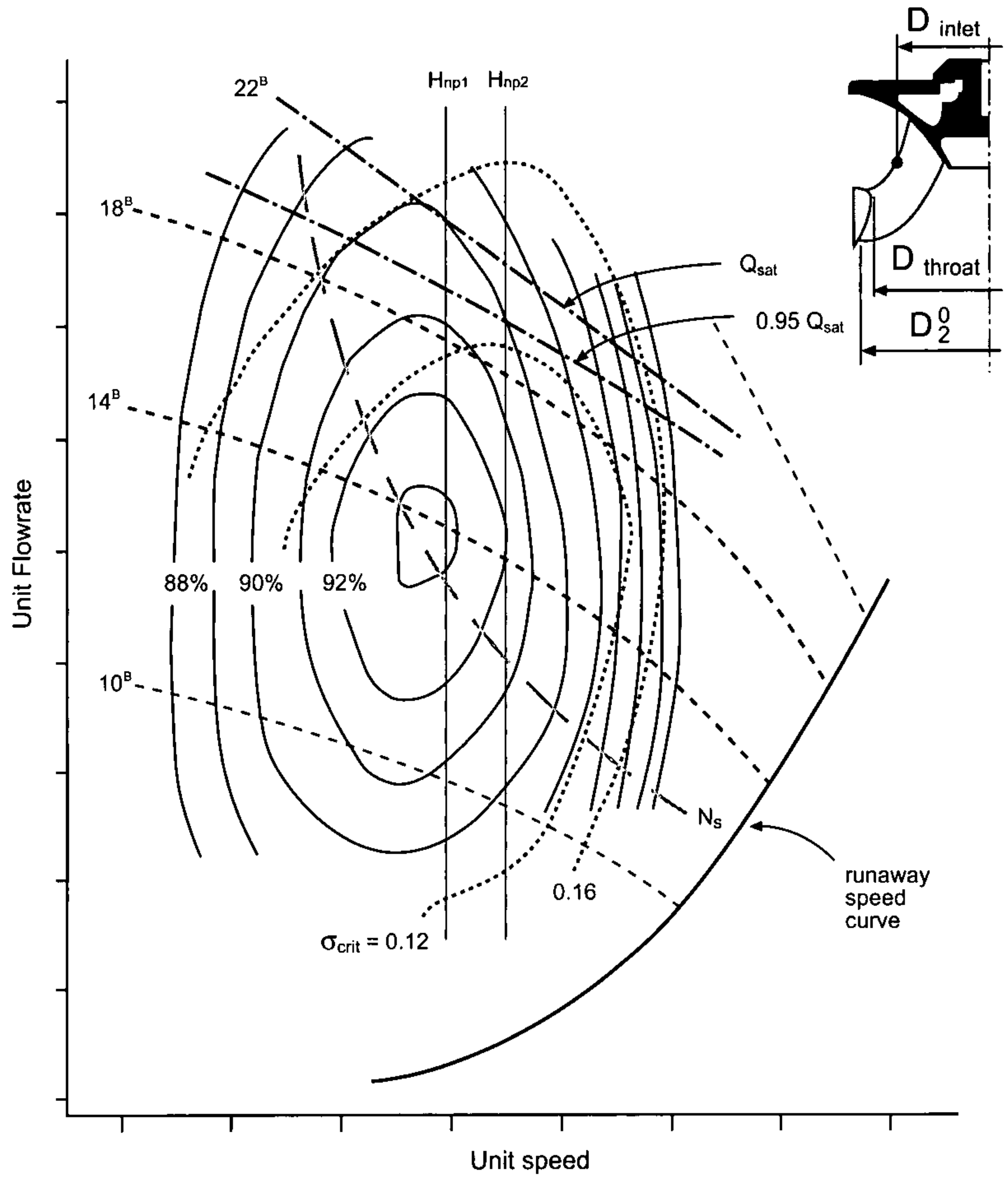

Fig. 6.1. Turbine performance characteristic.

$$Q_p = q_{11} \times \sqrt{H_n} \times D_p^2 \times \frac{\eta_m}{\eta_p} \tag{6.2}$$

with q_{11} values taken from a constant n_{11} line corresponding to the prototype head.

Prototype power is given by

$$P_p = \eta_p \rho g Q_p H_{n_p}. \tag{6.3}$$

Using the model turbine performance characteristic, plots of η_p versus P_p, guide vane angle versus P_p, Q_p versus P_p, and so forth can be plotted. See Figure 6.2 for example.

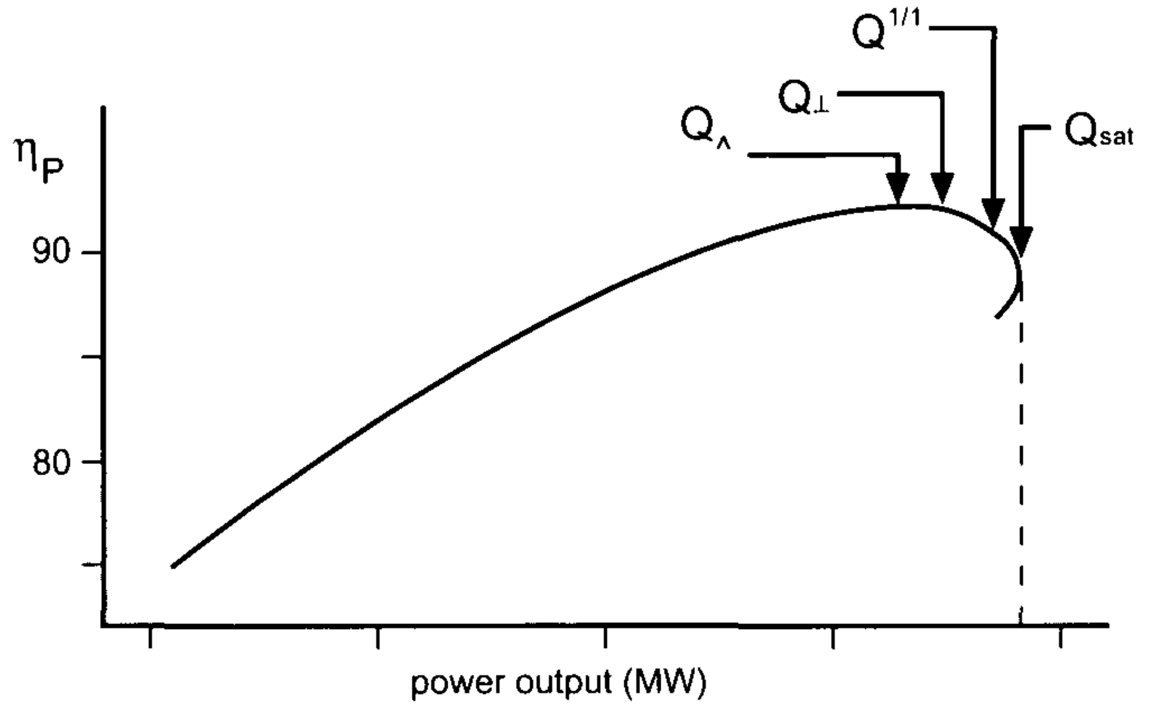

Fig. 6.2. Plot of prototype efficiency versus power.

Notice in Figure 6.2 that there is a saturation point where no more power can be produced, regardless of increasing guide vane opening. The flow rate corresponding to this maximum power is Q_{sat}.

Usually the turbine would be sized so that the maximum flow rate $Q_{1/1}$ is $0.95Q_{\mathrm{sat}}$, thus allowing a small performance margin for eventualities.

$Q_\wedge$ is the flow rate at maximum efficiency. $Q_\perp$ is the flow rate where (mostly) perpendicular discharge leaves the runner. Figure 6.3 shows the relationships between $Q_\perp$, $Q_{1/1}$, $Q_\wedge$ and specific speed.

Figure 6.4 shows a sample range of performance curves of both Francis and propeller turbines. These diagrams can be used to approximately size a Francis or propeller turbine. The development of these characteristics is largely approximate and may result in a turbine that performs, say with 15% more flow than designed.

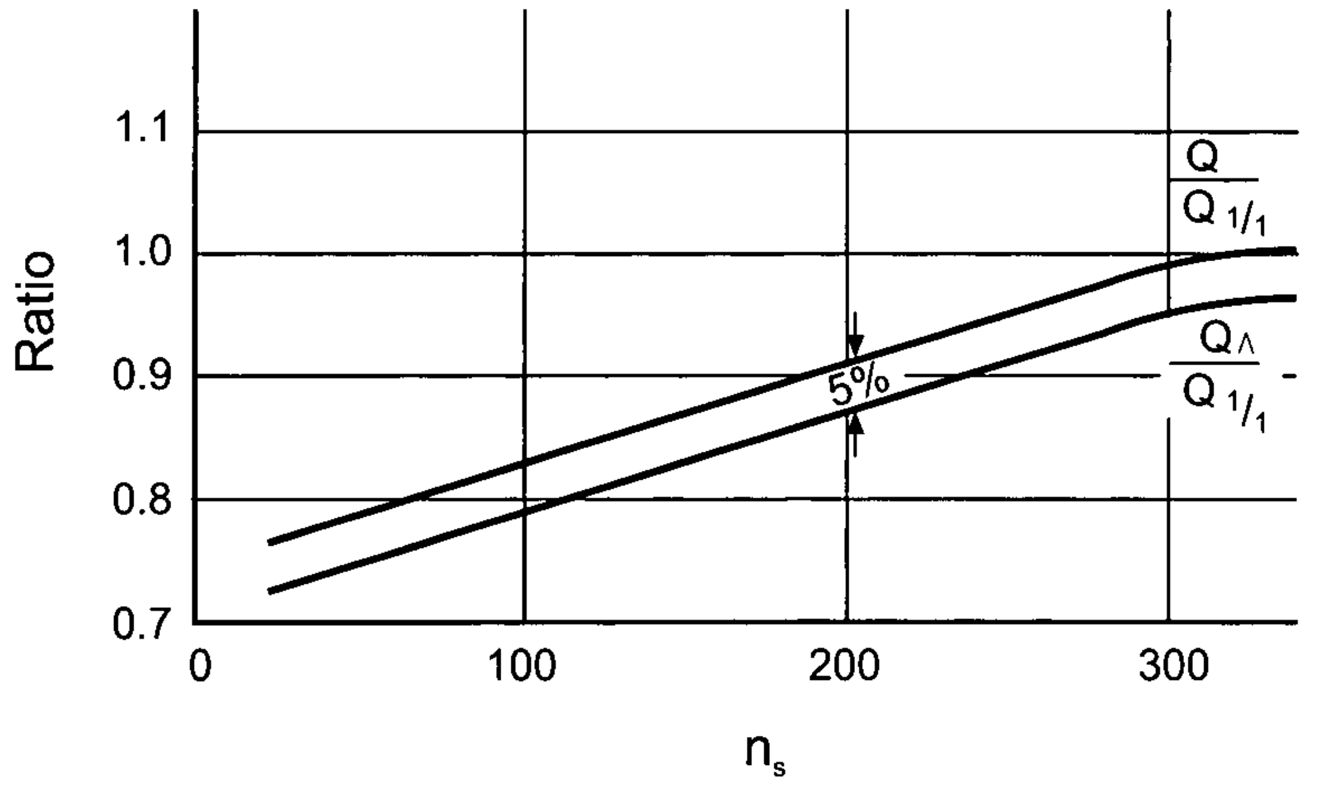

Fig. 6.3. Part load characteristics of a Francis turbine. Adapted from Quayle [1984].

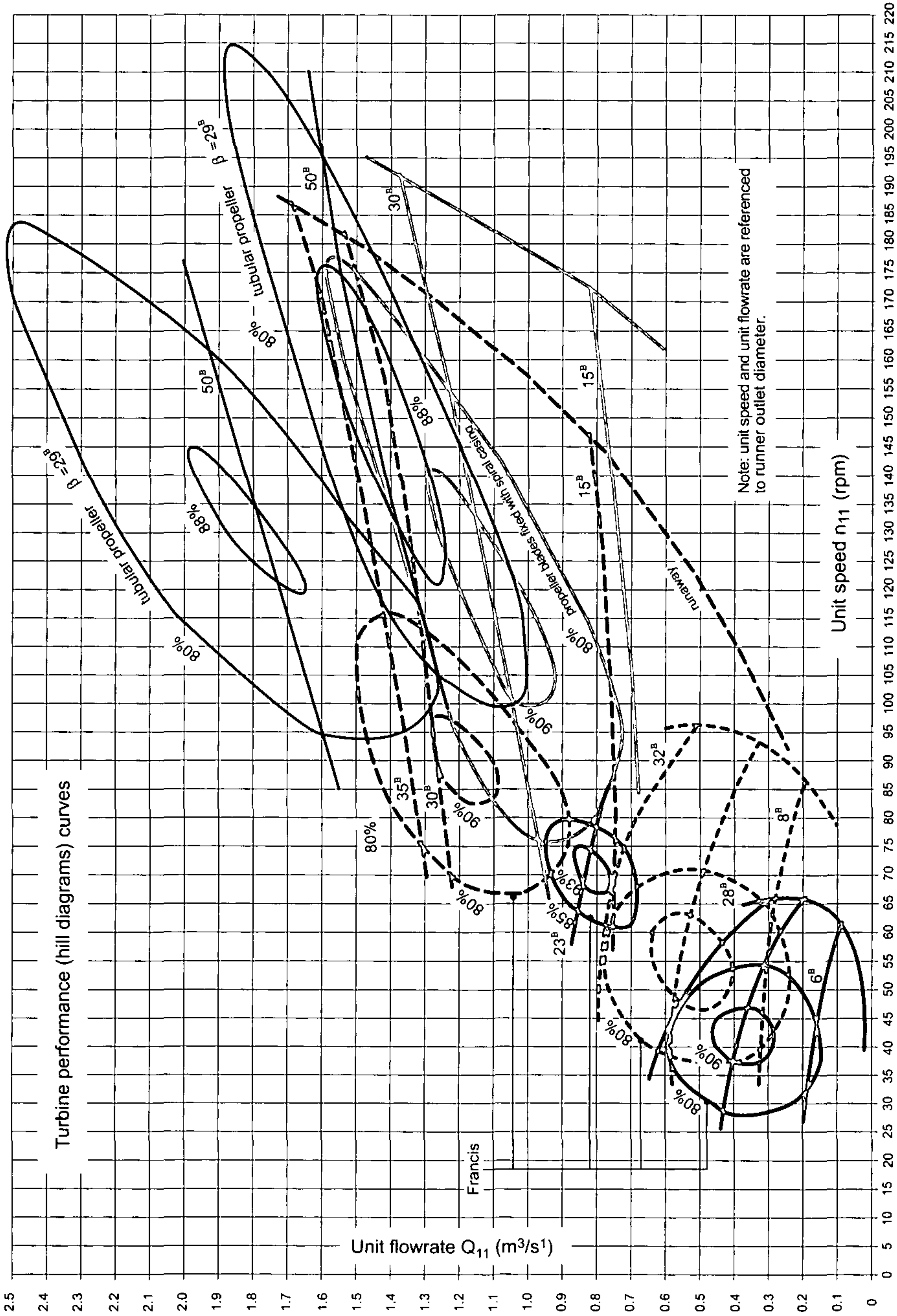

Fig. 6.4. Turbine performance curves for a range of Francis and propeller turbine specific speeds.

7 Designing efficient turbines

It is possible to achieve peak efficiencies for Francis turbines that reach the maximum values illustrated in Figure 7.1. Maximum Kaplan and propeller turbine efficiencies are likely to range from 92% to 88% decreasing as the specific speed increases. Achieving these values requires a proprietary in-depth knowledge of turbine model test data, an understanding of turbine losses and an ability to match the turbine components such as the spiral casing, stay vanes, guide vanes, runner blades and draft tube. For example, the flow leaving the runner should be a compromise between losing kinetic energy to the V_θ component and optimising the performance of the draft tube

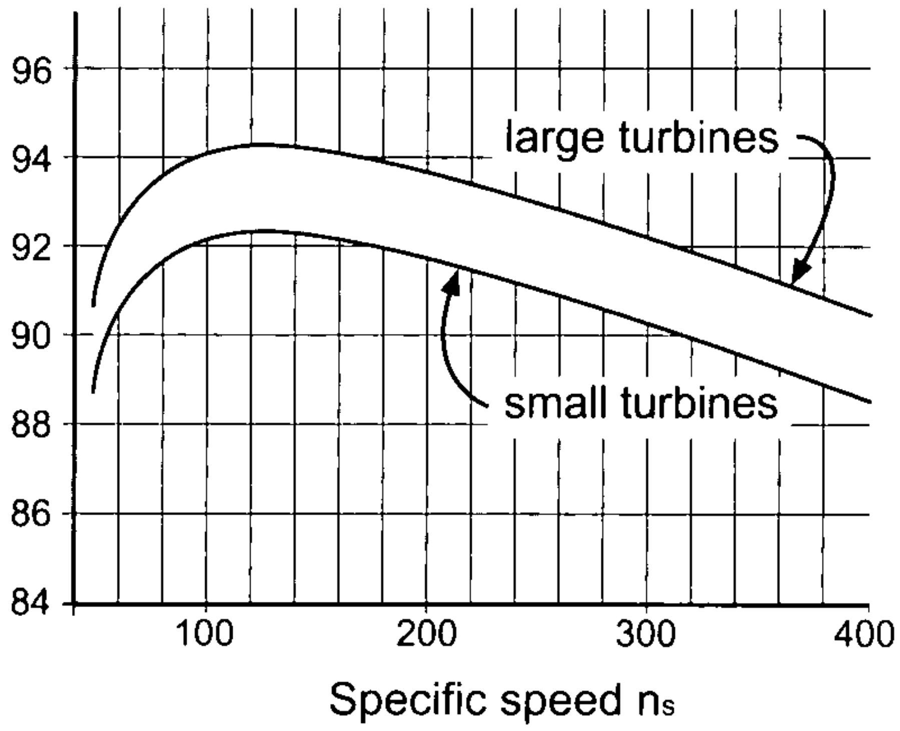

Fig. 7.1. Variation in Francis turbine efficiency with specific speed.

Well designed small turbines will have efficiencies one or two points below those of the large turbines predominantly due to majoration effects.

The design guidelines presented in this book do not allow blades with 'minimum loss' to be designed. The lack of accuracy in the calculation procedures necessitates some degree of conservatism in blade design, e.g. longer than necessary blades. It should however be possible to achieve efficiencies in the high eighties through using this book.

7.1 Hydrodynamic design guidelines

As a general rule, the turbine designer should try to 'offset turning with acceleration', to minimize losses. This implies selecting the envelope geometry and blade passage geometry in such a way as to ensure acceleration of the flow wherever possible. For example, the rV_θ produced by the spiral casing should be such that the acceleration of the flow is maintained through the stay vanes and guide vanes at all openings.

For Francis turbines, it is important to avoid separation on the pressure face, near the inlet, due to Coriolis loading. This criterion dictates the number of blades required by the Francis runner; the higher the head, the greater the inlet radius and the greater the Coriolis loading. Thus high head Francis runners usually have more blades than low head designs.

Efficient blade design also requires that the blades are correctly loaded. Insufficient blade area may mean the blades stall and experience excessive deviation and loss. Too much blade area creates excessive skin friction losses. The ideal blade loading is for the flow on the suction face near the trailing edge to be just near the point of separation. As mentioned above, there should be no pressure face separation.

For propeller turbines, an adequately loaded blade should result from using the Zweifel loading coefficient [Zweifel, 1945] at the hub section of the guide vanes and runner blades. For Francis turbines, the calculation for circulation velocity should provide an indication of the number of blades. Industry practice should also indicate typical blade numbers for a given turbine specific speed. Blade leading and trailing edge positions are also provided based on open literature turbine design practice.

Integral boundary layer calculations are an alternate, more detailed (and laborious), approach to determining blade loading. As a first step, the local velocities are required over the blade surface. These can be obtained by the mean streamline method. For turbines, the calculation would then proceed using Thwaites [1949] for the development of the laminar boundary layer, and then Head and Patel [1968] for the ensuing turbulent boundary layer. Cebici and Bradshaw [1977] contains a programmed version of Head and Patel [1968] in an appendix. There are other methods, see Schlichting [1979] for example of the Truckenbrodt method. The concept of using 2 dimensional (2D) flow solutions for actual complex 3 dimensional (3D) flow, is inherently flawed and probably does not justify using anything more sophisticated than the first two methods mentioned above.

7.2 Losses

A good general discussion of turbomachinery losses is provided in Denton [1993] and in Cumpsty [1989]. Ainley and Mathieson [1951] provided an early seminal paper on losses. A pictorial summary of turbine losses is presented in Figure 7.2. Higher head (low specific speed) machines have greater 'sealing/clearance' type losses. The flow between the guide vanes and the head cover in the clearance gap represents a loss. Consequently, the guide vane losses also increase with decreasing specific speed. High head Francis runners do not discharge significant kinetic energy into the draft tube as a percentage of their net head. Accordingly, their draft tube losses are smaller than for lower head, higher specific speed, runners.

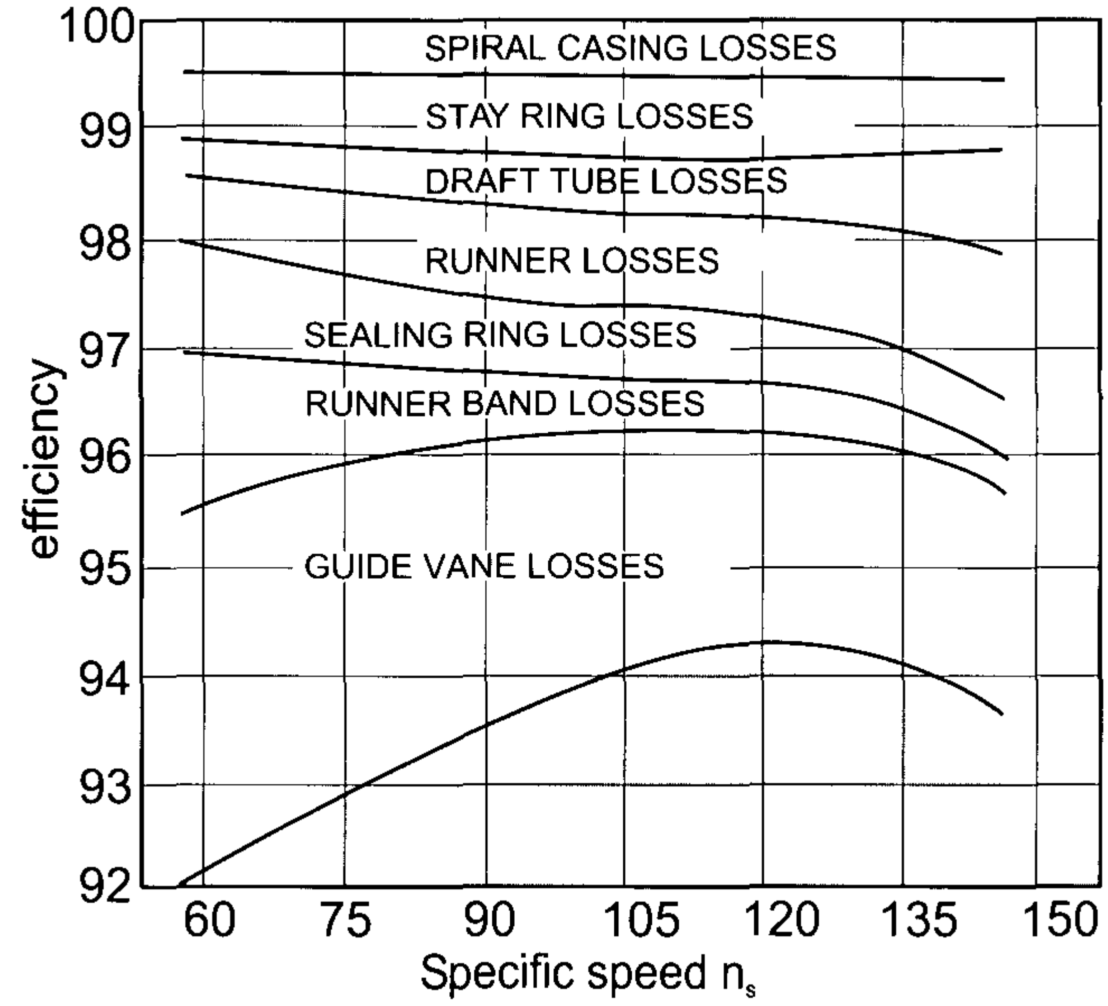

Fig. 7.2. Variation in Francis turbine component losses with specific speed, n_s.

To a turbine designer, a loss is anything that decreases the energy available to produce useful mechanical work, and, as such, a loss is equivalent to a reduction in head. Losses in a water turbine can be categorized as:

- skin friction losses (associated with flow over the turbine envelope and blade surfaces),
- secondary flow losses,
- trailing edge losses,

- losses arising from mal-incidence,
- disk friction losses,
- tip clearance flow losses (guide vanes and runner blade tips),
- and leakage flow losses (across turbine seals).

All losses are ultimately associated with the action of viscosity. For example, the loss at the trailing edge is not actually a loss near the trailing edge; there are still high values for the pressure and kinetic energy components of the flow. However, a chord length downstream of the trailing edge, much of the kinetic energy in the trailing edge wake has been dissipated by the action of viscosity into heat, raising the water temperature. This heat energy still exists but cannot be converted into useful work, hence it is regarded as a loss.

Poor performance of components upstream can introduce loss into downstream components. For example, separation on an upstream blade surface will result in increased deviation and ensuing incidence problems (and loss) on downstream blades.

Some simple methods of calculating losses in water turbines is instructive and allows the designer to make design decisions with some quantitative understanding of their significance.

7.2.1 Skin friction losses

As an example of skin friction losses, a calculation is provided for stay vanes.

With reference to Figure 7.3, the drag force is

$$\begin{aligned}\text{Drag Force} &= C_F \times \text{Area} \times \frac{1}{2}\rho V_{sv}^2\\ &= C_F \times 2B_{sv}L_{sv}\frac{1}{2}\rho V_{sv}^2\end{aligned}$$

where C_F is the skin friction coefficient with values given in Table 7.1, dependent on Reynolds number. Let $\bar{\beta} = (\beta_1 + \beta_2)/2$, then V_{sv} is a representative velocity through the stay vanes, e.g.

$$V_{sv} = \frac{\bar{V}_{msv}}{\sin\bar{\beta}}\left\{\frac{s}{s-t_c}\right\}.$$

Now

$$\text{Work/sec} = \text{Drag Force} \times V_{sv}$$

thus

$$\text{Head Loss} = \frac{\text{Work/sec}}{\rho g Q} = \frac{2Z_{sv}C_F}{Q}B_{sv}L_{sv}\frac{V_{sv}^3}{2g}.$$

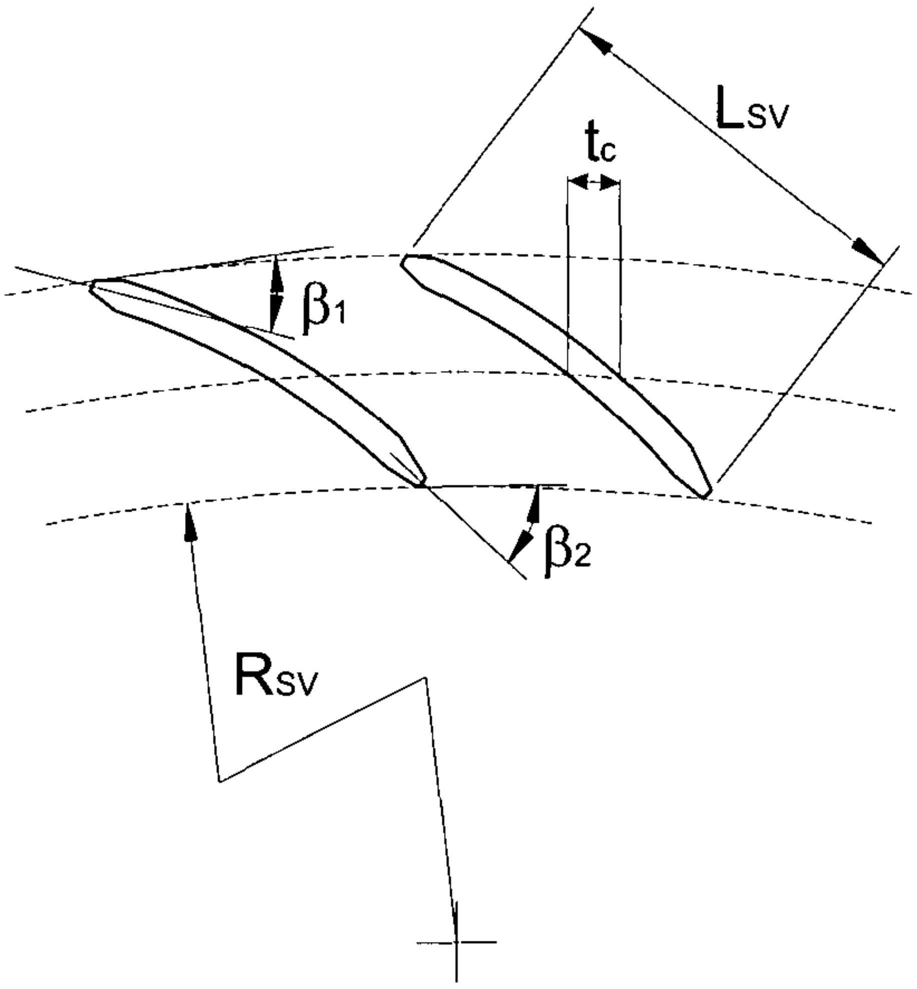

Fig. 7.3. Stay vane geometry.

Re	10^4–10^6	10^5–10^7	10^6–10^8	10^7–10^9	10^8–10^{10}
K	0.0718	0.0441	0.0293	0.0207	0.0153
n	5	6	7	8	9

Table 7.1. Determination of C_F based on Reynolds number. Generally $C_F = K/\mathrm{Re}^{1/n}$.

In general, losses tend to be proportional to the cube of the velocity. Sophisticated blade design might therefore try to minimise the peak suction face velocity W_s.

For specific speeds higher than 125, the skin frictional losses associated with the higher specific velocities start to dominate as Figures 7.1 and 7.2 demonstrate.

Frictional losses occurring in water turbines are least when the surfaces are 'hydraulically smooth'. The definition of a hydraulically smooth surface is a surface whose roughness peaks and troughs lie within the laminar sub layer of the boundary layer flow (and do not affect the outer turbulent layer). Further reducing the roughness value does not reduce the skin frictional losses. The ideal therefore is to achieve hydraulically smooth surfaces on all flow surfaces. In practice, those areas that experience high velocities, such as the guide vanes and the suction faces of the runner blades are key areas to provide acceptable surface finishes.

Defining the terms:

k_s Equivalent sand roughness. k_s/d is the familiar 'relative roughness' given in pipe friction charts (sometimes called Moody's diagram). See Massey [1989].

$k_{\mathrm{adm}} = R_{\mathrm{max}}$ Admissible roughness k_{adm} is the same as the maximum depth R_{max} (deepest trough to highest peak). $k_{\mathrm{adm}}/k_s \approx 2.6$ [Grein, 1975].

R_a Arithmetical centreline average. Grein [1975] found $R_{\mathrm{max}}/R_a = 6$, Forster [1966] found $R_{\mathrm{max}}/R_a = 5$).

Based on flat plate testing, a hydraulically smooth surface is achieved when

$$Vk_s/\nu \leq 100. \tag{7.1}$$

Table 7.2 is adapted from Grein [1975] and shows which surface finishes are required for a kinematic viscosity of 1.1×10^{-6} m^2/s (water at 16°C). For example, an N8 roughness number, when the grinding is carried out perpendicular to the flow direction, requires a velocity less than 17 m/s (or a better surface finish if the velocity is higher than 17 m/s).

	R_a surface comparator μm	R_a stylus μm	R_{max} profilometer μm	R_{max}/R_a	k_s	max. V m/s
N6 $\perp$	0.8	0.75	3.75	5.00	1.76	62.62
N6 $\parallel$		0.375	1.75	4.67	0.88	125.23
N7 $\perp$	1.6	1.6	10	6.25	3.75	29.35
N7 $\parallel$		0.62	4.5	7.26	1.45	75.75
N8 $\perp$	3.2	2.75	17.5	6.36	6.44	17.08
N8 $\parallel$		1.1	7.5	6.82	2.58	42.69
N9 $\perp$	6.3	6	32.5	5.42	14.05	7.83
N9 $\parallel$		1.75	12.5	7.14	4.10	26.84
N10 $\perp$	12.5	12.5	75	6.00	29.28	3.76
N11 $\parallel$	25	25	150	6.00	58.56	1.88

Table 7.2. Required surface finish. $\perp$ and $\parallel$ indicate measurement perpendicular and parallel to the grinding direction respectively. Adapted from Table 2 of Grein [1975].

The kinematic viscosity used should correspond to the turbine operating temperature. Variation in the kinematic viscosity of water with temperature is given by

$$\nu = \exp\left(\frac{396.13}{107.41 + T} - 16.921\right) \tag{7.2}$$

with T in °C and the kinematic viscosity measured in m^2/s. Thus, for a temperature change from 30°C to 0°C, an increase in surface finish of one roughness grade would be required to achieve a hydraulically smooth surface.

Grein [1975] also made the following additional points:

- One N class rougher than that required to achieve a hydraulically smooth surface results in a drop in efficiency of approximately 1%.
- σ_{crit} is not affected by roughness.
- Incipient cavitation, σ_{incip}, is affected by roughness.
- The position of cavitation inception moves towards the leading edge as roughness increases.
- Smoother surfaces increase the induction period before damage due to cavitation commences.

Further discussion on this subject can also be found in Schlichting [1979] and in Forster [1966].

7.2.2 Secondary flows

Secondary flows arise whenever there are cross-passage pressure gradients. In developed pipe flow there are no secondary flows. On the other hand, in flow around a pipe bend, the pressure on the outside of the bend is greater than that on the inside and secondary flows result. Secondary flows create the bulk of the head loss associated with the bend and are dissipated over several pipe diameters downstream of the bend.

In the field of turbomachinery, strictly speaking, almost all losses can be classified as secondary flow losses. Amongst designers though, there is a tendency to name a specific loss if it can be calculated relatively easily. Losses associated with tip clearance flows, for example, can be calculated approximately [Rains, 1954]; yet they are clearly generated by the dissipation of secondary flows downstream in the blade passages.

There are 'methods' to calculate secondary flow losses, e.g. Dunham [1970] and Came [1973]. These methods have not proved particularly useful in design. A 'full' modelling of the losses, and in particular, secondary flow losses, occuring in a turbine can only be done with a full 3D Navier Stokes solver. This type of modelling shows the presence of complex three-dimensional flows. For example, boundary layer build up occurs in the corners between the blades and the crown/skirt surfaces as well as the centrifuging of 'lossy' boundary layer (low momentum fluid) out into the tip regions can be seen. Whilst this method of analysis is beyond the scope of this book, commercial turbomachinery software is available, e.g. AS-turbodesign and CFXTascflow.

7.2.3 Trailing edge losses

Unlike most other types of loss, which tend to reduce with increasing Reynolds number, trailing edge losses can increase with Reynolds number. The physical explanation for this lies with the 'jet pump' effect. The fluid passing over the blade surface mixes with the wake fluid at the trailing edge. The intensity of fluid mixing is a measure of the loss associated with the trailing edge. The boundary layer, developed over the blade surface, acts as an insulating layer; a thin boundary layer allowing more intense mixing than a thick boundary layer. The trailing edge loss is seen to exhibit some dependency on the flow conditions upstream of the trailing edge.

$C_{FB} \equiv$ drag coefficient based on skin friction only and referenced to the trailing edge thickness t, height h and W_2.
$D_{FB} \equiv$ drag force due to forebody drag,
$C_B \equiv$ base drag coefficient due to trailing edge only,
$D_B \equiv$ base drag force due to trailing edge only,
$V_{m3} \equiv$ meridional velocity where wake has mixed out.

Hoerner [1965] defines

$$C_{FB} = \frac{D_{FB}}{\frac{1}{2}\rho W_2^2 (th)} = C_F \left\{ \frac{\text{blade wetted area}}{th} \right\}$$

and

$$C_B = \frac{0.135}{(C_{FB})^{1/3}} = \frac{D_B}{th\frac{1}{2}\rho W_2^2}. \tag{7.3}$$

C_F can be obtained from Table 7.1. Now the work done per unit second in overcoming the trailing edge drag is

$$\begin{aligned} \text{work/sec} &= D_B W_2 \\ &= \Delta H_{te} \rho g \frac{Q}{Z}, \end{aligned}$$

and since $Q/Z = V_{m3} sh$, $V_{m3} s = V_{m2}(s - t_c)$, $t_c = t/\sin\beta_2$ and

$$W_2 \sin\beta_2 = V_{m2},$$

and the head loss due to the trailing edge is

$$\Delta H_{te} = \frac{D_B W_2}{\rho g s V_{m3}} = C_B \frac{t_c}{(s - t_c)} \frac{W_2^2}{2g}. \tag{7.4}$$

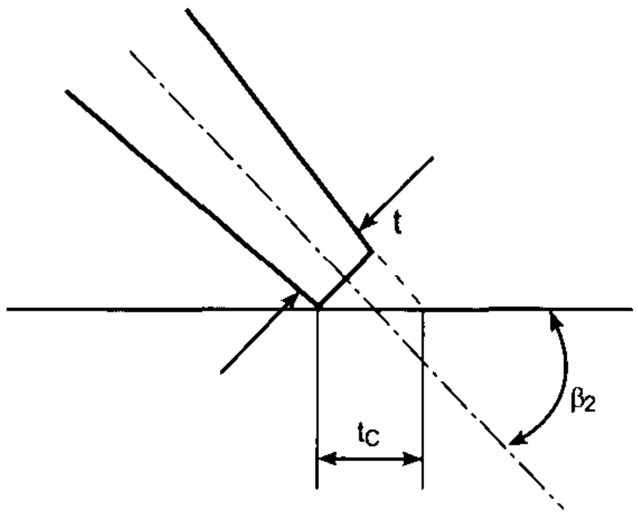

Fig. 7.4. Trailing edge geometry.

7.2.4 Incidence losses

Fortunately turbomachinery blades are quite tolerant of mal-incidence so long as the flow does not separate on either pressure or suction faces. A small separation bubble on the suction face does sometimes occur due to laminar boundary layer separation but does not usually lead to significant losses as the flow quickly reattaches.

Incidence loss can be modelled crudely using the concept of "loss at an abrupt enlargement".

With reference to Figure 7.5, for no energy lost between sections (1) and (t)

$$\frac{p_1}{\rho g} + \frac{W_1^2}{2g} = \frac{p_t}{\rho g} + \frac{W_t^2}{2g}$$

thus

$$p_1 - p_t = \frac{1}{2}\rho\left(W_t^2 - W_1^2\right).$$

The force in the x direction is equal to the rate of increase of momentum in the x direction hence

$$(p_1 - p_t)\, s \sin\beta = (W_t - W_1\cos(\beta-\alpha))\,\rho W_2 s \sin\beta$$
$$\text{Therefore, } W_t^2 - W_1^2 = 2W_tW_2 - 2W_1W_2\cos(\beta-\alpha).$$

Applying the cosine rule for the inlet velocity diagram gives

$$\Delta W_\theta^2 = W_1^2 + W_2^2 - 2W_1W_2\cos(\beta-\alpha)$$
$$\text{Therefore, } \Delta W_\theta^2 = W_t^2 + W_2^2 - 2W_tW_2 = (W_t - W_2)^2.$$

Massey [1989] gives the head loss at an abrupt expansion (see Figure 7.6) as $(V_1 - V_2)^2/(2g)$, hence the head loss associated with mal-incidence is

$$\Delta H = \frac{\Delta W_\theta^2}{2g}. \tag{7.5}$$

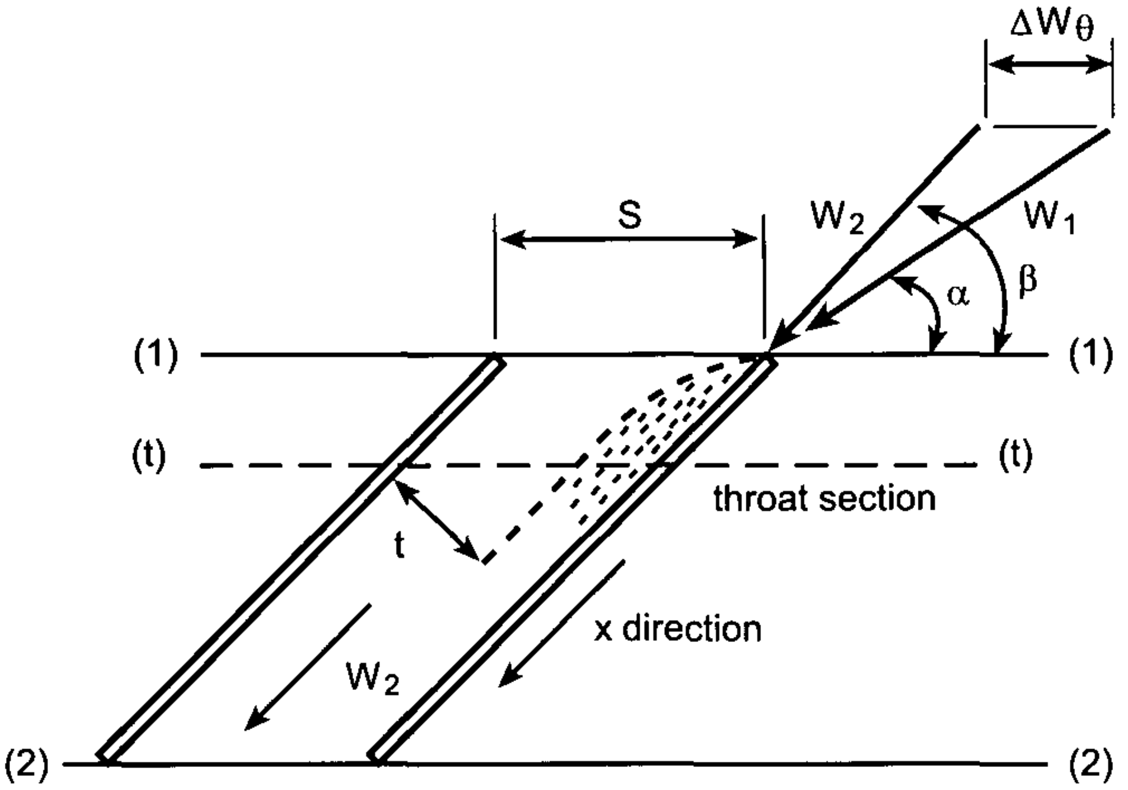
ΔWθ
S
W2
W1
α
β
(1)
(1)
(t)
(t)
throat section
t
x direction
W2
(2)
(2)

Fig. 7.5. Incidence loss model.

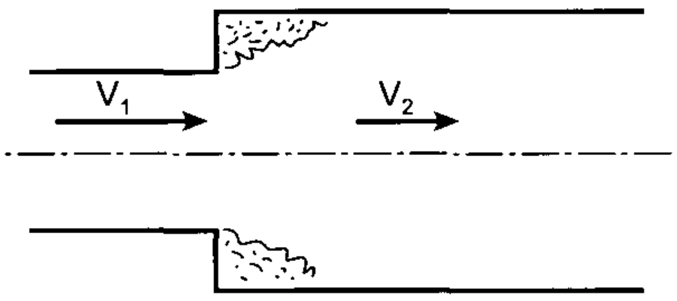

Fig. 7.6. Loss at an abrupt enlargement.

7.3 Leakage, tip clearance and disk friction loss

Leakage flow losses represent a decrease in flowrate and hence a loss in mechanical power. Chapter 12 calculates leakage flows as part of the hydrodynamic thrust calculation.

Tip clearance flows in unshrouded runners, such as are found in propeller and Kaplan turbines, represent an energy loss and create a significant 'blockage' which needs to be accomodated by the designer. Rains [1954] provides a tip clearance model. Freeman [1985] is another useful reference. Propellers are not generally shrouded (unlike Francis runners) as there are beneficial effects when small tip clearances are present (e.g. draft tube boundary layer re-energization). In fact, there is evidence to suggest that too small a tip clearance may reduce turbine efficiency [Freeman, 1985]. As a general guide, a radial tip clearance of between 0.5% and 1% of the blade span is acceptable.

Disk friction losses comprise all the losses associated with water friction in the seal passages and behind the crown and skirt due to the rotation of the runner. Schlichting [1979] provides a method for calculating these losses.

8 Turbine envelope geometry

The turbine envelope is shown highlighted (thick lines) in Figure 8.1 in the meridional plane. The leading and trailing edges of the stay vanes, guide vanes and runner blades are also shown. These leading and trailing edges may not lie in the meridional plane but are shown circumferentially projected into this plane.

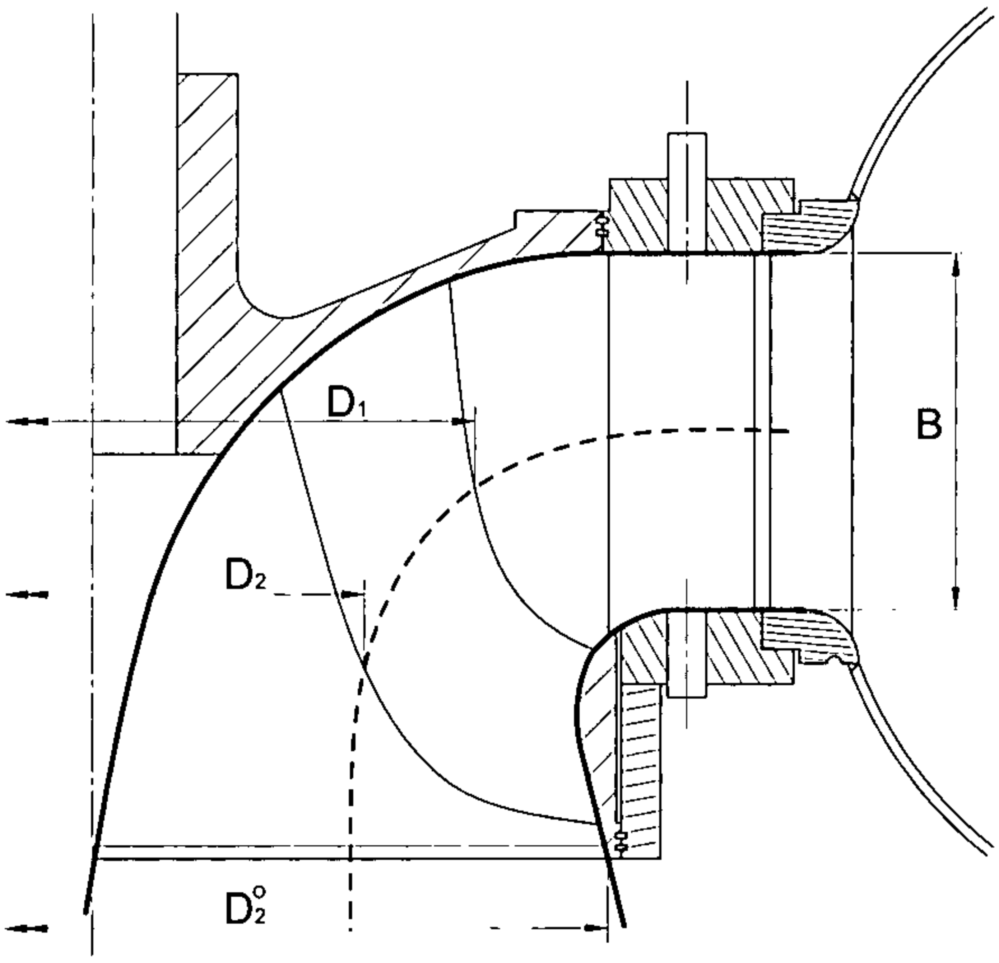

Fig. 8.1. Turbine envelope.

It is desirable to operate with as high a specific speed as possible. The limiting factor is the turbine setting and required cavitation margin for how high a specific speed can be achieved for a given head.

To understand how attempting to increase the specific speed of the design affects the envelope shape, the following analysis is presented.

$$P = \eta \rho g Q H_n, \tag{8.1}$$

$$U_1 = \frac{\pi D_1 N}{60}, \tag{8.2}$$

$$Q = \frac{\pi (D_2^o)^2}{4} \bar{V}_2, \tag{8.3}$$

$$n_s = \frac{N\sqrt{P/0.7355}}{H^{1.25}}, \tag{8.4}$$

$$U_1' = U_1/\sqrt{H_n}, \tag{8.5}$$

$$\bar{V}_2' = \bar{V}_2/\sqrt{H_n}. \tag{8.6}$$

Combining Equations 8.1 through 8.6 yields:

$$n_s = 25.7\sqrt{\frac{g}{\pi}} U_1' \frac{D_2^o}{D_1} \sqrt{\bar{V}_2' \eta}. \tag{8.7}$$

For the intermediate streamline shown in Figure 8.1, the velocity triangles of Figure 8.2 apply. These figures assume that the blade angles and flow angles are the same, i.e. $\beta = \chi$.

From Equation 8.7, specific speed increases as U_1' is increased, as D_2^o/D_1 is increased and to a lesser extent as $\bar{V}_2'$ is increased.

Increasing U_1' has a significant effect on β_1 and the inclination of the blades (see Figure 8.2 (b)). From test experience, higher efficiencies can be achieved when β_1 is not overly inclined. This has resulted in increased guide vane height, B, and a deeper (more axial) runner section.

In Figure 8.3, two Francis turbine envelopes are shown; one a low specific speed design, and one a high specific speed design. D_2^o/D_1 is seen to be higher for the high specific speed envelope.

At still higher specific speeds, D_2^o/D_1 will be close to unity as for the tip section of the medium to high specific speed Francis runners and Kaplan/propeller turbines.

The specific velocity $\bar{V}_2'$ entering the draft tube also increases with specific speed. This results in more kinetic energy entering the draft tube and consequently draft tube performance becomes more critical.

When designing a Francis turbine for a particular specific speed, select an envelope geometry which either consists of an existing envelope in such as one of those provided in Figures 9.8 through 9.14 or an intermediate envelope of your own creation.

Bear in mind that the envelope geometry selected will have a very significant influence on the optimum blade shape.

Having selected an envelope geometry, the next step is to position the leading and trailing edges of the runner within it. Figure 8.4, Kempe's Engineers yearbook, Quayle [1984], can be used for this.

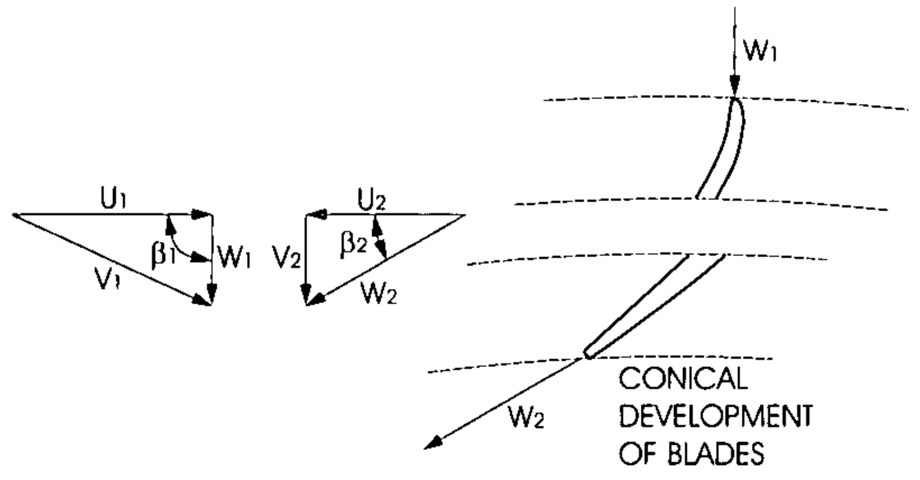
W1
U1
U2
β1
W1
V2
β2
V1
W2
CONICAL
DEVELOPMENT
OF BLADES
W2

(a) Typical

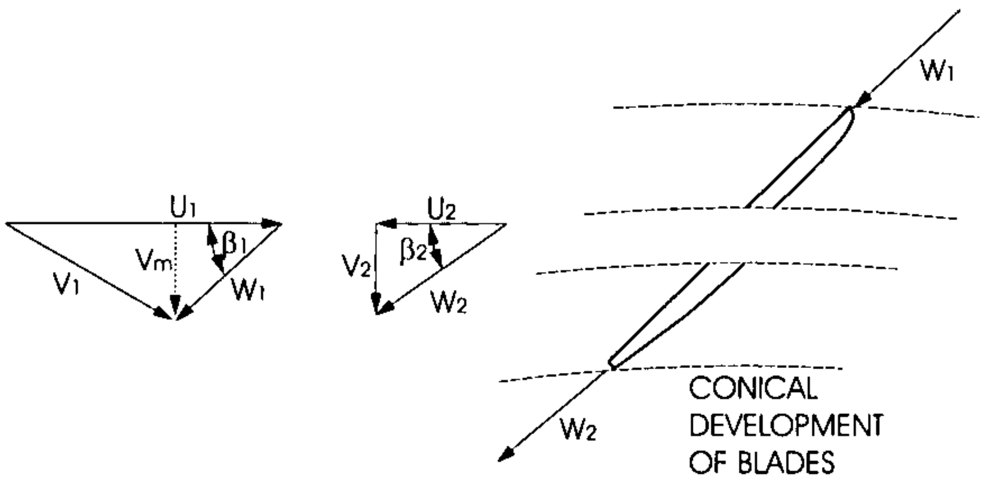
W1
U1
U2
β1
Vm
V2
β2
V1
W1
W2
CONICAL
DEVELOPMENT
OF BLADES
W2

(b) High U_1'

Fig. 8.2. Variation of inlet blade angles with specific speed.

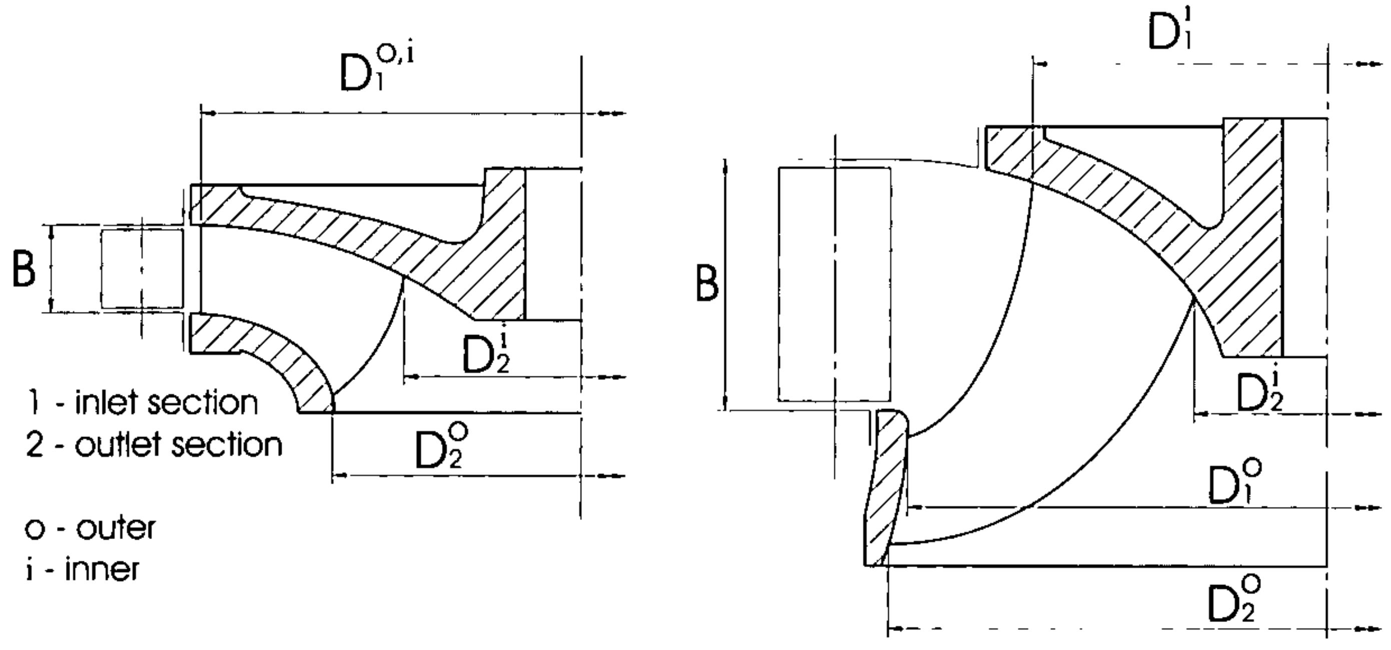
$D_1^{o,i}$
B
D_2^i
D_2^o
1 - inlet section
2 - outlet section
o - outer
i - inner
D_1^i
B
D_2^i
D_1^o
D_2^o

Fig. 8.3. Meridional section views of a low and a high speed Francis turbine.

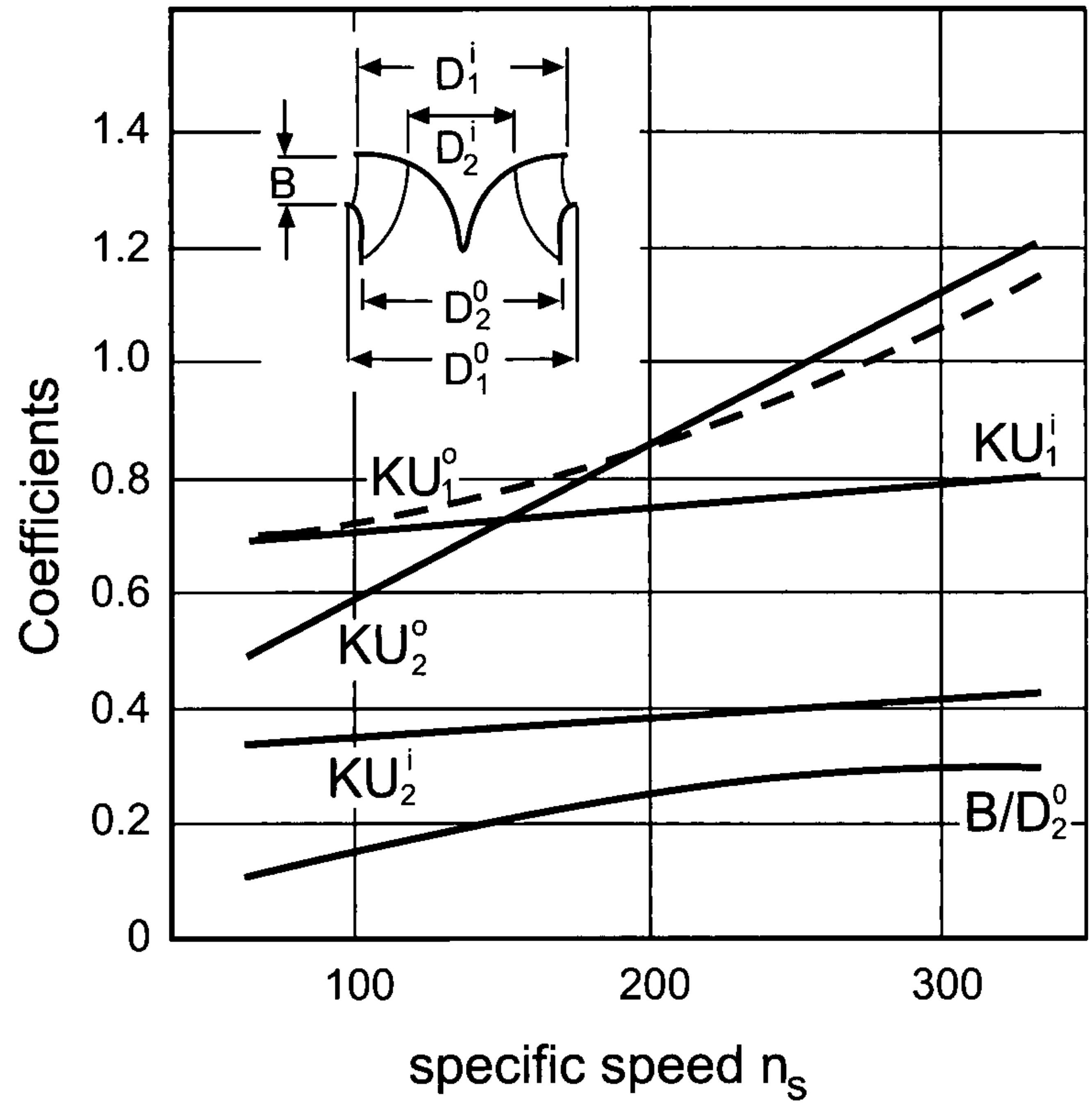

Fig. 8.4. Francis turbine coefficients. Adapted from Quayle [1984].

The peripheral velocity coefficients are defined by Equations 3.10 and 3.11. B/D_2^o, as defined in Figure 8.4, is the guide vane height divided by the runner exit diameter. (Superscripts ^{o} and ^{i} refer to outer and inner dimensions respectively).

The shape of the trailing edge, as projected onto the meridional plane has a strong influence on blade stacking. The designer has to vary this shape until a good stack is achieved. Experience plays an important part in this. Figure 8.4 only indicates where the trailing edge should end on the crown and skirt respectively.

For propeller turbines, Figure 8.5 from Kempe's Engineers yearbook, Quayle [1984], can be used. This diagram differs from Figure 8.4 in that the number of blades is also included. Blade length divided by blade pitch (l/s) is also provided, with $s = \frac{\pi D}{Z}$.

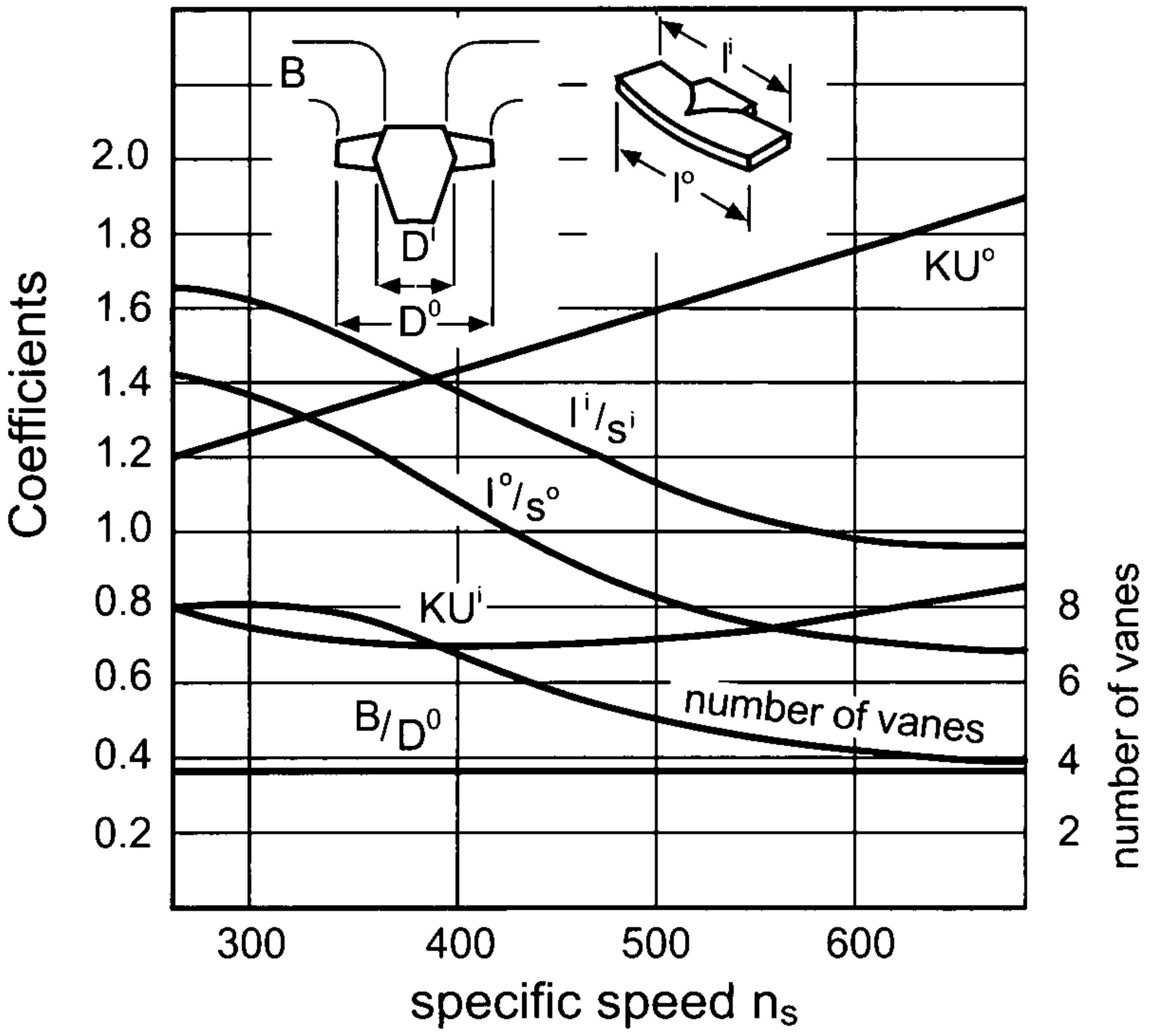

Fig. 8.5. Kaplan turbine coefficients. Adapted from Quayle [1984].

Nechleba [1957] provides similar non-dimensional data to Figures 8.4 and 8.5.

9 Throughflow calculations

The conventional approach to runner design is to construct blade profiles that lie along stream surfaces. An example of stream surfaces is illustrated in Figure 3.3. These stream surfaces project as streamlines onto the meridional plane. To determine the position of the stream surfaces, throughflow calculations need to be performed.

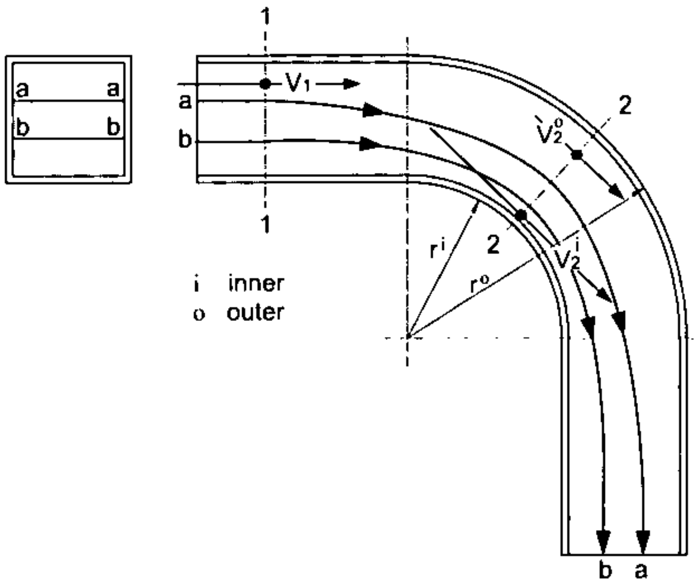

Fig. 9.1. Movement of stream surfaces in a rectangular sectioned bend.

Stream surfaces (and streamlines) move to satisfy the requirements of radial equilibrium. For irrotational inviscid flow in a simple rectangular pipe bend, Figure 9.1, the stream surfaces move towards the inside of the bend. This can be explained physically as follows: p_2^o, the pressure on the outside of the bend at section 2, has to be greater than p_2^i in order to be able to deflect the flow around the bend. Conservation of energy (Bernoulli's equation) requires that V_2^o must reduce from V_1 to compensate for the higher p_2^o for a flow with constant energy. Likewise $V_2^i > V_1$ and the stream surfaces have to adjust by moving inwards to accomodate the required changes in V_2. Across section 2, the forces acting on the flow must balance the centripetal acceleration. The flow is said to be in radial equilibrium. The flow in this contrived example is classified as irrotational flow or potential flow. Figure 9.1 is somewhat idealised, in reality the cross passage pressure gradient sets up additional secondary motion.The flow, in practise, around a 90° bend would behave differently to the idealised flow shown in the Figure due to the presence of these secondary flows and also due to boundary layer effects on the pipe wall.

Now in a Francis turbine, the flow in the space between the guide vanes and the runner, can also be considered as potential flow if the guide vanes are situated outside of the influence of the "bend" as Figure 9.2 shows.

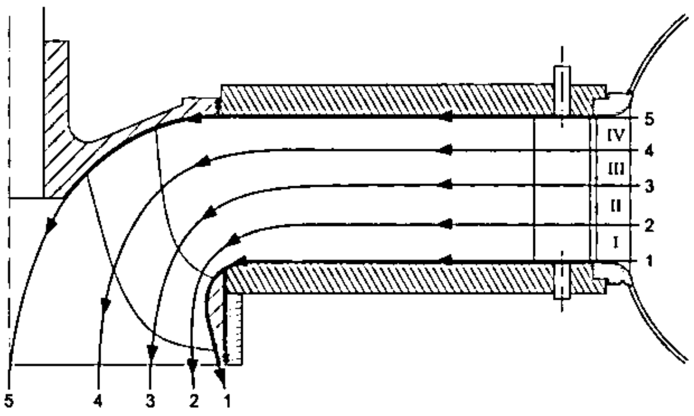

Fig. 9.2. Potential flow in the meridional view of a Francis turbine.

A requirement for potential flow is that the rV_θ exiting from the guide vanes is constant across the span. When potential flow exists, the graphical method described by Nechleba [1957] can be used (though it is quite time consuming to carry out).

When the guide vanes lie within the region of influence of the "bend", the rV_θ leaving the guide vanes is not constant. With reference to Figure 3.3, the curvature of the flow in the meridional plane pushes the streamlines outwards, towards the centre of curvature. At the guide vane exit, the tip streamtube has a higher meridional velocity $V_{m_{\mathrm{I}}}$ than that of the hub streamline $V_{m_{\mathrm{IV}}}$. As the flow angle leaving the guide vanes is (nominally) constant, at the guide vane exit there must be a higher tangential velocity component $V_{\theta_{\mathrm{I}}}$ at the tip than $V_{\theta_{\mathrm{IV}}}$ at the hub. Thus, along the guide vane trailing edge, rV_θ is not constant and the requirement for potential flow does not hold. In practice, this non-uniform guide vane rV_θ moves the stream surfaces significantly and must be accounted for.

An example of the difference in streamline positions is shown in Figure 9.3 for a high specific speed Francis turbine.

Two computational methods can be used to determine the position of the streamlines. The streamline curvature technique, Denton [1978], Cumpsty [1989], is the more common of these approaches and may be used for compressible as well as incompressible flows. Alternatively, the stream function method, described by Lewis [1996] and in the subsequent section, is available, though only for incompressible flows.

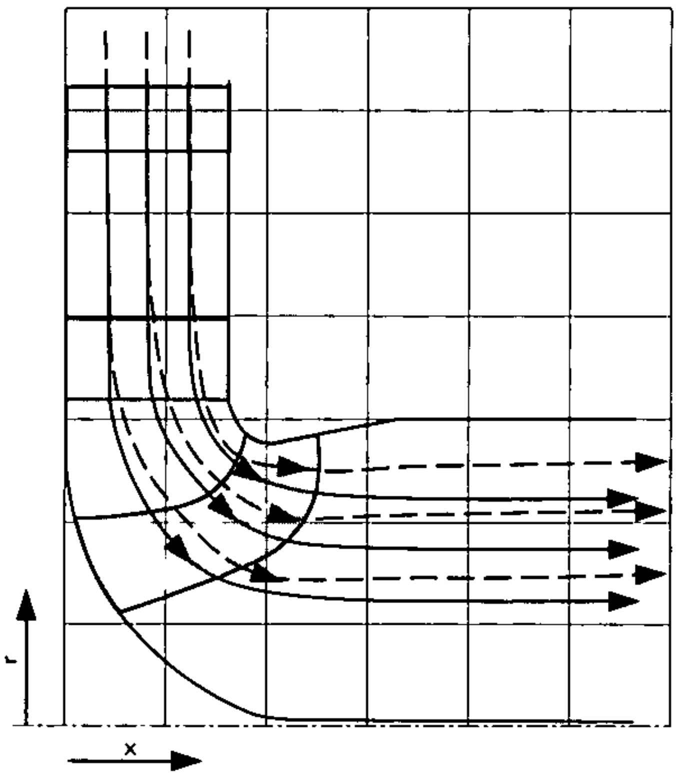

Fig. 9.3. Comparison between potential flow streamlines (solid lines) and streamlines associated with non-constant rV_θ at the guide vane.

Section 9.2 provides a library of streamline positions for different Francis turbine envelopes, as an alternative but less accurate means of determining streamline positions.

9.1 Stream function theory

Let x, r and θ denote a set of cylindrical polar coordinates. Surfaces of constant θ are called meridional planes, flow in these planes is referred to as meridional flow.

The stream function ψ satisfies the equation [Lewis, 1996, p. 152, eqn 6.21]

$$\frac{\partial^2\psi}{\partial r^2} - \frac{1}{r}\frac{\partial\psi}{\partial r} + \frac{\partial^2\psi}{\partial x^2} = -\omega_\theta r \tag{9.1}$$

where ω_θ is the tangential vorticity. Along a stream line $\psi =$ constant and

$$V_x = \frac{1}{r}\frac{\partial\psi}{\partial r}, \qquad V_r = -\frac{1}{r}\frac{\partial\psi}{\partial x}, \qquad V_m = \sqrt{V_x^2 + V_r^2}. \tag{9.2}$$

At the hub $\psi \triangleq 0$, at the casing $\psi \triangleq 1$.

For the geometry of Figure 9.4, at the inlet

$$V_x = \frac{1}{r}\frac{\partial\psi}{\partial r} = 0, \tag{9.3}$$

and at the outlet

$$V_r = -\frac{1}{r}\frac{\partial \psi}{\partial x} = 0. \tag{9.4}$$

In regions A and D of Figure 9.4 it may be assumed that the flow is irrotational, i.e. $\omega_\theta = 0$.

In region B, it is assumed that $\omega_\theta r$ is constant along a streamline, i.e. $\omega_\theta r = \mathcal{F}(\psi)$, and that

$$r\omega_\theta = \left(r_{gv} \tan \alpha_{gv}\right)^2 V_{r_{gv}} \frac{\partial V_{r_{gv}}}{\partial \psi} . \tag{9.5}$$

Along streamlines through region C it is assumed that

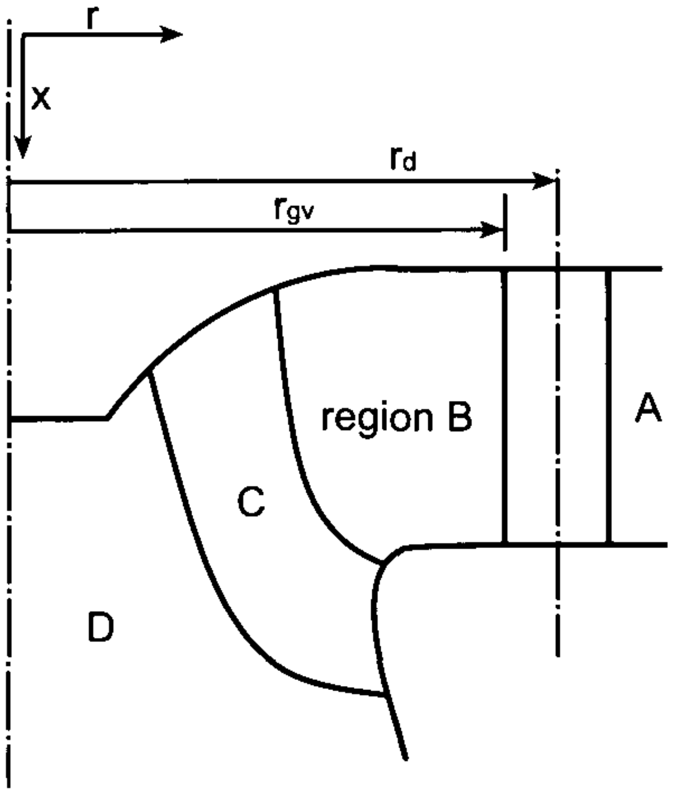

Fig. 9.4. Computational regions for stream function analysis of a Francis or Kaplan turbine.

$$(\omega_\theta r)_C = \lambda(\omega_\theta r)_B \tag{9.6}$$

with the vorticity scaling factor λ decreasing linearly with distance along the streamline from a value of 1 at the leading edge to a value of 0 at the trailing edge, as shown in Figure 9.5.

With reference to Figure 9.6, the computational approach is as follows:

1. Specify coordinates defining the hub and shroud surfaces, runner blade leading and trailing edges. A 30 x 30 grid should be sufficient.

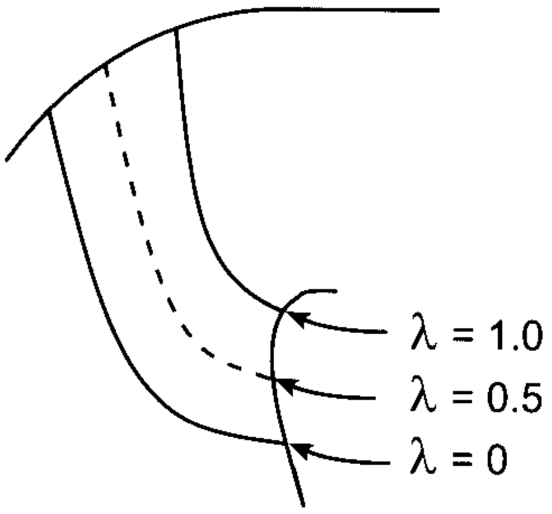

Fig. 9.5. Vorticity scaling factor λ.

2. Input r_g, r_d, Q, N and α_{gv}.
3. Specify λ at all grid points.
4. Set $r\omega_\theta = 0$
5. Solve Equation 9.1 to obtain $\psi^{(1)}$ at all grid points. Central difference formulae for the differentials in this equation are

$$\frac{\partial^2\psi}{\partial r^2} = \frac{1}{h^2}\left[\psi_{i,j-1} - 2\psi_{i,j} + \psi_{i,j+1}\right]$$
$$\frac{\partial^2\psi}{\partial x^2} = \frac{1}{h^2}\left[\psi_{i-1,j} - 2\psi_{i,j} + \psi_{i+1,j}\right]$$
$$\frac{\partial\psi}{\partial r} = \frac{1}{2h}\left[\psi_{i,j-1} - \psi_{i,j+1}\right].$$

Substituting these into Equation 9.1 and rearranging yields

$$\psi_{i,j} = \frac{1}{4}\left[\left(1 + \frac{h}{2r_j}\right)\psi_{i,j-1} + \left(1 - \frac{h}{2r_j}\right)\psi_{i,j+1} + (\psi_{i-1,j} + \psi_{i+1,j})\right] \tag{9.7}$$

When boundary points do not coincide with grid points, such as the case shown in Figure 9.7, Liebmanns formula

$$\psi_{i,j} = \frac{\left[\dfrac{\psi_a}{a(a+b)} + \dfrac{\psi_b}{b(a+b)} + \dfrac{\psi_c}{c(c+d)} + \dfrac{\psi_d}{d(c+d)}\right]}{\left[\dfrac{1}{ab} + \dfrac{1}{cd}\right]}. \tag{9.8}$$

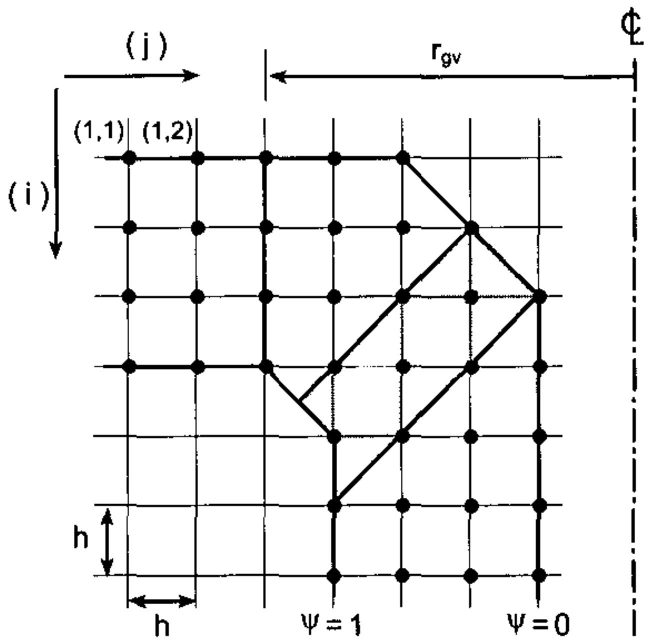

Fig. 9.6. Example of a computational grid.

may be used.

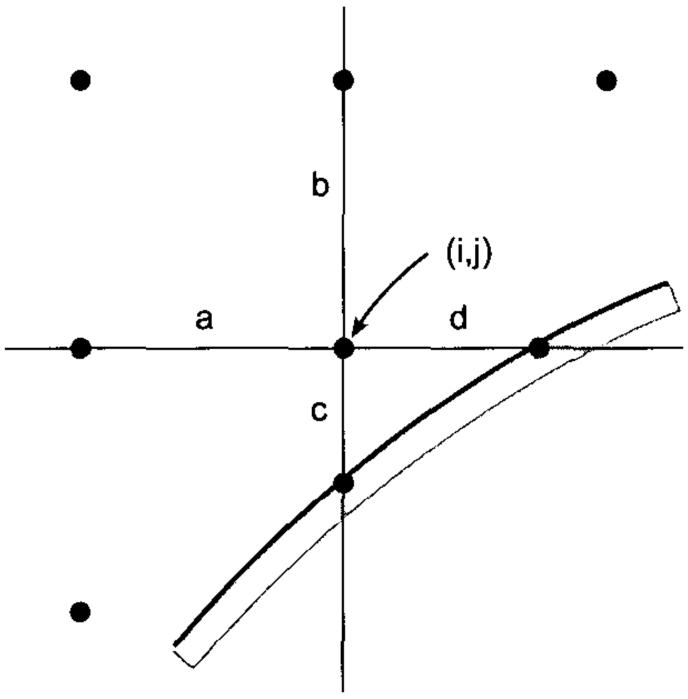

Fig. 9.7. Boundaries not on a point.

The (Neumann) boundary conditions at inlet

$$V_x = \frac{1}{r}\frac{\partial\psi}{\partial r} = 0 \quad \Longrightarrow \quad \frac{\partial\psi}{\partial r} = 0 \tag{9.9}$$

Thus

$$\psi_{i,j+1} = \psi_{i,j-1} \quad \text{for all } i \text{ along the inlet.} \tag{9.10}$$

Similarly at outlet

$$V_r = -\frac{1}{r}\frac{\partial \psi}{\partial x} = 0 \quad \Longrightarrow \quad \frac{\partial \psi}{\partial x} = 0 \tag{9.11}$$

Thus

$$\psi_{i+1,j} = \psi_{i-1,j} \quad \text{for all } j \text{ along the outlet.} \tag{9.12}$$

6. Calculate $V_{r_{gv}}$ for each point at r_{gv} using

$$V_{r_{gv}} = -\frac{1}{r}\frac{\partial \psi}{\partial x}$$

7. Calculate $(r\omega_\theta)_{gv}$ using Equation 9.5.
8. Specify $r\omega_\theta$ for the grid points in regions B and C ($r\omega_\theta = 0$ in regions A and D).
9. Convergence stability requires:
   First iteration $r\omega_\theta \leftarrow r f_1 \omega_\theta$
   Subsequent iterations $\psi^{(i)} \leftarrow (1 - f_2)\psi^{(i-1)} + f_2\psi^{(i)}$ then update $r\omega_\theta$ where f_1 is a scaling factor and f_2 is a decelerating factor.
   If the sucessive over-relaxation method (SOR) is applied then

$$f_2 = \frac{8 - 4\sqrt{4 - \alpha^2}}{\alpha^2} \tag{9.13}$$

   and $\alpha = \cos(\pi/m) + \cos(\pi/n)$ where m and n are the total number of increments into which the the vertical and horizontal sides of the rectangular domain are divided.
10. Compute V_m for all grid points using final values for ψ and Equations 9.2.
11. Interpolate V_m at the leading and trailing edges of the runner blade. Determine coordinates of final streamlines at guide vane trailing edge, and runner leading and trailing edges.
    Hence

$$\begin{aligned}
V_{\theta 1} &= \frac{r_{gv} V_{r_{gv}} \tan \alpha_{gv}}{r_1}, \\
\alpha_1 &= \tan^{-1} \frac{V_{\theta 1}}{V_{m1}}, \\
\beta_1 &= \tan^{-1} \frac{r_1 \Omega - V_{\theta 1}}{V_{m1}}, \\
\beta_2 &= \tan^{-1} \frac{r_2 \Omega}{V_{m2}} \quad \text{for} \quad Q_\perp
\end{aligned}$$

9.2 Meridional streamline library for Francis turbines

Figures 9.8 through 9.14 have meridional streamlines provided that correspond to the design condition of perpendicular discharge $Q_\perp$.

The designer of a Francis turbine can use these streamline positions with the envelopes given, or interpolate between streamline position for intermediate envelope profiles, corresponding to different specific speed designs.

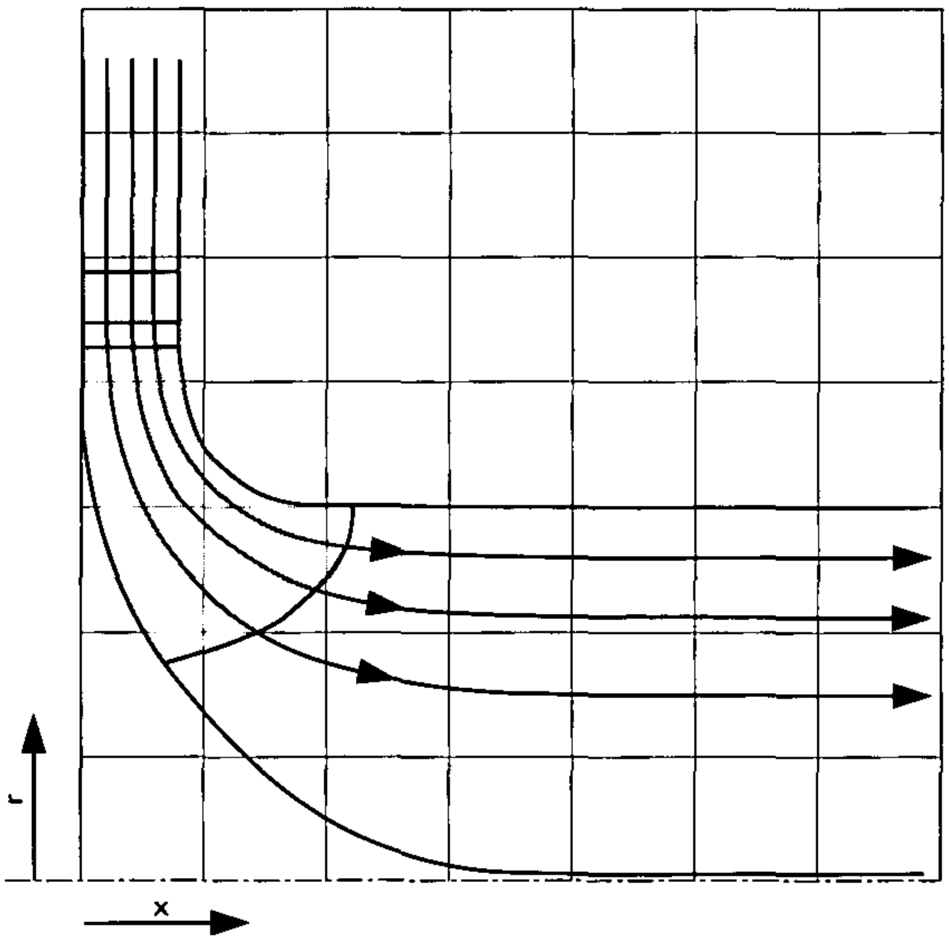

Fig. 9.8. Francis turbine envelope and streamlines, $n_s = 80$.

9.3 Throughflow analysis of tubular type propeller turbines

Propeller turbines which have little turning in the meridional plane, such as bulb and tubular type propellers, can have their streamline positions determined using simple radial equilibrium. Refer to Chapter 3 , Section 3.7, and Chapter 15.

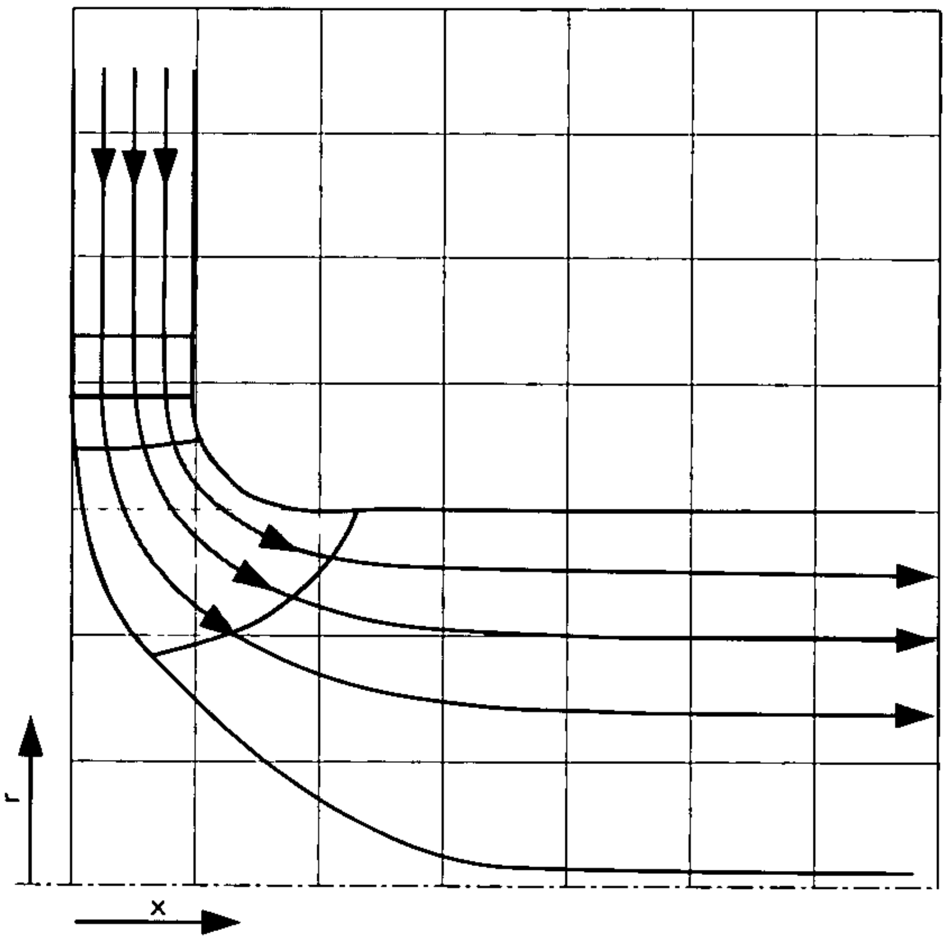

Fig. 9.9. Francis turbine envelope and streamlines, $n_s = 110$.

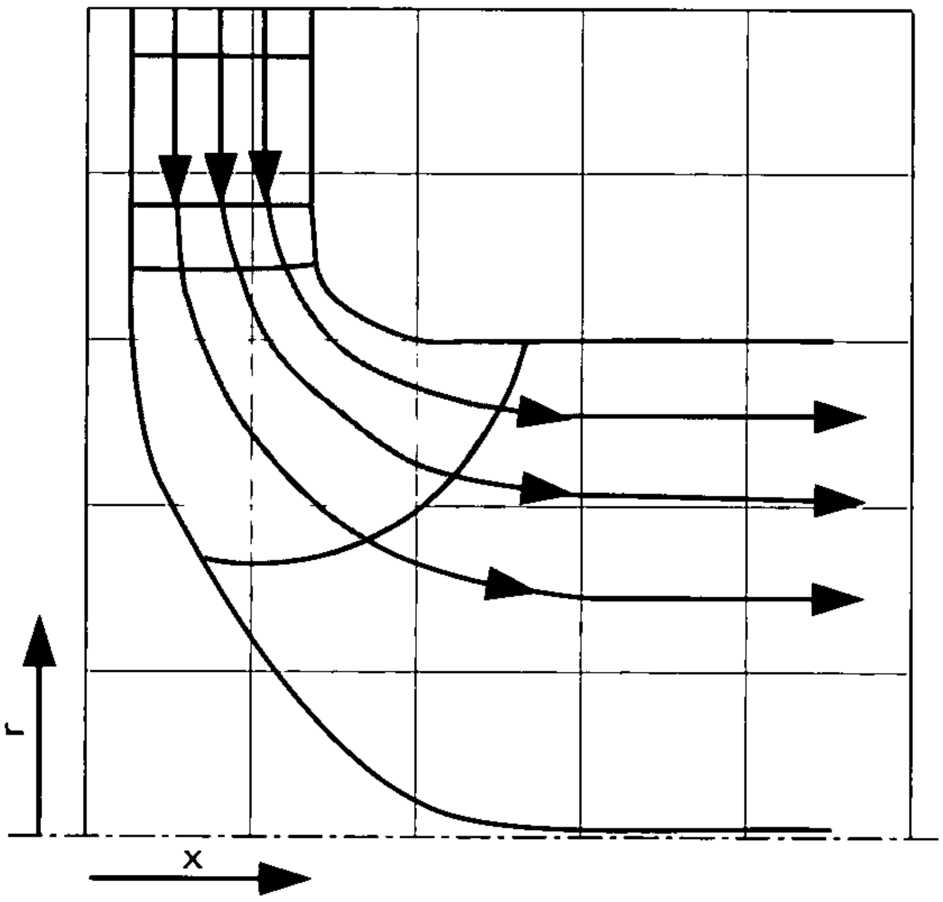

Fig. 9.10. Francis turbine envelope and streamlines, $n_s = 125$.

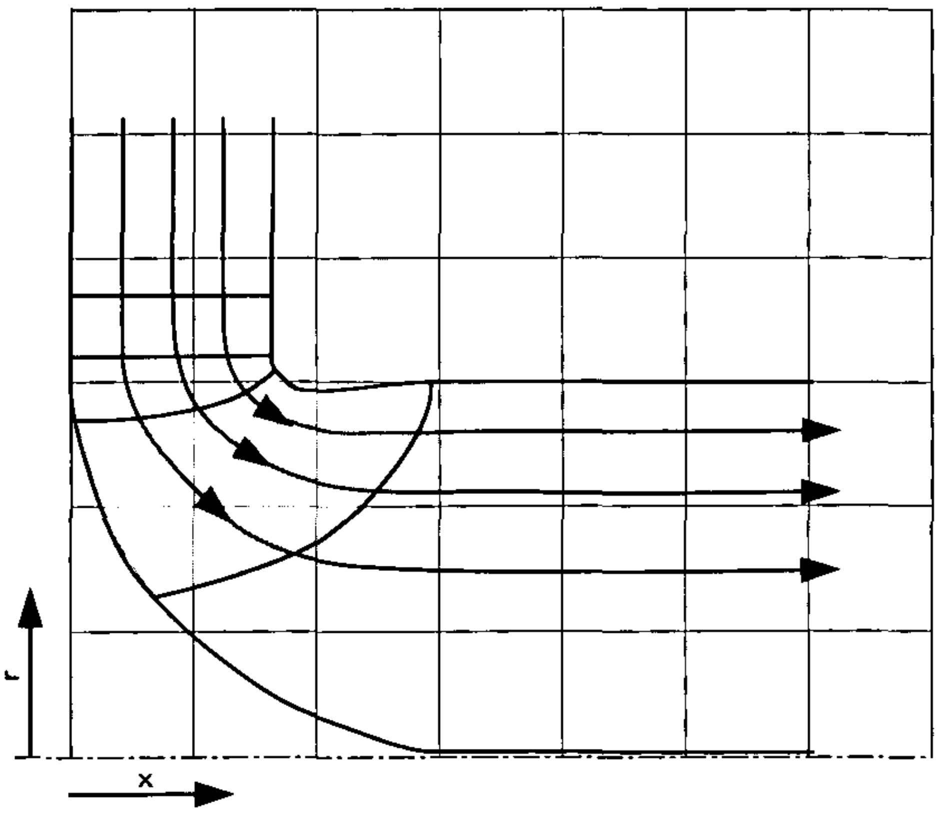

Fig. 9.11. Francis turbine envelope and streamlines, $n_s = 170$.

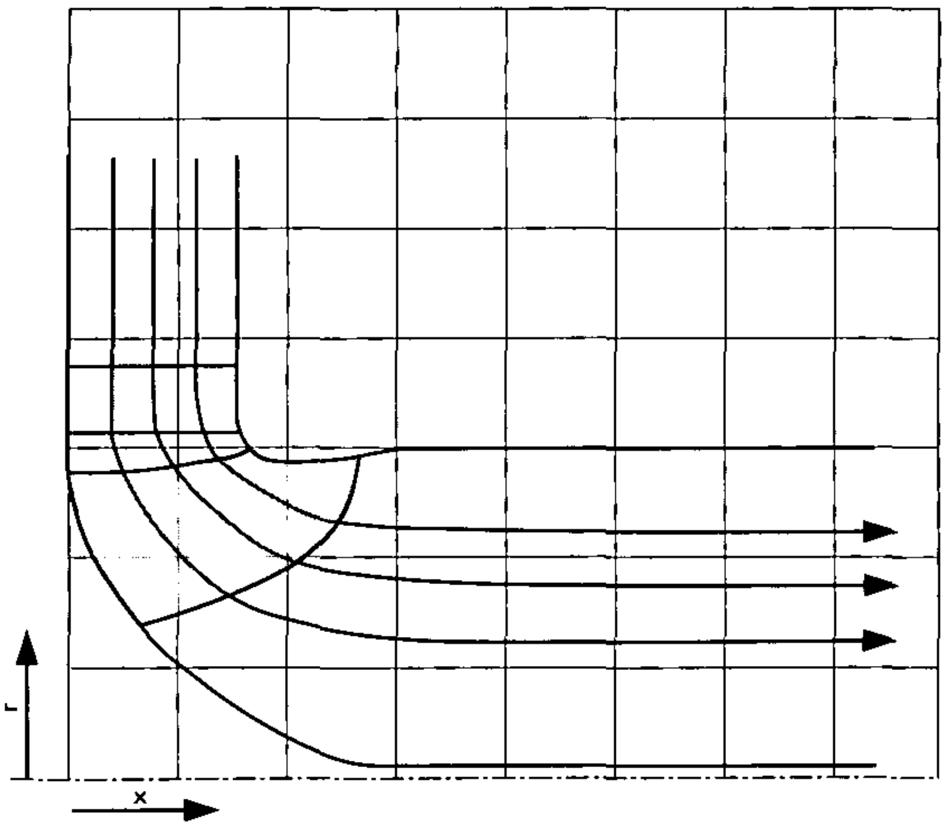

Fig. 9.12. Francis turbine envelope and streamlines, $n_s = 200$.

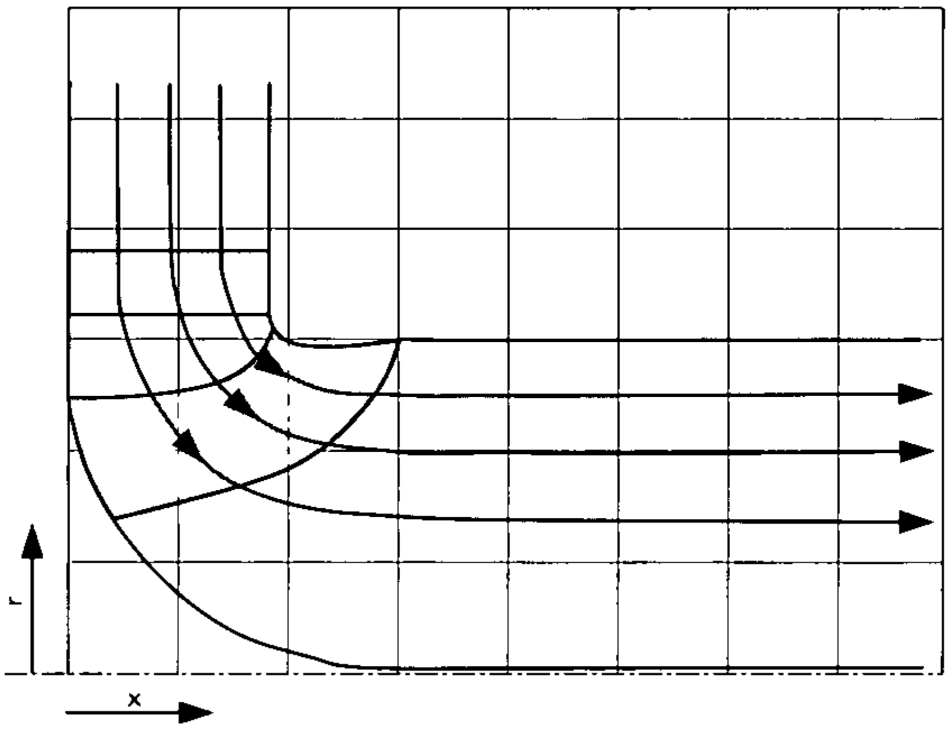

Fig. 9.13. Francis turbine envelope and streamlines, $n_s = 220$.

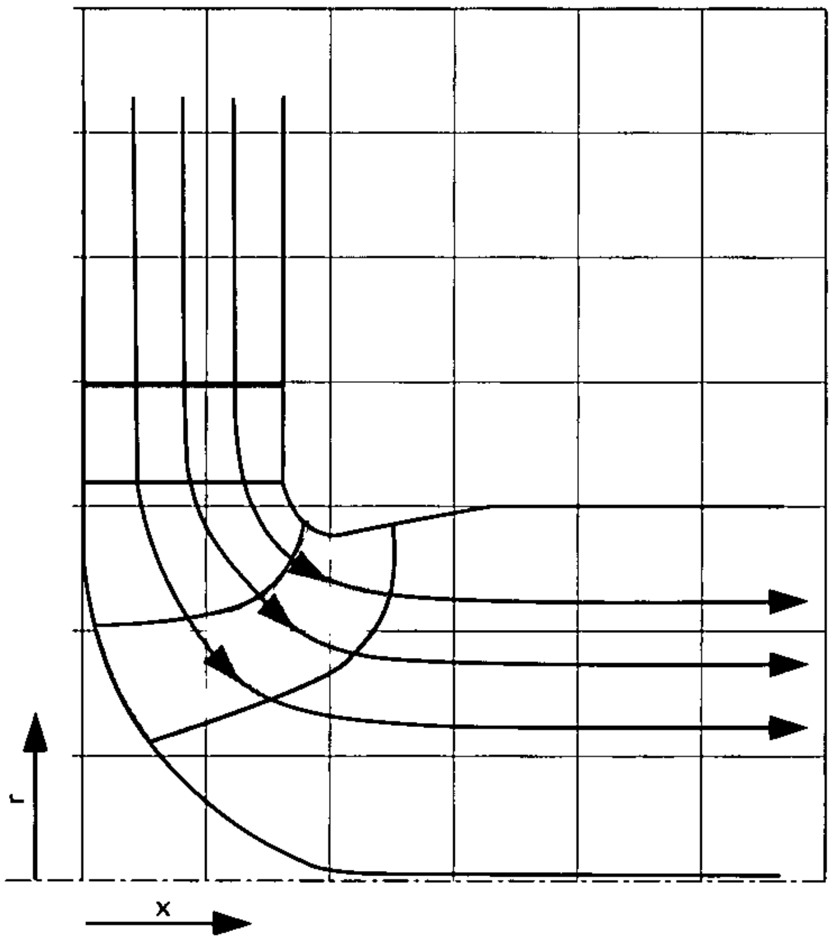

Fig. 9.14. Francis turbine envelope and streamlines, $n_s = 300$.

10 Blade design

Runner blades are designed in a rotating frame of reference. Guide vanes and stay vanes operate in a stationary (relative to the ground) frame of reference. Stay vanes are principally structural components and are thus dealt with in Chapter 11, though hydrodynamic principles need to be applied to their design.

The purpose of well designed blades is to deflect the flow by the required amount over a given stream surface, with minimum loss and with good cavitation performance.

The blade should exhibit low loss over a range of incidences. This usually requires

- no separation on the pressure face,
- reasonably heavy loading, e.g. suction face near the point of separating at the trailing edge.

Figure 3.3 has five streamlines drawn in the meridional plane, corresponding to the boundaries of partial turbines (stream tubes) I–IV. Two methods are presented in this Chapter for producing blade geometry. The first method is a graphical method used widely in the 1960's. The second method is not necessarily any better than the first, but allows use of computational techniques, permits some degree of unloading at the trailing edge, and can be interfaced with a solid modelling package for blade visualization.

10.1 Francis blade design by Prasil transform

The Prasil transform is a graphical procedure which controls the geometry only of the Francis runner blade shapes. Its purpose is to transform the intersection of the blade surface with each of the flow surfaces, 1, 2, 3 and 4, onto a flat plane. Refer to Figure 10.1. It is usual to deal either with the blade camberline or the suction face geometry only. The process requires a drawing board, good drawing skills and at least a month of time to produce a blading drawing suitable for manufacture. The method is superior to the method of conicals presented by Nechleba [1957]. The Prasil transform method is described fully by Wislicenus [1965] and is reproduced here. Note the corresponding Figures 10.1 to 10.4 show a pump design.

1. Divide developed section of runner into meridional streamtubes 1, 2, 3 and 4. Figure 10.1.

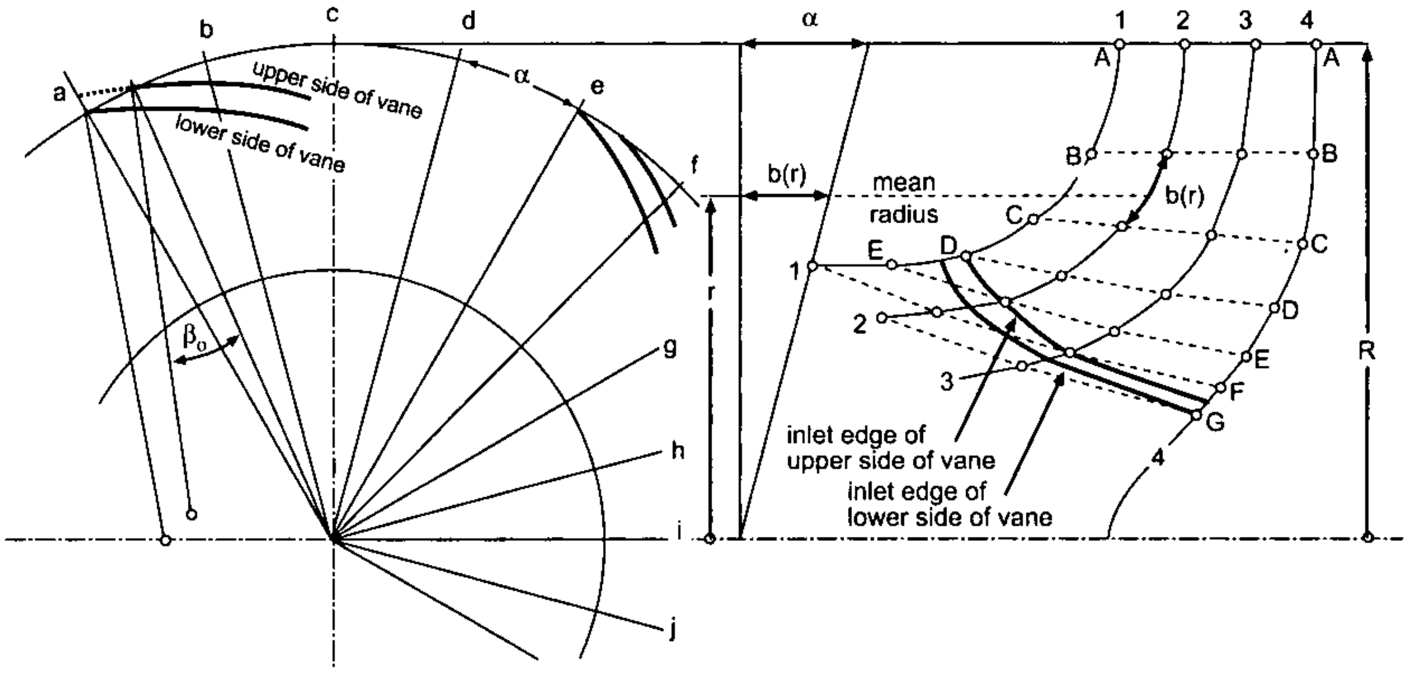
b
c
d
α
1
2
3
4
a
upper side of vane
lower side of vane
α
e
f
b(r)
mean radius
A
A
B
B
C
C
D
D
E
E
F
G
b(r)
1
2
3
4
r
R
β₀
g
h
i
j
inlet edge of upper side of vane
inlet edge of lower side of vane

Fig. 10.1. Reference lines for turbine blade layout by conformal transformation. (Reproduced courtesy Dover Publications)

2. For each flow surface, draw parallel lines *a* to *k* representing radial planes of constant angular spacing. α is the distance at the periphery between two radial planes, See Figures 10.1 and 10.4.

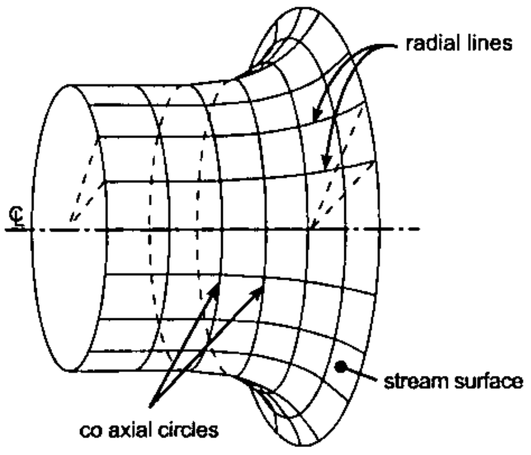
radial lines
℄
stream surface
co axial circles

Fig. 10.2. Sketch showing radial planes and co-axial circles.

Draw coaxial circles, A to G, whose spacing $b(r)$ follows the relationship

$$\frac{b(r)}{r} = \frac{\alpha}{R} \tag{10.1}$$

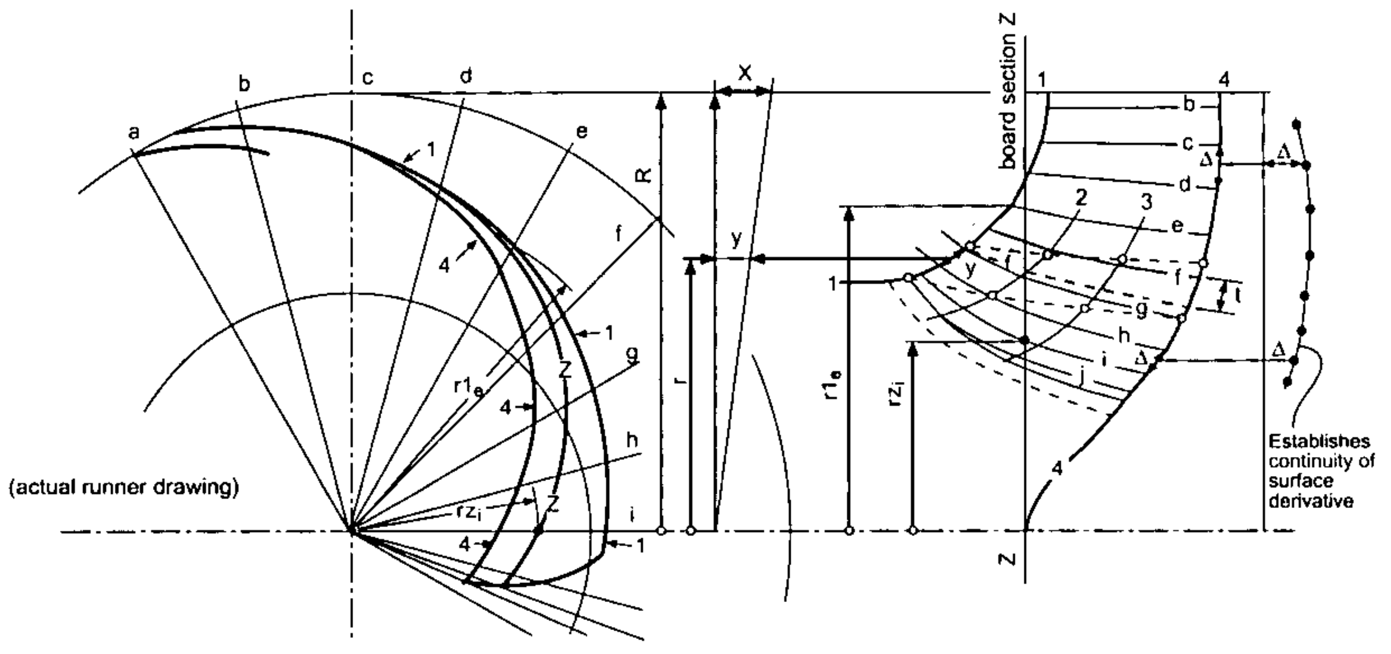
(actual runner drawing)
a
b
c
d
e
f
g
h
i
R
X
y
r
$r1_e$
rz_i
1
4
Z
board section Z
2
3
Δ
t
Establishes continuity of surface derivative

Fig. 10.3. Pump blade drawing derived from the conformal transformation. (Reproduced courtesy Dover Publications)

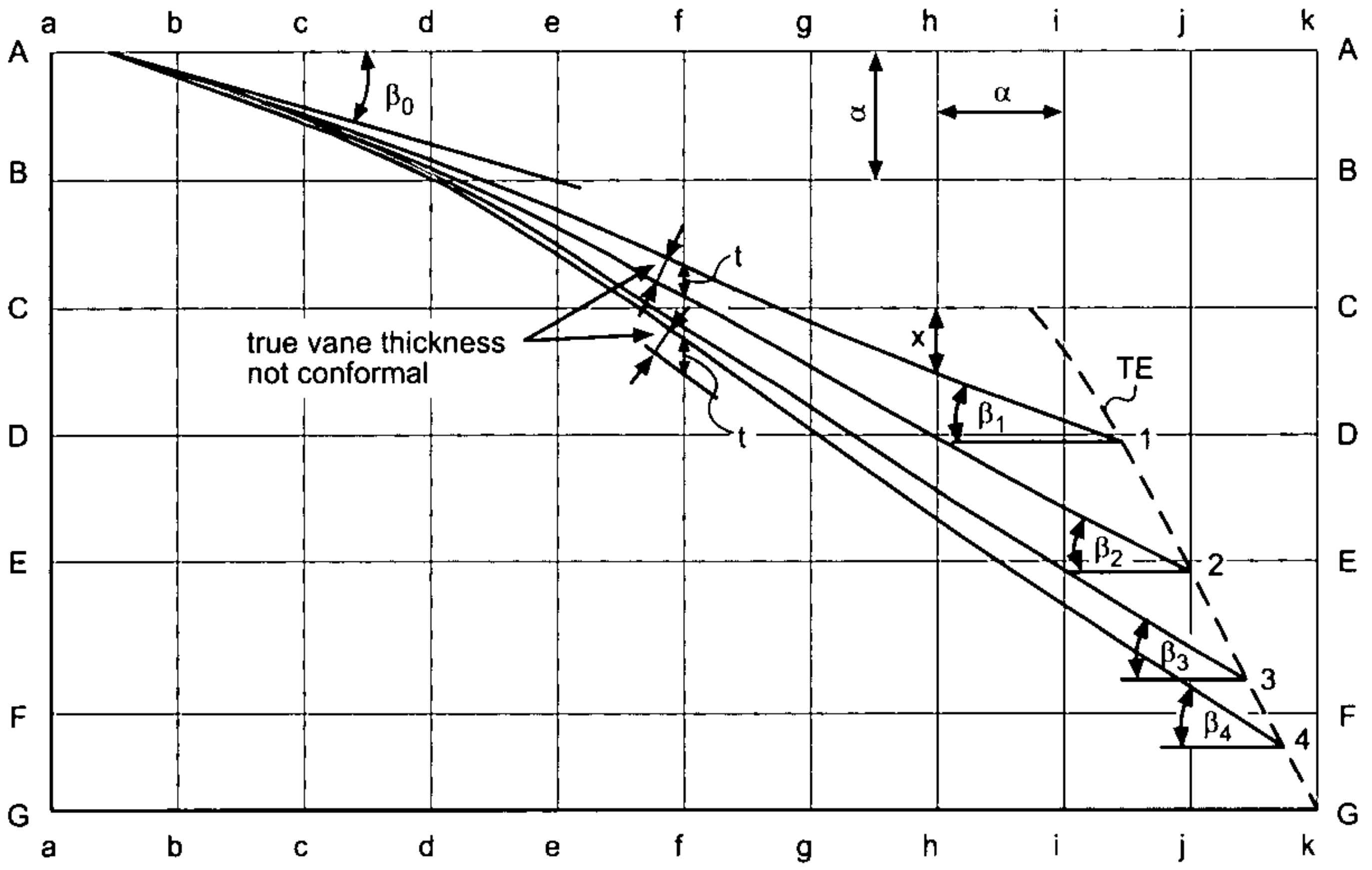
a b c d e f g h i j k
A B C D E F G
β_0
α
true vane thickness not conformal
t
x
TE
β_1
β_2
β_3
β_4
1
2
3
4

Fig. 10.4. Conformal representation of turbine blade camber lines for stream surfaces 1–4. (Reproduced courtesy Dover Publications)

A short process of successive approximation will be required. See Figure 10.1.

3. The process of blade layout is as follows. On Figure 10.4, determine vertical location of points 1A, 1B, 2A, etc from Figure 10.1. Note any distance X on Figure 10.4 is related to distance Y on Figure 10.3 by
$$\frac{X}{Y}=\frac{R}{r} \tag{10.2}$$
where r is the mean distance of Y (local scale of representation).
4. Actual blade angles χ_{inlet} to χ_{inlet_4} and χ_{outlet} to χ_{outlet_4} are assumed to be known (e.g. from velocity diagrams). Draw a smooth curve from inlet to outlet on Figure 10.4 with the horizontal positions of 1A, 1B, 2A, etc being adjusted to achieve the required curve. Tangency of the curve to the blade angles is required (double curvature is permissible). There must be geometric consistency in the selection of the horizontal positions.
5. Having produced a conformal representation of the blade intersecting with the stream surfaces, Figure 10.4 from Figure 10.1, it is now necessary to produce a runner drawing, Figure 10.3, and also Figure 10.7.
The radial cut lines in Figure 10.3 (b, c, d, etc) are produced as follows. For 1, measure x from C in Figure 10.4 and mark out y as shown in Figure 10.3 ($y = rx/R$). Repeat this for each stream surface 2, 3 and 4 to establish line h in Figure 10.3. Repeat to establish all the radial cut lines in Figure 10.3 representing *one* blade surface.
6. Board sections can be drawn, e.g. ZZ in Figure 10.3 and the corresponding plan view can be drawn; e.g. rZ_i corresponding to line i in the meridional view can be transferred to the plan view, see Figure 10.3.
7. The remaining blade surface can be established using the blade angles that can be obtained directly from Figure 10.4. For example, along radial cut line f, determine blade angle by measurement for 4 calculate t from
$$t=\frac{\text{true vane thickness}}{\cos\beta_{\text{local}}} \tag{10.3}$$
and plot on Figure 10.4 as shown.

The blade angles are determined from consideration of incidence/deviation issues, see Chapter 3. Note that this method has not provided any detailed control of the load distribution, for cavitation control, for example, on the blade profile.

Figure 10.6 illustrates a likely variation in achieved critical sigma using the method. The message here being: be conservative in the selection of turbine setting.

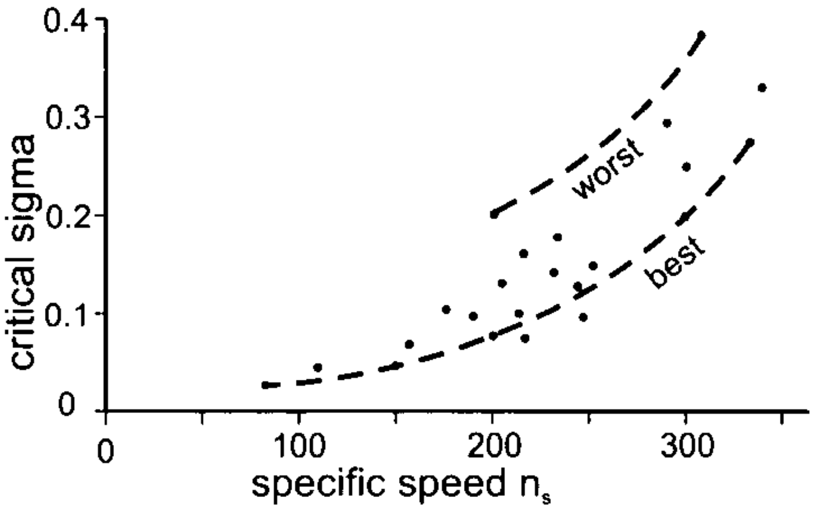

Fig. 10.5. Typical variation in critical sigma for turbines designed between 1950–1960.

10.2 Francis blade design by the mean streamline method

The mean streamline method, Section 3.9, was first published by Wislicenus [1965] and extended by McBride [1977]. The analysis and methodology presented in Section 3.9 and in this section is adapted from Huntsman [1993].

The streamlines determined from the throughflow methods of Chapter 9 are used to establish a blade camberline in x, $r\theta$, r coordinates. Blade sections can be designed either in the partial turbines as per Figure 10.6, or along the streamlines. A minimum of 4 blade definitions is usually required for Francis turbines. Considering partial turbine IV shown in Figure 10.6, the change in angular momentum between inlet and outlet is given by

$$\Delta r V_\theta = r_0 V_{\theta 0} - r_5 V_{\theta 5} \tag{10.4}$$

The next step is to specify the blade load distribution at the equi-spaced points 1 to 4 within the blade. This can be done with a graphical distribution of rV_θ with meridional streamline length m or analytically with an equation such as

$$r_n V_{\theta_n} = \Delta r V_\theta \left[\left(\frac{n}{K}\right) a + \left(\frac{n}{K}\right)^m (1-a) \right] \tag{10.5}$$

where $K = 5$ in this example, and n an intermediate station. With $a = 1$ gives a linear loading distribution of rV_θ, and , with $a = 0$, gives a parabolic distribution of rV_θ with $m = 2$.

A table can be constructed as follows:

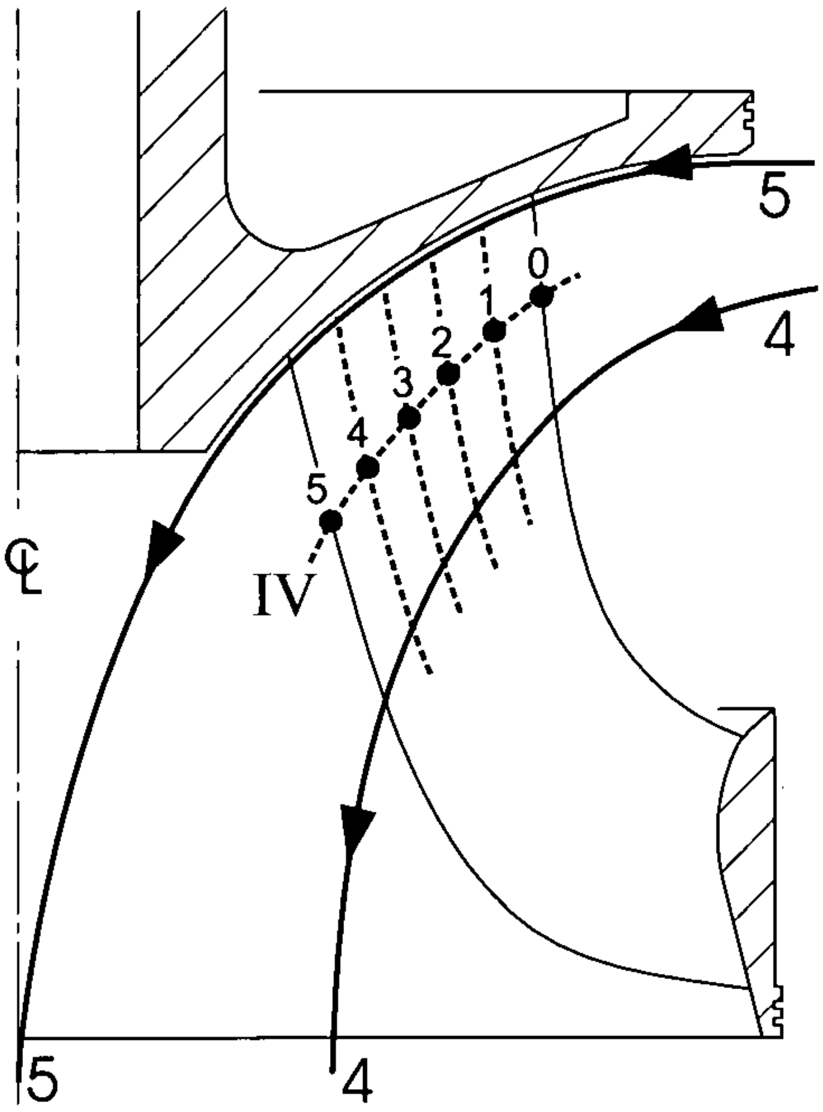

Fig. 10.6. Mid blade stations, partial turbine IV.

station	x	r	$\mathrm{d}m_n$	$\overline{V}_{m_n}$	$r_n V_{\theta_n}$	ωr_n	$\overline{W_{\theta_n}}$	β_n	$\mathrm{d}\theta_n$
0									
1									
2									
3									
4									
5									

x and r come from the partial turbine drawing. V_{m_n} is estimated from the change in streamtube thickness on the partial turbine drawing.

$$\overline{V}_{m_n} = \frac{V_{m_n} + V_{m_{n-1}}}{2} \tag{10.6}$$

$r_n V_{\theta_n}$ is calculated using Equation 10.5. ωr_n represents the peripheral velocity at station n. W_{θ_n} is given by:

$$\overline{W}_{\theta_n} = \frac{\left[\frac{r_n V_{\theta_n}}{r_n} - \omega r_n\right] + \left[\frac{r_{n-1} V_{\theta_{n-1}}}{r_{n-1}} - \omega r_{n-1}\right]}{2}, \tag{10.7}$$

$$\beta_n = \tan^{-1}\left(\frac{\overline{W}_{\theta_n}}{\overline{V}_{m_n}}\right), \tag{10.8}$$

$$\mathrm{d}m_n = \sqrt{(x_n - x_{n-1})^2 + (r_n - r_{n-1})^2}, \tag{10.9}$$

$$\mathrm{d}\theta_n = \frac{\mathrm{d}m_n \tan\beta_n}{r_n}. \tag{10.10}$$

The procedure is repeated for each partial turbine. Tables 15.7 and 15.8 provide an example in Chapter 15. This method can be improved to make the design of a blade more general, eg it could also contain a deviation term to increase blade turning to account for deviation, and an incidence term to allow the blade angles to be set at inlet to match a required incidence. Camberline thickness can also be applied.

It is necessary to check that a smooth surface has been achieved. This can be done by inputing the x, $r\theta$, r geometry into a solid or surface modelling package, or by manipulating the data to plot lines of intersection on the meridional plane of radial planes. Figures 10.7 (a) and (b) show the meridional plane and plane view plots of a Francis runner geometry. Figure 10.7 (a) shows lines of intersection of radial planes with the actual blade pressure and suction faces. Camberline intersection lines would lie between $9'$ and 9 and $7'$ and 7 etc.

One aspect of Francis runner geometry that needs to be checked is the angle between the blade surface and the skirt (and between the blade surface and the crown), as seen in the direction of flow. If this angle, sometimes known as dihedral, is too small, the blade passage will accumulate 'lossy' slow moving fluid. Too much blade 'lean' may also move the streamlines away from the positions calculated by the methods of Chapter 9. There is some advantage to a small amount of blade lean at the leading edge. The runner blades cross the guide vane wakes in a more distributed manner (in a similar fashion to the spiral blades of a cylindrical reel lawnmower).

Once a smooth profile has been achieved, the full blade drawing can be produced with blade profiles in Figure 10.7 (b) for each board section, a to k, shown in Figure 10.7 (a). Or a solid modelling package can manipulate the data for CNC machining of coreboxes, blade dies, etc.

The maximum output of a Francis turbine is strongly dependent on the runner 'gaps'. These gaps are the minimum opening at the trailing edge. For a given turbine design, they would typically be defined as shown in Figure 10.8.

The gaps can be determined by measurement on an actual design, or on a solid model or graphically from a blading drawing such as Figures 10.7 (a) and (b).

Often the maximum output of a turbine can be increased for a given guide vane maximum setting by increasing the runner exit gaps. Disadvantages with

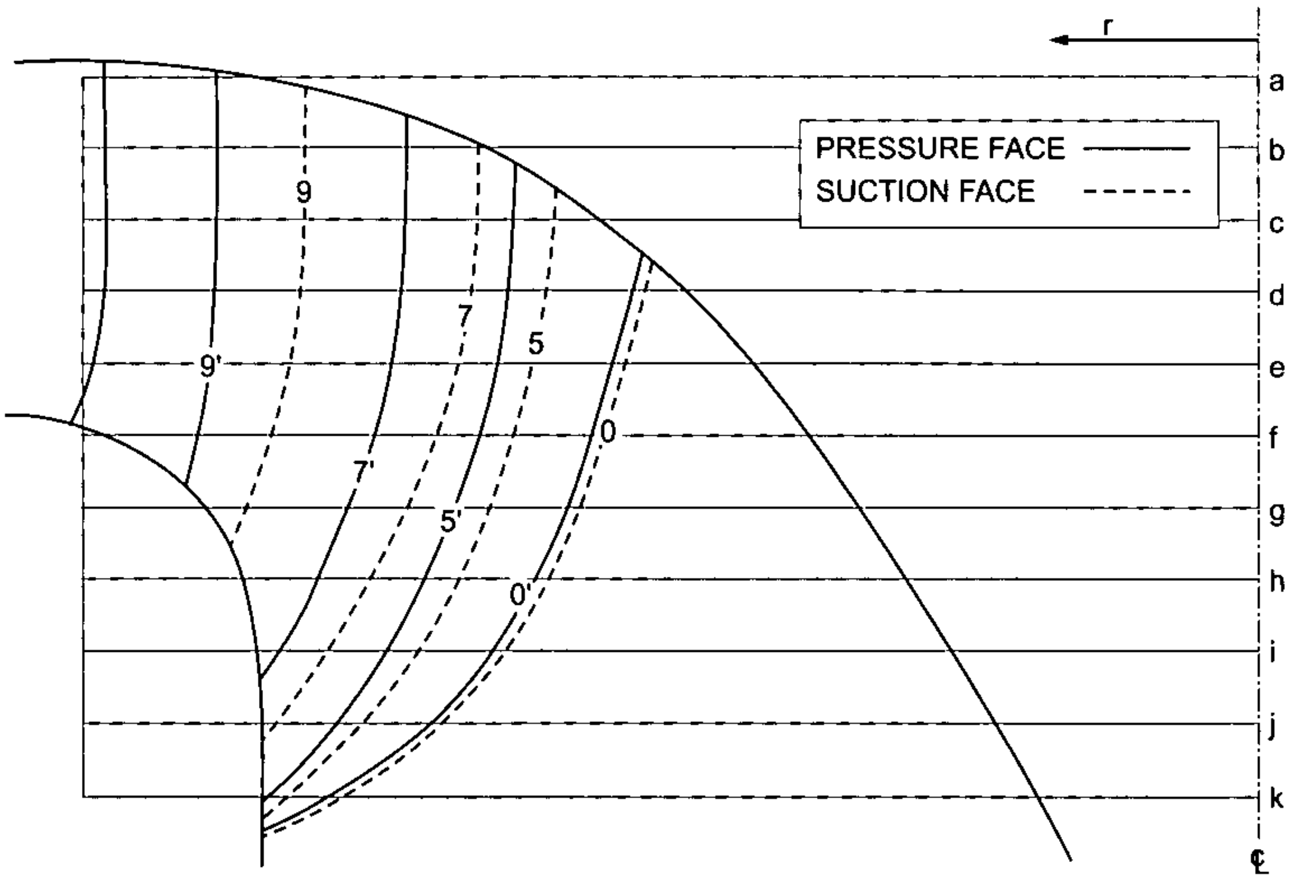
r
a
b
c
d
e
f
g
h
i
j
k
℄
PRESSURE FACE
SUCTION FACE
9
9'
7
7'
5
5'
0
0'

(a) Radial lines of intersection in meridional plane – Francis runner

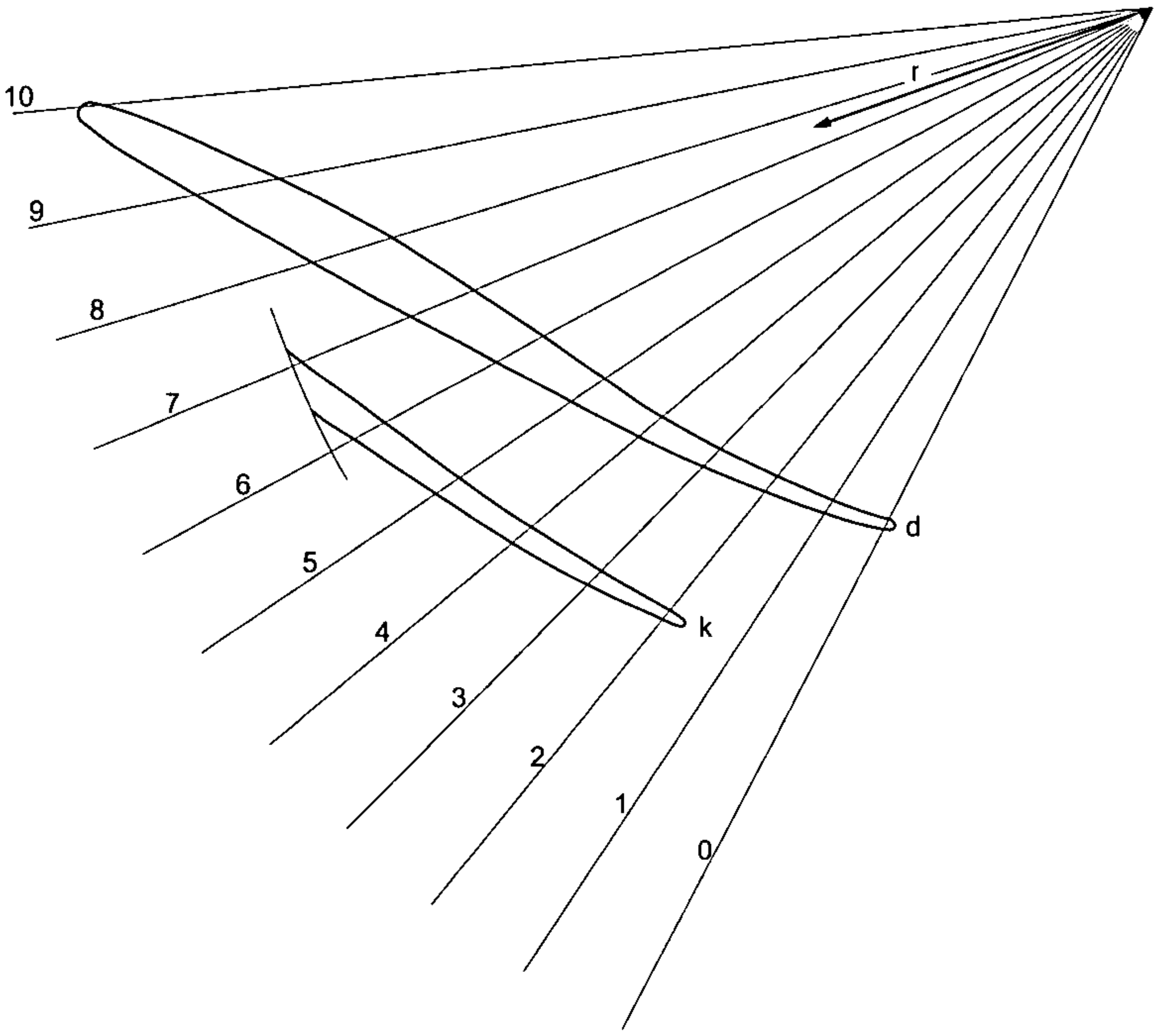
10
9
8
7
6
5
4
3
2
1
0
r
d
k

(b) Plan view of blade profiles for board sections a to k (only d and k shown)

Fig. 10.7. Blading drawing for Francis blade geometry definition.

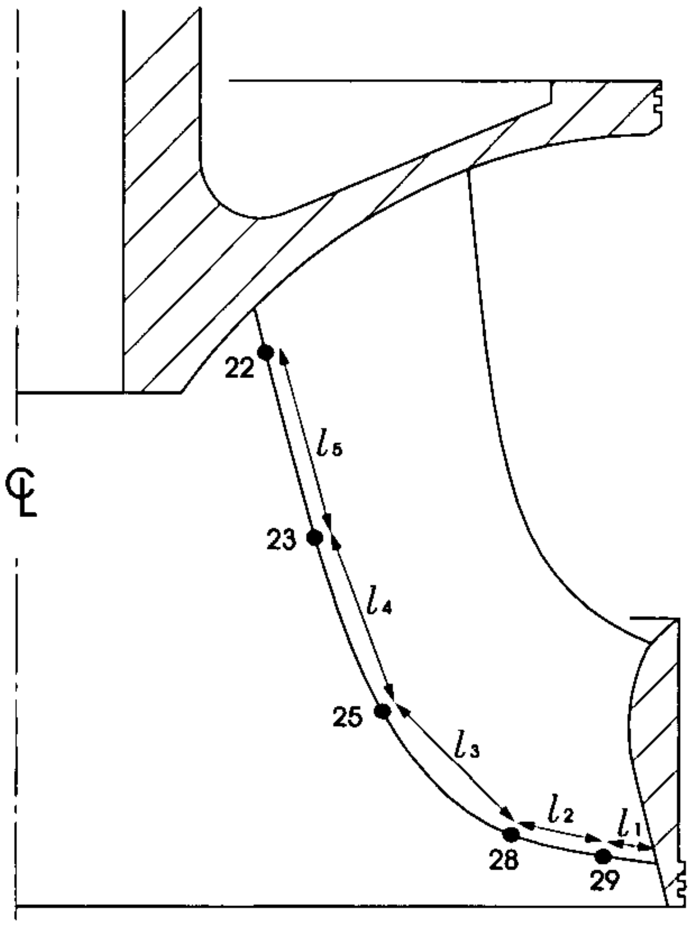

Fig. 10.8. Runner gaps. (position and size)

this might be a reduction in efficiency and an increased risk of cavitation damage.

It is usual to have an even number of guide vanes, perferably a multiple of 4, and a prime number of runner blades. Eg 12, 16 or 24 guide vanes, and 11, 13, 15, or 17 runner blades. The number of runner blades is not arbitary as there has to be sufficient to avoid separation of the flow on the pressure face.

In general, the excitation frequency is the smallest common multiple of the product of the runner blade number, the guide vane number and the runner rpm. See Liess [1987] for example.

Vortices that are shed from the trailing edges of Francis runners have been known to produce excitation forces which have caused blade cracking. Trailing edge treatments, [Heskestad and Olberts, 1960], and/or increased blade thickness in the trailing edge region, have been used to combat this problem.

10.3 Propeller blade design

The absence of strongly curved streamlines makes propeller turbine design 'simpler' than for Francis runners.

Essentially, the mean streamline method is applied for a given rV_θ versus blade distance distribution. Blade angles are adjusted for incidence and deviation and plotted on developed sections as shown in Figure 10.9. Blade thickness is predominantly determined by structural considerations.

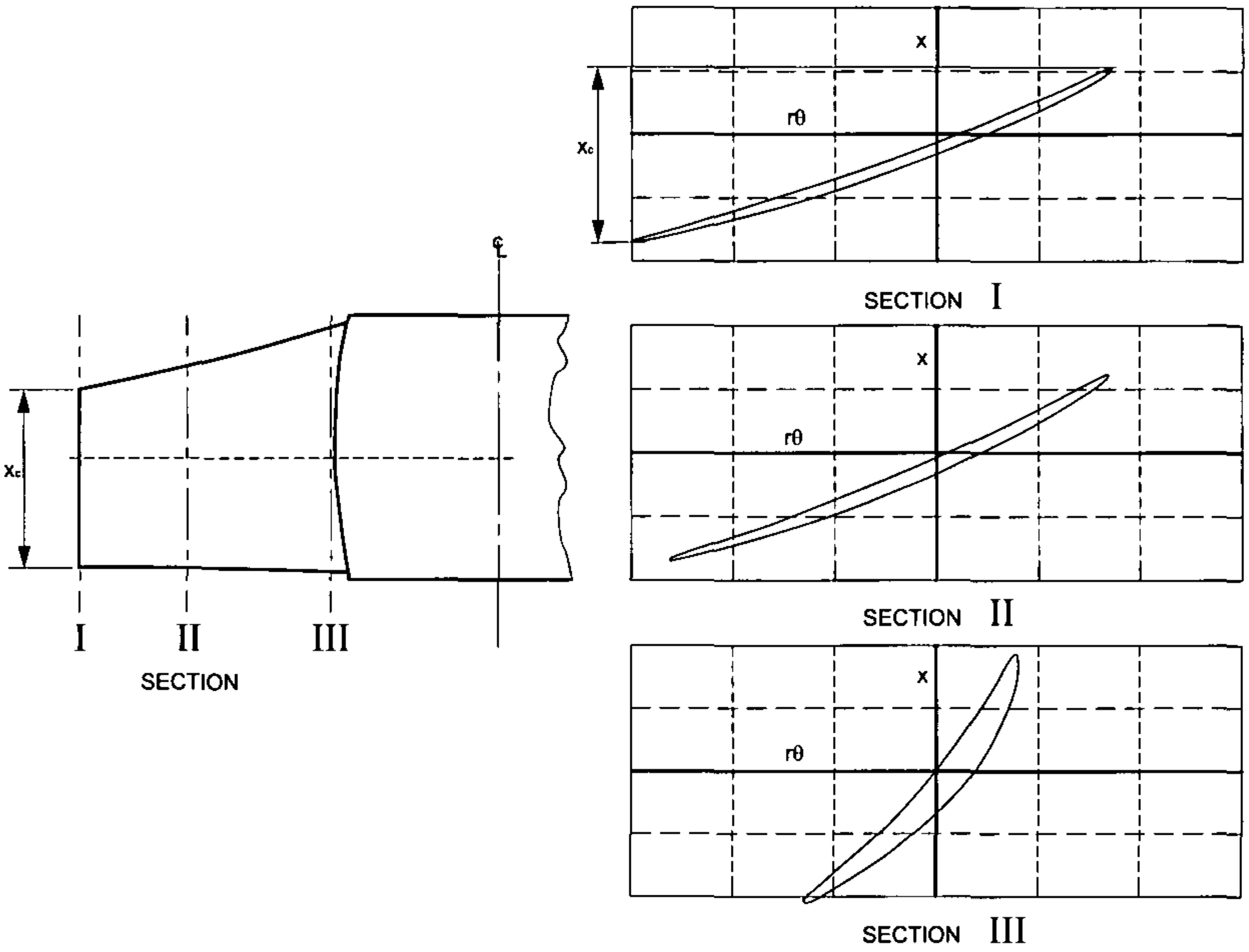

Fig. 10.9. Propeller turbine blading drawing.

Adopting specific blade profiles can be considered such as the profiles published by Numachi [1964]. Of greater import is unloading the trailing edge region as suggested in Chapter 3 by adopting non-circular camberline blades.

10.4 Guide vanes

The guide vanes control the discharge through the turbine, approximately in accordance with Equation 3.27. Modern turbines tend to use asymmetric profiles such as the example presented in Figure 10.10. Asymmetric profiles tend to have a greater throughput, for a given guide vane angle, than symmetrically profiled guide vanes.

The guide vane angle is taken as zero when the guide vanes are fully closed. Typical guide vane numbers would be between 22 and 24 for large water turbines. Smaller water turbines may use fewer guide vanes, e.g. 12. A

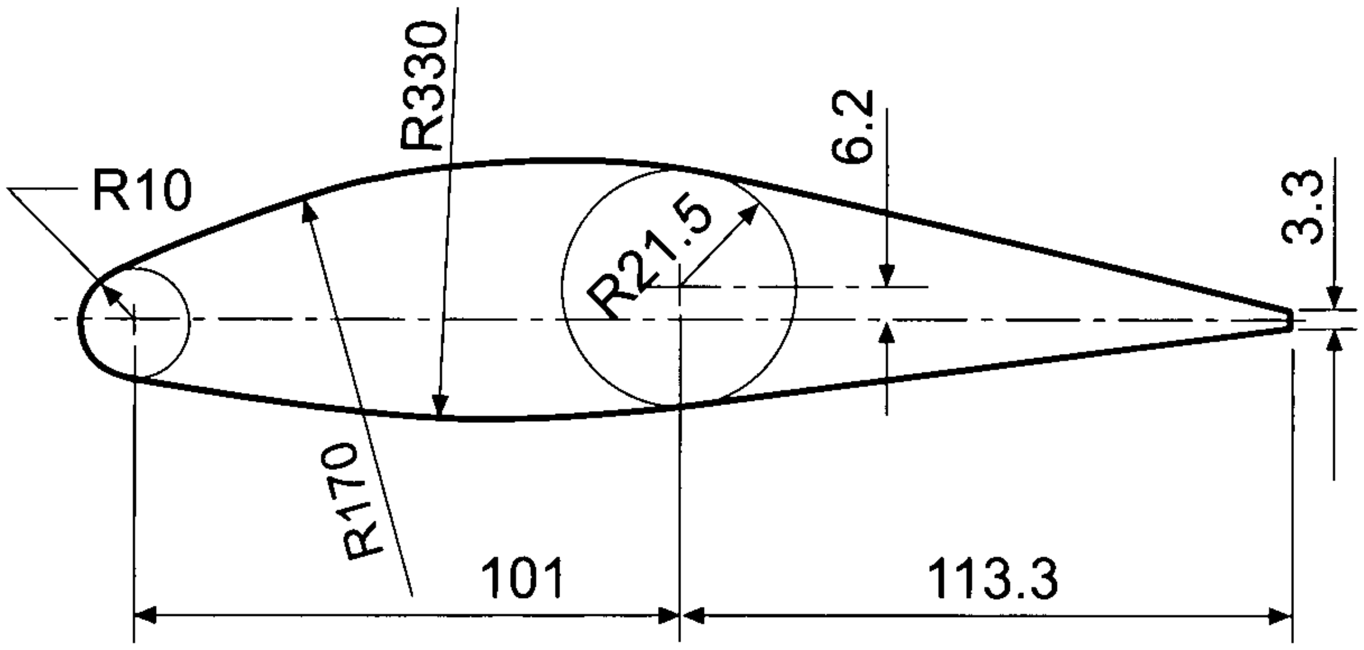

Fig. 10.10. Asymmetric guide vane profile.

consequence of reducing the guide vane number is that the entire turbine increases in diameter as the guide vanes have to be longer for a given guide vane pitch circle diameter in order to be able to close off the flow. The distributor ring thus has a larger radius. The guide vane pitch circle diameter is determined by the requirement that the guide vane does not contact the runner in the event that there is an actuating linkage failure (a possible alternative is to have failure proof mechanical stops).

It is necessary to calculate the torque to actuate the guide vanes for at least three positions; closed, for $0.6Q_{1/1}$ say, and for maximum discharge $Q_{1/1}$.

For the closed position, shown in Figure 10.11 (a), the pressures acting over the guide vane surface need to be summed. For Figure 10.11 (b), corresponding to a particular opening, the mean streamline method can be applied to obtain an approximate actuating torque.

Of importance is the need to ensure the flow is still accelerating through the guide vanes throughout their operating range.

During turbine operation, a guide vane linkage or other related failure may occur. In this instance it might be considered desirable to have a torque versus guide vane angle characteristic as shown in Figure 10.12. This characteristic excludes the possibility of the guide vanes slamming shut, causing a catastrophic pressure rise. The guide vanes going to the maximum opening position is also undesirable as maximum runaway speed may be attained.

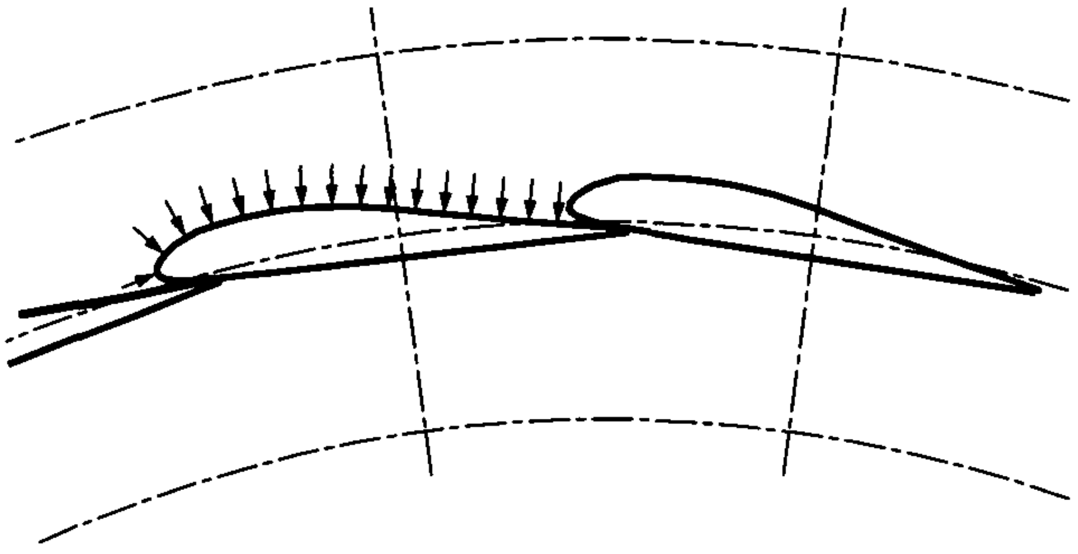

(a) Closed

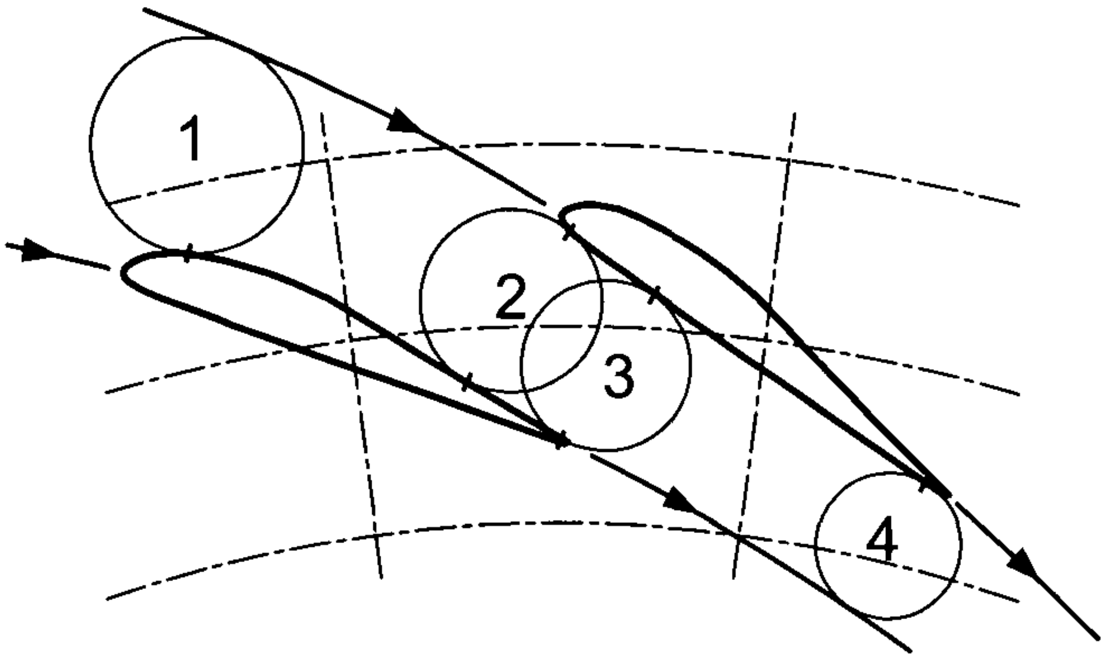

(b) $Q_\perp$

Fig. 10.11. Guide vane positions.

The guide vane profile presented in Figure 10.10 might provide a reasonable starting point for a guide vane design.

The relationship between guide vane angle and specific speed, at peak efficiency, is represented approximately by,

$$\frac{B_{gv}}{D_2^o} \tan \hat{\alpha}_{gv} = 2 \times 10^{-6} n_s^2 + 1 \times 10^{-4} n_s + 0.0107 \tag{10.11}$$

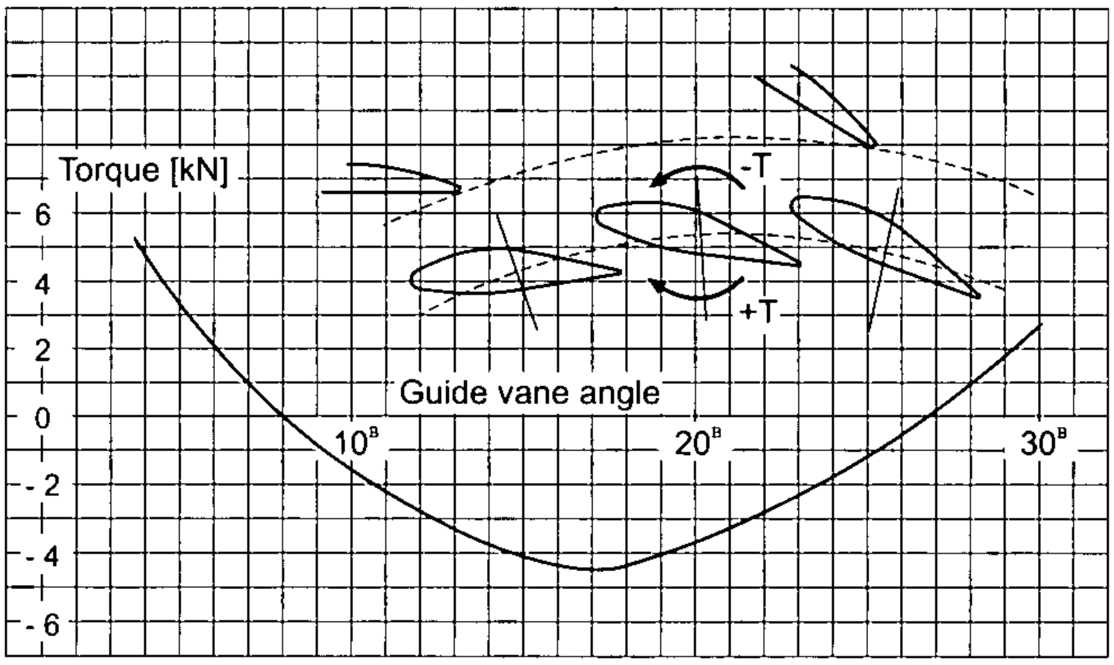

Fig. 10.12. Guide vane torque versus angle.

11 Spiral casing and stay vanes

The hydrodynamic function of the spiral casing is to introduce angular momentum (rV_θ) into the flow and to distribute the water uniformly around the stay vane assembly entrance (speed ring). The spiral casing, in theory, imparts the same angle to the flow, regardless of flowrate.

For potential flow, the 'correct' spiral casing design is obtained from the free vortex law, see Nechleba [1957] and Kovalev [1965] for example. However, due to boundary layer build up along the spiral casing wall, the free vortex design results in insufficient flow velocity through the lattermost sections, sometimes called the nose zone. Modern spiral casing design adopts a constant velocity design, with the spiral casing through flow area reducing approximately in proportion to spiral angle. This approach results in a larger spiral casing than would be the case if free vortex design rules were applied.

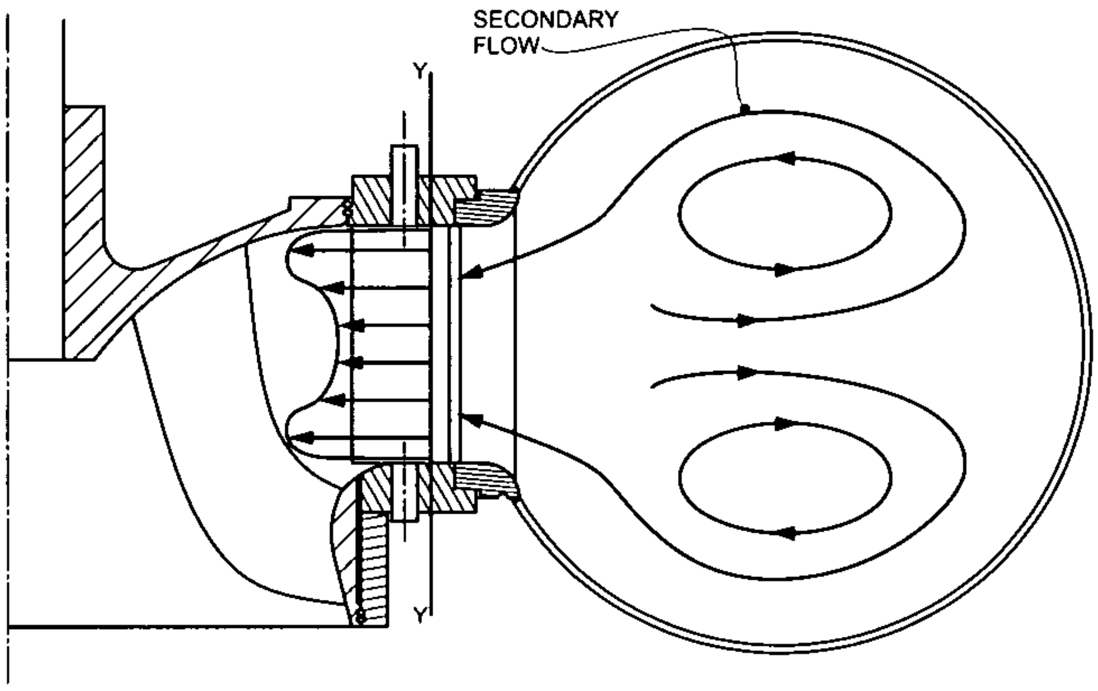

Fig. 11.1. Secondary flow in spiral casing and distributor.

The flow within the spiral casing develops secondary flow as illustrated in Figure 11.1. This secondary flow distorts the velocity profile entering the guidevanes. Attempts to model the flow using potential theory are likely to be inaccurate as the flow is highly three dimensional with these secondary flows and blockage effects playing a significant role. Modern, fully 3D, analyses of the flow through spiral casings have been performed [Ruprecht et al., 2000].

The number of truncated cone segments in a fabricated spiral casing tends to vary principally with turbine size. In large water turbines, material costs and handling issues result in a trend towards 18 to 24 segments. Small water turbines have a higher proportion of labour and machining costs. This results in designers using fewer segments, typically between 8 and 12.

The stay vane assembly serves two purposes; one structural and one hydrodynamic. Structurally, the assembly assists the spiral casing in resisting the pressure forces within it and carries the weight of the turbine when vertically mounted.

Hydrodynamically, the stay vanes should collect the flow from the spiral casing and feed it to the guide vane assembly at minimum loss. The designer can use the stay vanes to increase the rV_θ of the flow if required. To achieve minimum loss, the stay vanes should accelerate the flow, and have their inlet angles set to match the flow departing from the spiral casing.

Stay vane number either matches or is half the guide vane number. For example, 22 guide vanes and 11 stay vanes, or 12 guide vanes and 12 stay vanes.

11.1 Spiral casing design method

Spiral casing geometry is defined in Figures 11.2 and 11.3.

The throughflow area of the spiral, at a particular section, A_{sp}, is the area of the circle less the area of the segment. This is shown shaded in Figure 11.2 (b).

From geometry,

$$A_{sp} = \pi r^2 - r^2 \tan^{-1}\left[\frac{B_{sp}}{2e}\right] + \frac{B_{sp}e}{2} \tag{11.1}$$

where e, B_{sp} and r are defined in Figure 11.2. Note B_{sp}, the "springing point" height of the spiral casing, has to remain constant for each section around the spiral casing.

The design procedure is:

1. Establish the specific spiral casing entrance velocity KV_{sp}, where the empirical relationship,

   $$KV_{sp} = -2 \times 10^{-6} n_s^2 + 1.1 \times 10^{-3} n_s + 0.0465 \tag{11.2}$$

   applies for a turbine of specific speed n_s.
2. Determine D_{sp} and A_{sp} at the spiral inlet pipe from,

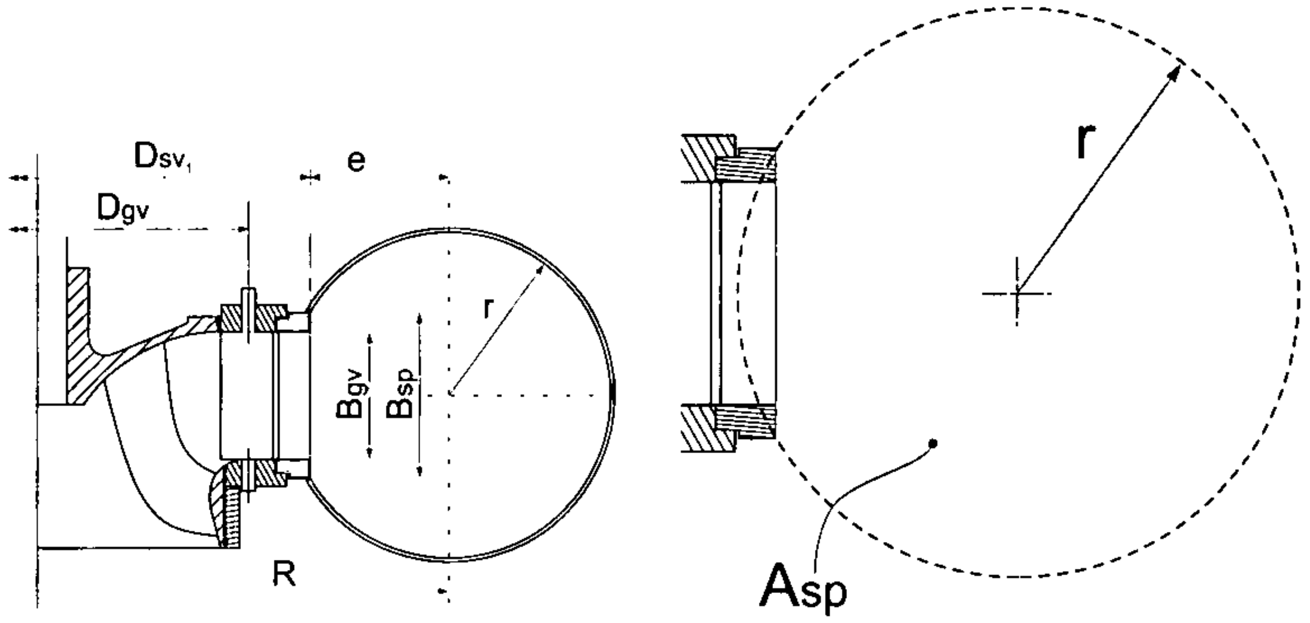
Dsv1
e
Dgv
r
Bgv
Bsp
R
r
Asp

(a) (b)

Fig. 11.2. Spiral casing cross-sectional geometry.

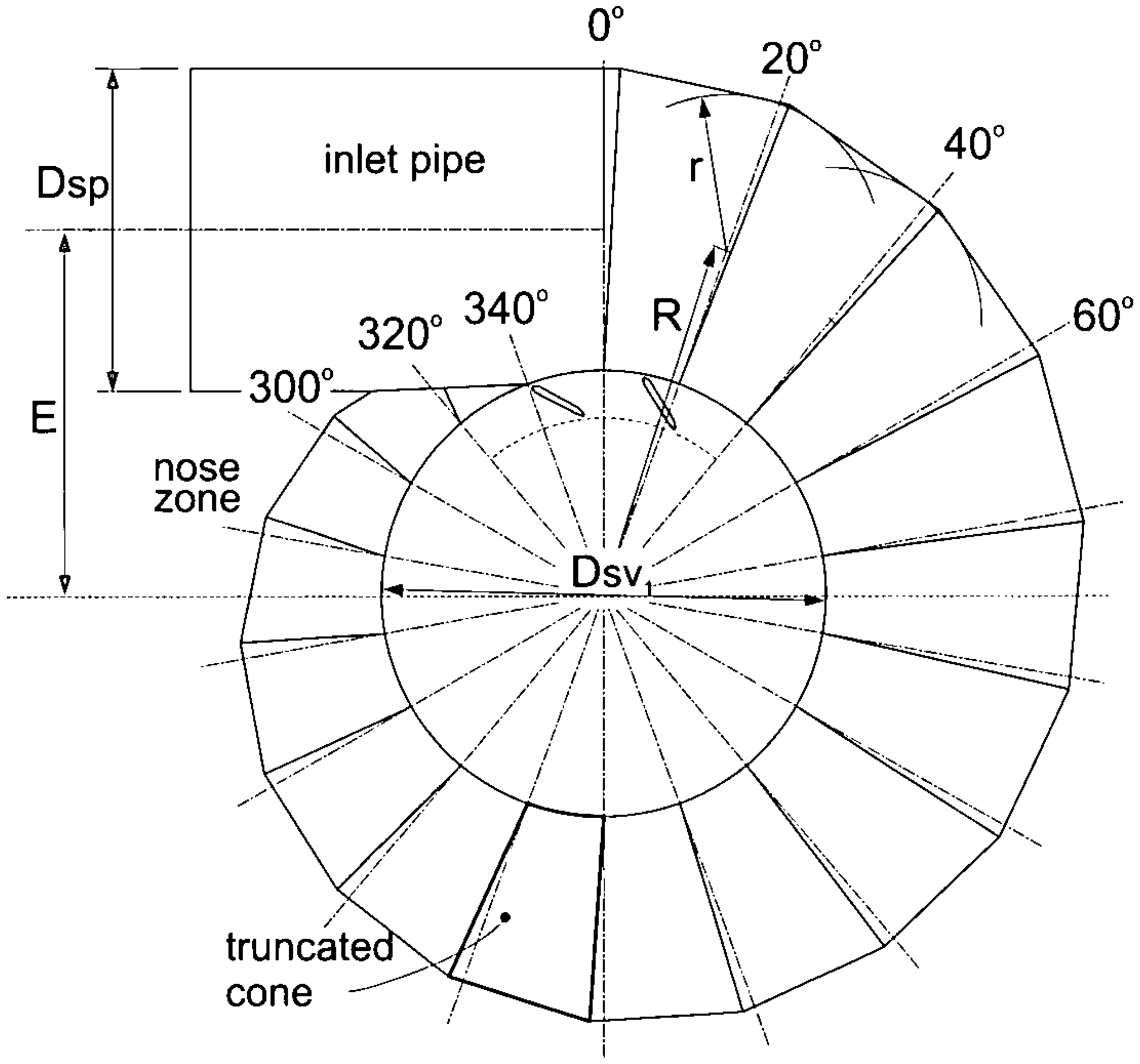
0°
20°
40°
60°
inlet pipe
Dsp
r
R
E
320°
340°
300°
nose zone
Dsv1
truncated cone

Fig. 11.3. Spiral casing plan view.

$$KV_{sp} = \frac{Q}{\pi \frac{D_{sp}^2}{4}} \frac{1}{\sqrt{2gH_n}} \tag{11.3}$$

with,

$$D_{sp} = \sqrt{\frac{4Q}{\pi KV_{sp}\sqrt{2gH_n}}}$$

and,

$$A_{sp} = \frac{\pi D_{sp}^2}{4}$$

3. Regarding Figure 11.3, let $A_{sp_{0^\circ}} \approx (0.96 \text{ to } 0.98)A_{sp}$
   The empirical formula

   $$\frac{A_{sp_\theta}}{A_{sp_{0^\circ}}} = -0.0028\theta + 1.005 \tag{11.4}$$

   provides a non-dimensional area variation based on the section angle, θ, around the spiral. This empirical relationship increases the area in the noze zone.
4. It is necessary to determine the spiral offset, E, and the springing point height, B_{sp}. With $R_{0^\circ} = E$, $e = e_{0^\circ} = R_{0^\circ} - D_{sv_1}$ and $r = r_{0^\circ} = \frac{D_{sp}}{2}$ B_{sp} is calculated from,

   $$B_{sp} = 2\sqrt{r^2 - e^2} \tag{11.5}$$

   Some small adjustments may be necesary to E and D_{sp} to get an acceptable value for B_{sp}. (an acceptable value being one which is close to B_{gv} plus the top and bottom cover thickness)
5. A spiral casing geometry table can now be constructed,

Section angle	Section area	R	r
0°			
20°			
40°			
60°			
etc			

Table 11.1. Spiral casing geometry table.

R and r in the spiral casing geometry table are obtained by iterating Equations 11.1 and 11.5, for each section area.

6. The spiral casing plan view can then be laid out as in Figure 11.3. The truncated cones are formed from connecting the outside radii, $r_{0°}$, $r_{20°}$, etc by lines tangential to their arcs. The noze zone requires some adjustment to blend in to the inlet pipe as shown.

11.2 Stay vane design guidelines

The method given below for determining stay vane inlet angle, in the absence of experimental data, is a tentative empirical method that has been tested against a couple of existing stay vane - spiral casing geometries.

$$\chi_{sv_i} = \tan^{-1}\left[\frac{0.2D_{sp}^2}{D_{sv_i}B_{gv}}\right] \tag{11.6}$$

Theoretical methods for determining stay vane inlet angle have not proved particularly sucessful. Only V_r is affected by boundary layer blockage. V_θ is affected by wall friction. Whilst the flow will attempt to obey the free vortex law, blockage and wall friction effects are significant, and Equation 11.6 may prove suitable. Baines and Japikse [1997] provides some additional material on volute design.

Kubota et al. [1984] provides a useful article on stay vane design issues.

12 Thrust loads, seals and bearings

12.1 Thrust load analysis

Water turbine runners experience a net thrust due to the hydrodynamic loading of the flow surfaces. The net thrust can be minimised by careful positioning of the labyrinth seals. See Figure 12.1 as an example; where principally D_{hc} and D_{bc} can be adjusted. Other examples can be found in Nechleba [1957] and Kovalev [1965].

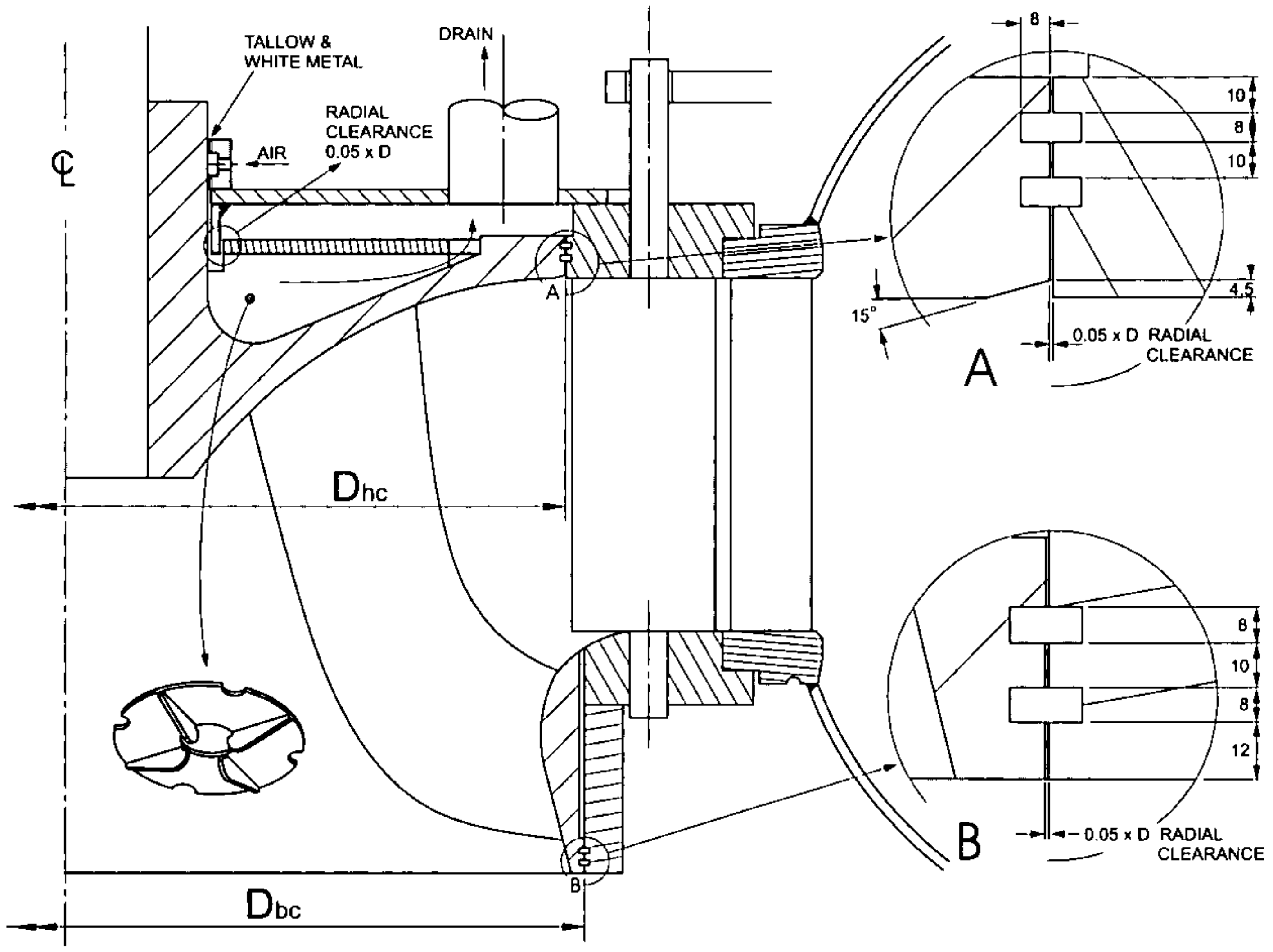
TALLOW & WHITE METAL
DRAIN
RADIAL CLEARANCE 0.05 x D
AIR
℄
A
Dhc
B
Dbc
8
10
8
10
4.5
15°
0.05 x D RADIAL CLEARANCE
A
8
10
8
12
0.05 x D RADIAL CLEARANCE
B

Fig. 12.1. Francis turbine non-contacting seal arrangement.

Figures 12.1 and 12.2 illustrate two methods of dealing with the leakage flows through the head cover labyrinth seal. Figure 12.1 shows a rotating baffle which reduces the pressure underneath the main shaft seal sufficiently to allow it to be a non-contacting seal. Figure 12.2 depicts a stationary baffle whose purpose is to prevent rotating flow above the runner. Rotating flows are to be avoided since a forced vortex velocity distribution imparts a higher thrust than would result from a non-rotating flow (or as is usually achieved a half vortex velocity distribution).

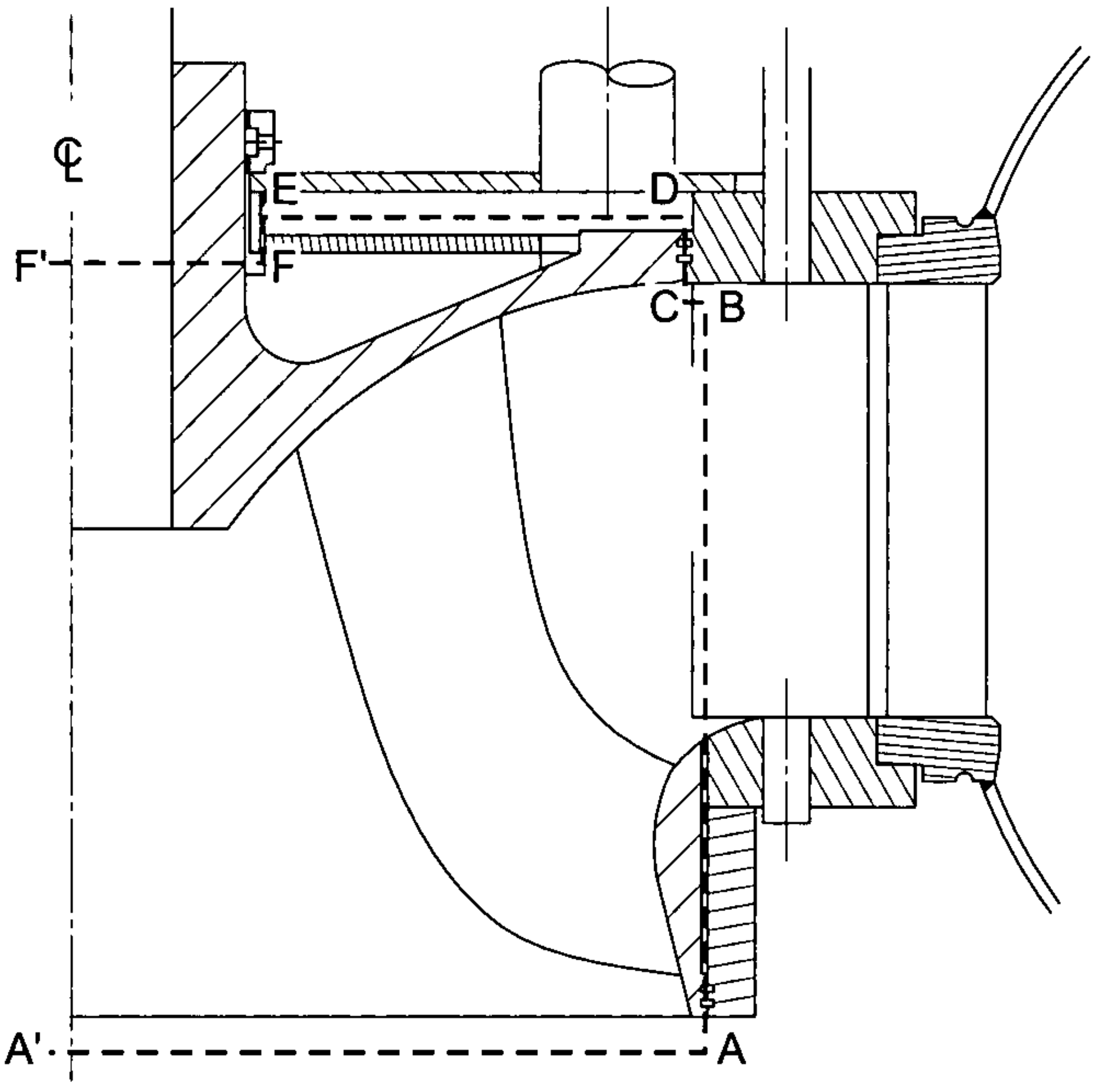

Fig. 12.2. Stationary drain arrangement.

A typical thrust curve might look like Figure 12.3. The solid thrust line represents the variation in thrust, for different guide vane settings (changes in discharge), at a constant unit speed n_{11}. Thrust needs to be checked for the operating head and for the runaway speed condition.

To determine the hydraulic thrust, it is necessary to consider a control volume. Examples of suitable control volumes are shown in Figures 12.2 and 12.4; only the control volume of Figure 12.2 is analyzed below.

For element BC, $H_{B_{\text{tot}}}$ is the total head at B. Assuming that the tangential velocities obey the free vortex law, $r_1 V_{\theta 1} = r_2 V_{\theta 2}$, then the force acting on the control surface BC is

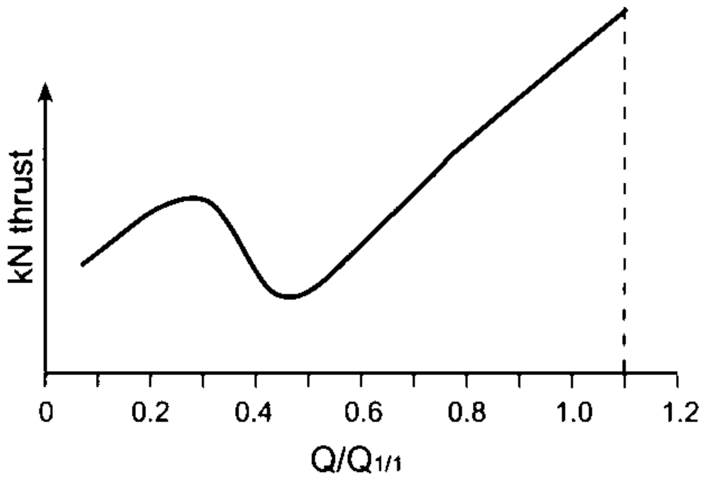

Fig. 12.3. Typical thrust curve for a Francis turbine.

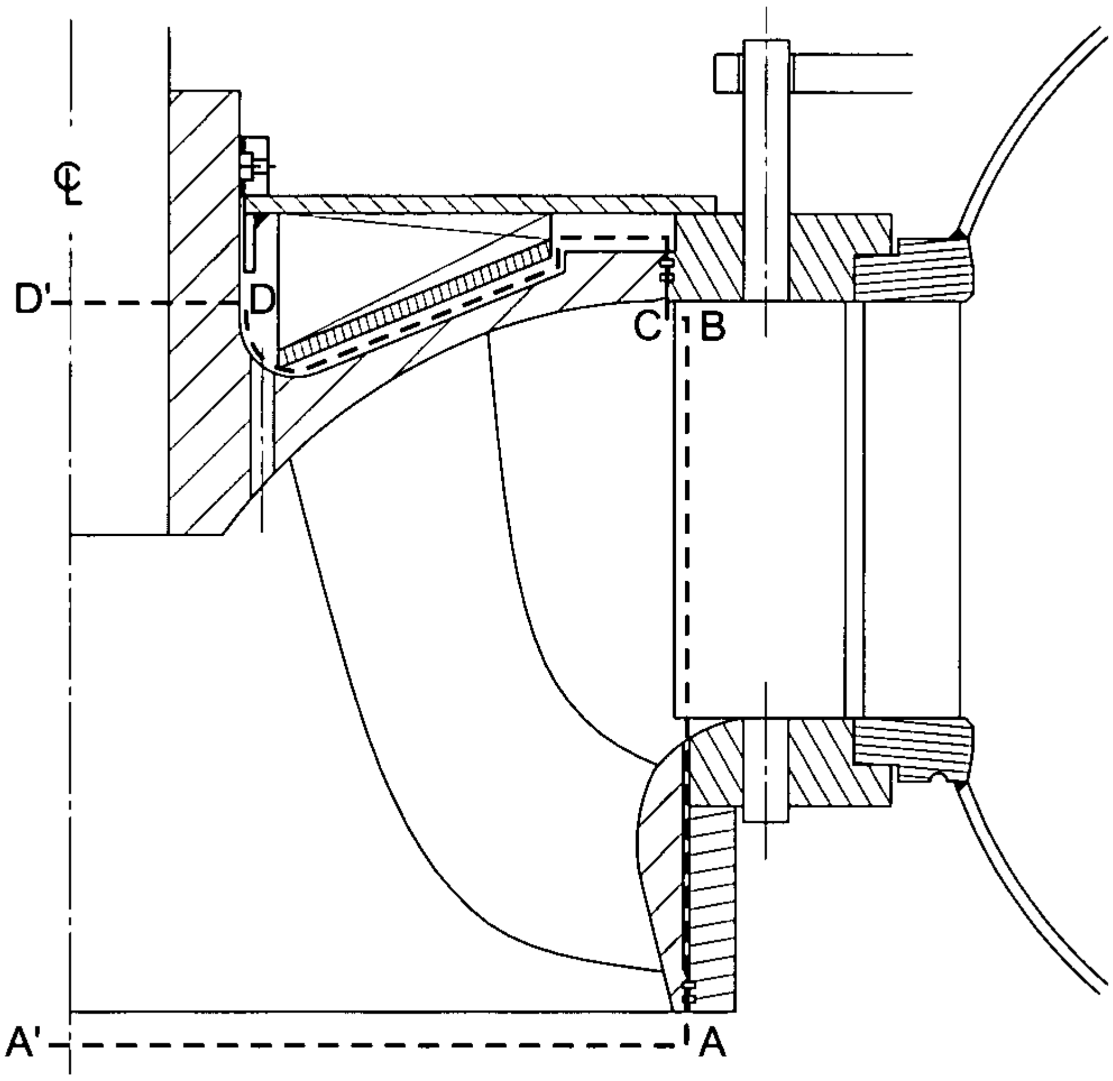

Fig. 12.4. Runner with drainage holes.

$$F_{BC} = \int_{r_C}^{r_B} \rho g \left(H_{B_{\text{tot}}} - \frac{V_m^2 + V_\theta^2}{2g} \right) 2\pi r \mathrm{d}r.$$

The length of BC depends on where the upper labyrinth seal is placed. Now

$$V_\theta = V_{\theta_{gv}} r_{gv}/r$$

and let

$$V_{m_{gv}} \approx V_m = constant$$

therefore

$$F_{BC} = \pi g \left[\left(H_{B_{\text{tot}}} - \frac{V_m^2}{2g} \right) \left(r_B^2 - r_C^2 \right) - \frac{(V_{\theta_{gv}} r_{gv})^2}{g} \ln \left(\frac{r_B}{r_C} \right) \right]. \tag{12.1}$$

Maximum thrust occurs at maximum discharge, an 'off design' condition. See Figure 12.3. At this condition there will be a V_θ component leaving the runner. One approach to determining the net force $F_{A'A}$ is to assume at the tip the mean pressure at the runner exit is given by

$$\bar{P}_{A'A} = P_{\text{atm}} - \rho g H_s - \tfrac{1}{2} \rho \eta_{dt} V_{m_2}^2.$$

Then

$$F_{A'A} = \pi r_A^2 \bar{P}_{A'A}. \tag{12.2}$$

Using an entrance loss factor of 0.5 and a combined entrance/exit loss factor of 1.1, the head drop across two labyrinth seals as shown in Figure 12.1 is

$$\begin{aligned} &0.5 \left(\frac{Q_s}{A_s} \right)^2 \frac{1}{2g} + \left[\left(\frac{Q_s}{A_s} \right)^2 - \left(\frac{Q_s}{A_L} \right)^2 \right] \frac{1}{2g} + 0.5 \left(\frac{Q_s}{A_s} \right)^2 \frac{1}{2g} \\ &+ \left[\left(\frac{Q_s}{A_s} \right)^2 - \left(\frac{Q_s}{A_L} \right)^2 \right] \frac{1}{2g} + 1.1 \left(\frac{Q_s}{A_s} \right)^2 \frac{1}{2g}, \end{aligned} \tag{12.3}$$

where Q_s is the leakage flow, A_s is the annulus area and A_L the labyrinth annulus area. Note that labyrinth seals work better if expansion chambers lie on both sides of the gap. A number of other approaches exist in the literature.

In the case of Figure 12.4, the stationary baffles reduce the forced vortex to a 'half vortex'.

$$H_D - H = \int_r^{r_D} \frac{(\frac{1}{2}\omega r)^2}{g} \frac{\mathrm{d}r}{r} = \frac{\omega^2}{8g} (r_D^2 - r^2) \tag{12.4}$$

$$\text{Therefore } F_{DE} = \int_{r_E}^{r_D} 2g\pi r \left(H_D - \frac{\omega^2}{8g} (r_D^2 - r^2) \right) \mathrm{d}r \tag{12.5}$$

$$= \pi g \left[\left(H_D - \frac{\omega^2 r_D^2}{8g} \right) (r_D^2 - r_E^2) + \frac{\omega}{16g} (r_D^4 - r_E^4) \right]. \tag{12.6}$$

In Figure 12.2, assuming a full vortex is the conservative choice and a similar analysis to Equation 12.4 through 12.6 is applied

Head loss through the drainage holes in Figure 12.2 can be calculated from the loss coefficient versus hole geometry plot of Figure 12.5. This Figure permits the head loss to be calculated based on the hole length to diameter ratio, L/D, and the ratio of peripheral hole velocity to the actual leakage flow velocity u/V_h. This plot applies to both bell-mouth and sharp edged entry drainage holes.

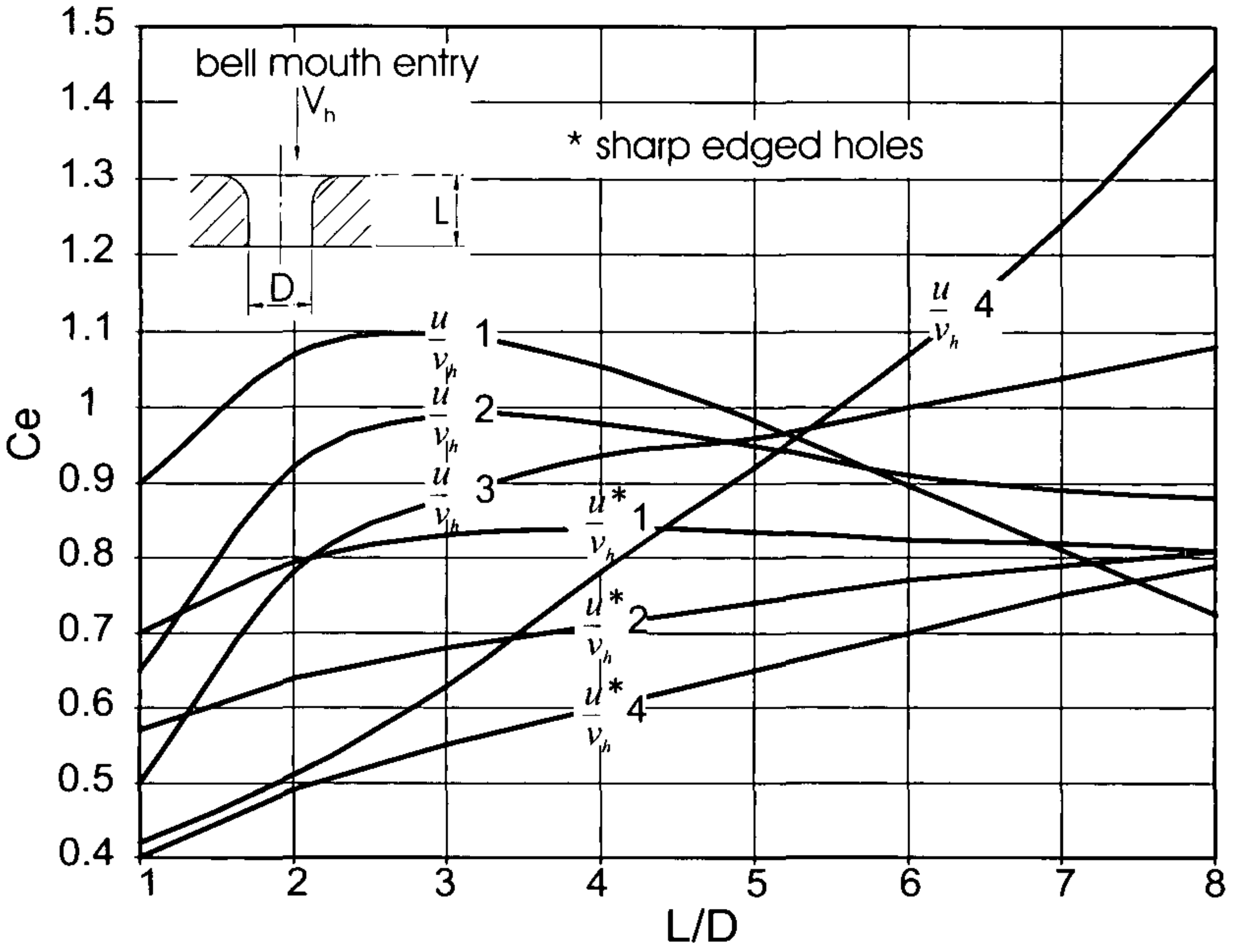

Fig. 12.5. Head loss through rotating holes.

The head loss through drainage holes is calculated using

$$h_L = \left(\frac{V_h}{C_E}\right)^2 \frac{1}{2g} \qquad (12.7)$$

with the loss factor C_E being obtained from Figure 12.5.

For engineering purposes, it is reasonable to assume the leakage flow is around 0.5% of $Q_{1/1}$. This enables equations 12.1, 12.3, 12.6 and 12.7 to be used to determine the hydraulic thrust on the runner.

12.2 Shaft seals

Figure 12.1 shows a non-contacting shaft seal arrangement. The combination of white metal and tallow allows a rubbing fit to be manufactured. Operation of the machine wears the seal surfaces so that they become non-contacting. As the pressure on the turbine side of the seal is below atmospheric, air will be drawn in.

Other common seal types are mechanical seals of synthetic or carbon material and gland packing type seals. To attain a long service life, these types of seals require filtered water to be supplied to the seal, typically around 4 litre/min per 100 mm of shaft diameter.

12.3 Main bearings

Turbines of low specific speed – with outputs of up to 6 MW – to high specific speed turbines – with outputs up to 3 MW – are likely to be mounted horizontally. Standard generators designs are usually available for these power ranges. Mounting the runner on the generator shaft is an economical arrangement for a horizontal turbine. The generator should either be supplied with rolling element bearings or mounted on white metal pedestal bearings. In the latter case, the bearing between the turbine and the generator should be capable of carrying both thrust and radial loads. See the example in Figure 12.6. The tail bearing needs to carry radial loads only.

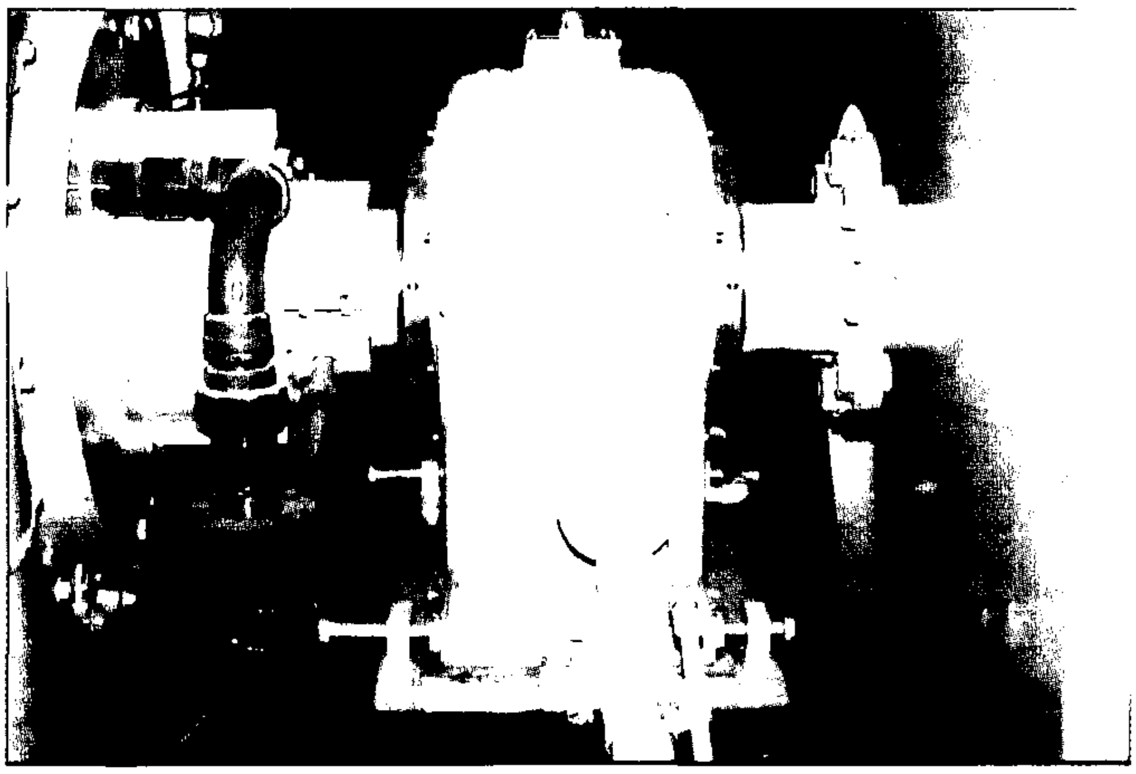

Fig. 12.6. Main thrust bearing example.

It is more reliable to use self-lubricating pedestal bearings such as the Mitchell HD bearing. External AC powered (with DC backup) lubrication systems have been known to fail.

If rolling element bearings are to be used, they should be designed for a life of at least 100,000 hours. Only commonly available stock items should be specified. As well as reducing the initial cost, this will increase the chance that replacement bearings will be available in 10–20 years time. Battery powered grease packs, such as SKF's LGP2 brand, can be used to maintain the bearing's grease charge.

Tubular type turbines operate with one bearing inside a water environment. They can be sealed mechanically and either rolling element or lubricated plain bearings can be considered. The employment of rubber marine cutlass bearings is an option that might suit smaller tubular propeller turbines. These bearings are water lubricated and relatively simple to install and operate. Silvertown, UK, is one supplier.

13 Manufacturing methods and materials

13.1 Manufacturing methods

13.1.1 Spiral casing

Spiral casings can be cast or fabricated, the latter technique being more common. The spiral casing is a pressure vessel, and should conform to the appropriate pressure vessel standards for structural design and welding. Figure 13.1(a) shows a partially complete spiral casing and stay ring assembly while Figure 13.1(b) shows a fully welded spiral casing and mounting legs.

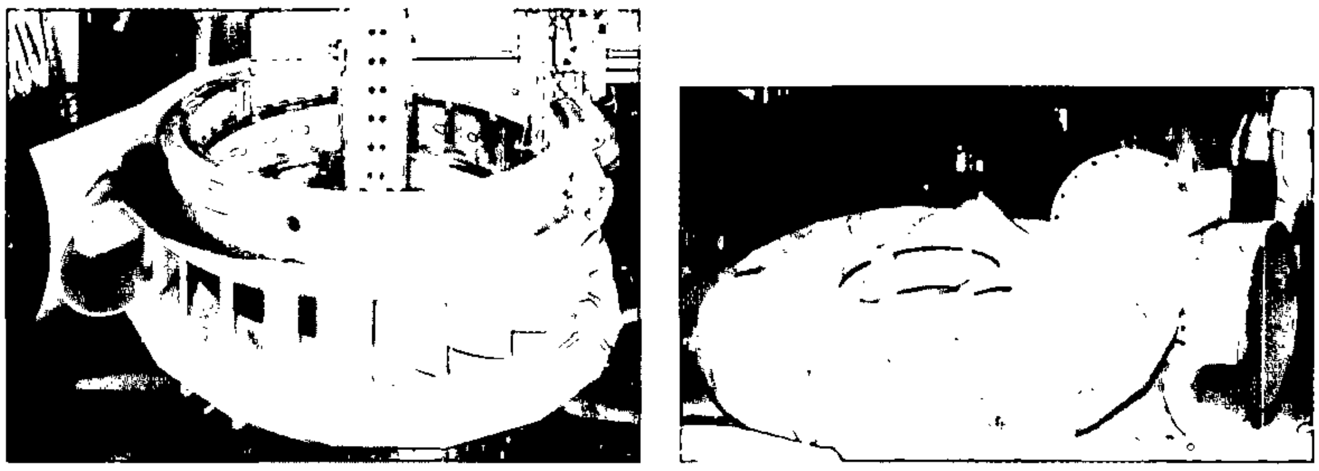

(a) Partially completed spiral casing and stay vane assembly (Reproduced courtesy VA TECH HYDRO)

(b) Completed spiral casing

Fig. 13.1. Welded spiral casing examples.

The spiral casing segments are developed from truncated cones. The larger diameter segments may require plate of thicker section than the smaller segments.

13.1.2 Runner

Runners can be of cast or cast and fabricated construction. See Figure 13.2.

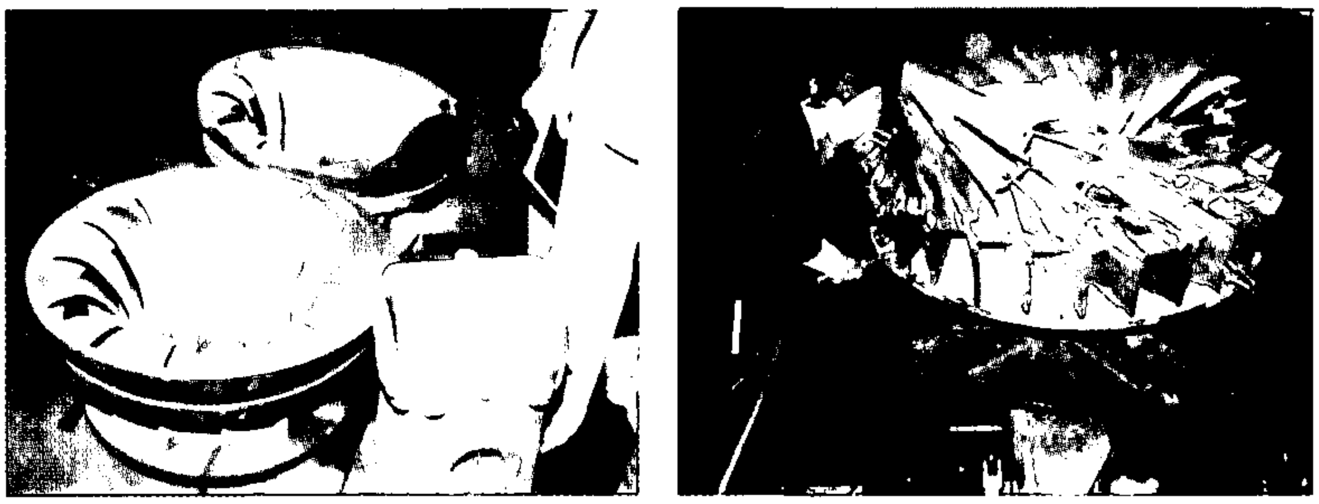

(a) Cast runners

(b) Cast crown, fabricated blades (Reproduced courtesy GE HYDRO)

Fig. 13.2. Runner construction examples.

The construction technique for an all cast runner using a manual pattern making process requires a runner blade drawing with accurately drawn horizontal runner blade profiles (board sections). Using these profiles, the pattern maker builds the runner pattern up by cutting and then stacking wooden boards. This board stack is then carefully shaped and smoothed by removing excess material. Figure 10.7 provides an example of a runner blade drawing along with two of the board sections required by a pattern maker.

Two types of pattern can be made. One type of pattern makes a core box that is used to make a sand core. The sand cores form radial segments which are fitted together to make a complete runner. The other type of pattern can be used to make a male and female die to press the runner blades. In this case, the blade plate material would be cut to the correct shape, and machined to remove excess material. The blade 'blanks' are heated and pressed between the dies. The blades are then welded onto a cast crown. See Figure 13.2 (b).

It is appropriate here to mention a modern manufacturing technique which lends itself well to the complex blade geometry of Francis and propeller turbine runners. Computer programs for solid and surface modelling are commercially available at cost effective prices. Using these programs, digital models of the turbine components, such as those illustrated in Figure 13.3, can be constructed. From these models tool path code for blade, core box or die tooling can be produced. This code can then be used to control CNC machinery, or in the case of softer materials such as wood, 5 axis robots.

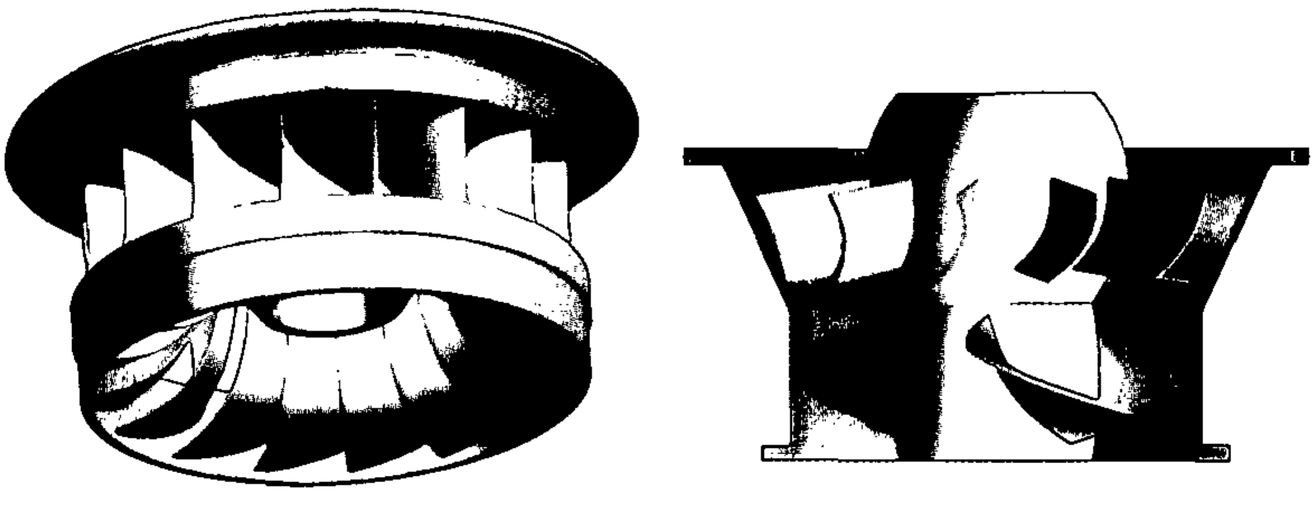

(a) Solid model of Francis runner

(b) Solid model of tubular propeller turbine

Fig. 13.3. Solid modelling of turbine components.

One way to generate the solid model geometry is to import the camberline geometry, or blade surface geometry, produced by the method outlined in Chapter 10, into a modelling package such as Rhino or SolidWorks. This geometry is provided in the form of x, y, z coordinate data; once imported it can be used to produce a digital computer model.

For propeller turbines, an alternative relatively straightforward method is to produce flat templates of both the suction and pressure faces as per Figure 13.4. It may be necessary to rotate the runner blade development drawing, e.g. Figure 14.3 to achieve a better definition of the blade surface on the template. The hub section in particular may lose definition if the datum surface for the pattern development is perpendicular to the axis.

13.1.3 Guide vanes

Guide vanes can be cast or forged. If cast of low modulus material such as aluminium bronze, there may be structural deflection problems in high specific speed turbines.

13.1.4 Other issues

Figure 13.5 illustrates some additional construction techniques.

Typically, the spiral casing is attached to the stay ring assembly using one of two methods. The first of these methods, method A, is slightly more efficient but prone to lamellar tearing in the cover plate. Note the stress concentration relieving groove used in method B.

The distributor ring comprises the guide vanes, the head cover and the bottom cover. Excessive leakage past the guide vanes, due to wear between

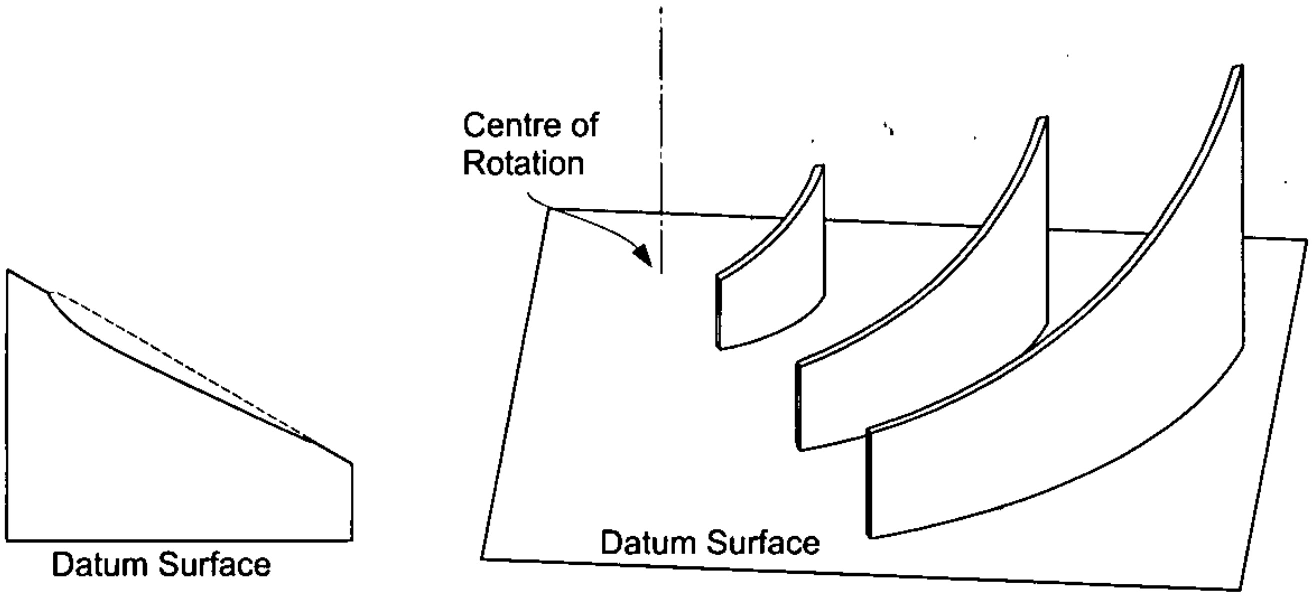
Centre of Rotation
Datum Surface
Datum Surface

Fig. 13.4. Propeller turbine blading details.

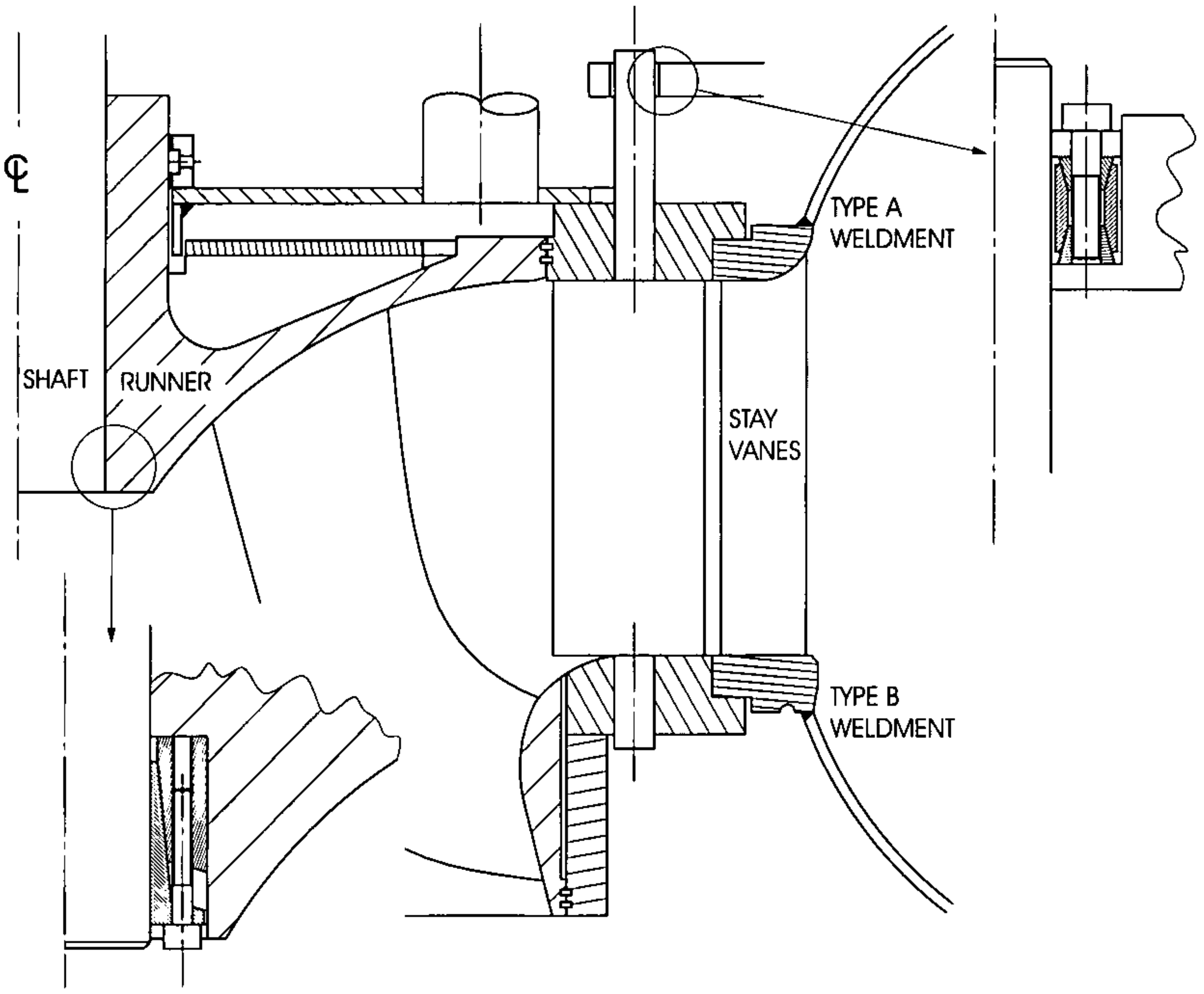
℄
SHAFT
RUNNER
STAY VANES
TYPE A WELDMENT
TYPE B WELDMENT

Fig. 13.5. Design and construction issues with a Francis turbine.

the guide vane ends and the head and bottom covers creates significant hydraulic loss and may prevent the runner from shutting down. If there is a main inlet valve, equalising the pressures on both sides of the valve is necessary to reduce actuation forces. This is usually done with a pipe that feeds water from the upstream side of the main inlet valve to its downstream side. Excessive leakage past the guide vanes may prevent actuation of the main inlet valve as the pipe across it may be insufficiently sized to deal with the leakage flows. The arrangement of the head and bottom covers in Figure 13.4 permits both the guide vane wear surface of these covers and the associated location flanges to be re-machined to re-establish design clearances. Typical small turbine guide vane bearings might be dry lubricated bearings such as DU, Fibreglide or X lube to name a few. Dry lubrication is probably a more reliable method as water lubrication bearings are prone to possible silting and abrasive wear. Grease lubrication is a common alternative but the lubrication system should be designed to force grease into the loaded section of the bearing. Note also in the Figure that the guide vane spindles are actuated via a friction coupling, such as a Ringfeder product. This method is becoming more popular as debris trapped between two guide vanes can be accommodated with the remaining guide vanes closing and only one guide vane partially closing. Another nice operational feature is to have positioning stops for the guide vanes at full opening. These stops can be used to reset a misplaced guide vane with minimal machine outage.

Runner-shaft location methods can include the traditional key and keyway, or a friction method such as shown in Figure 13.4. Larger runners are mounted using flanges. A novel approach adopted by one manufacturer, GE Hydro, is to use a tapered sleeve, along similar principles to the friction methods illustrated in Figure 13.4. GE Hydro's method applies to intermediate sized turbines (small megawatt sizes) and uses oil pressure to assemble and disassemble the joint. It has proved popular with plant operators.

13.2 Materials

To keep costs down in small locally produced turbines, locally available materials such as mild steel, cast steel and some of the more castable (but weaker) bronzes are more likely to be preferred. This Section presents some of the more common materials used in the larger MW+ hydro schemes. Some of these materials may not be appropriate for the reasons mentioned earlier but are recorded here as a guide to best practice.

Material presented in this Section has drawn heavily from a report published by Rodrigue [1986].

13.2.1 Carbon steel plate

Standard: ASTM A285 – Grade B; ASTM A516 – Grades 60, 65, 70, 75; ASTM A283; and ASTM A36

Materials meeting the ASTM A285 standard are suitable for fusion welded pressure vessels. Grade B has an ultimate tensile strength (UTS) in the range 345 to 485 MPa. ASTM 516 is a slightly higher spec material over A 285 where improved notch toughness is required.

The cavitation resistance is typical of carbon steel.

Typical component material specifications might be: A285 spiral casing, head cover; A516 stay vanes assembly; A283 or A36 draft tube liner.

13.2.2 Carbon steel castings

Standard: ASTM A27 – Grade 65–35 or 70–40; and ASTM A216 – Grade WCC.

These materials are used for turbine runners and guide vanes. Steel castings have been used on components such as stay vanes assembly, though these turbine parts would typically be of fabricated construction. ASTM A216 castings are of slightly higher strength (usually used for high temperature pressure vessel applications) than the more commonly used ASTM A27 material.

Grade 65-35 refers to the PSI UTS and yield point values respectively. (450 MPa min and 240 MPa).

13.2.3 Stainless steel plate

Standard: ASTM A167; ASTM A240 – Type 304 and 304L

This material is used on all turbine components of stainless steel plate construction. The material is an 18–8 austenitic stainless steel, easily weldable and similar in strength to low strength carbon steel. The 'L' suffix indicates it has low carbon content. The low carbon content allows the stainless steel to be welded without damaging the corrosion resistance of the heat–affected zone. Any grade of austenitic stainless steel rod or wire consumable can be used for welding. (Preferred grade 308L).

13.2.4 Stainless steel castings (martensitic)

Standard: ASTM A487 – Grade CA–6NM; and ASTM A743 – Grade CA–6NM.

CA–6NM castings are used for turbine runners and guide vanes. The material is a 13–4 chromium nickel martensitic stainless steel developed in the early 1960s as an alternative to CA–15 stainless steel (12% chromium only). The CA–6NM is easier to cast and has better weldability over CA-15 stainless steel. When welding CA–6NM, relatively high pre–heat and post–weld heat treatment is required to prevent cracking if martensitic weld material is used. Field repairs with austenitic weld material are feasible with minimal preheat and no post-weld heat treatment. The deposited material does not have the same strength as the CA–6NM base with cracks restarting a common experience. See Gysel [1968] for a description of the weld procedures. This material is of relatively high strength, and has a cavitation resistance comparable with 304 stainless plate. Because of the relatively low chromium and nickel content, the material is subject to pitting in salt water or a similarly corrosive environment.

17–4 and 16–5 precipitation hardening stainless steels (3% Cu) are finding wider use. The 17–4, whilst more expensive, is easier to machine than the CA–6NM material and the final heat treatment can be at a much lower temperature. 16–5 is also better in saltwater environments over CA–6NM.

13.2.5 Stainless steel castings (austenitic)

Standard: ASTM A487; and ASTM A743 – Grade CF–3, CF–3M, CF–8, CF–8M.

This material is an 18-8 austenitic stainless steel and is also used for runners and guide vanes. Castings from this material are easily field welded and are more corrosion-resistant than the CA–6NM stainless steel. However, the austenitic material is lower in strength than CA–6NM and 16–5 martensitic stainless steel and is more costly because of the higher chromium and nickel content.

13.2.6 Stainless steel overlay

Stainless steel welded overlay using 308L or 309L austenitic stainless weld material is common on cavitation-prone areas of carbon steel turbine components. Overlaying is a technique which is typically used on large castings/fabrications where material costs are a higher proportion on the total turbine price and composite materials offer the best price performance. The overlay is usually 3 mm to 5 mm in thickness and has cavitation resistance equal to or better than stainless steel castings and plate. 309L is often used in deeply pitted areas as a first pass over the carbon steel to reduce the possibility of weld cracking. More resistant (and expensive) cavitation filler electrodes are Cavitec, Stoody HQ–914 or the duplex alloy Ferralium 255.

13.2.7 Aluminum bronze castings

Standard: ASTM B148 – Grade C95500 or BS 1400 – AB2.

This material may be used as an alternative to cast stainless steel and has comparable cavitation resistance (though its abrasion resistance is not quite so good). Material composition is 78% Cu, 10% Al, and around 4% Fe and Ni. Aluminum bronze is lower in strength than the stainless steels (640 MPa UTS and 220 MPa yield). Large castings are also higher in cost than CA-6NM castings. Out-of-position welding is difficult, causing problems for in-situ repair work. Aluminum bronze might typically be used for smaller runners, under 1 m in diameter and commonly, for pump impellers. For salt-water application, aluminum bronze offers increased corrosion resistance over CA–6NM stainless steel.

14 Propeller design example

The philosophy behind this Chapter is to design an efficient propeller turbine, using the hydrodynamic tools provided in the earlier chapters of this design guide.

This Chapter demonstrates the design of a small (10 kW electrical power output) propeller turbine intended for use on an 8.5 m net head with a direct drive speed of 1500 rpm.

Sites with 8 to 10 m head and 200 l/s of flow are common. 10 kW is a useful amount of electrical power, either to power a single house or to provide lighting for a collection of houses. A rotational speed of approximately 1500 rpm allows direct drive to economically priced induction motors/alternators. Figure 14.1 illustrates a possible scheme arrangement.

The power output required is 10 kW, and allowance must be made for the electrical losses in the generator and frictional losses in the seals and bearings. Assume losses of 20% for the generator and 5% for friction giving a design mechanical output from the turbine of 13.2 kW (10 kW/0.8/0.95) at a speed of 1540 rpm (1540 rpm allows the use of a cheaper induction generator) and a net head of 8.5 m.

Using Equation 3.3 to calculate the specific speed,

$$n_s = 386.$$

Equation 3.14 allows the flowrate to be determined for a given turbine efficiency, say 0.85.

$$P = \eta \rho g Q H_n,$$

$$\text{Therefore, } Q = \frac{13200}{0.85 \times 1000 \times 9.80 \times 8.5} = 0.1864 \mathrm{m}^3\mathrm{s}^{-1}.$$

Figure 1.4 and Table 3.1 indicate a propeller turbine can be used in this application.

A propeller performance characteristic is given in Figure 6.4. From this diagram select a unit speed, n_{11} of 125. Applying Equation 3.7,

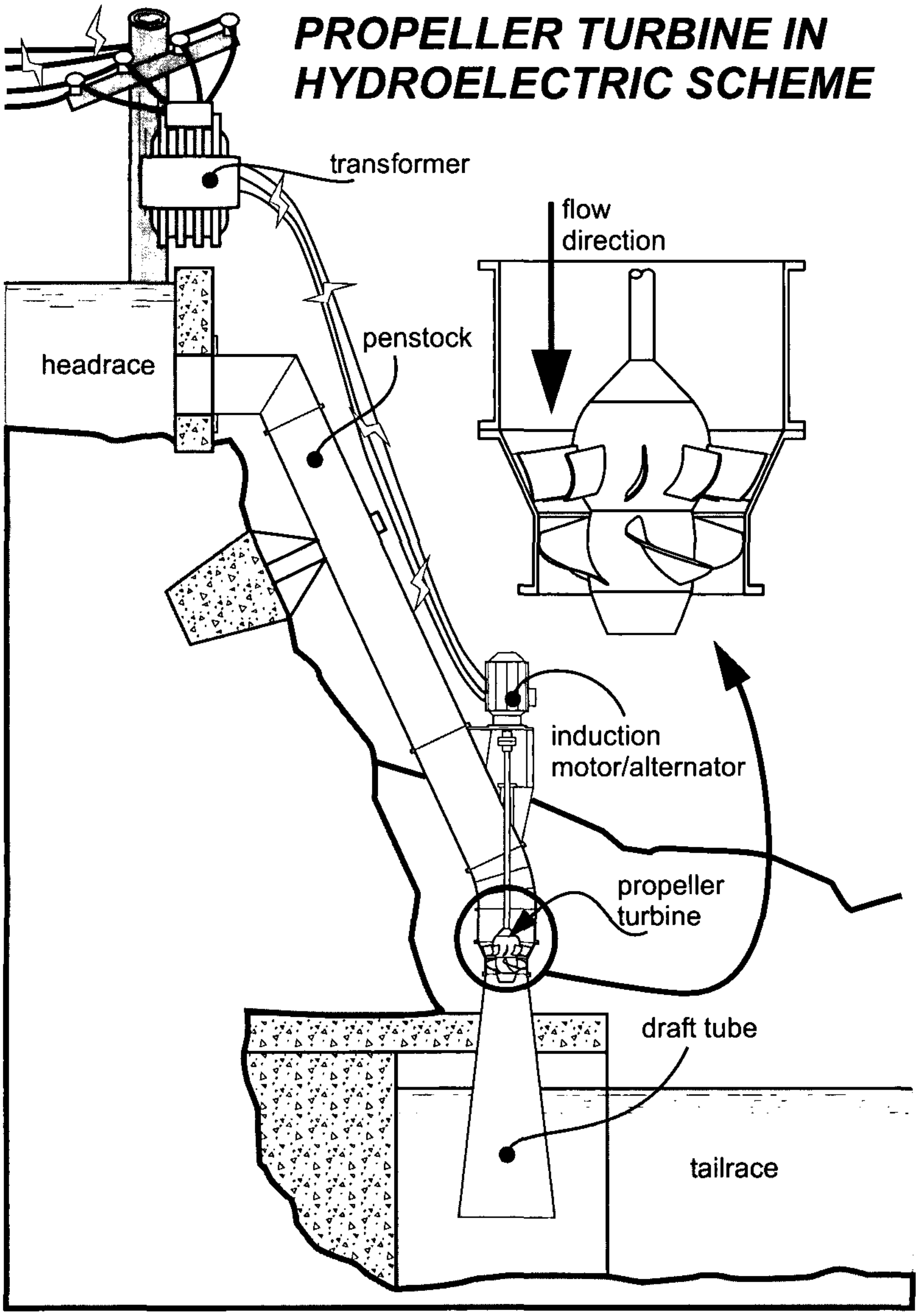
PROPELLER TURBINE IN HYDROELECTRIC SCHEME
transformer
flow direction
penstock
headrace
induction motor/alternator
propeller turbine
draft tube
tailrace

Fig. 14.1. Propeller turbine in a small hydroelectric scheme.

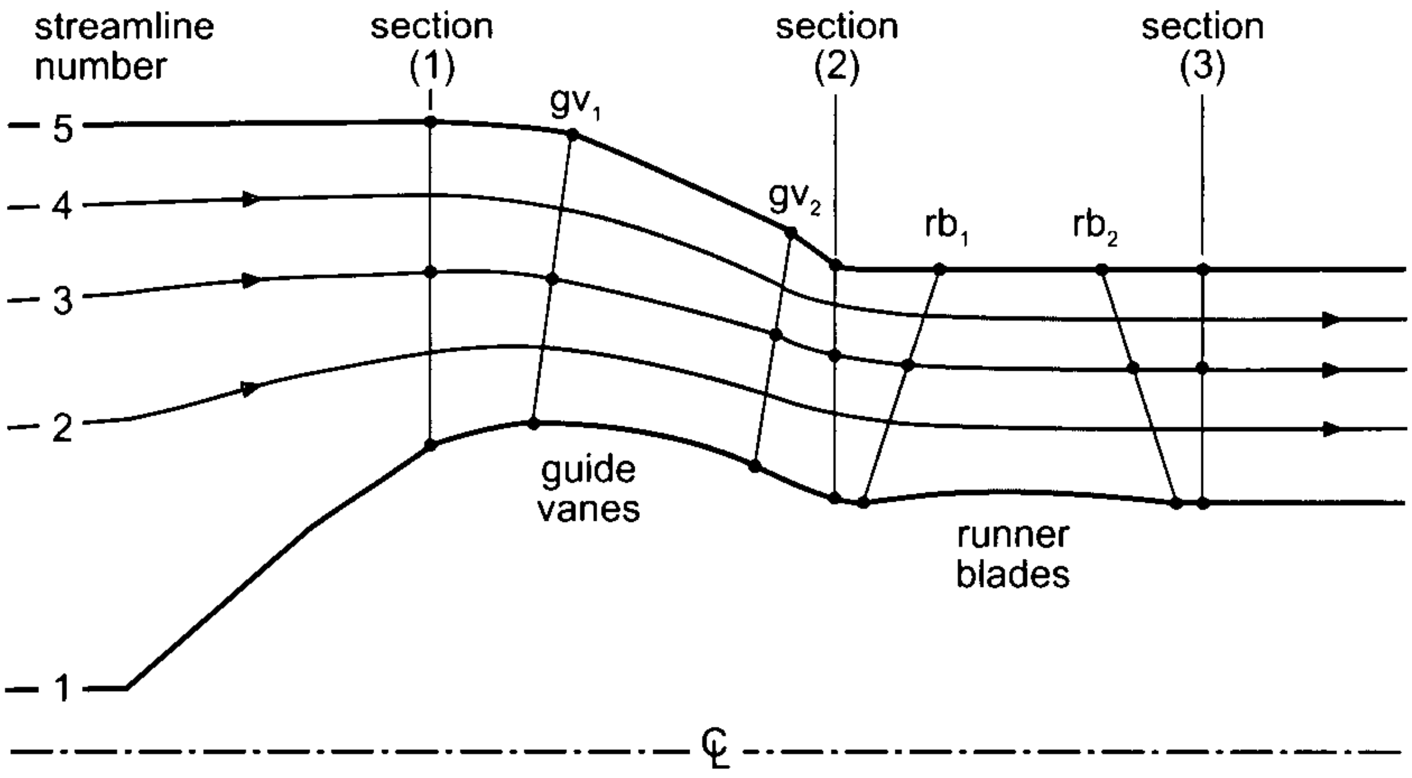

Fig. 14.2. Propeller turbine flow envelope and streamlines.

$$n_{11} = \frac{ND_2^o}{\sqrt{H_n}},$$

$$\text{Where } D_2^o = \frac{\sqrt{8.5} \times 125}{1540} = 0.2366\text{m},$$

$$q_{11} = \frac{Q}{(D_2^o)^2\sqrt{H_n}} = \frac{0.1864}{(0.2366)^2\sqrt{8.5}} = 1.142\text{m}^3\text{s}^{-1}.$$

The values of q_{11} and n_{11} apply close to the peak efficiency of the propeller turbine characteristic in Figure 6.4. This suggests that it is possible to design a reasonably shaped turbine consistent with established practice. This particular selection is perhaps not optimum as the tubular propeller turbines will permit a higher unit flowrate, see Figure 6.4.

Using Figure 8.5 as a guide, $KU^o = 1.41$ and $KU^i = 0.7$, applying Equation 3.10,

$$KU^o = \frac{\pi D^o N}{60\sqrt{2gH_n}},$$

$$\text{Therefore, } D^o = \frac{60 \times \sqrt{19.6 \times 8.5} \times 1.41}{\pi \times 1540} = 0.226\text{m}.$$

The selection of a larger diameter should make the design of the blades less critical with regard to cavitation performance.

Therefore select a casing diameter of 240mm with a propeller diameter of 238mm.

The hub diameter can be selected in accordance with Figure 8.5.

$$\text{Eg. } D^i = \frac{0.7}{1.41} \times 0.238 = 0.12\text{m}$$

The next step is to use Figure 4.5 (b) to determine a likely turbine setting. Using this Figure:

$$\sigma_T = 0.44$$

Assume the site is at an elevation of 1000m with an ambient water temperature of 20 °C. Most sites will be less restrictive than this with regard to cavitation performance.

Using Figure 4.6, the vapour pressure head of water H_v is determined as:

$$H_v = 0.17\text{m}$$

Using Figure 4.7, the atmospheric pressure head is determined as:

$$H_{atm} = 9.08\text{m}$$

From Equation 4.4:

$$\begin{aligned} 0.44 \times 8.5 &= 9.08 - 0.17 - H_s, \\ H_s &= 5.17\text{m}. \end{aligned}$$

The value of 5.17 m suggests that best practise design (allowing for some cavitation repair) will tolerate a turbine setting of 5.17m above the tailrace. Again, conservative design suggests that the setting should be less than this. Select 2.0m as the turbine setting.

With regard to general manufacturing considerations, the general arrangement with a vertical shaft and general shape as shown in Figure 14.1, can be chosen.

To ease manufacture the shape of the stator is kept simple with constant thickness guide vanes and straight generators. A slight barrelling of the rotor hub as is commonly seen on Kaplan turbines is applied. In this instance the barrelling is included to allow a change in blade angle on a common hub design for different operating conditions.

In general the lower the specific speed, the larger the number of blades and the greater the ratio of rotor hub diameter to rim diameter. Figure 8.5 for example suggests that 7 blades are appropriate (6 might be more likely). It has been decided to use a design with 4 blades having a hub to tip diameter ratio of 0.5. This is not necessarily the optimum but again was adopted for manufacturing convenience with no blade overlap and more simple pattern design.

The design flowrate is 186.4l/s. Therefore, the velocity entering the conical draft tube is:

$$V_3 = \frac{0.1864}{(\pi \times 0.24^2)/4} = 4.12\text{ms}^{-1}$$

The kinetic energy entering the draft tube as a percentage of the net head is:

$$\frac{4.12^2}{19.6 \times 8.5} \times 100\% = 10.2\%$$

An important function of the draft tube is to convert most of the velocity head of the fluid exiting the runner into useful pressure. To do this effectively the fluid must be decelerated without large scale boundary layer separation. The sizing is based on Figure 5.8 which plots contours of constant loss coefficients on a chart of length ratio versus area ratio. The use of the plot, which is for a thin boundary layer, is justified due to the thin highly turbulent energetic flow entering the draft tube. The draft tube performance can be improved by allowing 10 ° of rotation of the flow at the runner tip at the design condition. This "swirl" helps keep the boundary layer attached.

If a very high specific speed propeller turbine was to be designed, 20 ° to 30 ° of swirl might be allowed to enter the draft tube on design. The turbine designer has to optimise the design: on one hand, swirl represents energy loss as it is not recovered, but the percentage of energy entering the draft tube if significant also requires the best performing draft tube.

Diffuser performance is stable below the optimum design line of Figure 5.8, so we select an area ratio of 3. At this area ratio the minimum loss coefficient is given by a length over inlet radius of 10. The radius at exit from the turbine is 120mm giving a diffuser length of 1.2m. Although a longer conical section may have been possible, manufacture could have been more difficult. If the draft tube needs to be longer, as it does for a turbine setting of 2m, a cylindrical extension of diameter 0.415m and 2m length can be fitted. The cylindrical section after the diffuser will give some further pressure recovery as the flow becomes more uniform.

Unlike the Francis turbine design example, where a range of flow envelopes have been provided, we shall design our propeller turbine flow envelope from scratch.

A summary of the design thus far:

$$
\begin{aligned}
Q &= 0.1864\mathrm{m}^3\mathrm{s}^{-1},\\
D_3^o &= 0.238,\\
D_3^i &= 0.120,\\
\overline{V}_{m_3} &= 5.62\mathrm{ms}^{-1},\\
\omega &= 161.3\mathrm{rad/s},
\end{aligned}
$$

For 10 ° of 'swirl' at streamline 5, section 3,

$$
\begin{aligned}
V_{\theta_3}^{(5)} &\approx \overline{V}_{m_3} \tan 10\,^\circ = 0.99,\\
rV_{\theta_3}^{(5)} &= 0.118 \approx 0.12,
\end{aligned}
$$

Likewise, $rV_{\theta_3}^{(1)} = 0$.

To determine radial equilibrium conditions, Equation 3.30 can be used. The results at Section 3 are listed in Table 14.1,

Streamline	$r_{(3)}$	$V_{m_{(3)}}$	$V_{\theta_{(3)}}$	$P_{(3)}$
5	0.0600	5.23	1.01	0.95
3	0.0935	5.71	0.73	0.95
1	0.1190	5.61	0.0	0.97

Table 14.1. Section 3 flow properties.

Using Equation 3.19 with $H_n = 8.5$m, Table 14.2 results. In practise this rV_θ distribution is not ideal as there is likely to be more loss at the tip than at the hub. The attraction of using the $r_{(2)}V_{\theta_{(2)}}$ distribution above is that it achieves an approximately constant flow angle departing from the guide vanes.

Streamline	$r_{(3)}V_{\theta_{(3)}}$	$r_{(2)}V_{\theta_{(2)}}$	$\eta_n H_n$	η_n
1	0	0.46	7.6	0.9
3	0.07	0.54	7.7	0.91
5	0.12	0.60	7.9	0.93

Table 14.2. Section 2 flow properties.

To determine the flow angle departing the guide vanes, it is necessary to adjust the flow properties at Section 2 to those along the guide vane trailing edge. See Figure 14.2. The law of constant angular momentum (Equation 3.15) applies.

Streamline	$r_{(2)}V_{\theta_{(2)}}$	$r_{gv_2}V_{\theta_{gv_2}}$	$V_{m(2)}$	r_{gv_2}	$V_{\theta_{gv_2}}$	$V_{m_{gv_2}}$	β_{gv_2}
1	0.46	0.46	4.9	0.070	6.57	6.2	43.3
3	0.54	0.54	5.7	0.101	5.30	5.4	45.4
5	0.60	0.60	7.5	0.128	4.71	4.5	43.6

Table 14.3. Guide vane trailing edge flow properties.

$V_{m_{gv_2}}$ is obtained by adjusting $V_{m_{(2)}}$ by the change in area of the stream tubes. The streamlines in Figure 14.2 have been sketched using Equation 3.30 applied at Sections (1), (2) and (3). For the upstream Section (0), the position of the streamlines have been determined by applying the assumption of constant area for each streamtube.

At this point, a set of streamtubes, and a set of flow properties at Sections (1), (2) and (3) have been obtained. The next step is to design a set of runner blades and guide vanes that can deflect the flow by the required amount as specified at the respective sections.

Estimating the area change on the streamtubes, we have,

Streamline	$V_{m(1)}$	V_{mgv_1}	V_{mgv_2}	$V_{m(2)}$	V_{mrb_1}	V_{mrb_2}	$V_{m(3)}$
1	4.2	4.7	6.2	4.9	4.8	5.8	5.8
3	3.2	3.6	5.4	5.7	5.7	5.7	5.7
5	2.8	2.5	4.5	7.5	5.3	5.2	5.2

Table 14.4. Meridional velocities.

Streamline	$V_{\theta_{gv1}}$	$V_{\theta_{gv2}}$	$V_{\theta_{rb1}}$	$V_{\theta_{rb2}}$
1	0	6.6	7.7	0
3	0	5.3	5.7	0.7
5	0	4.7	5.0	1

Table 14.5. Cicumferential velocities.

The guide vane and runner blade flow angles are taken from the circumferential direction, see Table 14.7.

Streamline	r_{gv1}	r_{gv2}	r_{rb1}	r_{rb2}	U_{rb1}	U_{rb2}
1	0.080	0.070	0.060	0.060	9.68	9.68
3	0.117	0.101	0.095	0.095	15.3	15.3
5	0.153	0.128	0.119	0.119	19.2	19.2

Table 14.6. Streamline radii and runner peripheral velocities.

Streamline	β_{gv1}	β_{gv2}	β_{rb1}	β_{rb2}
1	90	43.4	67.3	31.2
3	90	45.4	32.8	21.6
5	90	43.6	20.7	16.1

Table 14.7. Flow angles.

An approximation of the required runner blade length at the hub can be obtained using Zweifel's loading coefficient defined in Equation 3.38,

$$\Psi_T = 2\frac{s}{L}\sin^2\beta_2(\cot\beta_2 - \cot\beta_1)$$

Where L is the axial chord, s the pitch, β_1 the inlet flow angle and β_2 is the outlet flow angle. A value of about 0.8 at the hub will give a good starting point. Using 4 blades, the blade pitch can be calculated,

$$\begin{aligned} \frac{2\pi \times 0.06}{4} &= 0.094, \\ L &= \frac{2 \times 0.094}{0.8}\left(\sin^2 31.2\right)\left(\cot 31.2 - \cot 67.3\right), \\ &= 0.078m. \end{aligned}$$

The reason that the guide vanes are positioned at an increased radius over the radius of the blades at the hub, is to reduce the guide vane hub Zweifel loading coeficient down to 0.8.

For example 11 blades,

$$\begin{aligned}\text{Pitch } &\approx \frac{2\times\pi}{11} = 0.0428\text{m},\\ \text{Average exit angle } &= \frac{43.3+45.4+43.6}{3} = 44.1,\\ L &= \frac{2\times 0.0428}{0.8}\sin^2(44.1)\left[\cot 44.1 - \cot 90\right],\\ &= 0.053\text{m}(55\text{mm selected}).\end{aligned}$$

As the guide vanes are going to be constructed from rolled sheet, the 55mm axial chord is held constant from hub to tip.

The runner blade axial chord at the tip has to be reduced significantly over the hub axial chord. This is because the blade stagger angle is inclined more to the circumferential. Having the same axial chord at the tip over the hub would result in an excessively long blade. The correct approach to determining blade length is to carry out a boundary layer calculation, selecting a blade length such that the flow is about to separate at the trailing edge on the suction face.

The approach for this design has been a bit cruder, selecting an axial chord of approximately 40mm. This axial length results in a tip blade chord roughly the same length as the hub blade chord. Other approaches that have been used include using a lift coefficient under 0.3 or assuming a very simple pressure distribution on the blade, eg 40% pressure, 60% suction and checking that the axially projected runner area is sufficient to support the net head without the pressure falling to absolute zero on the suction face.

To calculate incidence and deviation, Figures 3.12 and 3.13 are applied respectively. For deviation, assuming circular arc camber lines,

Streamline	Pitch s	β_{rb1}	β_{rb2}	Stagger angle	Axial chord	Chord	Carter m	Camber θ	δ
1	94.2	67.3°	31.2°	49.3°	78	103	0.19	36.1°	6.3°
3	147	32.8°	21.6°	27.2°	55.8	122	0.19	11.2°	2.6°
5	187	20.7°	16.1°	18.4°	39.5	125	0.20	4.6°	1.4°

Table 14.8. Calculation of trailing edge deviation.

Note m is calculated from Figure 3.13 and δ from Equation 3.40.

The effect of blockage (boundary layer build up) is to increase the core velocity. The effect of this is shown as follows for a blockage of 6% on the runner blades:

Carter generally underpredicts deviation. So assume the error is 1% for Carter. The final blade angles at exit are thus:

For the guide vanes at exit:

Streamline	U_{rb2}	$V_{\theta rb2}$	V_{mrb2}	6% V_{mrb2}	β_{rb2} no blockage	β_{rb2} 6% blockage	blockage adjustment
1	9.7	0	5.6	5.9	30.0	31.3	1.3
3	15.1	0.73	5.7	6.0	21.6	22.7	1.1
5	19.2	1.01	5.2	5.5	16.0	16.8	0.8

Table 14.9. Calculation of deviation due to blockage effects.

Streamline	β_{rb2}	Deviation	χ_{rb2}
1	30	$6.3 + 1 - 1.3 = 6$	24
3	21.6	$2.6 + 1 - 1.1 = 2.5$	19.1
5	16.0	$1.4 + 1 - 0.8 = 1.6$	14.4

Table 14.10. Final blade exit angles.

$$\begin{aligned}
\beta_{gv_1} &= 90, \\
\beta_{gv_2} &= 43.3, \\
\text{Stagger angle} &= 66.7, \\
\text{Axial chord} &= 56.5, \\
\text{Chord} &= 61.6, \\
m &= 0.19, \\
\text{Camber} &= 46.6, \\
s &= 62.3, \\
\text{Carter's deviation} &= 9.0, \\
\chi_{gv_2} &= 34.4\,^{\circ}.
\end{aligned}$$

The position of the stagnation point on the leading edge is affected by blade loading and by blade blockage effects. Figures 3.12 (a) and (b) allow the calculation of these effects.

Streamline	c/s	Stagger angle	Camber angle	Incidence angle (loading)	t/c	Incidence angle (blockage)	Incidence applicable	β_{rb_1}	χ_{rb_1}
1	1.1	49.3	36.1	8 °	0.04	2 °	6 °	67.3 °	73.3
3	0.84	27.2	11.2	3 °	0.03	1 °	2 °	32.8 °	34.8
5	0.67	18.4	4.6	2 °	0.03	1 °	1 °	20.7 °	21.7

Table 14.11. Runner leading edge blade angles.

For the leading edge of the guide vanes at the mean streamline position:

$$\begin{aligned} \text{Solidity} &= 0.99, \\ \text{Camber angle} &= 46.4\,^{\circ}, \\ \text{Stagger angle} &= 66.7\,^{\circ}, \\ \text{Incidence due to loading} &= 12.5\,^{\circ}, \\ t/c &= 0.065, \\ \chi_{gv} &= 100\,^{\circ}. \end{aligned}$$

To sum up the design process so far: stream surfaces have been calculated from radial equilibrium, and inlet and exit angles for the blades/guidevanes along 3 stream surfaces have been determined.

The next step is to plot out a camber line profile in a cylindrical development view. Equation 3.34 for a parabolic camberline could be applied as could a similar equation for circular arc camberline profiles. Note in the case of the guide vanes, a conical development has been used. Thickness is applied to the camberline geometry in accordance with structural requirements. Maximum thickness can be somewhere between 0.4 and 0.5 of the blade chord. See Figure 14.3.

After the blade sections have been laid out, the sections are stacked. The stack geometry needs to be defined. See Chapter 13 for a discussion of a stacking method using blade templates.

Runner blade construction can be undertaken by several methods.

One method is to convert surface points on the developed sections in Figure 14.3 into x, y, z geometry (cartesian co-ordinates) and import them into a solid modelling package. A B–spline curve can be fitted through the surface points for each blade section. The solid modelling package then is used to loft a surface through the blade curves. An example of such a solid model is shown in Figure 13.3 (b) with a rapid prototype model illustrated in Figure 14.4, and the actucal turbine under manufacture, Figure 14.5.

An alternative method is to use the blade templates, Chapter 13, to develop a pattern for casting the blades.

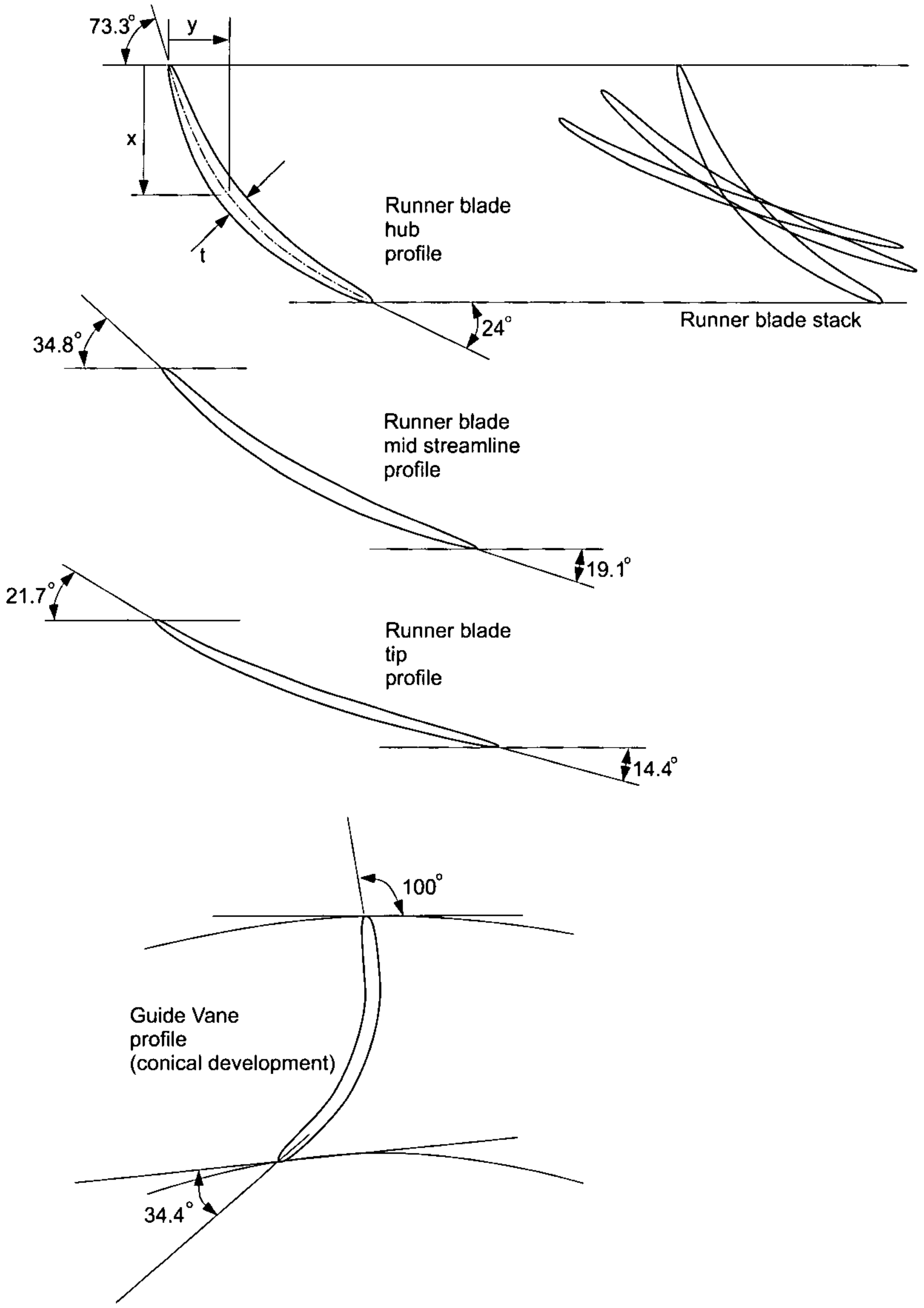
73.3°
y
x
t
Runner blade
hub
profile
24°
Runner blade stack
34.8°
Runner blade
mid streamline
profile
19.1°
21.7°
Runner blade
tip
profile
14.4°
100°
Guide Vane
profile
(conical development)
34.4°

Fig. 14.3. Propeller turbine blading design.

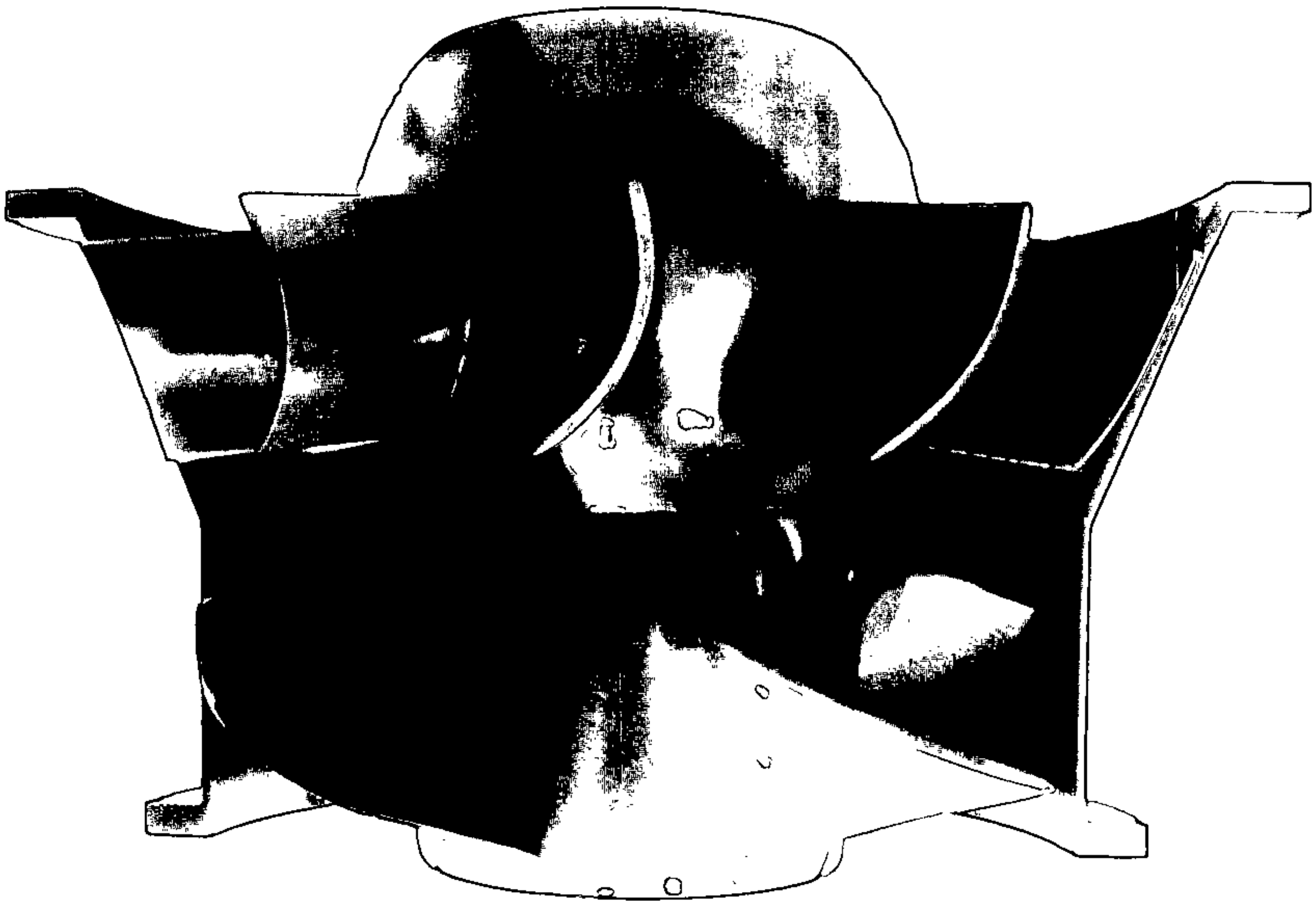

Fig. 14.4. Rapid prototype blade model.

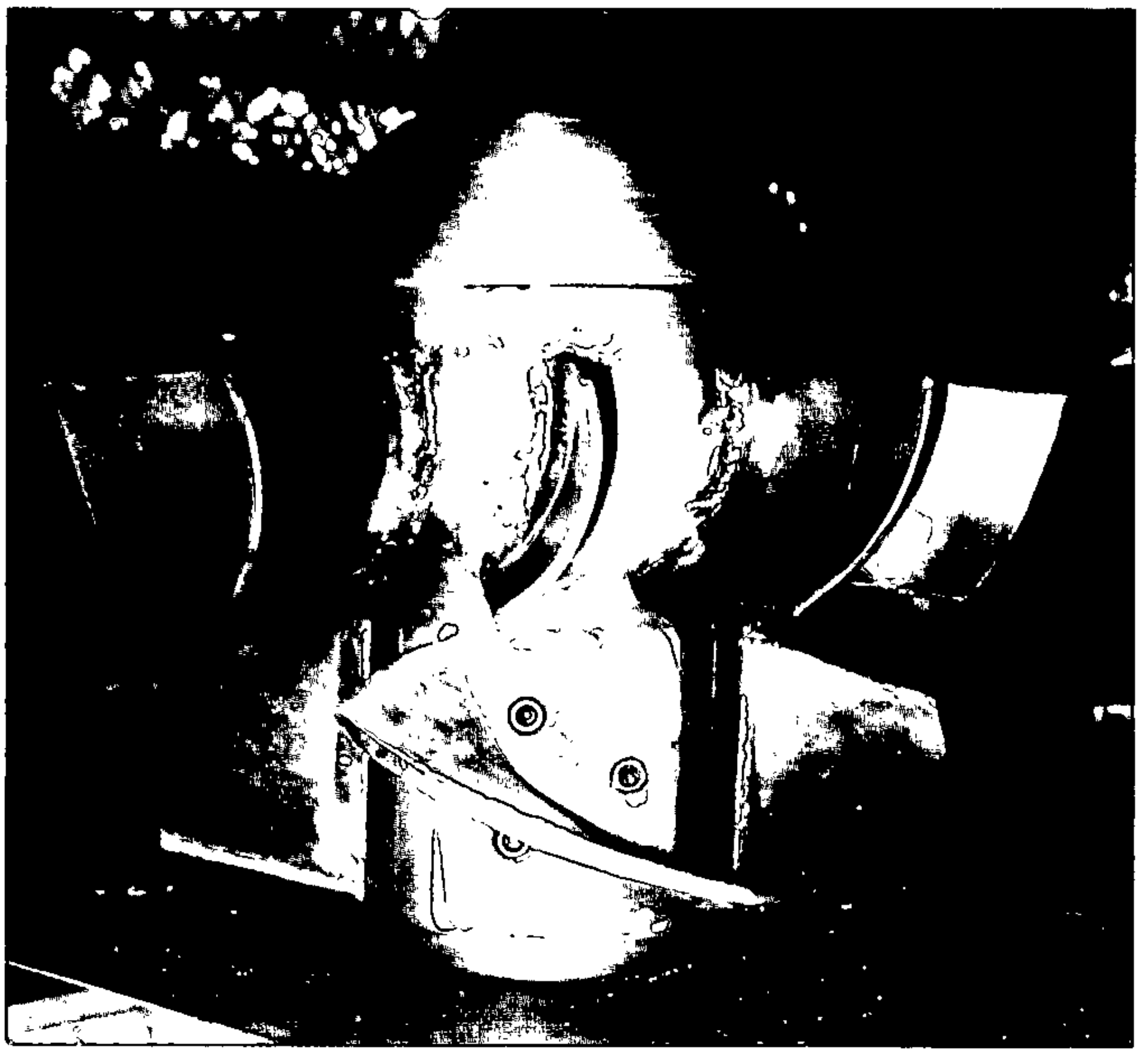

Fig. 14.5. Cast propeller, fabricated guide vane assembly.

15 Francis turbine design example

15.1 Specific speed and design flowrate

This example is based on a replacement runner design carried out recently by Aotearoa Software Ltd for Trustpower NZ Ltd. The example is a little contrived as it was conducted first using proprietory turbomachinery design software, and then repeated using the methods outlined in this design guide.

The turbine is an existing Francis turbine, originally built in 1930. It is horizontally mounted with a 90 ° draft tube elbow. The turbine setting is 5.1m from the tailrace surface to the shaft centre line. The net head is 74m as defined by Equation 3.1. Rotational speed is 750rpm.

Figures 15.1 (a) through 15.1 (d) show the turbine and turbine runner features.

Current performance figures from efficiency tests are believed to be at max efficiency:

$$\begin{aligned} \hat{P} &= 1278\text{kW}, \\ \hat{Q} &= 2.05\text{m}^3\text{s}^{-1}, \\ H_n &= 74\text{m}, \\ N &= 750\text{rpm} \end{aligned}$$

The specific speed is calculated using Equation 3.4,

$$n_s = \frac{750 \times (1278)^{1/2}}{74^{5/4}} = 123.5$$

Turbine efficiency, Equation 3.14 is,

$$\hat{\eta} = \frac{1278}{9.8 \times 2.05 \times 74} = 86\%$$

This value is probably about right for a 70 year old turbine with worn clearances and weld repaired surfaces.

Using Figure 6.3,

(a) Front view of Mangorei machine No. 4, 1400kW output.

(b) Side view of Mangorei turbine showing draft tube elbow.

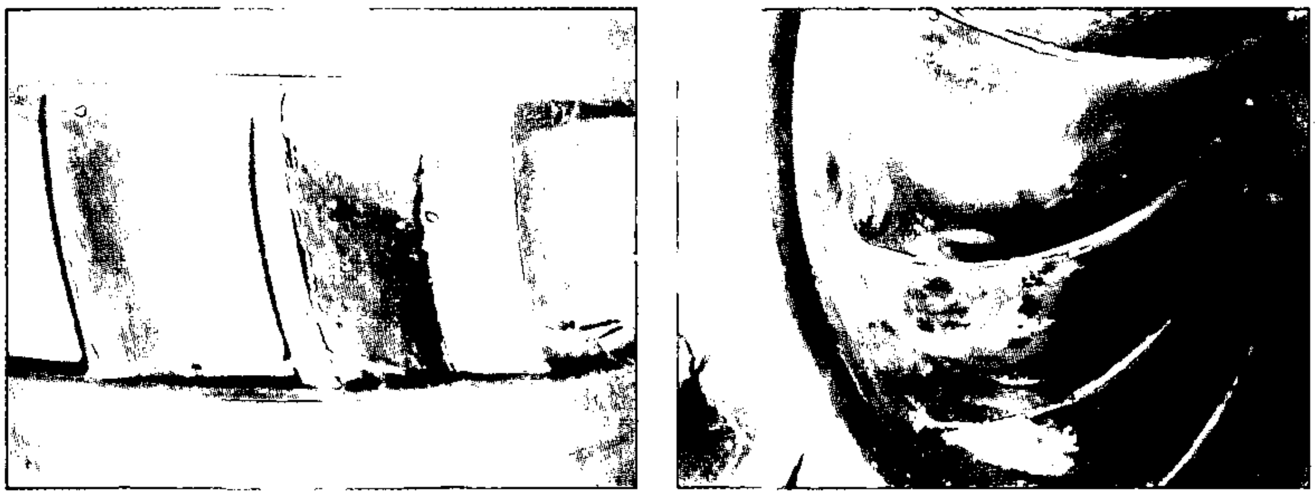

(c) Runner inlet blade profiles.

(d) Runner outlet blade profiles showing cavitation repairs.

Fig. 15.1. Francis turbine and runner features.

$$
\begin{aligned}
\frac{Q_\perp}{Q_{1/1}} &= 0.86, \\
\frac{Q_\wedge}{Q_{1/1}} &= 0.81, \\
Q_\wedge &= 2.05\mathrm{m^3s^{-1}}, \\
\text{then as } Q_{1/1} &= \frac{2.05}{0.81} = 2.53, \\
Q_\perp &= 2.177\mathrm{m^3s^{-1}}.
\end{aligned}
$$

Treat $Q_\perp$ as the design flowrate where the rV_θ leaving the runner is predominantly zero.

Assume the efficiency of the new runner is 2% greater than the old runner, then,

$$Q_\perp = 2.13\mathrm{m}^3\mathrm{s}^{-1}$$

15.2 Runner envelope

Figure 15.2 shows the envelope geometry used in the redesign, the dimensions for the leading and trailing edge intersection points with the hub and casing, and the position of the streamlines, assuming constant yaw angle from the guide vanes.

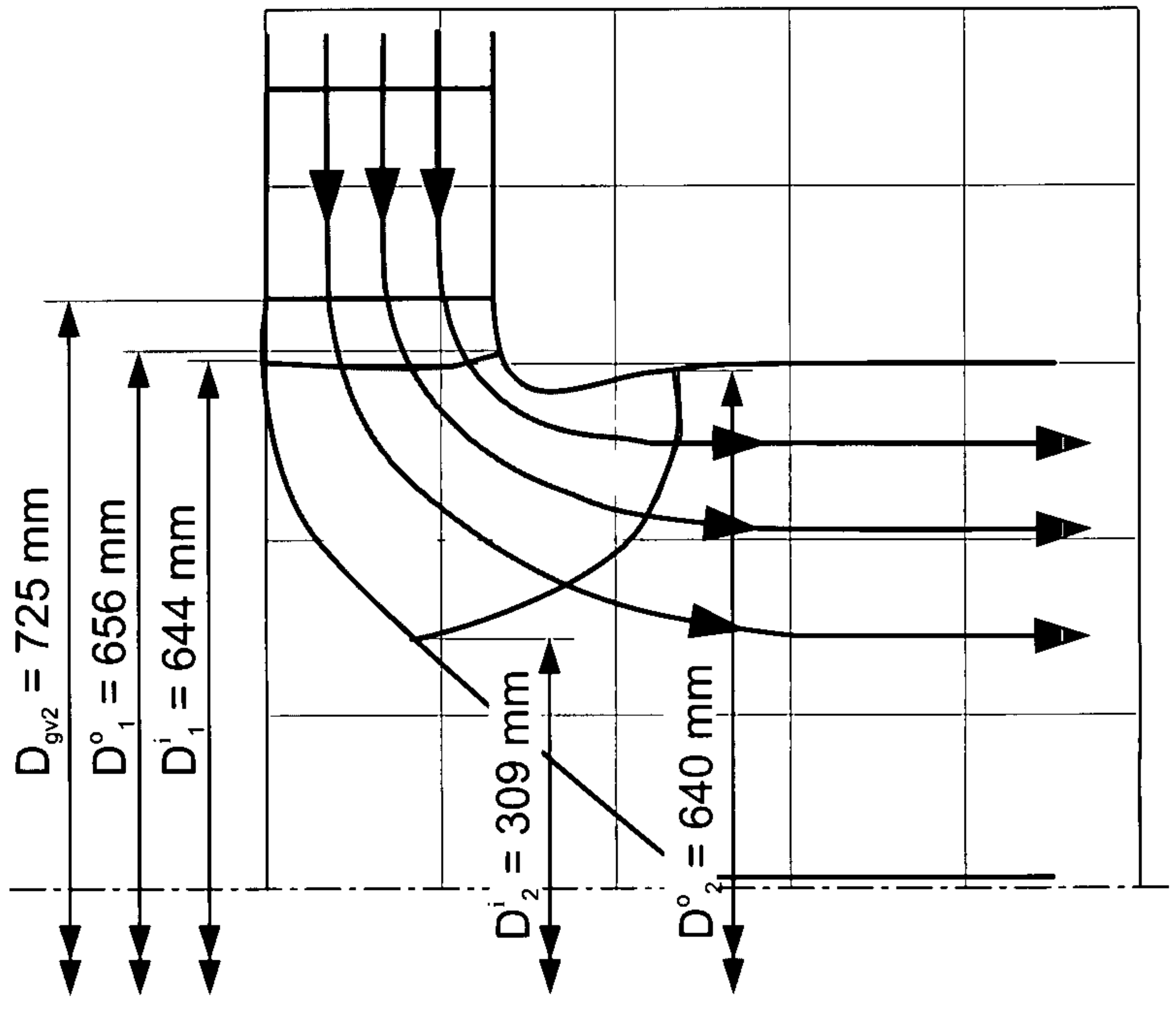

Fig. 15.2. Francis turbine envelope geometry.

The guide vane height and runner exit diameter are determined from the existing envelope geometry. The runner leading edge radius cannot be increased due to potential interference with the guide vanes, if a guide vane linkage broke.

For a specific speed of 123.5, the peripheral velocity coefficients are obtained from Figure 8.4. See Table 15.1.

	Figure 8.4	Actual
KU_1^o	0.74	0.678
KU_1^i	0.72	0.664
KU_2^o	0.65	0.662
KU_2^i	0.36	0.318
B_{gv}/D_2^o	0.19	0.219

Table 15.1. Peripheral velocity coefficients

These peripheral velocity coefficients determine where the leading edge/trail edge intersect with the crown and skirt. KU is defined as per Equation 3.10.

In Table 15.1, with the exception of KU_2^o, the peripheral velocity coefficients are down on established practice, for the Mangorei flow envelope.

Figure 15.3 shows the new envelope that would be obtained from the Figure 8.4 peripheral velocity coefficients, overlaid on Figure 15.2. The streamlines shown in Figure 9.10 apply to this new envelope.

The construction of the new envelope involved connecting the points established from the peripheral velocity coefficients by simple radii. The increased radius of the leading edge together with the reduced guide vane height allow a runner of between 11 and 13 blades to be developed without incurring separation on the pressure face due to Coriolis loading. The replacement runner design, constrained by envelope restrictions, needs a larger number of blades and will still probably experience pressure face separation.

15.3 Draft tube design, setting and cavitation conditions

The draft tube comprises a cone ($\varnothing 640$ to $\varnothing 700, L = 150$), a 90° constant area bend. ($\varnothing 700, r/d = 1.14$), an expansion leg of $\varnothing 700$ to $\varnothing 800$ with a full cone angle of 7°, and a draft tube extension of $\varnothing 800$ down to the tail race.

For a pressure gauge mounted a distance a_g above the bend entrance, Bernoulli's equation with section 2 being the runner exit/draft tube entrance, and section 3, the draft tube exit:

$$\left(\frac{p_{g2}}{\rho g} + a_{g_2}\right) + \frac{V_2}{2g} + H_s = H_{atm} + \frac{V_3^2}{2g} + K_b \frac{V_3^2}{2g} + (1 - \eta_{dt}) \frac{V_2^2}{2g}$$

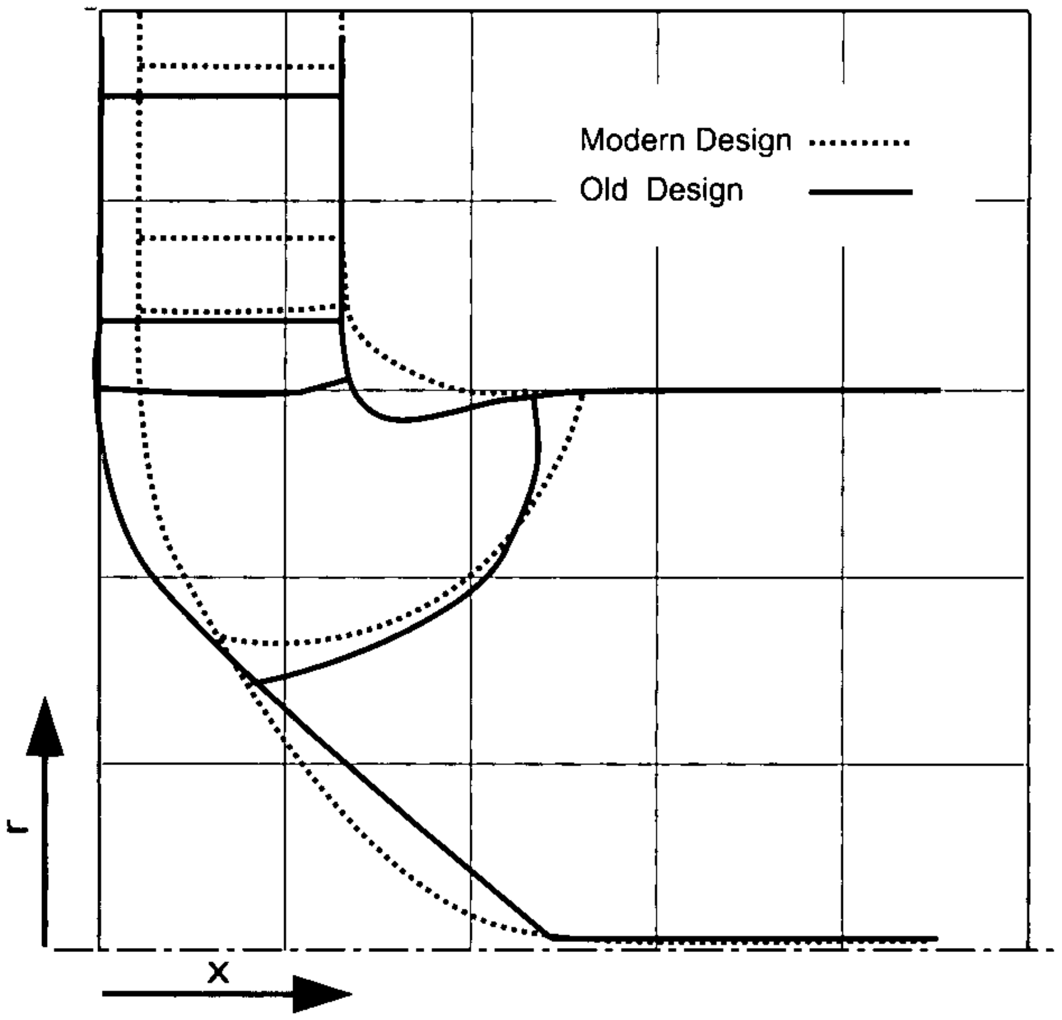

Fig. 15.3. Comparison between 'old' 1930's envelope and an 'improved' new envelope for $n_s = 123.5$.

The exit loss of $V_3^2/2g$ has an additional 'bend' loss as the water has to do a 90 ° turn from the vertical ⌀800 leg into the tailrace.

$(1 - \eta_{dt}) \frac{V_2^2}{2g}$ comprises those draft tube losses that exclude the exit losses.

$$
\begin{aligned}
Q &= 2.13\mathrm{m^3s^{-1}}, \\
H_s &= 5.1\mathrm{m}, \\
a_{g_2} &= 0.5, \\
\eta_{dt} &= 0.8, \\
H_{atm} &= 10.22\mathrm{m}, \\
K_b &\approx 1.0, \\
\frac{p_{g_2}}{\rho g} &= 4.66\mathrm{m} \quad \text{(absolute pressure head)}, \\
\text{Vacuum gauge head} &= H_{atm} - \frac{p_{g_2}}{\rho g}, \\
&= 5.56\mathrm{m} \quad (18.2').
\end{aligned}
$$

This is in fact what the gauge read ($\approx 18'$), suggesting the assumption of a draft tube efficiency, $\eta_{dt} = 0.8$, is a reasonable one.

The reader could use Figures 5.8, 5.9 and 5.10 to determine a theoretical draft tube efficiency and compare with the efficiency used above.

With $n_s = 123$ and using Figure 4.5 (a), $\sigma_T = 0.07$. From Equation 4.4, and Figures 4.6 and 4.7, $H_v = 0.14$m, $H_a = 10.1$m, $H_n = 74$m, then $H_s = 4.78$m. As $H_s = 5.1$m, one might expect cavitation to be present during normal running of this turbine. This is in fact the case with the old runner, shown in Figure 15.1 (d), requiring frequent cavitation repair.

15.4 Runner design

Using $n_s = 123$, Figure 7.2 can be used to proportion the losses inside the turbine. See the second column of Table 15.2.

	Figure 7.2	86% efficiency	90% efficiency
Spiral casing and stay vane losses	22%	2.3m	1.6
Guide vane losses	34%	3.5m	2.5
Runner sealing losses	17%	1.8m	1.3
Runner losses	16%	1.7m	1.2
Draft tube losses	11%	1.1m	0.8

Table 15.2. Francis turbine losses

For a measured efficiency of 86%, the losses are a total of $(1-0.86)\times 74 = 10.4$m, and are proportioned according to the third column of Table 15.2. Assuming the turbine is to be refurbished by improving the runner sealing losses and the guide vane clearance losses, the net head across the new runner might be:

$$74 - 2.3 - 2.5 - 1.1 = 68.1\text{m}$$

Using this figure for the net head in Equation 3.18 or the value of $\eta_h = 0.92$ in Equation 3.19, the inlet rV_θ can be determined. Note that this analysis is for perpendicular discharge, $Q_\perp$, so $r_2 V_{\theta_2} = 0$.

$$\omega = \frac{2\pi \times 750}{60} = 78.54\mathrm{rad/s},$$

$$r_1 V_{\theta_1} = \frac{68.1 \times 9.8}{78.54} = 8.5.$$

The streamlines for this design have been set up as shown in Figure 15.2. This design will be presented on three streamlines, crown (hub) = 1, mid-streamline = 3 and skirt = 5. Subscripts 1 and 2 refer to leading and trailing edges respectively.

	Streamline 1	Streamline 3	Streamline 5
$Vm_{gv_2}{}^*$	6.6	6.8	7.0
r_{gv_2}	0.3625	0.3625	0.3625
α_{gv_2}	16.0	16.0	16.0
$V\theta_{gv_2}$	23.0	23.7	24.4
$(rV_\theta)_{gv_2}$	8.34	8.59	8.84
$(rV_\theta)_1$	8.34	8.59	8.84
r_1	0.3220	0.322	0.3288
$Vm_1{}^*$	5.5	7.3	17.0
$V\theta_1$	25.9	26.7	26.9
U_1	25.3	25.3	25.8
β_1	-83.8	-79.1	-86.3
$(rV_\theta)_2$	0	0	0
$V_{m_2}{}^*$	6.2	7.6	4.8
r_2	0.1543	0.2253	0.320
U_2	12.1	17.7	25.1
β_2	30.0	22.7	12.1

Table 15.3. Flow properties at inlet and exit.

* Obtained from $Q = 2.13\mathrm{m^3s^{-1}}$ and the streamline positions.

To investigate the effects of Coriolis loading at the leading edge of the runner, Equation 3.39 can be used.

For $\chi_1 \approx 80\,^\circ$ and $Z = 16$ blades:

$$\sigma_w = 1 - \frac{\sqrt{\sin 80\,^\circ}}{16^{0.7}} = 0.86$$

Equation 3.39 applies to radial flow. At the hub section, streamline 1: From Equation 3.39:

$$0.86 = 1 - \frac{V_s}{U_1},$$
$$V_s = 3.54,$$
$$\beta_1 = -83.8\,°,$$
$$\beta_1' = -52.4\,°.$$

From geometry considerations, Figure 15.4 applies

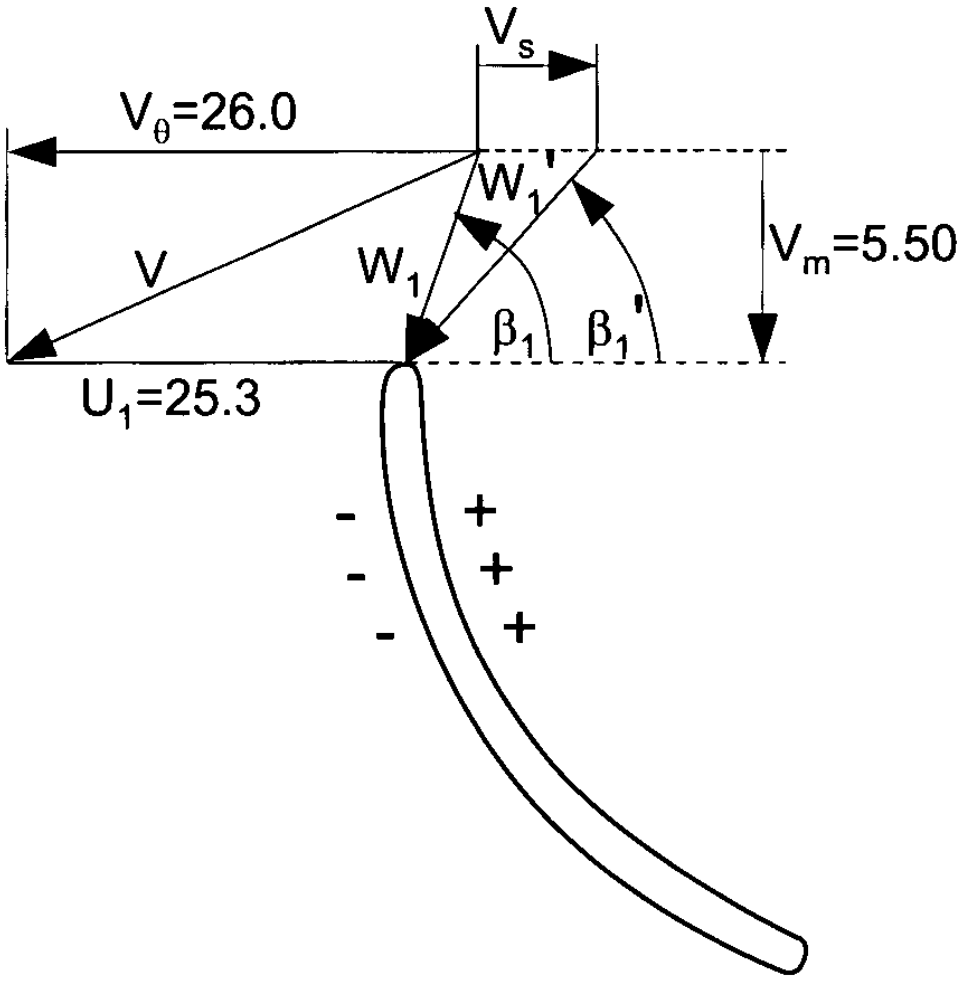

Fig. 15.4. Hub section streamline one, slip velocity applied.

Some 30 ° of incidence is present on the leading edge at the hub. The magnitude of this incidence will almost certainly ensure separation on the pressure face near the leading edge. This in turn causes loss and a reduction in turbine efficiency. The three approaches to dealing with this incidence are:

1. To increase U_1 by increasing D_1, as illustrated in Figure 15.3.
2. To increase blade number (but try to keep the blockage flow the same).
3. To turn the blades towards the stagnation point and try to change the loading distribution within the blade row.

Options 1 and 2 are not possible; 1 because of the presence of existing guide vanes, and 2 because of manufacturing considerations. Option 3 marginally alleviates some of the loading but causes stacking problems, and leads to a turbine blade shape well outside established design practice.

The other causes of incidence are also present, incidence due to blade camber/stagger type loading and due to blade blockage. In this design, rightly or wrongly, the blade inlet angles have somewhat arbitarily been selected as:

Streamline	1	3	5
χ_1	$-78.8°$	$-74.6°$	$-73.5°$

Table 15.4. Blade inlet angles.

The leading edge angles selected in Table 15.4 provide about 2° to 3° more 'hook' than the original blades, shown in Figure 15.1 (c). This extra 'hook' was about as far as the designer of the replacement runner was prepared to go to reduce the Coriolis loading.

To determine if separation on the pressure face is likely to occur, the designer can use the mean streamline method to determine the local velocities over the blade camberline, and then use the Head and Patel [1968] integral boundary layer method. A more simplistic and less accurate approach is to see if there is inviscid flow reversal on the pressure face. Equation 3.37 can be used for this. If there is flow reversal, ie $W_c > W_p$, then blade geometry needs to be modified. Note that Head and Patel [1968] will not work with inviscid flow reversal.

For the Mangorei runner, there is flow reversal on the pressure face and likely pressure face separation. Unfortunately envelope restrictions do not permit a more modern design to be implemented, hence the somewhat arbitary selection of the inlet blade angles in Table 15.4.

Blade exit angles can be determined from considerations of blade blockage, inviscid deviation due to blade turning, Carter [1950], and deviation associated with Coriolis. Chapter 14 provides an illustration of the first two causes of deviation. A sample calculation is presented below for the Coriolis deviation.

The Coriolis deviation can be accounted for again by using Equation 3.39.

$$\chi_2 = 30\,^\circ,$$

$$\sigma_w = \left[1 - \frac{\sqrt{\sin 30\,^\circ}}{16^{0.7}}\right],$$

$$= 0.93,$$

$$1 - \frac{V_s}{U_2} = 0.93,$$

$$V_s = 0.072 \times 12.1,$$

$$= 0.87.$$

As the flow direction is not radial, the inclination of the streamlines to the axial, $\sin\phi$ in Figure 3.14, needs to be accounted for. This departure from radial reduces the Coriolis effect. Adjusting for $\sin\phi$: $V_s = 0.87 \times 0.77 = 0.67$ Using Table 15.3 and the exit velocity diagram relationships:

$$\beta_{\text{actual}} = 31.5\,^\circ$$

The blade would thus be adjusted back to $30 - 1.5 = 28.5\,^\circ$.

The flowrate through Francis turbines is strongly dependent on the runner gaps. These gaps are the blade passage minimum widths at exit. The design criterion is to match the existing runner exit gaps. Figure 15.5 presents runner exit gaps for the replacement Mangorei runner, curve D, and as an additional comparison, gaps of other runners of different specific speeds (A, $n_s = 300$: B, $n_s = 200$: C, $n_s = 110$). These gaps have been scaled to a common runner exit diameter, D_2^0, of 640mm.

Runner gaps are dependent on the number of blades, the blade thickness, the blade camberline geometry and the blade angles. The use of runner exit gaps provides a direct empirical approach to determining the new runner's exit flow angles.

Figure 15.5 could also have been plotted as,

$$\sin^{-1}\frac{o}{s}$$

where o is the maximum opening at the trailing edge and s the pitch.

The blade exit angles selected are shown in Table 15.5

Streamline	1	3	5
χ_2	22.7°	17.8°	10.8°

Table 15.5. Blade exit angles.

These blade exit angles together with the camberline geometry and blade thickness, produce the gaps shown in Figure 15.5. The process is an iterative one and only the last iteration is shown in this Chapter. For the blade

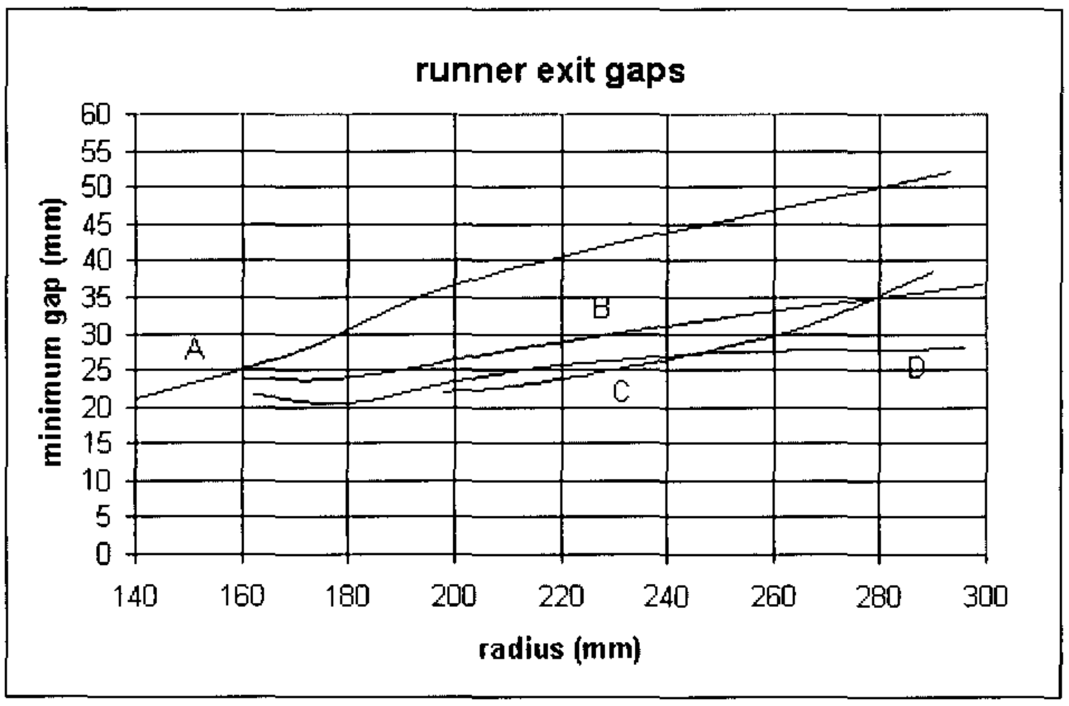

Fig. 15.5. Runner exit gaps comparison.

angles selected in Tables 15.4 and 15.5, the rV_θ can be recalculated and the Equations in Chapter 10 used to develop turbine geometry. Tables 15.6-15.8 provide an example for the hub camberline geometry.

As mentioned in Chapter 10, Prasil transform methods could be applied instead. Note that there is no reason why the Prasil transform method could not also be automated.

θstart	0.518
rpm	750
$V_m$start	5.5
$V_m$finish	6.2
rV_θstart	8.5
rV_θfinish	−0.413
loading (a)	0.95
power (m)	0.5
no. blades	16

Table 15.6. $n_s = 123$ turbine hub camberline geometry.

15.5 Guide vane design

Assuming 12 guide vanes are selected, then a suitable guide vane can be constructed by multiplying the dimensions given in Figure 10.10 by 1.094, based on using a guide vane pitch circle diameter (PCD) of 904mm. This

section	x	r	dx	dr	dm	ds	Vm	Vm aver	rV_θ	ωr	V_θ
0	0.30	322.0					5.50		8.50	25.29	26.40
1	0.25	309.0	-0.05	-12.98	13.0	13.3	5.55	5.52	7.91	24.27	25.58
2	0.32	296.1	0.07	-12.96	13.0	13.3	5.59	5.57	7.31	23.25	24.70
3	1.04	283.2	0.72	-12.88	12.9	13.3	5.64	5.62	6.72	22.24	23.72
4	3.32	270.4	2.28	-12.77	13.0	13.4	5.69	5.66	6.12	21.24	22.64
5	6.57	257.8	3.25	-12.57	13.0	13.3	5.73	5.71	5.53	20.25	21.44
6	10.77	245.5	4.19	-12.30	13.0	13.2	5.78	5.76	4.93	19.28	20.10
7	15.92	233.6	5.15	-11.91	13.0	13.0	5.83	5.80	4.34	18.35	18.58
8	21.98	222.2	6.06	-11.46	13.0	13.0	5.87	5.85	3.75	17.45	16.86
9	28.85	211.1	6.87	-11.02	13.0	13.2	5.92	5.90	3.15	16.58	14.93
10	36.48	200.6	7.63	-10.54	13.0	14.0	5.97	5.94	2.56	15.76	12.75
11	44.85	190.8	8.38	-9.86	12.9	15.4	6.01	5.99	1.96	14.98	10.30
12	53.92	181.6	9.06	-9.15	12.9	17.7	6.06	6.04	1.37	14.26	7.54
13	63.50	172.9	9.58	-8.70	12.9	21.2	6.11	6.08	0.78	13.58	4.48
14	73.49	164.6	9.99	-8.34	13.0	25.7	6.15	6.13	0.18	12.92	1.10
15	83.80	156.5	10.31	-8.06	13.1	31.2	6.20	6.18	-0.41	12.29	-2.64

Table 15.7. $n_s = 123$ turbine hub camberline geometry contd.

section	W_θ	$d\theta$	θ	$r\theta$	y	z	W mean	dP	Wc	Ws	Wp
0			0.518	166.7934	159.4	279.8					
1	1.21	0.0092	0.5272	162.9139	155.5	267.1	5.65	99266	8.78	14.43	-3.12
2	1.38	0.0108	0.538	159.2903	151.7	254.2	5.74	100303	8.74	14.48	-3.00
3	1.46	0.0119	0.5499	155.7189	148	241.4	5.8	101576	8.75	14.55	-2.95
4	1.44	0.0122	0.5621	152.0036	144.1	228.8	5.84	101845	8.71	14.56	-2.87
5	1.3	0.0115	0.5736	147.8949	139.9	216.6	5.86	102619	8.76	14.62	-2.91
6	1	0.0092	0.5828	143.1071	135.1	205	5.84	103403	8.85	14.69	-3.00
7	0.52	0.005	0.5878	137.3334	129.6	194.4	5.83	104392	8.96	14.78	-3.13
8	-0.18	-0.0018	0.586	130.1989	122.9	185.1	5.85	105264	8.99	14.85	-3.14
9	-1.12	-0.0117	0.5743	121.2723	114.7	177.3	6	105931	8.82	14.83	-2.82
10	-2.33	-0.0254	0.5489	110.1202	104.7	171.1	6.38	106603	8.35	14.73	-1.97
11	-3.85	-0.0435	0.5054	96.4024	92.4	166.9	7.12	108037	7.59	14.71	-0.47
12	-5.7	-0.067	0.4384	79.6121	77.1	164.4	8.31	109386	6.59	14.89	1.72
13	-7.91	-0.0973	0.341	58.9673	57.8	162.9	9.98	109652	5.50	15.47	4.48
14	-10.46	-0.135	0.2061	33.9086	33.7	161.1	12.12	109865	4.53	16.65	7.59
15	-13.38	-0.181	0.025	3.9141	3.9	156.5	14.73	110163	3.74	18.47	11.00

Table 15.8. $n_s = 123$ turbine hub camberline geometry contd.

PCD does not allow the guide vanes to contact the runner blades in the event of a guide vane linkage breaking.

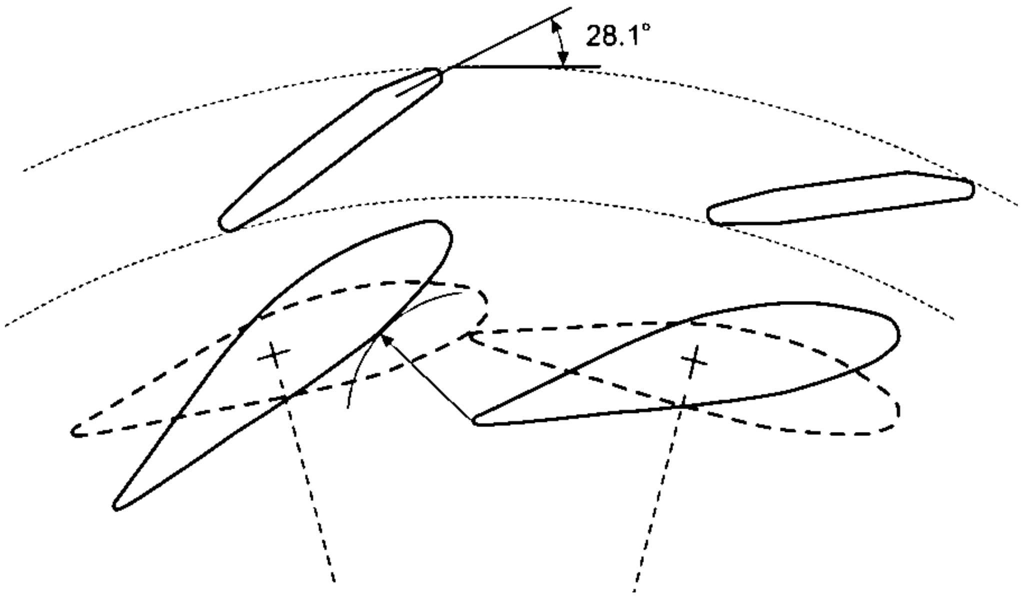

Fig. 15.6. Guide vane and stay vane arrangement.

15.6 Stay vane inlet and outlet diameters

Stay vane inner diameter has been determined at $D_{sv_2} = 1.054\text{m}$.

Stay vane strength considerations, to support the spiral casing, require either stay bolts Ø50 × 12 of the equivalent strength stay vanes.

For stay vanes constructed of 20mm thick flat plate, a diameter for the stay vane inlet, D_{sv_1}, of 1.2m is possible.

Caution : The calculations in this book which are of a structural nature are provided only to allow the hydrodynamic design to proceed. These structural sizes are NOT intended as a design guide.

15.7 Spiral casing design

The design procedure outlined in Chapter 11 is followed here.

$$\hat{n_s} = 123$$
$$KV_{sp} = 0.1515 \qquad \text{Equation 11.2}$$

For a design flow of $2.05\text{m}^3\text{s}^{-1}$, which pertains at $\hat{n_s} = 123$

$$D_{sp} = 0.6725\text{m} \approx 0.670\text{m} \qquad \text{Equation 11.3}$$
$$A_{sp} = 0.3552\text{m}$$

Select an area reduction factor of 0.98 then, $A_{sp_{0^o}} = 0.98 \times 0.3552 = 0.3481$ Table 15.9 sets out the calculation procedure.

Select an 18 section spiral, with $\theta = 0^\circ$ to 340° in the first column. Equation 11.4 is used to determine the non-dimensional area for each section. The actual area is obtained in column 3 based on the non-dimensional area $\times A_{sp_{0^o}}$.

Columns 4 and 5 solve for R and r iteratively using Equations 11.1 and 11.5 and assume a constant springing point height of 0.2126m.

The spiral casing is hydrodynamically defined with the exception of the nose zone and the inlet pipe which requires blending, as per Figure 11.3.

The development of each truncated cone segment, defined by R_θ and r_θ at each angular section is a relatively straight forward drawing exercise.

angle	non-dim area	spiral area	R	r
0	1.005	0.3498	0.9176	0.3349
20	0.949	0.3303	0.9075	0.3254
40	0.893	0.3109	0.8920	0.3108
60	0.837	0.2914	0.8869	0.3060
80	0.781	0.2719	0.8759	0.2957
100	0.725	0.2524	0.8645	0.2851
120	0.669	0.2329	0.8526	0.2741
140	0.613	0.2134	0.8400	0.2625
160	0.557	0.1939	0.8269	0.2506
180	0.501	0.1744	0.8129	0.2380
200	0.445	0.1549	0.7981	0.2248
220	0.389	0.1354	0.7819	0.2107
240	0.333	0.1159	0.7644	0.1958
260	0.277	0.0964	0.7449	0.1797
280	0.221	0.0769	0.7225	0.1622
300	0.165	0.0574	0.6958	0.1431
320	0.109	0.0379	0.6608	0.1225
340	0.053	0.0184	0.6062	0.1065

Table 15.9. Spiral casing design geometry.

Equation 11.6 produces a stay vane inlet angle of 28.1° based on $D_{sv_1} = 1.2m$, $D_{sp} = 0.67m$, and $\beta_{gv} = 0.14m$.

15.8 Guide vane & stay vane matching

It is necessary to design the stay vane angles such that losses within the guide vanes are minimised.

Flow conditions corresponding to $Q_{1/1}$, $\hat{Q}$ and $Q_{60\%}$ are analysed.

Equation 3.27 can be applied to establish an approximate relationship between Q and α_{gv}. A nominal exit angle of 20° is assumed together with a mean exit radius of 0.226m based on the root mean square of the exit diameter D_2^0. The efficiencies can be estimated from Figure 6.4 and Figure 1.5. See Table 15.10

% load	α_{gv}	η	Q
100 %	23°	0.82	$2.51 \approx Q_{1/1}$
87 %	18°	0.85	$2.18 \approx Q_{\perp}$
82 %	16.5°	0.86	$2.07 \approx \hat{Q}$
59 %	11.5°	0.78	$1.49 \approx Q_{60\%}$

Table 15.10. Estimated matching efficiencies.

The analysis presented in Table 15.11 assumes an $r_{sv_2} V_{\theta_{sv_2}} = 7.5$ at $Q_{1/1}$. This is a somewhat arbitary selection which is aimed at ensuring a torque characteristic similar to Figure 10.12

Stay vanes								
Q	Vm_{sv_1}	$V_{\theta_{sv_1}}$	V_{sv_1}	$rV_{\theta_{sv_1}}$	Vm_{sv_2}	$V_{\theta_{sv_2}}$	V_{sv_2}	$rV_{\theta_{sv_2}}$
2.53	4.79	8.87	10.08	5.32	5.46	14.23	15.24	7.50
2.05	3.88	7.18	8.17	4.31	4.42	11.53	12.35	6.08
1.50	2.84	5.26	5.98	3.15	3.24	8.44	9.04	4.45
Guide vanes								
Q	Vm_{gv_1}	$V_{\theta_{gv_1}}$	V_{gv_1}	$rV_{\theta_{gv_1}}$	Vm_{gv_2}	$V_{\theta_{gv_2}}$	V_{gv_2}	$rV_{\theta_{gv_2}}$
2.53	5.56	7.50	14.51	15.54	7.02	16.53	17.95	6.78
2.05	4.51	6.08	11.75	12.59	5.68	19.19	20.01	7.87
1.50	3.30	4.45	8.60	9.21	4.16	20.44	20.86	8.38

Table 15.11. Variation in velocities and loading through the guide vanes and stay vanes.

In Table 15.11, α_{gv} comes from Table 15.10. The stay vane exit angle of 21° is a flow angle. As the stay vanes are adding rV_θ to the flow, there will be a small amount of deviation associated with blade loading and blockage.

These two effects oppose one another and the stay vane angle is held to 21° in this design.

Figure 15.6 shows the stay vane arrangement selected. In this case the stay vanes are 20mm flat plates, appropriately chamfered to achieve the design entrance and exit angles.

The guide vanes in Figure 15.6 are shown in the open and closed positions. An additional guide vane positions could be drawn, corresponding to $Q_{60\%}$. For these three guide vane positions, the values of $\sin^{-1}\frac{o}{p}$ can be determined and checked against α_{gv} in Table 15.11.

References

D. G. Ainley and G. C. R. Mathieson. An examination of the flow and pressure losses in blade rows of axial flow turbines. Technical Report 2891, ARC R&M, 1951.

A. Akhtar. Materials technology for turbine performance. *Water Power and Dam Construction*, Aug 1986.

ASME. Test code for hydraulic prime movers, 1949.

N. C. Baines and D. Japikse. *Introduction to Turbomachinary, Concepts ETI*. 1997.

BS EN 60995: 1995. BS EN 60995: 1995, IEC 995: 1991, Determination of the prototype performance from model acceptance tests of hydraulic machines with consideration of scale effects, 1995.

Bureau of Reclamation. Stress analysis of hydraulic turbine parts. Eng. Monograph 30, 1962.

P. M. Came. Secondary loss measurements in a cascade of turbine blades. In *Conf. Pub. No. 3*. I. Mech. E., 1973.

A. D. S. Carter. The low speed performance of realted airfoils in cascade. Technical Report CP29, ARC, 1950.

T. Cebici and P. Bradshaw. *Momentum transfer in boundary layers*. Hemisphere, Washington, 1977.

N. Cumpsty. *Compressor aerodynamics*. Longman, 1989.

F. de Siervo and F. de Leva. Modern trends in selecting and designing Francis turbines. *Water Power and Dam Construction*, Aug 1976.

F. de Siervo and F. de Leva. Modern trends in selecting and designing Kaplan turbines. part 1. *Water Power and Dam Construction*, December 1977.

J. D. Denton. Throughflow calculations for transonic axial flow turbines. *ASME*, 100, Apr 1978.

J. D. Denton. Loss mechanisms in turbomachines. ASME IGTI Scholar Award Paper, 1993.

W. J. Duncan, A. S. Thom, and A. D. Young. *The mechanics of fluids*. Edward Arnold, London, 2nd edition, 1970.

J. Dunham. A review of cascade data on secondary losses in turbines. *J. Mech. Eng. Science*, 12(1), 1970.

V. T. Forster. Performance loss of modern steam-turbine plant due to surface roughness. *Proc. Inst. Mech. Engs.*, Nov 1966.

C. Freeman. Tip clearance effects in axial turbomachines. Lecture series 1985-05, Von Karman Institute for fluid dynamics, April 15-19, 1985, 1985.

H. Grein. Some considerations on the surface roughness of wetted components of large hydraulic machines. *Escher Wyss News*, 1, 1975.

W. Gysel. Weldability of high tensile martensitic cast steel with 13% Cr and 4% Ni. Central Laboratory Report No. 12/1968, George Fisher Ltd., Schaffhausen, Schweißtechnik, 1968.

M. R. Head and V. C. Patel. Improved entrainment method for calculating turbulent boundary layer development. Technical Report 3643, ARC, Mar 1968.

Gunnar Heskestad and D.R. Olberts. Influence of trailing–edge geometry on hydraulic–turbine–blade vibration resulting from vortex excitation. *ASME Journal of Engineering for Power*, pages 103–110, April 1960.

S. F. Hoerner. *Fluid-dynamic drag; practical information on aerodynamic drag and hydrodynamic resistance.* Midland Park, N.J., 1965.

R. J. Hothersall. Turbine selection under 1 MW, cross-flow or conventional turbine. *Hydro Review*, Feb 1987.

R. J. Hothersall. Assessing the design of draft tubes. *Water Power and Dam Construction*, April 1988.

I. Huntsman. *An investigation of radial inflow turbine aerodynamics.* PhD thesis, Cambridge University, 1993.

IEC 60193 (1999). CEI IEC 60193 2nd Edn. 1999-11, Hydraulic turbines, storage pumps and pump turbines – model acceptance tests, 1999.

R. T. Knapp. *Cavitation mechanics and its relation to the design of hydraulic equipments. James Clayton Lecture, April 1952.* Inst. Mech. Engrs., 1952.

R. T. Knapp, J. W. Daily, and F. G. Hammitt. *Cavitation.* McGraw Hill, 1970.

N. K. Kovalev. *Hydro turbines, design and construction.* Israel Program for Scientific Translations, Jerusalem, 1965.

T. Kubota, S. Takimoto, and M. Kawashima. Effect of stay vane shape on the performance of hydraulic turbine. In *Symposium on Hydraulic Machinary in the Energy related Industries (12th IAHR Symposium)., Stirling, Swed*, pages 634–648. Natl Engineering Lab, Conference Section, 1984.

R. I. Lewis. *Turbomachinery performance analysis.* Arnold, 1996.

C. Liess. Flow induced vibrations. In *International Conference, BHRA, Bowness-on-Windermere, England*, 1987.

B. S. Massey. *Mechanics of fluids.* Chapman & Hall, sixth edition, 1989.

M. W. McBride. Refinement of the mean streamline method of blade section design. *J. Fluids Eng.*, page 561, September 1977.

D. S. Miller. Internal flow systems. 2nd Edition. BHRA (Information Services), 1990.

E. Mosonyi. Water power development. Vols. 1 & 2. Akademiai, Budapest, 1987.

M. Nechleba. *Hydraulic turbines, their design and equipment.* Artia, Prague, 1957.

F. Numachi. Accelerating cascade data. *J. Basic Eng.*, Sep 1964.

J. P. Quayle, editor. *Kempe's Engineers year book.* Morgan-Grampian, London, 89th edition, 1984.

D. A. Rains. Tip clearance flows in axial flow compressors and pumps. Technical Report 5, California Institute of Technology, Hydrodynamics Laboratory, 1954.

P.R. Rodrigue. Cavitation pitting mitigation in hydraulic turbines. vol 1 & 2. Technical Report Final Report EPRI AP-4719 Project 1745-10, Electric Power Research Institute, Palo Alto, CA, August 1986.

A. Ruprecht, M. Heitele, T. Helmrich, W. Moser, and T. Aschenbrenner. Numerical simulation of a complete francis turbine including unsteady rotor/stator interactions, 2000. URL `http://www.ihs.uni-stuttgart.de/forschung/veroeff/stroem/2000_03.pdf`.

H. Schlichting. *Boundary-layer theory.* McGraw-Hill, 7th edition, 1979.

R. Simoneau. Vibratory, jet and hydroturbine cavitation erosion. In O. Furuya and H. Kato, editors, *Cavitation and Multiphase Flow Forum*, volume FED-Vol 109. ASME, Bokk No. G00597, 1991.

J. D. Stanitz. Effect of blade-thickness taper on axial velocity distributions at the leading edge of an entrance rotor blade row with axial inlet and the influence of this distribution on the alignment of the rotor row for zero angle of attack. Technical Report TN-2986, NACA, 1953.

R. H. Thicke. Practical solutions for draft tube instability. *Water Power and Dam Construction*, Feb 1981.

B. Thwaites. Approximate calculation of the laminar boundary layer. *Aeronautical Quarterly*, pages 245–280, 1949.

F. Weinig. *Die Stromung und die Schaufeln von Turbomaschinen.* J. H. Borth, Leipzig, 1935.

F. J. Wiesner. A review of slip factors for centrifugal impellers. *Trans. ASME J. Eng. Power*, 1967.

D. A. Williams. Selection of water turbines for small hydro electric projects. (Gilbert Gilkes & Gordon) Int Course for small hydropower development, 7–11 Oct 1996. New Delhi. (Int. Assoc. for Small Hydro), 1996.

G. F. Wislicenus. *Fluid mechanics of turbomachinery.* McGraw-Hill, New York, 2nd edition, 1965.

G. F. Wislicenus. Preliminary design of turbo pumps and related machinery. Technical Report 1170, NASA, 1986.

O. Zweifel. The spacing of turbomachine blading, especially with large angular deflection. *Brown Boveri Review*, 32(12):436–444, December 1945.

UNITED NATIONS INDUSTRIAL DEVELOPMENT ORGANIZATION
Energy and Cleaner Production Branch
Vienna International Centre, PO Box 300, A 1400 Vienna, Austria
Telephone: +(43) (1) 26026-4575, Fax: +(43) (1) 26026-6855
E-mail: energy@unido.org Internet: www.unido.org